

UNIVERSITÉ DE MONTRÉAL

**ENABLING TECHNOLOGIES FOR DISTRIBUTION OF BROADBAND
RADIO OVER FIBER**

BOUCHAIB HRAIMEL

DÉPARTEMENT DE GÉNIE ÉLECTRIQUE
ÉCOLE POLYTECHNIQUE DE MONTRÉAL

THÈSE PRÉSENTÉE EN VUE DE L'OBTENTION
DU DIPLÔME DE PHILOSOPHIAE DOCTOR (Ph.D.)
(GÉNIE ÉLECTRIQUE)

AOÛT 2010

© Bouchaib Hraimel, 2010.

UNIVERSITÉ DE MONTRÉAL

ÉCOLE POLYTECHNIQUE DE MONTRÉAL

Cette thèse intitulée:

ENABLING TECHNOLOGIES FOR DISTRIBUTION OF BROADBAND RADIO OVER
FIBER

présentée par : M. HRAIMEL Bouchaib

en vue de l'obtention du diplôme de : Philosophiae Doctor

a été dûment acceptée par le jury d'examen constitué de :

M. AKYEL Cedvet, D.Sc.A., président

M. WU Ke, Ph.D., membre et directeur de recherche

M. KASHYAP Raman, Ph.D., membre

M. CHEN Lawrence R., Ph.D., membre

DEDICATED TO

My wife

Karla Ortega Dolovitz

My loving kids: Jacob and Isaac

For their continuous love and support

ACKNOWLEDGMENTS

I would like to express my sincere gratitude to my supervisor Dr. Ke Wu for his guidance, discussions and long hours devoted to guiding my research and writings.

My thanks goes also to Dr. Xiupu Zhang for his insightful discussions and giving me the opportunity to work at the Advanced Photonics System Lab at Concordia University, Montréal, Canada that allowed me to fulfill all experimental work in my thesis.

I thank Dr. Mohmoud Mohamed for his help and discussions.

I would also like to extend my gratitude to my wife Karla for her encouragement and support throughout my studies.

Last but not least, I am very grateful to my parents and family for their support, encouragement and understanding.

ABSTRACT

Bouchaib Hraïmel, Ph. D.

École Polytechnique de Montréal, 2010

Radio over fiber (RoF) has been considered as a very promising technology that will indisputably compete as a viable solution for the distribution of current and future broadband wireless communication systems such as IEEE 802.15.3a WPAN using Multiband-Orthogonal Frequency Division Multiplexing Ultra-Wideband (MB-OFDM UWB) signal. The RoF technology makes use of subcarrier modulation (SCM) to modulate an RF signal on light, which in turn will be transmitted by optical fiber. Unfortunately, the transmission of RF signal over fiber is subject to a number of impairments. These impairments include: low optical to electrical conversion efficiency, fiber chromatic dispersion, and nonlinearity of the optical front end, etc..

The objective of this thesis is to develop enabling technologies for broadband RoF systems. The proposed design platforms and techniques should address nonlinear distortion induced by the optical transmitter; combat optical power fading issue induced by the chromatic dispersion; and improve modulation efficiency of the optical small-signal modulation without significantly adding excessive expense and complexity to the RoF system.

First of all, the performance of MB-OFDM UWB wireless over fiber transmission system is investigated considering optical modulation and demodulation aspects. Theoretical analysis of the effects of fiber chromatic dispersion, relative intensity noise (RIN), optical transmitter and optical receiver response on system performance is carried out considering amplitude and phase distortion. Experiments are conducted, which have verified our theoretical analysis and a good agreement is obtained. It is found that low RF modulation index (4%) for optical transmitter with Mach-Zehnder modulator (MZM), and optical receiver with Chebyshev-II response is the best for MB-OFDM UWB over fiber. The wireless transmission performance is limited by the UWB receiver sensitivity. Moreover, a high received optical power is required for transmission of MB-OFDM UWB signal over fiber. It is also found that the parameters like laser output power, laser linewidth and fiber dispersion that control RIN, will critically affect the overall performance of a UWB over fiber system.

Then, the performance of MB-OFDM UWB over fiber transmission system is also studied considering the effect of in-band jammers such as WiMAX, WLAN MIMO, WLAN and marine radar. Experiments were performed to show the effect of fiber transmission under various interferer power levels. It is found that in-band interferers can cause a severe degradation in system performance if certain interferer to UWB peak power ratio is not maintained.

Second, a novel technique for the suppression of intermodulation distortion (IMD) using a mixed-polarization MZM is proposed. A comprehensive investigation was conducted in theory, simulation and experiment. It is found that the suppression of third order IMD (3IMD) using the mixed-polarization MZM is independent of modulation index. The power fading of the RF carrier and crosstalk due to IMD via fiber chromatic dispersion is significantly suppressed compared to using the conventional OSSB MZM. It was shown that an improvement of ~ 12.5 dB in spurious free dynamic range (SFDR) using discrete optical components was achieved and a good agreement with theory and simulation is obtained. The experimental demonstration of the proposed technique for MB-OFDM UWB signal shows an improvement of the error vector magnitude (EVM) by 2 dB when transmitted over 20km of single mode fiber.

Because an EAM is polarization independent it is usually preferred to be used at the RoF base station. However, mixed polarization technique cannot be applied to an EAM. Then a pre-distortion circuit for the linearization of EAM using reflective diode pair has been designed for the MB-OFDM UWB system at bandgroup-1. It is found that the designed predistortion circuit leads to 11 dB improvements in the SFDR at the center frequency of bandgroup-1, and more than 7 dB improvements in the suppression of 3IMD over the whole bandgroup-1. By evaluating the predistortion circuit with the MB-OFDM UWB signal, a 1 dB EVM improvement is obtained for MB-OFDM UWB over 20 km fiber. This suggests that the proposed predistortion circuit is a cost effective broadband linearization technique for MB-OFDM UWB over fiber.

Third, a novel modulation technique is also proposed to overcome the fiber chromatic dispersion that can cause power fading when ODSB modulation is used. This modulation technique also improves the RF power by up to 3 dB compared to OSSB modulation. The main advantage of the proposed technique is its simplicity and implementation in the electrical domain with phase shifting. Theoretical analysis was made to obtain the optimum conditions for best performance, such as optimum phase shift and impact of MZM extinction ratio. Then simulation

was used to further analyze the proposed modulation and compared to the theory. Moreover, we present an experimental proof to validate our concept for single RF tone and an MB-OFDM UWB signal.

Fourth, we proposed and investigated for the first time a technique that improves the modulation efficiency in RoF system. We have shown that a dual parallel MZM (dMZM) can be used for obtaining not only OSSB modulation but also a wide dynamic range of optical carrier suppression ratio (OCSR) tunability can be obtained by varying the bias voltage applied to the inner MZMs. It is found that the optimum OCSR to obtain maximum RF output power depends on the modulation index and extinction ratio of the dMZM. To achieve an OCSR of 0 dB there is a minimum required extinction ratio that decreases with the increase of the modulation index. Moreover, the impact of OCSR on the performance of MB-OFDM UWB signal is also investigated. It is found that the maximum received RF power is obtained at 0 dB OCSR while minimum EVM of the received MB-OFDM UWB constellation is achieved at 5.4dB OCSR.

Finally, the performance of millimetre-wave (MMW) MB-OFDM UWB signal generation and transmission over fiber using an MZM and EAM for optical frequency up and down-conversion technique for down and up-link, respectively, is investigated. For MMW up-conversion, it is found that the MZM modulation index of 60% (theoretically) and 70% (experimentally) is needed to achieve the minimum required EVM of -16 dB after 20 km of fiber transmission. It is also found that a typical extinction ratio does not have significant impact on the EVM, while MZM bias drift of 20% degrades the EVM by less than 1 dB. For MMW down-conversion, four-wave-mixing (FWM) in an EAM is used. FWM efficiency has been experimentally investigated versus reverse bias voltage and input pump power to the EAM. It is found that maximum FWM efficiency is obtained at 2.3 V reverse bias and increases by a slope of 2 in dB scale with respect to the input pump power. At 2.3 V reverse bias voltage, it is found that $\sim 7.5\%$ is the best RF modulation index for the EAM driven by the MMW MB-OFDM UWB, and the down-conversion is almost insensitive to the received optical power. This investigation shows a potential possibility for the proposed techniques to be used for MMW up/down conversion of MB-OFDM UWB signal over fiber.

RÉSUMÉ

La radio sur fibre (RoF) a été considérée comme une technologie prometteuse qui concurrencera de manière indisputable comme solution viable pour la distribution des systèmes de communication sans fil à bande large actuels et futurs. La technologie RoF emploie la modulation d'onde sous-porteuse (SCM) pour moduler la lumière par un signal RF, qui à son tour sera transmise par la fibre. Malheureusement, la transmission du signal RF sur la fibre est sujette à un certain nombre de défauts. Ces défauts incluent le faible rendement de la conversion optique en électrique, à la dispersion chromatique de la fibre, et à la non-linéarité de l'émetteur optique.

L'objectif de cette thèse est de développer des technologies habilitantes pour la radio sur fibre à large bande. Les conceptions proposées devraient adresser la déformation non linéaire induite par l'émetteur optique, combattre le problème de l'affaiblissement de la puissance RF induit par la dispersion chromatique de la fibre, et améliorer l'efficacité de modulation optique au petit signal sans augmenter de manière significative le coût et la complexité du système RoF. Pour le signal RF à large bande, nous considérons le signal à bande ultra large utilisant le multiplexage par répartition orthogonale de la fréquence (ULB MB-MROF), qui a été proposé comme solution pour le réseau de secteur personnel sans fil d'IEEE 802.15.3a (WPAN).

D'abord, la performance de la transmission de l'ULB MB-MROF par la fibre est étudiée en considérant l'impact de modulation et démodulation optique. L'analyse théorique de l'effet de la dispersion de la fibre, de la réponse de l'émetteur optique et du récepteur optique sur la performance du système est effectuée en considérant la distorsion de la phase et de l'amplitude. Des expériences sont réalisées pour vérifier notre analyse théorique et une bonne concordance est obtenue. Il est constaté que l'index de modulation RF de $\sim 4\%$ est optimum pour l'émetteur optique avec le modulateur de Mach-Zehnder (MZM), et le récepteur optique avec la réponse de Tchebychev-II est le meilleur pour l'ULB MB-MROF sur fibre. Aussi, la performance de la transmission sans fil est limitée par la sensibilité du récepteur ULB MB-MROF. Il est aussi trouvé qu'une haute puissance optique reçue est exigée pour la transmission du signal de l'ULB MB-MROF sur fibre.

L'analyse théorique de l'effet sur la performance du système est effectuée pour la dispersion chromatique de la fibre qui convertit le bruit de phase du laser en bruit d'intensité ou bruit d'intensité relative (RIN). Des expériences sont entreprises pour vérifier notre analyse théorique. La simulation est aussi effectuée pour montrer la relation entre le RIN et la fréquence centrale des bandes de l'ULB. Il est constaté que la performance globale du système ULB sur fibre est clairement affectée par les paramètres comme la puissance de sortie du laser, largeur spectrale du laser et la dispersion de la fibre qui contrôlent le RIN.

Il est aussi étudié la performance de la transmission de l'ULB MB-MROF par la fibre en considérant l'effet des brouilleurs dans la bande tels que WiMAX, WLAN MIMO, WLAN et radar de marine. Des expériences ont été effectuées pour montrer l'effet de la transmission par fibre sous différents niveaux de puissance du brouilleur. Il est constaté que les brouilleurs dans la bande peuvent causer une dégradation sérieuse dans la performance du système si un certain rapport de la puissance du brouilleur sur la puissance crête de l'ULB n'est pas maintenu.

Pour supprimer de la distorsion d'intermodulation on propose une technique originale utilisant un mélange de polarisation du MZM. Une étude détaillée a été effectuée par théorie, simulation et expérimentation. On a constaté que la suppression de la distorsion d'intermodulation du troisième ordre (IMD3), utilisant le mélange de polarisation du MZM, est indépendante de l'index de modulation. L'évanouissement du signal RF et de la diaphonie due à l'intermodulation par l'intermédiaire de la dispersion chromatique de la fibre est considérablement supprimé comparé à l'usage du modulateur MZM à band latérale unique optique (OSSB) conventionnel. Ensuite, nous avons expérimentalement vérifié la technique de modulation par mélange de polarisation. On a montré qu'une amélioration de ~ 12.5 dB de la gamme dynamique libre de parasites (SFDR) a été réalisée en utilisant des composantes optiques distinctes, et une bonne concordance avec les résultats de la théorie et la simulation est obtenue. L'application expérimentale de la technique proposée au signal ULB MB-MROF montre une amélioration de l'EVM de 2 dB après la transmission sur 20 km de fibre optique monomode.

Puisqu'un modulateur par électroabsorption (EAM) est indépendant de la polarisation, il est préférable d'être employé à la station de base de la RoF. Cependant, la technique de polarisation mixte ne peut pas être appliquée à un EAM. Alors, un circuit de pré-distorsion pour la linéarisation de l'EAM, utilisant une paire de diodes réfléchissantes, a été conçu pour le système

de l'ULB MB-MROF à la bande de groupe 1 (3.1~ 4.8 GHz). On a constaté que le circuit conçu de pré-distorsion mène à 11dB d'amélioration du SFDR à la fréquence centrale de la bande de groupe 1, et plus de 7 dB d'amélioration dans la suppression de IMD3 sur toute la bande de groupe 1. En évaluant le circuit de pré-distorsion avec un signal ULB MB-MROF, on a amélioré l'EVM de 1dB pour les trois premières bandes ULB MROF sur 20 km de fibre. Ceci suggère que le circuit proposé de pré-distorsion soit une technique de linéarisation à large bande rentable pour l'ULB MB-MROF sur fibre.

On propose aussi une technique originale de modulation pour surmonter l'évanouissement du signal causé par la dispersion chromatique de la fibre quand la modulation optique à double bande latérale (ODSB) est employée. Cette technique de modulation améliore aussi la puissance RF par 3dB comparé à la modulation OSSB. Le principal avantage de la technique proposée est sa simplicité et son application dans le domaine électrique avec un déphaseur. L'analyse théorique a été faite pour obtenir les conditions optimales pour la performance optimale, telle que le déphasage optimal et l'impact du rapport d'extinction de MZM. La simulation a été faite pour une analyse supplémentaire de la modulation proposée et ensuite pour la comparer à la théorie. En outre, nous présentons une preuve expérimentale pour valider notre concept pour un signal RF d'une seule porteuse et un signal ULB MB-MROF. En utilisant notre technique de modulation proposée, une amélioration de puissance RF de 3dB, comparée à OSSB, a été réalisée expérimentalement sans dégradation de la qualité du signal.

Après, nous avons proposé une technique de modulation qui améliore l'efficacité de modulation dans la transmission du signal radio sur fibre. Nous avons montré qu'un modulateur de deux MZMs en parallèle (dMZM) peut être employé pour obtenir non seulement la modulation OSSB mais aussi un rapport variable de la porteuse optique sur la bande latérale (OCSR). Le dMZM est intégré dans une puce de Niobate de Lithium, tranchée perpendiculairement à l'axe électrique, et se compose d'un MZM externe avec un MZM interne inséré dans chaque bras. La fonction d'ajustement du OCSR utilisant ce modulateur est proposée et étudiée pour la première fois à notre connaissance. On a montré qu'une large plage dynamique d'ajustement de l'OCSR peut être obtenue en variant la tension de polarisation appliquée aux MZMs internes. On a constaté que un OCSR optimale pour obtenir le maximum de puissance de sortie RF dépend de l'index de modulation et du rapport d'extinction du dMZM. Pour réaliser un

OCSR de 0 dB il y a un rapport d'extinction minimal exigé qui diminue avec l'augmentation de l'index de modulation. En outre, nous avons étudié l'impact du OCSR sur la performance du signal ULB MB-MROF. On a constaté que le maximum de puissance RF reçue est obtenu à un OCSR de 0 dB, tandis que le minimum d'EVM de la constellation du ULB MB-MROF reçue est obtenu à un OCSR de 5.4dB.

On a expérimentalement démontrée la performance de la génération et de la transmission de signaux à l'onde millimétrique ULB MB-MROF par fibre utilisant une technique optique comme changeur élévateur de fréquence. On a constaté que $\sim 4\%$ est l'indice optimal de modulation RF du MZM commandé par le ULB MB-MROF, et un indice de modulation LO de 60% (théoriquement) et 70% (expérimentalement) est nécessaire pour obtenir un EVM maximum de -16dB requis après 20 km de transmission par fibre. On a aussi constaté qu'un rapport d'extinction typique n'a pas d'impact significatif sur l'EVM, tandis que l'instabilité de la différence de potentiel de 20% peut dégrader l'EVM par au plus 1 dB.

Finalement, nous avons expérimentalement étudié et démontré une nouvelle technique utilisant mélange à quatre ondes (FWM) dans un modulateur à électro-absorption (EAM) pour convertir l'onde millimétrique (MMW) en fréquence intermédiaire pour des liaisons montantes de l'onde millimétrique sur fibre. L'efficacité de FWM a été étudiée en fonction de la tension de polarisation inverse et de la puissance de pompe à l'entrée de l'EAM. On a constaté que l'efficacité maximum de FWM est obtenue à de la tension de polarisation inverse de 2.3 V et augmente par une pente de 2 à l'échelle décibels par rapport à la puissance de pompe d'entrée. Nous avons également étudié la performance de la transposition par abaissement de fréquence de signal MMW ULB MB-MROF par FWM dans un EAM. On a trouvé que $\sim 7.5\%$ est l'indice de modulation RF optimal de l'EAM commandé par le ULB MB-MROF, et la transposition par abaissement de fréquence est presque insensible à la puissance optique reçue. Cette recherche montre une potentielle possibilité pour que les technique photoniques, de la transposition par élévation ou abaissement de fréquence, proposées soient employées pour le signal MMW ULB MB-MROF sur fibre.

CONDENSÉ EN FRANÇAIS

Dans les systèmes de distribution de Radio sur Fibre (RoF), la modulation optique d'onde sous-porteuse (SCM) est adoptée pour produire en général deux bandes latérales autour de la porteuse optique, c.-à-d., la double bande latérale SCM. Il a été constaté que modulation optique à double bande latérale (ODSB) d'onde sous-porteuse présentera un affaiblissement de la puissance RF dans les systèmes de la RoF à cause de la dispersion chromatique de la fibre [10]. Cet affaiblissement de puissance peut causer une pénalité de puissance RF dans la performance du système [11] et par la suite le système RoF ne fonctionnera pas à certaines longueurs de la fibre.

Ainsi, la modulation optique à bande latérale unique (OSSB) d'onde sous-porteuse a été proposée et a été utilisée pour supprimer cet affaiblissement de puissance [12]. Cependant, comparé à l'ODSB, lorsque l'OSSB est employée la moitié de la puissance RF est perdue à cause de la suppression de l'une des deux bandes latérales. Plusieurs approches ont été proposées pour contrer l'affaiblissement de la puissance, induite par la dispersion chromatique de la fibre, dans la transmission photonique analogue utilisant ODSB conventionnelle, y compris un récepteur en diversité de modulation [13], réseaux non linéaire chirp [14] et la conjugaison optique de phase mi-chemin [15]. Ces techniques augmentent la complexité du récepteur et limitent la largeur de bande [13]. En plus, elles doivent être activement accordées, ou introduisent une dispersion différentielle causant un évanouissement du signal RF [14], ou sont limitées par le changement asymétrique de puissance [15-16].

En outre, la performance de RoF est sensible aux distorsions non linéaires induites par les non-linéarités dans les lignes de transmission et la réponse du modulateur optique. Par exemple, le modulateur externe tel que le modulateur de Mach-Zehnder (MZM) ou le modulateur à électro-absorption (EAM) exhibe une réponse non-linéaire dans sa fonction de transfert. Les non-linéarités produisent des distorsions harmoniques (HD) et d'intermodulations (IMD) optiques, que s'elles ne sont pas supprimées, dégraderont sévèrement la transmission RoF. Parmi les distorsions non-linéaires, les produits IMD peuvent nuire à la transmission de la RoF, parce qu'ils sont plus probables de coexister dans la même bande que la porteuse RF et sont difficiles à filtrer.

La modulation optique en petit signal est la façon la plus simple pour réduire au minimum les harmoniques optiques d'ordre supérieur. Ceci est particulièrement important pour des systèmes non linéaires sensibles aux harmoniques d'ordre élevé, tels que les liens incorporant le multiplexage par répartition en longueur d'onde dense (DWDM), le SCM, ou le multiplexage par répartition orthogonale de la fréquence (MROF). Dans la modulation optique du petit signal, le rapport optique de la porteuse sur la bande latérale (OCSR) peut excéder 20 dB, c.-à-d., comparé à la porteuse optique, la puissance optique de la bande latérale modulée est très faible. Donc, la majorité de la puissance optique reçue par photo-détection est convertie en courant continu (C.C) tandis qu'une petite fraction est convertie en signal RF. Ceci mène à une très faible efficacité de transmission du signal RF. En outre, puisque l'information est portée par les bandes latérales optiques, dans le lien de la RoF avec la modulation optique du petit signal, une puissance optique du récepteur relativement élevée est nécessaire pour obtenir le rapport signal sur bruit (SNR) nécessaire. Par conséquent, un C.C relativement élevé, qui est principalement produit par la porteuse optique, peut endommager le photo-détecteur. En plus, une grande puissance optique du récepteur résulte en un plus faible bilan de puissance et une distance de transmission plus courte de la liaison par fibre. Aussi, les problèmes de non-linéarité liés à la fibre optique soumise à une puissance optique élevée, comme le mélange à quatre ondes (FWM) dans les systèmes de DWDM, peuvent surgir et mener à une détérioration additionnelle des performances.

Une méthode efficace pour améliorer l'efficacité de modulation des liens RoF, avec la modulation optique de petit signal, est de réduire le rapport de puissance de la porteuse optique sur celle de la bande latérale. En supprimant la porteuse optique, une grande portion de la puissance optique est convertie en signal RF et ainsi le gain intrinsèque du lien RoF est augmenté. Un certain nombre de méthodes pour supprimer la porteuse optique ont été proposées et démontrées [17-21]. En général, la plupart des méthodes démontrées sont basées sur le filtrage optique avec: filtre coupe-bande [17-18]; filtre optique de blocage hyperfin [19]; filtrage par diffusion de Brillouin non linéaire [20]; ou basées sur la tension de polarisation du MZM [21]. Cependant, ces techniques ont besoin d'accorder la porteuse optique [17-18], souffrent d'une grande perte par insertion et une pénalité de puissance [19], tolèrent une déformation de signal et une instabilité de la puissance transmise [20, 22]; ou expérimentent une dispersion chromatique induisant un affaiblissement de puissance [21].

D'autre part, pour fournir des services sans fil à large bande et de haute capacité dans des architectures pico-cellulaire ou micro-cellulaire, il faut opérer à des fréquences d'onde millimétriques (MMW). Transférer la fréquence d'opération radio dans la région d'onde millimétrique surmonte la congestion spectrale dans la région inférieure de micro-onde. En outre, les principaux avantages de l'utilisation de l'onde millimétrique (57-64 GHz, par exemple) sont 7 GHz de disponibilité de largeur de bande aussi bien que la perspective des réseaux de multi-gigabit au téra-bit. Pour réaliser des réseaux d'accès de haute capacité, les normes IEEE 802.15.3a [5] et IEEE 802.15.3c [23] ont été proposées pour le réseau d'accès local personnel à large bande (WPLAN). Dans IEEE 802.15.3a, 14 canaux RF ultra-large-bande (ULB) à multiplexage par répartition orthogonale de la fréquence (MROF), utilisant la bande de 3.1-10.6 GHz, ont été suggérés et chaque canal peut supporter des données à un débit jusqu'à 480 Mb/s. Dans IEEE 802.15.3c, 4 canaux d'onde millimétrique de MROF ont été proposés, utilisant la bande de 56-67 GHz et chaque canal peut fournir des données à un débit jusqu'à 3 Gb/s. Ainsi, l'onde millimétrique sans fil, dans IEEE 802.15.3c, peut transmettre des signaux de plus haut débit binaire comparé à IEEE 802.15.3a. Cependant, l'onde millimétrique peut être sévèrement atténué lorsqu'elle est transmise par air, selon la bande de fréquence, telle que ~ 15 dB/km à 60 GHz. Alors, la transmission de l'ULB à la bande d'onde millimétrique sans fil est limitée à quelques mètres et beaucoup de stations de base doivent être déployées pour assurer la couverture d'un grand secteur. Il est certes que la fibre optique ait une énorme largeur de bande, mais elle ne supporte pas la mobilité des utilisateurs et la reconfiguration flexible du système. Par conséquent, si l'on combine, dans les réseaux d'accès, la communication sans fil d'onde millimétrique et la communication par fibre optique, il serait possible de réaliser simultanément des réseaux locaux d'accès de haute capacité avec des avantages de: grande portée, mobilité et faible coût; et plus particulièrement la complexité du système et les dispositifs coûteux pourraient être déplacés à la station centrale (SC). Cependant, en plus des perturbations précédemment cités, la transmission d'onde millimétrique sur de la fibre optique peut devenir impraticable à cause de l'indisponibilité et du défi de conception des composants électriques à large bande et à haute fréquence tels que: les mélangeurs, les amplificateurs de puissance, les oscillateurs locaux, les récepteurs et les émetteurs optiques, etc. Dans une liaison RoF montante, le signal sans fil à onde millimétrique, qui est converti par conversion optique-électrique (O/E), est toujours en bande de fréquence millimétrique, ce qui nécessite l'usage d'un récepteur optique

plus cher. De façon similaire, une liaison RoF descendante exigera un émetteur et un récepteur optique à large bande. Par conséquent, des techniques simples et rentables seront exigées pour produire et distribuer des signaux sans fil d'onde millimétrique de capacité élevée pour les deux liaisons : montante et descendante.

L'objectif de ces travaux de recherche est de développer de nouvelles technologies habilitantes pour surmonter l'affaiblissement de puissance du signal RF dû à la dispersion chromatique de la fibre, les non-linéarités dans les modulateurs optiques, pour améliorer l'efficacité de la modulation optique et pour transmettre l'onde millimétrique sur la fibre. Les technologies proposées apporteront des améliorations par rapport à celles existantes, afin de rendre les systèmes de RoF une alternative économique aux réseaux sans fil, réseaux optiques à large bande et passifs (PONs) existants. Basé sur ces travaux de recherche, nous avons:

- Proposé, développé et étudié en détail par théorie, simulation et expérience, des technologies et conceptions originales pour :
 - Linéariser des modulateurs optoélectroniques à large bande,
 - Compenser l'affaiblissement de la puissance du signal RF dû à la dispersion chromatique de la fibre,
 - Améliorer l'efficacité de la modulation optique,
 - Élever/Abaissé la fréquence à l'onde millimétrique pour la liaison RoF descendante/montante.
- Vérifié et évalué expérimentalement la performance de la transmission du signal ULB MB-MROF par fibre en appliquant nos techniques proposées.

Dans ce travail de thèse, nous avons étudié tout d'abord, en termes d'erreur de magnitude du vecteur (EVM), la dégradation de la performance de transmission du signal ULB MB-MROF sur fibre causée par divers perturbations comprenant les non-linéarités du MZM, la dispersion de la fibre, la puissance optique reçue et la réponse du récepteur. En outre, la performance de l'ULB MB-MROF sans fil a été expérimentalement étudiée, en termes de taux d'erreur par paquets (PER), une fois transmise plus de 20 kilomètres de fibre monomode (SMF). PER a été mesuré à différents débits binaires pour évaluer la sensibilité du récepteur, la puissance de l'ULB

transmise minimale requise, effet de la distance sans fil, index de modulation du MZM, et la puissance optique reçue etc. En plus, la performance de l'ULB MB-MROF transmise par fibre a été étudiée sous l'influence du bruit relatif d'intensité (RIN) en considérant les paramètres du système tels que: la puissance de sortie du laser, la largeur spectrale et la longueur de transmission par fibre. La performance de transmission de l'ULB MB-MROF par fibre a été également évaluée considérant l'effet des brouilleurs dans la bande tels que: WiMAX, WLAN MIMO, WLAN et radar de marine.

Basé sur ces travaux de recherche on a trouvé :

- Pour un MZM modulé à OSSB, l'index de modulation RF de $\sim 4\%$ est optimum pour obtenir la meilleure performance en EVM de transmettre l'ULB MB-MROF par fibre,
- Un récepteur optique avec la réponse de Tchebychev-II de cinquième ordre et de la largeur de bande de 3 GHz est le meilleur pour la meilleure performance en EVM de transmettre l'ULB MB-MROF par fibre considéré dans notre travail,
- La sensibilité du récepteur optique dans la transmission de l'ULB par fibre est raisonnablement faible et la performance se dégrade presque linéairement avec la diminution de la puissance optique du récepteur,
- La transmission par fibre optique est encore limitée par le bruit de phase du laser, qui est converti en RIN, et par la distorsion de phase induits par la dispersion chromatique de la fibre,
- Le système devrait être opéré à une haute puissance de sortie du laser pour éviter la dégradation du RIN,
- Un laser d'une largeur spectrale étroite avec un faible RIN améliorera de manière significative la performance du système,
- La portée de transmission sans fil de l'ULB MB-MROF est limitée par la sensibilité de récepteur,
- La performance de transmission de l'ULB MB-MROF est sévèrement affectée par différents signaux brouilleurs dans la bande si certain rapport de puissance du signal brouilleur sur la puissance crête de l'ULB n'est pas maintenu : Pour répondre à

l'exigence de -16 dB EVM, qui est le seuil de l'EVM spécifié par l'essai de conformité selon la norme récente de WiMedia pour l'ULB, ce rapport est de ~ 14 , ~ 15 , ~ 17.5 et ~ 20 dB pour les signaux WiMAX, radar, WLAN MIMO et WLAN, respectivement, pour la distribution sur 20 kilomètres de fibre monomode.

Nos résultats permettront aux futurs chercheurs, dans le domaine de la transmission de l'ULB MB-MROF par fibres optiques, d'optimiser la performance de la transmission de l'ULB par fibres optiques en fonction des paramètres du système et sous la présence de tous les signaux brouilleurs coexistant sur la même bande de fréquence.

Dans ce travail, nous avons proposé, développé et étudié en détail par théorie, simulation et expérimentation, des nouvelles technologies et techniques de conception habilitante pour la linéarisation à large bande, compensation de l'évanouissement du signal RF dû à la dispersion chromatique, amélioration de l'efficacité de la modulation optique, et la transposition par élévation/abaissement de fréquence d'onde millimétrique pour la liaison descendante/montante de la RoF. Nous avons également vérifié et évalué expérimentalement la performance de la transmission par fibre optique du signal ULB MB-MROF en utilisant nos techniques proposées.

Pour la linéarisation à large bande, nous avons proposé la technique de mélange de polarisation pour un MZM et de distorsion préalable analogique pour un EAM. On a trouvé que le troisième ordre d'intermodulation (3IMD) est supprimé indépendamment de l'index de modulation. Le coefficient électro-optique du MZM dépend fortement de la polarisation de la lumière incidente et par suite différente quantité de 3IMD peut être générée à différente polarisation. Si les deux polarisations orthogonales du MZM sont mélangées dans une certaine proportion, le 3IMD total peut être compensé. Dans la technique de mélange de polarisation, l'évanouissement du signal RF et la diaphonie due à l'intermodulation par l'intermédiaire de la dispersion chromatique de la fibre sont considérablement supprimés en comparaison avec l'usage du modulateur MZM à OSSB conventionnel. La gamme dynamique libre de parasites (SFDR) est améliorée de ~ 12.5 dB expérimentalement et nous avons obtenu une bonne concordance avec les résultats prévus par la théorie et la simulation. En outre, la technique proposée montre une amélioration de 2dB en EVM une fois appliquée au système de transmission de l'ULB MB-MROF par fibre. Un circuit de distorsion préalable pour la linéarisation du EAM, utilisant une paire de diodes réfléchissantes, a été conçu pour le système

de l'ULB MB-MROF dans la bande du groupe 1 (3.1~ 4.8 GHz). Une paire de diodes Schottky balancées a été utilisée pour générer seulement la fondamentale et le 3IMD qui seront injectés dans le EAM. Le 3IMD généré par la fondamentale injectée dans le EAM sera compensé par le 3IMD injecté dans le EAM. On a constaté que le circuit conçu de distorsion préalable mène à 11 dB d'amélioration du SFDR à la fréquence centrale de la bande de groupe 1, et plus de 7 dB d'amélioration dans la suppression de 3IMD sur toute la bande de groupe 1. En évaluant le circuit de distorsion préalable avec le signal ULB MB-MROF, une amélioration de 1-dB en EVM est obtenue pour les trois premières bandes de l'ULB MROF transmises sur 20 km de fibre. Ceci suggère que les conceptions proposées soient des techniques de linéarisation à large bande rentable pour l'ULB MB-MROF sur fibre.

Pour surmonter l'évanouissement du signal causé par la dispersion chromatique de la fibre quand la modulation ODSB est utilisée, nous avons proposé une technique originale de modulation. Un modulateur MZM, à deux électrodes polarisé en quadrature, est configuré en tandem OSSB avec un déphasage entre les deux OSSB qui peut être contrôlé par un déphaseur électrique et ainsi compenser la dispersion chromatique de la fibre. Cette technique de modulation améliore aussi la puissance RF de 3dB comparé à la modulation OSSB. Le principal avantage de la technique proposée est sa simplicité et son application dans le domaine électrique avec un déphaseur. L'analyse théorique a été faite pour obtenir les conditions optimales pour la performance optimale, telle que le déphasage optimal et l'impact du rapport d'extinction de MZM. La simulation a été faite pour une analyse supplémentaire de la modulation proposée et ensuite pour la comparer à la théorie. En outre, nous présentons une preuve expérimentale pour valider notre concept pour un signal RF d'une seule porteuse et un signal ULB MB-MROF. En utilisant notre technique de modulation proposée, une amélioration de puissance RF de 3dB, comparée à OSSB, a été obtenue expérimentalement sans dégradation de la qualité du signal.

Après, nous avons proposé une technique de modulation qui améliore l'efficacité de modulation dans la transmission du signal radio sur fibre. Nous avons montré qu'un modulateur de deux MZMs en parallèle (dMZM) peut être employé pour obtenir non seulement la modulation OSSB mais aussi un OCSR variable. Pour obtenir OSSB modulation la tension de polarisation du modulateur MZM principal est accordée afin de mettre les deux MZMs intégrées en quadrature de phase optique. La fonction d'ajustement de l'OCSR utilisant ce modulateur est

proposée et étudiée pour la première fois à notre connaissance. On a montré qu'une large plage dynamique d'ajustement de l'OCSR peut être obtenue en variant la tension de polarisation appliquée aux MZMs internes. On a constaté que un OCSR optimale pour obtenir le maximum de puissance de sortie RF dépend de l'index de modulation et du rapport d'extinction du dMZM. Pour réaliser un OCSR de 0 dB il y a un rapport d'extinction minimal exigé qui diminue avec l'augmentation de l'index de modulation. En outre, nous avons étudié l'impact de l'OCSR sur la performance du signal ULB MB-MROF. On a constaté que le maximum de puissance RF reçue est obtenu à un OCSR de 0 dB, tandis que le minimum d'EVM de la constellation du ULB MB-MROF reçue est obtenu à un OCSR de 5.4dB.

Ensuite, on a expérimentalement démontrée la performance de la génération et de la transmission de signaux ULB MB-MROF à l'onde millimétrique par fibre utilisant une technique optique basée sur un MZM à deux électrodes comme changeur élévateur de fréquence. Le MZM a été polarisé et configuré pour le maximum de transmission afin de produire principalement des harmoniques optiques d'ordre paire et ainsi générer une onde millimétrique de fréquence égale à quatre fois la fréquence de l'oscillateur local qui commande le MZM. On a constaté que $\sim 4\%$ est l'indice optimal de modulation RF du MZM commandé par le ULB MB-MROF, et un indice de modulation LO de 60% (théoriquement) et 70% (expérimentalement) est nécessaire pour obtenir un EVM maximum de -16dB requis après 20 km de transmission par fibre. On a aussi constaté qu'un rapport d'extinction typique n'a pas d'impact significatif sur l'EVM, tandis que l'instabilité de la différence de potentiel de 20% dégrade l'EVM de moins de 1 dB.

Finalement, nous avons expérimentalement étudié et démontré une nouvelle technique utilisant le FWM dans un EAM pour convertir l'onde millimétrique (MMW) en fréquence intermédiaire pour des liaisons montantes de l'onde millimétrique sur fibre. En injectant deux lumières pompes, avec une fréquence de séparation de l'ordre de l'onde millimétrique f_{LO} , dans un EAM modulée par une onde millimétrique f_{mm} , une lumière FWM (comme porteuse optique) et une bande latérale (comme sous-porteuse modulée) séparées de $|f_{LO} - f_{mm}|$ sont générées à la sortie de l'EAM. Après filtrage et photo-détection, un signal RF est généré à une fréquence intermédiaire $|f_{LO} - f_{mm}|$. On a constaté que l'efficacité de FWM peut être maximisée on accordant la tension de polarisation inverse (2.3 V) et augmente par une pente de 2 à l'échelle décibels par rapport à la puissance de pompe d'entrée. Nous avons également étudié la performance de la

transposition par abaissement de fréquence de signal MMW ULB MB-MROF par FWM dans un EAM. On a trouvé qu'il existe est l'indice de modulation RF optimal ($\sim 7.5\%$) de l'EAM commandé par le ULB MB-MROF, et la transposition par abaissement de fréquence est presque insensible à la puissance d'entrée LO et RF. Cette recherche montre le potentiel d'application des techniques photoniques proposées dans la transposition par élévation/abaissement de fréquence millimétrique d'un signal MMW ULB MB-MROF transmis par une liaison montante/descendante sur fibre.

Puisque ces travaux de recherche sont concernés par une multitude d'aspects de la RoF et plusieurs sujets sont traités et étudiés en détail, le tableau suivant récapitule les contributions principales décrites dans cette thèse avec des commentaires sur chaque technique proposée.

Tableau. Contributions Majeures et Commentaires.

Contributions	Avantages	Inconvénients
Mélange de polarisation du MZM	<ul style="list-style-type: none"> ▪ suppression du 3ème d'ordre ▪ Indépendant de l'index de modulation ▪ SFDR améliorée ▪ Transmission à band latérale unique optique ▪ large bande, faible coût et moins de complexité 	<ul style="list-style-type: none"> ▪ 10 dB de pénalité en puissance RF ▪ Appliqué seulement aux modules dépendant de la polarisation
Circuit analogique de distorsion préalable utilisant une paire de diodes réfléchissantes	<ul style="list-style-type: none"> ▪ suppression du 3ème d'ordre ▪ Indépendant de l'index de modulation ▪ SFDR améliorée ▪ Appliqué à tous composants non linéaires ▪ large bande, faible coût et moins de complexité 	<ul style="list-style-type: none"> ▪ 3 dB de pénalité en puissance RF
Compensation électrique de l'évanouissement de puissance due à la dispersion chromatique de fibre dans l'ODSB	<ul style="list-style-type: none"> ▪ 3 dB amélioration de puissance RF comparée à l'OSSB ▪ Mise en application simple dans le domaine électrique 	<ul style="list-style-type: none"> ▪ Exige un déphaseur électrique accordable
OSSB & OCSR accordable utilisant un dMZM	<ul style="list-style-type: none"> ▪ Large dynamique d'accordabilité de l'OCSR ▪ Efficacité de modulation améliorée ▪ transmission à band latérale unique optique bande latérale ▪ large bande, faible coût et moins de complexité 	<ul style="list-style-type: none"> ▪ Dépend de la polarisation en courant continue.
Abaisseur de fréquence millimétrique utilisant FWM dans un EAM	<ul style="list-style-type: none"> ▪ Réduit la fréquence LO requise de quatre fois ▪ Transmission à band latérale unique optique ▪ large bande, faible coût et moins de complexité 	<ul style="list-style-type: none"> ▪ faible rendement

Les contributions de recherches présentées dans cette thèse peuvent être étendues de plusieurs façons.

D'abord, ULB MB-MROF sur fibre est une technologie émergente. Cependant, beaucoup de domaines ULB MB-MROF sur fibre doivent encore être explorés:

- ULB MB-MROF sur fibre avec multiplexage par répartition en longueur d'onde optique (WDM) ouvre de nouveaux horizons et défis dans la recherche.
- La transmission bidirectionnelle sur la fibre en est un autre sujet important qui doit être abordé. L'ULB MB-MROF bidirectionnel a de grandes perspectives pour des applications des réseaux d'accès futurs. Si la même longueur d'onde optique est utilisée, l'étude de la rétrodiffusion de Rayleigh (RBS) et de la diffusion Brillouin stimulée (SBS) sera un domaine de recherche intéressant.
- Étudier la performance de la transmission optique utilisant des modulateurs optiques à faible coût tel que l'EAM ou EAM avec un laser à rétroaction répartie (DFB) intégré (EML).
- En outre, l'effet de l'interférence croisée des brouilleurs à bande étroite n'est pas étudié dans cette thèse. Pratiquement deux brouilleurs peuvent exister simultanément dans la bande par exemple IEEE 802.11b/g à 2.4 GHz et 802.11a à 5.8 GHz peut se mélanger pour créer des harmoniques à 3.4 GHz qui interféreront avec la sous-bande 1 de la bande de groupe 1.
- La technologie de l'ULB MB-MROF sur fibre profitera des études sur les couches de protocole MAC pour optimiser la performance de la transmission.

En second lieu, il serait intéressant d'étudier s'il y a une façon d'améliorer d'avantage la technique de linéarisation par un mélange de polarisation du MZM en réduisant ou en supprimant les ~10 dB de pénalité en puissance de la porteuse RF. En outre, puisque le mélange de polarisation du MZM a été réalisé avec des composantes optiques discrètes, la prochaine expérience pratique importante serait d'incorporer le MZM avec le mélange de polarisation sur un seul substrat ou module pour étudier d'avantage ses performances.

Troisièmement, des améliorations supplémentaires dans la conception du circuit de distorsion préalable peuvent être étudiées :

- Réduire la taille du circuit distorsion préalable. Dans cette thèse, l'adaptation d'impédance à large bande (de 3.1-4.8 GHz) a été réalisée en utilisant un transformateur d'impédance quart d'onde de trois sections. Toutefois, la taille du circuit peut être réduite en utilisant un substrat dur ou d'autres techniques d'adaptation d'impédance, par exemple en utilisant un mélange d'éléments localisés et des lignes de transmission dans le circuit d'adaptation; ou en augmentant la résistance interne de la diode en insérant une résistance; ou en cascade plusieurs diodes en série. De cette façon, non seulement la taille sera réduite mais aussi la largeur de bande sera élargie. Après avoir rendu sa taille plus petite, le circuit de distorsion préalable peut être fabriqué par la méthode du circuit intégré hybride micro-onde (HMIC), et être intégré dans un boîtier de circuit intégré micro-onde prêt à être commercialisé.
- Le circuit de distorsion préalable peut aussi être modifié pour linéariser les lasers DFB ou le MZM. Le circuit de distorsion préalable et le laser DFB ou le MZM peuvent être montés sur la même carte de circuit imprimé, et après avoir été intégré, le laser DFB ou le MZM linéarisé pourrait être commercialisé.
- Au lieu d'utiliser la diode, des transistors peuvent également être utilisés dans la polarisation symétrique pour produire le signal préalablement distordu. De cette façon, le circuit de distorsion préalable peut non seulement fonctionner comme linéariseur mais également comme amplificateur à faible bruit.

Quatrièmement, la modulation en fréquence d'une sous-porteuse (SCM) ODSB pré-compensée, immunisée contre l'évanouissement du signal causé par la dispersion chromatique de la fibre, peut être très attrayante si un déphaseur électrique à large bande accordable est disponible. Ceci est possible en utilisant des techniques photoniques de micro-onde.

Cinquièmement, pour réduire le coût du convertisseur photonique élévateur de fréquence millimétrique proposée, un MZM balancé avec une seule électrode peut être utilisé au lieu d'un MZM à double électrodes.

Sixièmement, afin de réduire le coût de l'abaisseur photonique de fréquence millimétrique proposée, il est intéressant d'étudier la possibilité de substituer l'amplificateur à fibre dopée à l'erbium, utilisé avant le modulateur EAM, par un amplificateur optique semiconducteur.

Enfin et notamment, étudier la possibilité d'intégrer toutes les techniques proposées dans un seul système avec l'utilisation du WDM.

TABLE OF CONTENTS

DEDICATED TO	III
ACKNOWLEDGMENTS	IV
ABSTRACT	V
RÉSUMÉ	VIII
CONDENSÉ EN FRANÇAIS	XII
TABLE OF CONTENTS.....	XXV
LIST OF TABLES.....	XXX
LIST OF FIGURES	XXXI
LIST OF ACRONYMS	XLII
LIST OF SYMBOLS	XLVI
CHAPTER 1 INTRODUCTION	1
1.1 Introduction.....	1
1.1.1 Advantages of RoF Systems	2
1.1.2 Applications of RoF Systems.....	3
1.1.3 Ultra-wideband Technology	4
1.2 Multiband OFDM Ultra-wideband	6
1.2.1 UWB over Fiber Technologies	7
1.3 Impairments of MB-OFDM UWB in RoF.....	8
1.4 VPI Transmission Maker Simulation Tool	9
1.5 Motivation.....	9
1.6 Research Objectives.....	12
1.7 Thesis Outline	13

CHAPTER 2	TRANSMISSION PERFORMANCE OF MB-OFDM UWB WIRELESS SYSTEMS OVER FIBER	15
2.1	Introduction.....	15
2.2	Theoretical Analysis	16
2.2.1	Calculation of EVM for Transmission through Optical Fiber using DE-MZM	16
2.2.2	Wireless Transmission of UWB	20
2.3	Experimental System Configuration.....	21
2.4	Simulation Setup.....	25
2.5	Single Channel UWB over Fiber System	26
2.5.1	Impact of Optical Modulation and Fiber Transmission.....	27
2.5.2	Impact of Optical Demodulation	33
2.5.3	Effect of Receiver Noise and Received Optical Power	38
2.6	Single Channel Wireless UWB over Fiber System	40
2.6.1	Transmitted UWB signal power and Receiver Sensitivity	40
2.6.2	Effect of Wireless Link.....	41
2.6.3	Impact of Optical Received Power and Receiver Response.....	42
2.7	Impact of Relative Intensity Noise	43
2.7.1	Laser Intrinsic RIN, Resonant Frequency and Laser Output Power.....	43
2.7.2	Laser Linewidth, Fiber Dispersion and RF frequency.....	46
2.8	Performance of Multi-band OFDM Ultra-Wideband over Fiber Transmission under the Presence of In Band Interferers.....	49
2.8.1	UWB over Single Mode Fiber Stand Alone Operation	51
2.8.2	Performance of Band Group 1 of MB OFDM UWB under the presence of WiMAX with Fiber Distribution.....	52

2.8.3	Performance of Band Group 2 of MB OFDM UWB under the presence of WLAN MIMO and WLAN with Fiber Distribution.....	54
2.8.4	Performance of Band Group 4 of MB OFDM UWB under the presence of Marine Radar with Fiber Distribution	57
2.9	Chapter Summary	59
CHAPTER 3	PROPOSED LINEARIZATION TECHNIQUE FOR MZM.....	62
3.1	Introduction.....	62
3.2	Proposed Mixed-Polarization OSSB Mach-Zehnder Modulator	63
3.3	SFDR and Sensitivity Analysis.....	67
3.4	Simulation Results and Analysis	70
3.5	Experimental Results with Two RF Tones	74
3.6	Experimental Results with MB-OFDM UWB Signal	77
3.7	Chapter Summary	78
CHAPTER 4	PROPOSED PREDISTORTION CIRCUIT FOR EAM	79
4.1	Introduction.....	79
4.2	Principle and Theory.....	80
4.3	Proposed Predistortion Circuit.....	82
4.4	Performance Evaluation in Back to Back RoF System with Two RF Tone Test	85
4.5	Performance Evaluation in MB-OFDM over Fiber System	89
4.6	Chapter Summary	91
CHAPTER 5	PRE-COMPENSATED OPTICAL DOUBLE-SIDEBAND SUBCARRIER MODULATION IMMUNE TO FIBER CHROMATIC DISPERSION INDUCED RF POWER FADING	92
5.1	Introduction.....	92
5.2	Theoretical Analysis	93

5.2.1	Optimum Phase Shift	93
5.2.2	Power Efficiency Improvement	94
5.3	Verification and Analysis by Simulation	95
5.4	Experimental Verification using One RF Tone	99
5.5	Experimental Verification using MB-OFDM UWB Signal	101
5.6	Chapter Summary	106
CHAPTER 6 TUNABLE OPTICAL CARRIER SUPPRESSION SINGLE SIDEBAND TECHNIQUE FOR IMPROVED OPTICAL MODULATION EFFICIENCY OF RF AND MB- OFDM UWB SIGNAL OVER FIBER.....		107
6.1	Introduction.....	107
6.2	Principle and Theory of Tunable Optical Carrier Suppression Single Sideband Modulation Technique	108
6.2.1	Theoretical Analysis for Single RF Tone	109
6.2.2	Theoretical Analysis for Two RF Tones.....	118
6.3	Simulation using Commercial Software and Comparison to Theory	128
6.4	Experimental Results and Discussion using Commercial dMZM.....	131
6.4.1	Experimental Setup.....	131
6.4.2	Distortion Effects using Two RF Tone Test.....	132
6.4.3	Performance of MB-OFDM UWB using the Proposed Technique	134
6.5	Chapter Conclusion.....	137
CHAPTER 7 PHOTONIC UP/DOWN CONVERSION AND DISTRIBUTION OF MILLIMETER WAVE MB-OFDM UWB WIRELESS SIGNAL OVER FIBER SYSTEMS..		138
7.1	Introduction.....	138
7.2	Photonic UP-Conversion of MMW MB-OFDM UWB Signal Using MZM	139
7.2.1	Proposed Technique.....	139

7.2.2	Simulation Results and Discussion.....	140
7.2.3	Experimental Results and Discussion.....	144
7.3	Photonic Down-Conversion of MMW MB-OFDM UWB Signal using FWM in an EAM	148
7.3.1	Proposed Technique.....	148
7.3.2	Experimental Setup.....	150
7.3.3	Characterization of Four Wave Mixing in EAM	153
7.3.4	Application to MMW MB-OFDM UWB	155
7.4	Chapter Summary	157
CHAPTER 8	CONCLUSION.....	159
8.1	Concluding Remarks.....	159
8.2	Future Work.....	163
8.3	List of Publications	165
REFERENCES	168
APPENDIX A	173
APPENDIX B	ANALYSIS OF OPTICAL RECEIVER NOISE.....	180
APPENDIX C	183
APPENDIX D	SIMULATED MAGNITUDE AND DELAY RESPONSE OF CHEBYSHEV-II FILTER	185
APPENDIX E	EXTRACTION OF NONLINEAR TRANSFER FUNCTION OF THE PREDISTORTION CIRCUIT	186
APPENDIX F	DERIVATION OF OPTIMAL PHASE SHIFT AND IMPROVED POWER EFFICIENCY	194

LIST OF TABLES

Table 1.1 Comparison between SMF and coaxial cable.....	2
Table 2.1 Generated UWB sub-bands and corresponding interferers.	50
Table 2.2 Generated UWB sub-bands, interferers and their corresponding PSD.....	50
Table 2.3 Measured EVM Performance for Stand Alone UWB Transmission.....	51
Table 3.1 Physical experimental parameters	75
Table 8. 1 Main Contributions and Comments.....	162
Table A. 1 Timing Related Parameters of MB OFDM [5].....	176
Table A. 2 Band Group allocation for MB OFDM UWB [7].....	177
Table A. 3 Time frequency codes for Group-1 MB OFDM system [7].....	177
Table A. 4 Data rate dependent parameters MB OFDM system [7].	178
Table A. 5 Sensitivity of UWB receiver [7].	178
Table A. 6 Permissible Relative Constellation Error (EVM).	179
Table F. 1 Variation of function η versus φ	199

LIST OF FIGURES

Figure 1.1 Basic RoF system.	2
Figure 1.2 FCC UWB emission spectrum [4].....	6
Figure 1.3 Optical impairments in point to point radio-over fiber link.	8
Figure 1.4 Radio-over fiber link mentioning the parts to which the thesis work will be related.	13
Figure 2.1 Experimental setup for externally modulated MB-OFDM UWB over fiber system (BW: bandwidth, G: gain, NF: noise figure, R: responsivity)	22
Figure 2.2 Simulation setup for MB OFDM UWB.	25
Figure 2.3 First three bands of MB-OFDM UWB wireless in (a) Optical spectrum, (b) spectral mask test according to FCC, (c) frequency domain, (d) frequency-time domain and (e) received constellation.....	27
Figure 2.4 Measured EVM with RF modulation index with a parameter of fiber length for bit rate of (a) 53.3Mb/s and (b) 200Mb/s.....	28
Figure 2.5 Relative amplitude of subcarriers in second band versus RF modulation index for back-to-back UWB over fiber.....	30
Figure 2.6 Calculated relative amplitude of subcarriers at 1, 32, 64, 96 and 128 in band 2 versus RF modulation index for UWB over fiber at (a) 20 and (b) 40 km of fiber.	30
Figure 2.7 Calculated phase distortion of subcarriers (1, 32, 64, 96 and 128) in band-two versus RF modulation index at (a) 20 and (b) 40 km of fiber transmission.....	31
Figure 2.8 Calculated EVM degradation versus fiber length with respect to back to back and 0 dBm received optical power. Black square: experimental results for 20, 40 and 52 km.....	32
Figure 2.9 (a) Measured magnitude $ S_{21} $ and (b) measured phase response of the experimental filter measured with a HP 8720 vector network analyzer.....	34
Figure 2.10 Measured (symbol) and simulated (line) EVM using two receivers. Black square: experimental results using optical Rx with Chebyshev-I response, Black circle: experimental results using the “ideal” optical Rx.....	34

Figure 2.11 Simulated EVM using optical receiver with different responses. The used filters are fifth order centered at frequency $f_c = 4\text{GHz}$ with a 3dB bandwidth of 3GHz.	35
Figure 2.12 Simulated EVM with Chebyshev-II filter order and bandwidth for 200 Mb/s UWB signal transmitted over 20 km of fiber.	37
Figure 2.13 Measured EVM versus received optical power at photodetector.	39
Figure 2.14 Calculated EVM degradation versus received optical power for back-to-back transmission with respect to 0 dBm received optical power.	39
Figure 2.15 PER versus UWB power and data rate for 20 km optical link and 1 m wireless link.	41
Figure 2.16 PER versus wireless range and data rate for 20 km of optical link.	42
Figure 2.17 Effect of receiver response and received optical power on PER for 200 Mb/s with modified optical response (dashed) and with ideal receiver response (solid) after 20km of fiber and 1m wireless transmission.	43
Figure 2.18 Measured spectral density of RIN as a function of frequency for back to back transmission.	44
Figure 2.19 Measured RIN peak frequency and corresponding spectral density of RIN for back to back transmission.	45
Figure 2.20 Measured EVM with laser output power for back to back transmission at bit rate of 200Mb/s.	45
Figure 2.21 Calculated RIN versus frequency for 20, 40 and 60 km (Solid: linewidth of 30 MHz. Dotted: linewidth of 1 GHz).	47
Figure 2.22 Calculated EVM degradation versus fiber length with respect to back-to-back. Square: experimental results for 20, 40 and 52 km.	47
Figure 2.23 Simulated (line) EVM versus bands in an MB UWB over fiber system. Square: experimental results for 0, 20 and 40 km centered at 3.432, 3.96 and 4.488 GHz band.	48
Figure 2.24 Spectrum of UWB signal with narrow band interferers.	49

Figure 2.25 RF spectrum of UWB band group 1 and WiMAX (a) transmitted at point B (b) received at point D in Figure 2.1 for bit rate of 200 Mb/s with 20 km fiber transmission (Interferer to UWB peak power ratio is 20 dB).	53
Figure 2.26 EVM performance of UWB over fiber transmission under the presence of WiMAX as a function of WiMAX to UWB peak power ratio (Solid lines: best fitted curves, dotted lines: without interference).	53
Figure 2.27 RF spectrum of UWB band group 2 and WLAN MIMO (a) transmitted at point B (b) received at point D in Figure 2.1 for bit rate of 200 Mb/s with 20 km fiber transmission (Interferer to UWB peak power ratio is 20 dB).	54
Figure 2.28 EVM performance of UWB over fiber transmission under the presence of WLAN MIMO as a function of WLAN MIMO to UWB peak power ratio (Solid lines: best fitted curves, dotted lines: without interference).	55
Figure 2.29 RF spectrum of UWB band group 2 and WLAN (a) transmitted at point B (b) received at point D in Figure 2.1 for bit rate of 200 Mb/s with 20 km fiber transmission (Interferer to UWB peak power ratio is 20 dB).	56
Figure 2.30 EVM performance of UWB over fiber transmission under the presence of WLAN as a function of WLAN to UWB peak power ratio (Solid lines: best fitted curves, dotted lines: without interference).	56
Figure 2.31 RF spectrum of UWB band group 4 and marine radar (a) transmitted at point B (b) received at point D in Figure 2.1 for bit rate of 200 Mb/s with 20 km fiber transmission (Interferer to UWB peak power ratio is 20 dB).	57
Figure 2.32 EVM performance of UWB over fiber transmission under the presence of WLAN as a function of WLAN to UWB peak power ratio (Solid lines: best fitted curves, dotted lines: without interference).	58
Figure 2.33 Received time domain waveform for band group 4 after 20 Km of fiber transmission with bit rate of 200Mb/s without any signal interferer.	58

Figure 2.34 Received time domain waveform for band group 4 after 20 Km of fiber transmission with bit rate of 200Mb/s with radar signal as interferer (Interferer to UWB peak power ratio is 20 dB).....	59
Figure 3.1 The mixed polarization OSSB MZM considered.....	64
Figure 3.2 (a) Theoretical SFDR versus angular detuning $\Delta\phi$ with electro-optic coefficient ratio of $\gamma = 1/3$ and (b) theoretical SFDR versus electro-optic coefficient ratio γ with $\Delta\phi = 0$ for the mixed-polarization OSSB MZM.....	69
Figure 3.3 Simulated optical spectra at the input of the photodetector, for a RoF system through 20 km of SMF using (a) conventional OSSB MZM and (b) mixed polarization OSSB MZM with polarizer angles optimally set to $\pm 79^\circ$	71
Figure 3.4 Simulated RF spectra corresponding to Figure 3.3	72
Figure 3.5 Simulated RF carrier and 3IMD power versus fiber length for a RoF system using the conventional and mixed polarization OSSB MZM, respectively, with compensated fiber loss.	72
Figure 3.6 Simulated spurious free dynamic range for a RoF system using the mixed polarization and conventional OSSB MZM in (a) back-to-back and (b) through 20 km of single mode fiber.....	73
Figure 3.7 Experimental setup for a RoF system using the mixed polarization OSSB MZM. SSG: Synthesized Sweep Generator, PC: Polarization controller.....	75
Figure 3.8 Experimentally measured optical spectrum for the conventional and mixed polarization OSSB MZM.....	76
Figure 3.9 Measured SFDR in a normalized 1 Hz noise bandwidth for (a) back-to-back and (b) 20 km RoF system using the conventional and mixed polarization OSSB MZM.....	76
Figure 3.10 Measured waveform, constellation and EVM of received MB-OFDM UWB signal after 20 km of fibre transmission when using conventional MZM (a) and (c), and mixed polarization MZM (b) and (d), respectively. The RF modulation index is 6.54%.	77
Figure 4.1 Traditional predistortion circuit.....	80

Figure 4.2 Normalized transfer function of EAM and the power of IMD3 and fundamental carrier versus EAM bias. Input power is 3 dBm per RF tone.....	81
Figure 4.3 Block diagram of predistortion circuit and EAM.....	82
Figure 4.4 Schematic of predistortion circuit	83
Figure 4.5 Measured, simulated and calculated RF power of (a) fundamental carrier and (b) IMD3. The input power is -5 dBm per RF tone.....	84
Figure 4.6 Experimental setup for a RoF system using predistortion circuit. Two tone test A connected to B, and MB-OFDM UWB test C connected to B.	85
Figure 4.7 Fabricated predistortion circuit.....	86
Figure 4.8 Measured spectra at the output of the EAM, (a) without and (b) with predistortion circuit. Input power is 3.5 dBm per RF tone and EAM reverse bias is 0.5 V.	87
Figure 4.9 Simulated (a) and measured (b) spurious free dynamic range. EAM reverse bias is 0.5 V.....	88
Figure 4.10 Measured frequency response of the EAM with and without predistortion circuit. Input power is 3.5 dBm per RF tone and EAM reverse bias is 0.5 V.....	89
Figure 4.11 Measured EVM versus UWB input power for (a) back to back and (b) after 20 km of fiber transmission with and without predistortion circuit.	90
Figure 5.1 RoF link setup where the proposed modulator is used.....	93
Figure 5.2 Calculated optimum electrical phase shift versus dispersion induced phase shift θ_2 for different MZM extinction ratios (ER): 15, 20 and 30 dB. A laser emitting at 1550 nm and fiber dispersion of 16 ps/(nm.km) are used.	94
Figure 5.3 Calculated RF power efficiency improvement versus dispersion induced phase shift θ_2 for different MZM extinction ratios (ER): 15, 20 and 30 dB, and when using optimum electrical phase shift ϕ . A laser emitting at 1550 nm and fiber dispersion of 16 ps/(nm.km) are used.	95

Figure 5.4 Simulated RF power versus electrical phase shift at different fiber length. A laser emitting at 1550 nm, $f_{RF}=12$ GHz, fiber dispersion of 16 ps/(nm.km), MZM extinction ratio of 30 dB and RF modulation index of $\sqrt{2}/10$ are used.	96
Figure 5.5 RF power improvement versus MZM extinction ratio at different fiber length obtained by using simulation (lines) and theory (marks).	97
Figure 5.6 Q factor for OSSB and proposed ODSB versus received optical power for 12 GHz RF signal carrying NRZ data at 625Mb/s bit rate.	98
Figure 5.7 Eye diagram for OSSB: (i) back to back (B-T-B), (ii) 52 km, and for proposed ODSB: (iii) B-T-B, (iv) 52 km. The received optical power is -15.9 dBm and -17.4 dBm for OSSB and proposed ODSB, respectively.	98
Figure 5.8 Experimental set up for proof of concept.	99
Figure 5.9 Measured optical spectrum using OSSB (solid line), conventional ODSB (dashed line) and our proposed ODSB (mark) modulation.	100
Figure 5.10 Measured electrical spectrum for (a) back-to-back and (b) after 52 km of fiber transmission.	101
Figure 5.11 Measured EVM versus UWB input power for OSSB, conventional and proposed ODSB for (a) back to back and (b) 20 km of fiber transmission.	102
Figure 5.12 Measured constellation with minimum EVM at optimum input UWB power to MZM at back to back (B-T-B) for (i) OSSB, (ii) proposed ODSB and (iii) conventional ODSB, and after 20 km for (iv) OSSB, (v) proposed ODSB and (vi) conventional ODSB.	104
Figure 5.13 Measured optical spectrum using OSSB modulation (dashed line), and the conventional ODSB (solid line) and our proposed ODSB (mark) modulation.	104
Figure 5.14 RF spectrum of the (a) transmitted and (b) received UWB signal for OSSB, conventional and proposed ODSB for back-to-back transmission.	105
Figure 5.15 Received power versus transmitted power of the UWB MB-OFDM signal for OSSB and proposed ODSB at back to back transmission.	106

Figure 6.1 Dual parallel MZM used for OSSB modulation with tunability of optical carrier suppression.....	108
Figure 6.2 Optical power ratio of second harmonic to the carrier $2P_{2\omega}/P_0$ and third harmonic to the fundamental $P_{3\omega}/P_0$	111
Figure 6.3 Optical spectrum at the output of the dMZM showing the generation of the RF signal from the contribution of different optical components.	111
Figure 6.4 Distortion power level relative to the RF output carrier versus modulation index. .	112
Figure 6.5 Relative RF power versus OCSR for constant received optical power.....	113
Figure 6.6 Optimum OCSR and corresponding phase shift versus modulation index for different extinction ratio (ER): 15, 20, 28.5 and 35 dB.	115
Figure 6.7 Approximated phase shift versus modulation index for high extinction ratio.	116
Figure 6.8 Optimum OCSR versus extinction ratio (ER) for different modulation index: 1, 5, 10, 19, 20 and 50%.	117
Figure 6.9 Minimum required ER to achieve an OCSR=1 versus modulation index.....	117
Figure 6.10 Optimum phase shift versus extinction ratio (ER) for different modulation index: 1, 5, 10, 19, 30, 40 and 50%.	118
Figure 6.11 Optical spectrum showing the generation of the RF component at ω_1 and 3IMD at $2\omega_1 - \omega_2$ after beating at the photodetector.	119
Figure 6.12 Optical power ratio of optical components at second harmonics and 2 nd IMDs frequencies to the optical carrier $(4(P_{2\omega_1} + P_{\omega_2 - \omega_1})/P_0)$, and the optical components at 3 rd IMD to the optical subcarriers at fundamental frequencies $(P_{2\omega_1 - \omega_2}/P_{\omega_1})$ versus modulation index.....	120
Figure 6.13 Power level of in-band distortion relative to the RF output power in the carrier versus modulation index.	122
Figure 6.14 Relative RF power versus OCSR for constant received optical power.....	123

Figure 6.15 Optimum OCSR and corresponding phase shift versus modulation index for different extinction ratio (ER): 15, 20, 28.5 and 35 dB.....	125
Figure 6.16 Approximated phase shift versus modulation index for high extinction ratio in two tone case.....	125
Figure 6.17 Optimum OCSR versus extinction ratio (ER) for different modulation index: 1, 2, 5, 8, 10, 14, 15 and 31%.	126
Figure 6.18 Minimum required ER to achieve an OCSR=2 versus modulation index.....	127
Figure 6.19 Optimum phase shift versus extinction ratio (ER) for different modulation index: 1, 2, 5, 8, 10, 14, 15 and 31%.	127
Figure 6.20 Optical and RF spectrum for one RF tone (3.96 GHz) at OCSR (a-d) -20 dB, (b-e) 0 dB and (c-f) 20 dB. The extinction ratio is 28.5dB and the modulation index is 28.28 %.	128
Figure 6.21 Optical and RF spectrum for two RF tones (3.96 and 4.46GHz) at OCSR of (a-d) -20 dB, (b-e) 3 dB and (c-f) 23 dB, respectively. The extinction ratio is 28.5dB and the modulation index is 28.28 %.	129
Figure 6.22 Optimum OCSR and RF power versus modulation index for 28.5dB extinction ratio. Simulation (mark) and theory (line). (a) One RF tone and (b) two RF tones.....	130
Figure 6.23. Compared theory (lines) and simulation (marks) of OCSR and RF power versus phase shift at different modulation index: 14.14, 22.63 and 28.28%. (a) One RF tone and (b) two RF tones. an extinction ratio of 28.5dB are used. The extinction ratio is 28.5 dB.	130
Figure 6.24 Compared theory (lines) and simulation (marks) of RF power versus OCSR for (a) one and (b) two RF tones and at different modulation indices: 14.14, 22.63 and 28.28%. The extinction ratio is 28.5dB.....	131
Figure 6.25 Experimental setup for the proposed OSSB with tunable OCSR using dual-parallel MZM modulator. PC: Polarization controller.....	132
Figure 6.26 RF power and power ratio of 3 rd order intermodulation distortion to carrier (3IMD/C) versus OCSR for two tones. Two RF tones at 3.96 and 3.964GHz with 12 dBm RF power per RF tone are used.....	133

Figure 6.27 RF and optical spectrum at different OCSR (a) OCSR = 1 dB, (b) OCSR = -20 dB and (c) OCSR = 21.4 dB. An RF input power of 12 dBm per RF tone is used.	134
Figure 6.28 First three bands of MB-OFDM UWB wireless in (a) frequency domain and (b) received constellation.	135
Figure 6.29 Measured EVM and RF output power versus OCSR for (a) back to back and (b) after 20 km of fiber transmission. The UWB input power to the dMZM is -6.14 dBm.	135
Figure 6.30 Optical spectrum, constellation and waveform for 20 km at different OCSR: 18.8, 5.4 and -7.4 dB.	136
Figure 7.1 Schematic of the proposed MMW MB-OFDM RoF link.	140
Figure 7.2 Simulated EVM versus RF modulation index of second MZM. LO modulation index of 67.5 % is used.	141
Figure 7.3 Simulated EVM versus LO modulation index of first DE-MZM for MMW generation. RF modulation index of 4% is used.	141
Figure 7.4 Calculated relative power of the generated MMW MB-OFDM UWB signal vs. LO modulation index for proposed technique.	142
Figure 7.5 EVM vs. bias drift of the DE-MZM used in the proposed technique for MMW generation after transmission over 20 km of SMF. RF and LO modulation index of 4% and 70% is used, respectively.	143
Figure 7.6 Simulated EVM versus extinction ratio of the MZM used in the proposed technique for MMW generation after transmission over 20 km of SMF. RF and LO modulation index of 4% and 70% is used, respectively.	143
Figure 7.7 Experimental setup for the MMW MB-OFDM UWB over fiber system using proposed MMW generation (dashed box).	144
Figure 7.8 Measured optical spectrum after transmission over 20-km of fiber.	145
Figure 7.9 Measured electrical spectrum of MB-OFDM UWB wireless system. (a) before and (b) after electrical frequency down-conversion.	145

- Figure 7.10 Measured EVM versus RF modulation index for back-to-back, and after 20-km of fiber transmission. LO modulation index of 83.5% is used..... 146
- Figure 7.11 Measured constellation of QPSK MMW MB-OFDM for (a) back-to-back and (b) after 20-km of fiber transmission. RF and LO modulation index of 4% and 83.5% is used, respectively. 147
- Figure 7.12 EVM vs. LO modulation index of first MZM for MMW generation after transmission over 20 km of SMF. Marks: measured EVM. Dashed line: simulated EVM. RF modulation index of 4% is used..... 147
- Figure 7.13 Schematic of MMW over fiber uplink using an EAM for frequency down-conversion. 149
- Figure 7.14 Experimental setup for photonic MMW down-conversion using FWM in an EAM. OC: optical circulator..... 150
- Figure 7.15 (a), (b), (c) and (d) represents the measured optical spectrum at point A, C, D and E, and (e) and (f) shows the RF spectrum of the transmitted MMW and received IF MB-OFDM UWB signal at point B and F, respectively in Figure 7.14. 152
- Figure 7.16 Measured relative transmission of the EAM at optical wavelength of 1548.823 nm and calculated relative third intermodulation distortion (3rd IMD)..... 153
- Figure 7.17 Measured FWM efficiency at the output of the EAM as a function of the reverse bias voltage. Pump and Probe input optical power is 6.5 dBm. 154
- Figure 7.18 Measured FWM efficiency and output pump power at the output of the EAM as a function of the input pump power. Reverse bias voltage of the EAM is 2.3 V..... 154
- Figure 7.19 EVM versus RF modulation index of the EAM. Received optical power is 0 dBm and the LO power to the DE-MZM is 16.5 dBm..... 155
- Figure 7.20 EVM performance versus received optical power. RF modulation index is 7.5 % and LO signal power to the DE-MZM is 16.5 dBm ($m_{lo} = 42\%$)..... 156
- Figure 7.21 EVM versus LO modulation index. RF modulation index of the EAM is 7.5%. Received optical power is 0 dBm. 157

Figure A. 1 UWB transmitter and receiver [5].	175
Figure A. 2 QPSK constellation [5].	175
Figure A. 3 Band Group allocation for MB OFDM UWB [7].	176
Figure B. 1 Noise power level at the receiver versus received optical power for back-to-back transmission.	181
Figure B. 2 Calculated total RIN versus fiber length.	182
Figure C. 1 Measured optical signal (a) OSSB and (b) ODSB.	183
Figure C. 2 Measured EVM using OSSB and ODSB.	184
Figure C. 3 QPSK OFDM constellation in a) two dimension b) three dimension received at the real time oscilloscope for band group 1 after 20 Km of fiber transmission with bit rate of 200Mb/s (Colors indicate intensity of power concentration in the received symbol).	184
Figure D. 1 Simulated (a) magnitude and (b) delay response of Chebyshev-II filter.	185
Figure E. 1 Equivalent circuit of the diode, where $G(v)$ indicates the nonlinear conductor of the diode.	186
Figure E. 2 Equivalent circuit of the nonlinear diode connected with a voltage source and load.	187

LIST OF ACRONYMS

ACPR	Adjacent Channel Power
ADS	Advanced Design System
ASE	Amplified Spontaneous Emission
AM/AM	Amplitude/ Amplitude
PM/AM	Phase/ Amplitude
BER	Bit error rate
BPF	Bandpass filter
BPSK	Binary Phase Shift Keying
BS	Base Station
CATV	Cable antenna television
CS	Central Station
CTB	Composite triple beat distortion
CW	Continuous Wave
DE	Dual Electrode
dB	Decibel
dBm	The measured power referenced to one milliwatt
DC	Direct Current
DCM	Dual Carrier Modulation
DFB	Distributed feedback
dMZM	dual parallel MZM
DSB	Double sideband
DWDM	Dense wavelength division multiplexing
EAM	Electro-absorption modulator
EBF	Electrical Bandpass Filter

ECMA	European Computer Manufacturers' Association
EDFA	Erbium Doped Fiber Amplifier
EIRP	Effective Isotropic Radiated Power
EML	EAM integrated distributed feedback laser
EVM	Error Vector Magnitude
FBG	Fiber Bragg grating
FCC	Federal Communications Commission
FFT	Fast Fourier Transform
FWM	Four wave mixing
Gb/s	Gigabit per second = 10^9 bits per second
GHz	Gigahertz
GVD	Group Velocity Dispersion
HEC	Hybrid electrical coupler
HD	Harmonic distortion
HP	Hewlett Packard
Hz	Hertz
km	Kilometer = 10 ³ meters
IEEE	Institute of Electrical and Electronic Engineers
IF	Intermediate frequency
IFFT	Inverse Fast Fourier Transform
IMD	Intermodulation distortion
IMD3 (3IMD)	Third Order Intermodulation Distortion
IP	Internet protocol
LiNbO ₃	Lithium niobate oxide
LNA	Low noise amplifier

LO	Local oscillator
MAC	Media Access Control
MATB	Maximum transmission bias
MB	Multi-Band
MB-OFDM UWB	Multiband Orthogonal Frequency Division Multiplexing Ultra-Wideband
MIMO	Multiple input, Multiple output
MZM	Mach-Zehnder Modulator
OC	Optical Circulator
ODSB	Optical Double Side Band
O/E	Optical-to-Electrical
OFDM	Orthogonal Frequency Division Multiplexing
OSSB	Optical Single Side Band
OSA	Optical Spectrum Analyzer
PAPR	Peak-to-Average Power Ratio
PC	Polarization controller
PCB	Printed Circuit Board
PD	Photodiode
PER	Packet Error Rate
PHY	Physical Layer
PLL	Phase-locked-loop
PON	Passive optical network
PRBS	Pseudo-random bit sequence
QAM	Quadrature Amplitude Modulation
QPSK	Quadrature Phase Shift keying
RBS	Rayleigh Back Scattering
RF	Radio Frequency

RIN	Relative Intensity Noise
RMS	Root Mean Square
RoF	Radio over Fiber
RSA	RF Spectrum Analyzer
SMF	Single Mode Fiber
SNR	Signal to Noise Ratio
SBS	Stimulated Brillouin Scattering
SCM	Subcarrier Modulation
SFDR	Spurious Free Dynamic Range
SSB	Single Sideband
TE	Transverse Electric
TFC	Time Frequency Code
TM	Transverse Magnetic
TSSB	Tandem Single Sideband
UWB	Ultra Wideband
WLAN	Wireless Local Area Network
WPAN	Wireless Personal Area Network
WIMAX	Worldwide Interoperability for Microwave Access
VA	Variable Attenuator
VPI	Virtual photonics Inc. (simulation software manufacturer)

LIST OF SYMBOLS

ASE	Amplified spontaneous emission
B_e	Bandwidth of electrical filter
B_o	Bandwidth of optical filter
R_b	Bit rate
A	Ampere
F	Amplifier noise figure
ω_{LO}	Angular frequency of the LO signal
ω_{RF}	Angular frequency of the RF signal
V_{Lo}	Voltage of the LO driven sinusoid
V_{RF}	Voltage of the RF driven sinusoid
m_{RF}	RF modulation index
m_{Lo}	LO modulation index
K	Boltzman's constant
h	Plank's constant
R_L	Receiver resistance load
V_π	Half wave switching voltage
$J_n(\cdot)$	The n th order Bessel function of the first kind
N_{th}	Thermal noise
σ_s^2	Received UWB signal power
σ_n^2	Receiver noise power
f_c	RF carrier frequency

N_{ST}	Number of subcarriers
s	Dispersion slope ($ps/(nm^2 \cdot km)$)
T_{CP}	Cyclic prefix (ns)
T_{GI}	Guard interval
Δf	Subcarrier frequency spacing (MHz)
λ	Wavelength (nm)
α	Fiber loss (dB/km)
v_g	group velocity
c	Speed of light
D	Chromatic dispersion parameter
L	Fiber length
β_2	GVD coefficient (ps^2/km)
m	Modulation index
\Re	Responsivity
q	Electron charge
k_i	Coefficient of the nonlinear transfer function of EAM
a_i	Coefficient of the nonlinear transfer function of predistortion circuit
g_i	Coefficient of the nonlinear conductance of the diode
K	Boltzmann's constant, $1.37 \cdot 10^{-23} J/K$
T	Absolute temperature
V_T	Threshold Voltage of Diode
C_{j0}	Zero Bias Capacitance
Z_0	Characteristic Impedance of the Transmission Line

Z_s	Impedance of the RF Power Source
Z_{load}	Impedance of the Load
V_{in}	Output Voltage from the RF Power Source
$i(t)$	Current in time domain
$V(t)$	Voltage in time domain
Γ	Reflection Coefficient
I_s	Diode Saturation Current
mA	Milli Ampere
B_e	Electrical noise bandwidth or channel bandwidth
B_o	Optical filter bandwidth
G_A	RF Amplifier gain
G	EDFA gain
n_{sp}	Population inversion parameter
t_{ff}	MZM insertion loss
ER	MZM extinction ratio
P_{out}	Output power
P_{in}	Input optical power
V_m	Modulating signal voltage
E_{in}	Input optical field
E_{out}	Output optical field
$\Delta\phi$	Angular detuning from ideal
$\Delta\tau$	Propagation delay

CHAPTER 1 INTRODUCTION

1.1 Introduction

Radio over fiber (RoF) has been considered as a very promising technology for the distribution of future high capacity wireless signals such as ultra-wideband and millimeter-wave wireless communications. In such systems, the access links between the central and base stations (CSs and BSs) are implemented by using optical fibers to fully use an almost unlimited bandwidth (50-THz from 1260nm to 1600nm wavelength), and the links from BS to end users are provided by radio frequency (RF) wireless, which can greatly extend the transmission distance and user mobility.

RoF technology was developed by US Defense Advanced Research Projects Agency (DARPA) during early 1980s mainly for military applications. The purpose of the project was to place the radars and antennas far away from the command and control centers due to the development of new radar-seeking missiles at that time. However, the technology has initially limited applications mainly due to high manufacturing cost of wide bandwidth lasers. Later, mass production of lasers and photodetectors and the need for communication networks covering wide areas eventually lead to RoF projects like *Quasi-Sync* in Europe and *Simulcast* in US. Since then RoF technology has moved forward a long way. Now, it is thought as one of the potentially most viable technologies for 4-G communication systems. Major players in telecommunication industry like Nortel (Ciena) and Telus have already implemented RoF links for commercial purposes. It is expected that RoF technology will be widely used for home networking applications over the coming years.

A basic RoF configuration consists of a two-way interface that contains a laser transmitter and photodiode (PD) receiver which connects the base station transmitters and receivers to a pair of single mode optical fibers [1] as shown in Figure 1.1. At the other end of the fibers is a remote unit that uses a similar PD receiver and laser transmitter to convert optical signals to and from an antenna.

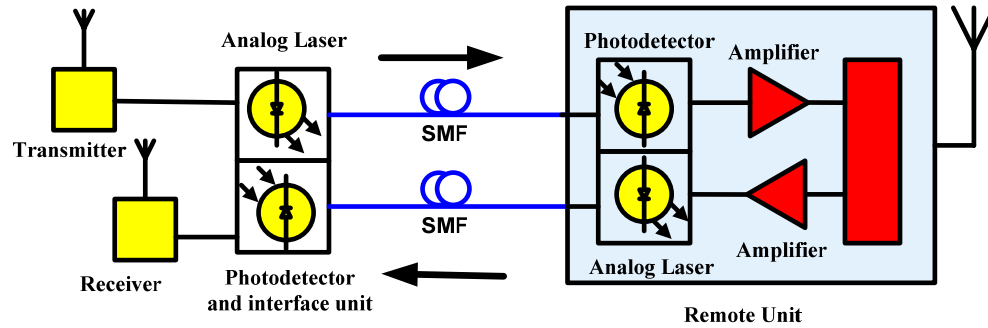


Figure 1.1 Basic RoF system.

1.1.1 Advantages of RoF Systems

Some of the benefits of RoF technology are discussed below:

- **Low attenuation** – The transmission loss through optical fiber is very low. Table 1.1 shows a relative comparison of transmission loss and cost using standard single mode fiber (SMF), standard coaxial cable and special coaxial cable for high frequency application. The table shows that SMF will perform much better than coaxial cable for the transmission of high frequency signals.

Table 1.1 Comparison between SMF and coaxial cable

Frequency	SMF	Standard coaxial cable	Special coaxial cable
1 GHz	0.2 dB/km	0.29 dB/Ft.	0.2 dB/Ft.
18 GHz	0.2 dB/km	4 dB/Ft.	1.1 dB/Ft.
Cost	20 USD/km	50 USD/Ft.	70 USD/Ft.

- **Wide bandwidth** – One of the most important advantages of optical fiber communication is that it has a very large bandwidth. As a result it is transparent to any type of network or application.
- **Immune of interference** – In optical fiber communication, information is transmitted by modulating the light with RF signal. As a result RoF communication is free from

electromagnetic interference. Also, RoF does not suffer from multipath interference which is a common problem in normal wireless communication.

- **Low RF power** – Low RF power antennas are required if fiber is used for distribution; this has many advantages. For instance, reducing the RF power radiated by antennas reduces interference. Reducing emitted power is also environmentally friendly.
- **Economical solution** – Optical fiber is very cheap (Table 1.1). If low cost lasers and photodetectors are used RoF can provide a very economic solution for broadband access networks. Also optical fiber communication is more reliable and costs less for maintenance.
- **Easier cell planning** – In conventional wireless communication, cell planning is a complicated task. Designers have to be careful that interference from the edge of one cell does not affect the other. Also RoF reduces the number of handovers.

1.1.2 Applications of RoF Systems

Some of the applications of RoF technology are discussed below:

- **CATV distribution systems** – RoF technology has been widely used to provide video distribution services in 40 GHz band over the last decade. Fiber to home networks (FTTH) are used for multi-point video distribution service (MVDS) and transmission of IEEE 802.16 broadband services.
- **Local access networks** – Recently there has been growing interest in transmitting wireless signals over fiber networks for local access network (LAN) applications. Fiber can provide a low cost communication under office environments. Over the last few years, many work has been done on transmission of 2.4 GHz IEEE 802.11b over fiber [2-3] and it is found that fiber has superb potential for this application. In December 2008, Nortel (Ciena) inaugurated their solution for Ethernet over fiber in USA for LAN applications.
- **Cellular networks** – Under densely populated areas, RoF fiber can become very handy for transmission of mobile signals. In fact, during 2000 Sydney Olympics, Allen Telecom installed *BriteCell*, a fiber optic-based mobile communications system. According to press releases on the opening day of the Olympics, over 500,000 wireless calls were

made from Olympic Park venues. RoF systems are an effective solution under situations like this where the number of subscriber increases suddenly in an area at a particular time. In Canada, Telus has established their network for transmission of mobile signals through optical fiber.

- **Vehicular Technology** – RoF is also used for toll collection data transfer, intelligent transport and road to vehicle communication systems. Also a wireless sensor network with fiber distribution is used for traffic control and traffic data collection.

1.1.3 Ultra-wideband Technology

The basic concept of ultra wideband (UWB) is to use ultra short pulse (<2 ns) in time domain to spread the frequency energy over wide bandwidth (>500 MHz) to a low level, in order to share the spectrum with existing narrowband transmission without causing unwanted interference. The US Federal Communications Commission (FCC) was the first to open radio spectrum of 3.1-10.6 GHz for UWB use [4]. The wireless personal area network (WPAN) working group of IEEE responded by the draft 802.15.3a standard, which divides the whole spectrum into 14 bands with bandwidth of 528 MHz for each band [7]. The 14 channels are organized in five groups. Each group has three channels except group five which has only two channels. A variable throughput from 53.3 to 480 Mb/s in each channel is suggested. To enable the operation of multiple UWB systems at the same time, the carrier hops around in frequency. The carrier can hop to one of fourteen channels ($2904 + 528n$ MHz, $n = 1, 2, \dots, 14$). Other countries quickly followed the FCC and IEEE initiative. Though in Japan, Korea, China and European Union countries, transmission in band group two (4.752-6.336 GHz) is not permitted to avoid interference with existing IEEE 802.11a (wireless local area network) WLAN. The greatest advantage with UWB radio is that it is software configurable. Therefore, any of the frequency bands can be turned off to meet specific spectral requirements.

However, the WiMedia alliance was the first to take major initiative towards the implementation by selecting multi-band (MB) orthogonal frequency division multiplexing (OFDM) for high speed UWB wireless [6]. In December 2007, European Computer Manufacturers' Association (ECMA) adopted the WiMedia approach and ratified ECMA-368 standard [7] which gave a huge boost for the industry and academia. Various prototypes of

WiMedia UWB devices are already in the market. Low cost UWB devices are expected to hit the mass market by early 2012.

UWB technology shows a lot of potential. It has many important applications. These include the following:

- ***Broad Band Wireless Access Networks*** – The most important use of UWB is in the field of broadband WLANs. UWB devices can support bit rates of up to 480 Mb/s compared to 54 Mb/s in IEEE 802.11 WLAN and 3 Mb/s in Bluetooth, respectively. IEEE 802.11 requires high power so it cannot be used in portable handheld devices. Using Bluetooth, it takes about 45 minutes to transfer data from a 1 Gb memory card; whereas it takes about only 3 minutes to transfer the same data if UWB is used. Sony and Hitachi already included UWB interfaces with their new DVD cameras. It is thought that small UWB device will soon replace USB pen drives, garage door openers, etc.
- ***Stealth*** – In order to satisfy the effective isotropic radiated power (EIRP) requirement defined by FCC, UWB signals are designed to have noise-like properties and the energy of the high frequency signal is spread over a very large bandwidth. As a result, the signal appears to be very low level background noise to an unintended narrowband receiver.
- ***Sensor Application*** – UWB can transfer data over a high bit rate without causing interference to other narrowband systems. In the field of medical sensors, UWB can replace wires connected to a patient's body and improve comfort.
- ***Position Location*** – UWB systems are capable of determining the 3D location of any of its transponders to within a few centimeters.
- ***Radar Imaging*** – UWB systems can be used as an open-air through-wall or ground-penetrating radar imager. In several airports of Denmark and Netherlands UWB radar imaging systems are used for searching guns and explosives. Also UWB's ability to penetrate through walls makes it perfect for use in cubicles under office environments.
- ***Vehicular Radar Systems*** – UWB also has applications in vehicular radar systems for use in collision avoidance and parking aids.

Despite all its promises, UWB has a serious limitation in terms of transmission coverage. Due to very low transmitted power, it is impossible to distribute UWB signals over air for more than tens of meter. On the other hand, due to the wide bandwidth of 7.5 GHz it is very hard and

expensive to distribute UWB radio signals over coaxial cable. Optical fiber is well known for its low loss, low cost and wide bandwidth in addition to light weight and mature technology. Therefore, it will be more advantageous to use UWB radios over fiber technique for UWB distribution.

1.2 Multiband OFDM Ultra-wideband

During February 2002, the FCC of United States approved a spectrum in the range 3.1-10.6 GHz to be available for the unlicensed use of UWB signals. The US FCC provided the following guidelines-

Definition of UWB

According to FCC UWB signal either occupies at least 500 MHz of spectrum or its 10 dB bandwidth is at least 20% of the size of the center frequency.

Spectrum Allocation

FCC requires that the spectrum must use the band allocation showed in Figure 1.2.

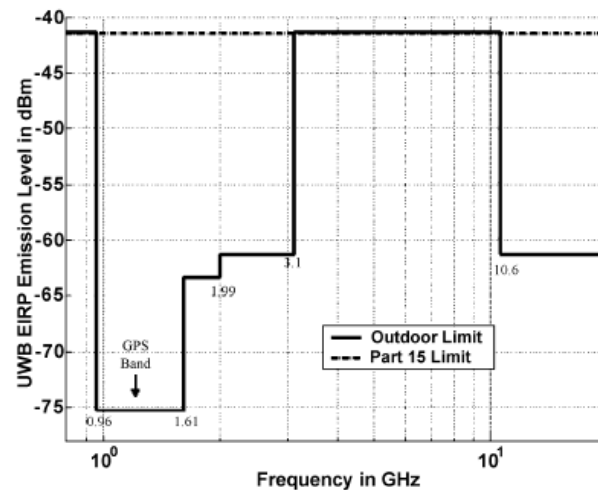


Figure 1.2 FCC UWB emission spectrum [4].

Emission Limits

The power spectral mask is depicted in Figure 1.2. The average in band power emission is limited to -41.3 dBm/ MHz in terms of EIRP.

FCC only provides a guideline for UWB rather than giving details about the PHY layer implementation. So, several UWB transmission techniques have been proposed. These techniques can be categorized in two major groups: single band and MB UWB. The single band approach is implemented by direct modulation of information into a sequence of impulse like waveforms which occupy the available bandwidth of 7.5 GHz [8]. Multiple users are supported by using a complex time hopping sequence. But building devices to handle ultra short pulse signal is quite challenging. Also this approach requires a very complex receiver structure. In multi-band approach the information is processed over a small bandwidth of at least 500 MHz [5]. This reduces design complexity and provides flexible worldwide compliance.

An MB OFDM signal consists of 128 subcarriers using quadrature phase shift keying (QPSK) for lower bit rates. However, advanced dual carrier modulation technique is used for bit rate of higher than 200 Mb/s.

In Appendix A the physical layer (PHY) of MB OFDM system is described as proposed in the IEEE 802.15.3a [5] and ECMA-368 standard [7].

1.2.1 UWB over Fiber Technologies

FCC imposed a strict spectral mask for the UWB to avoid interference with existing narrow band wireless systems. It is required that allowed EIRP is -41.3 dBm/MHz, and the total transmitted power from a UWB antenna is limited to 0.5 mW only. In order to satisfy the EIRP requirement defined by FCC, UWB signals are designed to have noise-like properties and the energy of the high frequency signal is spread over a very large bandwidth. This is why the distribution of UWB over coaxial cable is exceedingly expensive. Optical fiber provides an excellent alternative for the distribution of UWB signals due to its low loss, low cost and wide bandwidth characteristics.

First the UWB signal is generated from an UWB transmitter and directly drives a laser or an optical modulator as shown in Figure 1.1, and then MB OFDM UWB signal becomes optical subcarriers. After fiber distribution PD directly converts optical UWB subcarrier to UWB radio signal, which will be emitted by a UWB antenna at user's location. All the features of UWB over fiber will be discussed in details in Chapter 2.

1.3 Impairments of MB-OFDM UWB in RoF

Figure 1.3 shows a point-to-point radio-over-fiber link connecting a remote antenna base station and a central office. The MB-OFDM UWB wireless signal undergoes different signal impairments as they propagate in the hybrid link. When the MB-OFDM UWB wireless signal is received at the remote antenna base station, the signal is first amplified and converted to optical signals. The electro-optical modulation can be carried out either by direct modulation using an optical source or by external modulation combining an external modulator with an optical carrier. The electro-optical modulation can be carried out either by direct modulation using an optical source or by external modulation combining an external modulator with an optical carrier.

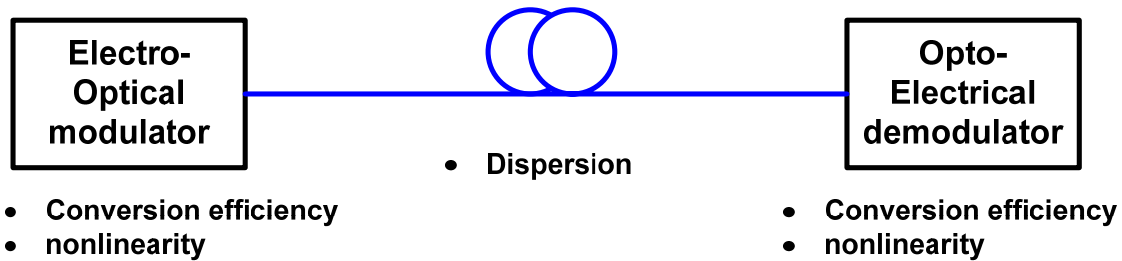


Figure 1.3 Optical impairments in point to point radio-over fiber link.

The MB-OFDM UWB signal modulated onto the optical carrier is typically very weak as a result of low modulation efficiency at RF frequencies. The conversion efficiency in this context refers to optical-electrical-optical conversion. In addition, the nonlinear characteristics of the optical intensity modulator limit the amplitude of electrical modulation to a very narrow window for linear operation. Once the MB-OFDM UWB signals are modulated onto the optical carrier, the optical signal will be transported over the optical fiber link to the central office. The optical distribution of the MB-OFDM UWB signals is subject to the effects of fiber chromatic dispersion that will severely limit the overall transmission distance [1]. In addition, in a long-reach environment, the optical signal may experience fiber nonlinearities if the optical signal power is required to be amplified in order to overcome the link losses while the amplified optical power is also sufficiently large to trigger the nonlinear fiber effects. Upon reception at the receiver, the optical signal undergoes an optical-to-electrical conversion using a PD. The PD is

also a nonlinear device and is governed by the square-law process. Thus, the detection process will further introduce distortions into the system. Therefore it is of great importance that these impairments be mitigated to improve the signal quality and performance of hybrid fiber–wireless links.

1.4 VPI Transmission Maker Simulation Tool

VPI Transmission maker is a sampling based optical simulation tool developed by VPI Photonics Inc. The simulation tool is composed of components, e.g. laser, optical modulator, fiber, wavelength multiplexers/demultiplexers and photodetectors that are placed on a worksheet in the desired configuration and independently configured with parameters to model true-off-the-shelf components including components being tested before fabrication. Some of the adjustable parameters include thermal noise, shot noise, dispersion, etc. The samples may be processed by each component in the design by independent samples or blocks of samples. The sample window may be adjusted accordingly to allow for a greater resolution at the expense of extra processing time. Included in the simulation package are visualizers, such as universal bit error rate (BER) analyzer, optical spectrum analyzer (OSA), RF spectrum analyzer (RSA), oscilloscopes etc. Design parameters may be swept dynamically to study the performance and stability of a design platform. The simulation tool has the ability to track transit time and custom variables. The package has the ability to run co-simulations with such 3rd party packages as © Matlab and © Python [9].

1.5 Motivation

In RoF distribution systems, optical subcarrier modulation (SCM) is used to generate typically two sidebands around the optical carrier, i.e., double sideband SCM. It was found that optical double sideband (ODSB) subcarrier modulation will introduce RF power fading in RoF systems due to fiber chromatic dispersion [10]. This power fading can cause power penalty in system's

performance [11] and eventually the RoF system does not work at some fiber lengths. Thus, optical single sideband (OSSB) subcarrier modulation was proposed and has been used to remove this power fading [12]. However when OSSB is used 3 dB RF power is lost due to the suppression of one of the two sidebands compared to ODSB. Several approaches were proposed to compensate for the dispersion-induced power fading in conventional ODSB analog photonic transmission, including a modulation diversity receiver [13], nonlinearly chirped gratings [14] and midway optical phase conjugation [15]. These techniques have increased complexity of the receiver and limited bandwidth [13]. Also they either must be actively tuned, or introduce differential dispersion-causing RF fading [14], or are limited by the asymmetric power change [15-16].

Moreover RoF performance is susceptible to nonlinear distortions that can be induced by nonlinearities in the transmission lines and optical modulator response. For example, the external modulator such as Mach-Zehnder modulator (MZM) or Electro-absorption modulator (EAM) exhibits a nonlinear transfer function response. The nonlinearities generate optical harmonic distortion (HD) and intermodulation distortion (IMD), which if not suppressed will severely degrade RoF transmission. Among the nonlinear distortions, IMD components may be the most detrimental to the RoF transmission, because it is a high probability for them to lie very close to and/or overlapped with the RF carriers. These undesirable components are difficult to filter out.

Optical small-signal modulation is a straightforward way to minimize optical high-order harmonics. This is particularly important for systems sensitive to nonlinear high-order harmonics, such as links incorporating dense-wavelength division multiplexing (DWDM), SCM, or OFDM. In optical small-signal modulation, the optical carrier to- sideband ratio (OCSR) can be more than 20 dB, i.e., compared to optical carrier, the generated modulated optical sideband(s) is (are) very weak. Then in photodetection most of the received optical power is converted to direct current (DC) while a small portion is converted to RF signals. This leads to a very low transmission efficiency of RF signals. Moreover, since information is carried by optical sideband(s), in RoF link with optical small-signal modulation, a relatively strong optical receiver power is required to achieve the required signal-to-noise ratio (SNR). The consequent relatively strong DC, which is mainly generated from the optical carrier, may damage the photodetector. In addition, higher optical receiver power results in smaller link budget and shorter fiber link

distance. Also, nonlinearity problems associated with optical fiber under high optical power, like four-wave mixing in DWDM systems, may arise and lead to additional performance deterioration.

An effective method to improve the modulation efficiency of RoF links with small-signal optical modulation is to reduce the optical carrier-to-sideband ratio. By suppressing the optical carrier, more portion of optical power is converted to RF signal thus the intrinsic gain of the RoF link is increased. A number of schemes suppressing optical carrier have been proposed and demonstrated [17-21]. In summary, most of the demonstrated schemes are based on optical filtering with: optical notch filter [17-18]; optical hyperfine blocking filter [19]; nonlinear Brillouin scattering/filtering [20]; or MZM bias voltage [21]. However, these techniques need optical carrier tuning [17-18], suffer from high insertion loss and power penalty [19], endure signal distortion and instabilities in the transmitted power [20, 22] ; or experience chromatic dispersion induced power fading [21].

Millimeter wave (MMW) frequency operation can provide high-capacity broadband wireless services in picocellular or microcellular architecture. Moving the radio operating frequency into the MMW region overcomes the spectral congestion in the lower microwave region. In addition, the main advantages in the use of MMW band (57-64 GHz, for example) are 7 GHz bandwidth availability as well as the prospect of multi-gigabit to terabit networks. To achieve high capacity access networks, IEEE 802.15.3a [5] and IEEE 802.15.3c [23] were proposed for wideband personal local access networks (WPLAN). In IEEE 802.15.3a 14-channel OFDM UWB wireless using RF of 3.1-10.6 GHz band was suggested, and each channel can carry data of up to 480 Mb/s. In IEEE 802.15.3c, 4-channel OFDM millimeter-wave wireless using RF of 56-67 GHz band was proposed and each channel can deliver data of up to 3 Gb/s. Therefore, MMW wireless, IEEE 802.15.3c, can transmit higher data rate signals compared to IEEE 802.15.3a. However, MMW may have a very high attenuation for transmission over air, depending on frequency ranges, such as ~15 dB/km at 60 GHz. Therefore, the transmission of ultra-wideband (UWB) at MMW band wirelessly is limited to a few meters and many base stations have to be deployed for large coverage area. It is well known that optical fiber has tremendous bandwidth, but it does not support users' mobility and flexible system reconfiguration. Therefore, if combining MMW wireless and optical fiber communications for access networks, it would be

possible that high capacity local area access networks with advantages of large coverage, mobility and low cost can be achieved simultaneously especially when shifting the system complexity and expensive devices to the central station (CS). However, in addition to the previously cited impairments, MMW transmission over fiber may become impractical due to unavailability and design challenge of broadband and high frequency electrical components such as mixers, power amplifier, local oscillators, and optical receivers and transmitters, etc. For MMW over fiber uplinks, optical-to-electrical (O/E) converted wireless signal is still in MMW frequency band, resulting in high cost optical receivers. Similarly for downlinks, broadband optical transmitters and receivers are required. Therefore simple and cost effective techniques are required to generate and distribute high capacity MMW wireless signals for both downlinks and uplinks.

1.6 Research Objectives

The objective of this research is to develop new enabling technologies to overcome chromatic dispersion induced power fading, nonlinearities in optical modulators, improve optical to electrical efficiency and transmit millimeter wave over fiber. The proposed technologies improve upon existing ones, so as to help making RoF systems an economical alternative to existing wireless, broadband and passive optical networks (PONs). Based on this research, we

- Proposed, developed and extensively investigated by theory, simulation and experiment, novel technologies and designs for:
 - Linearization,
 - Compensation of chromatic dispersion induced power fading,
 - Improving optical modulation efficiency,
 - MMW up/down conversion for RoF down/up-links.
- Verified and evaluated experimentally the performance of using our proposed techniques for MB-OFDM ultra-wideband (UWB) signal transmission over fiber.

This work is concerned with a multitude of RoF aspects and many subjects are discussed and studied in detail. A graphic sketch describing the entire system is given in Figure 1.4 mentioning the part to which the thesis work will be related.

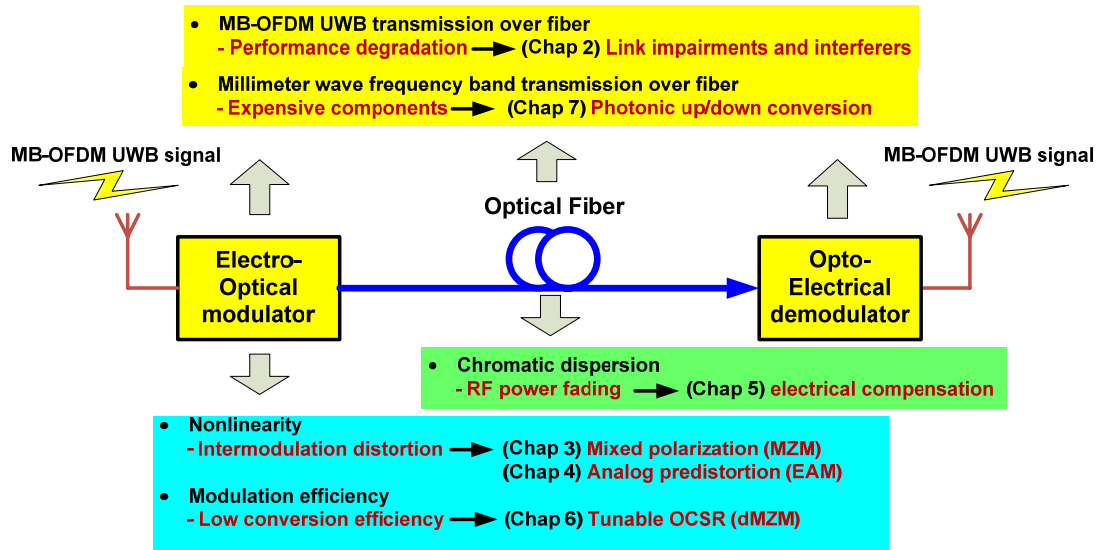


Figure 1.4 Radio-over fiber link mentioning the parts to which the thesis work will be related.

1.7 Thesis Outline

This thesis is organized as follows.

Chapter 2 will investigate in terms of error vector magnitude (EVM) the performance degradation of MB-OFDM UWB transmission over fiber caused by various impairments including MZM nonlinearities, fiber dispersion, receiver optical power and optical receiver response. Also, the performance of MB-OFDM wireless UWB in terms of packet error rate (PER) when transmitted over 20 km of SMF is experimentally investigated. PER was measured at different bit rates to evaluate the receiver sensitivity, required minimum transmitted UWB power, effect of wireless distance, MZM modulation index, and received optical power etc. The performance of MB-OFDM UWB was investigated when transmitted over fiber under the effect of relative intensity noise (RIN) considering system's parameters such as laser output power, linewidth and fiber transmission length. The performance of MB-OFDM UWB over fiber transmission system is also studied considering the effect of in-band jammers such as WiMAX, WLAN MIMO, WLAN and marine radar.

Chapters 3 and 4 propose two linearization techniques using an optical mixed polarization for MZM and electrical pre-distortion circuit for EAM, respectively. The performance of the

proposed techniques will be evaluated by theory, simulation and experiment. Moreover the proposed designs will experimentally be demonstrated for MB-OFDM UWB signal transmission over fiber to show the potential and cost effectiveness of these techniques to be applied in current and future broadband wireless over fiber systems.

Chapter 5 will introduce the proposed electrical compensation for chromatic dispersion induced power fading and provide mathematical formulations behind its principle. Simulation and experiment are also conducted for single RF tone and MB-OFDM UWB signal. The results show the potential and cost effectiveness of the proposed technique for broadband wireless over fiber transmission system.

Chapter 6 will present a tunable optical carrier suppression-based single sideband technique to improve the optical modulation efficiency and receiver sensitivity in subcarrier multiplexing RoF system. The proposed technique will be investigated by theory, simulation and experiment. The performance improvement of the proposed technique will also be demonstrated for MB-OFDM UWB signal to show the potential and cost effectiveness of this technique for broadband wireless over fiber system.

Chapter 7 will describe two proposed techniques for photonic up- and down conversions of millimeter-wave, respectively, in radio over fiber system. The millimeter-wave up conversion is accomplished by using dual electrode MZM (DE-MZM) for frequency quadrupling. The millimeter-wave down-conversion is achieved by using four-wave mixing in EAM. Both techniques are comprehensively investigated and applied to MB-OFDM UWB signal showing their potential use in broadband wireless millimeter-wave over fiber system.

Chapter 8 will conclude the thesis with summarizing the amount of progress that was accomplished and potential implication to knowledge, theory and practice. Also discussed is the future work that remains and over all insights.

CHAPTER 2 TRANSMISSION PERFORMANCE OF MB-OFDM UWB WIRELESS SYSTEMS OVER FIBER

2.1 Introduction

MB-OFDM UWB wireless, which provides high data rate access, is required to be distributed by using optical fiber. In this chapter, we, for the first time to our knowledge, investigate the combined effect of fiber dispersion, and nonlinearities of optical transmitter's and optical receiver's response on the OFDM subcarriers for MB OFDM UWB over fiber system through a detailed theoretical and experimental analysis. Theoretical analysis of the effect of fiber dispersion, optical transmitter and optical receiver response on system performance is carried out considering amplitude and phase distortion. Theoretical analysis of the effect of fiber chromatic dispersion induced laser phase to intensity noise or RIN on system performance is carried out. Simulation is also made to show the relationship between RIN and center frequency of UWB bands. Experiments are also conducted to verify our simulation and theoretical analysis and a good agreement is obtained. The performance of MB-OFDM UWB over fiber transmission system is also studied considering the effect of in-band jammers such as WiMAX, WLAN MIMO, WLAN and marine radar. Experiments are performed to show the effect of fiber transmission under various interferer power levels.

The chapter is organized into nine sections. Theoretical analyses for OSSB modulation are given in Section 2.2 considering amplitude and phase distortion experienced by each of the OFDM subcarriers within one symbol after transmission over fiber. In Sections 2.3 and 2.4, the experimental and simulation setups are described, respectively. In Section 2.5, the performance of UWB over fiber system is clarified with focus on the ECMA-368 standard using MB OFDM. Optical transmitter's nonlinearities and fiber dispersion effect on system performance are studied experimentally and compared to the theoretical analysis. Also, simulations and experiments are performed to assess the effect of optical receiver's response and received optical power on UWB performance. The transmission performance of wireless MB-OFDM signals over 20 km of SMF is also investigated in Section 2.6 by measuring packet error rate (PER) at different bit rates, transmitted and received UWB power level, RF modulation index of the MZM, wireless transmission range, received optical power and optical receiver response. Next, the impact of

various physical parameters that control laser RIN and fiber transmission with focus of MB UWB technology is discussed in Section 2.7. Thereafter, error vector magnitude (EVM) performance of MB UWB over fiber under different in band interference scenarios is analyzed in Section 2.8. Finally, our conclusions are drawn in Section 2.9.

2.2 Theoretical Analysis

In this section we theoretically analyze MB-OFDM UWB wireless over fiber transmission with OSSB modulation. The common way to generate OSSB is to use a DE-MZM modulator. However, an MZM modulator is known to be inherently nonlinear in response and may introduce high nonlinear distortion to which OFDM signals are exposed. On the other hand, at the receiver side a narrowband electrical bandpass filter (EBF) is usually used to filter out the data modulated RF carrier, and the filter determines the optical receiver's response. This filter may have a great impact on the performance of the received data because of its response that may introduce phase and amplitude distortion to which MB UWB OFDM signal is vulnerable. Therefore the theoretical analysis should include the effect of DE-MZM response nonlinearities, fiber dispersion and optical receiver's response. Finally EVM due to fiber dispersion and RF carrier phase noise induced phase distortion is given.

On the other hand, the radiation from a UWB system can cover 2 to 7 GHz of bandwidth. This wide bandwidth operation makes the UWB wireless channel distinct from narrow band channels. The wireless path loss will be expressed and the received UWB power will be calculated.

2.2.1 Calculation of EVM for Transmission through Optical Fiber using DE-MZM

The MB OFDM RF signal ($y_{RF}(t)$) is related to the complex baseband signal ($x_k(t)$) of k^{th} OFDM symbol as [5]

$$y_{RF}(t) = \text{Re} \left\{ \sum_{k=0}^{N-1} x_k(t - kT_{SYM}) V_{RF} \exp(j(2\pi f_c t + \varphi(t))) \right\} \quad (2.1)$$

where T_{SYM} is the symbol period, N is the number of OFDM symbols, V_{RF} is the driving voltage of the UWB signal, and f_c and $\varphi(t)$ is the carrier frequency and phase noise of RF carrier local oscillator, respectively.

The OFDM symbols $x_k(t)$ can be constructed using inverse Fast Fourier transform (IFFT) with a certain coefficients C_n , which can consist of data symbols, pilots, and training symbols,

$$\begin{aligned} x_k(t) &= \sum_{n=-N_{ST}/2}^{N_{ST}/2} C_n \exp(j2\pi n\Delta f(t - T_{CP})) \\ t &\in [T_{CP}, T_{FFT} + T_{CP}] \text{ , otherwise } 0 \end{aligned} \quad (2.2)$$

where, $N_{ST} = 128$ is the total number of subcarrier used, $\Delta f = BW / N_{ST} = 4.125 \text{ MHz}$ is the subcarrier frequency spacing, n is the subcarrier number, $T_{CP} = 60.61 \text{ ns}$ is the cyclic prefix, $T_{FFT} = 1 / \Delta f = 242.42 \text{ ns}$ is the IFFT/FFT period, and BW is the signal bandwidth.

For one OFDM symbol we have

$$\begin{aligned} y_k(t) &= \text{Re} \left\{ x_k(t) \exp(j(2\pi f_c t + \varphi(t))) \right\} \\ &= \text{Re} \left\{ \sum_{n=-N_{ST}/2}^{N_{ST}/2} C_n \exp\{j2\pi n\Delta f(t - T_{CP})\} \right. \\ &\quad \left. \times \exp(j(2\pi f_c t + \varphi(t))) \right\} \\ &= \sum_{n=-N_{ST}/2}^{N_{ST}/2} |C_n| \cos[\omega_c t + n\Delta\omega(t - T_{CP}) + \theta_n + \varphi(t)] \end{aligned} \quad (2.3)$$

where ω_c is angular frequency of the RF carrier, $\Delta\omega$ is the subcarrier angular frequency spacing and $C_n = |C_n| \exp(j\theta_n)$ is the baseband QPSK signal.

The MB- OFDM UWB signal is applied to the DE-MZM to modulate a continuous wave (CW) light with optical power P_{in} and random phase $\phi(t)$ at wavelength λ . For OSSB modulation the DE-MZM is biased at quadrature. The DE-MZM is assumed to have an optical insertion loss of t_{ff} . The output optical field from the modulated DE-MZM can be written as

$$\begin{aligned} E_{out}(t) &= \sqrt{P_{in} t_{ff} / 2} \left[\exp\left(j\pi \frac{m_{RF}}{\sqrt{2}} y_k(t)\right) + j \exp\left(j\pi \frac{m_{RF}}{\sqrt{2}} \tilde{y}_k(t)\right) \right] \\ &\quad \times \exp\left\{j\left(\frac{2\pi c}{\lambda} t + \phi(t)\right)\right\} \end{aligned} \quad (2.4)$$

where c is the speed of light in vacuum, $m_{RF} = V_{RF} / V_{\pi}$ is RF modulation index, $V_{\pi} = 3.8$ V is the voltage required to induce a π phase shift at the DE-MZM, and $\tilde{y}_k(t)$ denotes the Hilbert transform of $y_k(t)$.

After transmission over optical fiber of length L , loss α and dispersion D , the optical field can be rewritten

$$\begin{aligned}
 E_{out}(t) = & \sqrt{2P_{in}t_{ff}Ge^{-\alpha L}} \exp\left\{j\left(\frac{2\pi c}{\lambda}t + \phi(t)\right)\right\} \\
 & \times \sum_{n_{-\frac{1}{2}N_{ST}}, n_{-\frac{1}{2}N_{ST}+1}, \dots, n_{\frac{1}{2}N_{ST}}}^{\infty} \cos\left[\left(1 + \sum_{k=-N_{ST}/2}^{N_{ST}/2} n_k\right)\frac{\pi}{4}\right] \\
 & \times \exp\left\{-j\frac{\lambda^2 DL}{4\pi c}\left(\sum_{k=-N_{ST}/2}^{N_{ST}/2} n_k \omega_k\right)^2\right\} \prod_{k=-N_{ST}/2}^{N_{ST}/2} J_{n_k}\left(\frac{\pi}{\sqrt{2}}m_{RF}\right) \quad (2.5) \\
 & \times \exp\left\{j\sum_{k=-N_{ST}/2}^{N_{ST}/2} n_k \left[\omega_k\left(t + \frac{L}{v_g}\right) + k\Delta\omega\left(\frac{L}{v_g} - T_{CP}\right)\right]\right. \\
 & \quad \left.+ \frac{3\pi}{4} + \theta_k + \varphi(t)\right\}
 \end{aligned}$$

where G is the gain of the optical amplifier, $\omega_k = \omega_c + k\Delta\omega$ is the k^{th} angular frequency subcarrier of the symbol, $J_n(\cdot)$ is the n^{th} order Bessel function of first kind, v_g and $\beta_2 = -\lambda^2 DL / (2\pi c)$ are group velocity and group velocity dispersion (GVD) coefficient of the fiber, respectively.

After the photodetection and electrical filtering, the received r^{th} subcarrier current of the OFDM symbol can be expressed as (2.6), where \Re is the responsivity of the photodetector, $H_e(\omega)$ is transfer function of the optical receiver, and φ_r is Gaussian random phase noise with zero mean and variance σ_{φ}^2 from the RF carrier. The laser phase noise $\phi(t)$ is cancelled in equation (2.6) due to self heterodyne detection.

$$\begin{aligned}
i_r(t) = & -\frac{1}{2} P_{in} t_{ff} G e^{-\alpha L} \Re(\omega_r) H_e(\omega_r) \exp \left\{ j \left[\omega_r \left(t + \frac{L}{v_g} \right) - r \Delta \omega T_{CP} + \frac{\pi}{4} + \theta_r + \varphi_r \right] \right\} \\
& \times \left\{ \begin{aligned} & \sqrt{2} J_1 \left(\sqrt{2} \pi m_{RF} \sin \left(\frac{1}{2} \beta_2 L \omega_r^2 \right) \right) \prod_{k=-N_{ST}/2, \neq r}^{N_{ST}/2} J_0 \left(\sqrt{2} \pi m_{RF} \sin \left(\frac{1}{2} \beta_2 L \omega_r \omega_k \right) \right) \\ & + j J_1 \left(\sqrt{2} \pi m_{RF} \sin \left(\frac{1}{2} \beta_2 L \omega_r^2 + \frac{\pi}{4} \right) \right) \prod_{k=-N_{ST}/2, \neq r}^{N_{ST}/2} J_0 \left(\sqrt{2} \pi m_{RF} \sin \left(\frac{1}{2} \beta_2 L \omega_r \omega_k + \frac{\pi}{4} \right) \right) \\ & + j J_1 \left(\sqrt{2} \pi m_{RF} \cos \left(\frac{1}{2} \beta_2 L \omega_r^2 + \frac{\pi}{4} \right) \right) \prod_{k=-N_{ST}/2, \neq r}^{N_{ST}/2} J_0 \left(\sqrt{2} \pi m_{RF} \cos \left(\frac{1}{2} \beta_2 L \omega_r \omega_k + \frac{\pi}{4} \right) \right) \end{aligned} \right\} \quad (2.6)
\end{aligned}$$

Equation (2.6) shows that each subcarrier will be distorted in amplitude and phase. This distortion results from intrinsic nonlinearities of the DE-MZM response, fiber dispersion and frequency response of the optical receiver.

Considering a low RF modulation index of $m_{RF} \ll 1$ and the ideal optical receiver, we can simplify equation (2.6) into

$$\begin{aligned}
i_r(t) = & -\frac{1}{2\sqrt{2}} P_{in} t_{ff} G e^{-\alpha L} \pi \frac{V_{RF}}{V_\pi} \\
& \times |C_r| \exp \left\{ j \left[\omega_r \left(t + \frac{L}{v_g} \right) - r \Delta \omega T_{CP} + \frac{3\pi}{4} - \frac{1}{2} \beta_2 L \omega_r^2 + \theta_r + \varphi_r \right] \right\} \quad (2.7)
\end{aligned}$$

Using the approximation of $\omega_r^2 \sim \omega_c^2 + 2r\omega_c\Delta\omega$, the received OFDM symbol can be written as

$$\begin{aligned}
y_k(t) & \propto \sum_{r=-N_{ST}/2}^{N_{ST}/2} i_r(t) \\
& \propto \sum_{r=-N_{ST}/2}^{N_{ST}/2} \hat{Y}_r \exp \left\{ j r \Delta \omega \left(t + \frac{L}{v_g} - T_{CP} \right) \right\} \quad (2.8)
\end{aligned}$$

where $\hat{Y}_r = X_r \exp \{ j(-r\beta_2 L \omega_c \Delta \omega + \varphi_r) \}$ is the normalized received symbol corresponding to the transmitted symbol $X_r = |C_r| \exp(j\theta_r)$ of the r^{th} subcarrier. Assuming that constant delay will be compensated by cyclic prefix, the EVM can be approximated using [24]

$$\begin{aligned}
EVM_0^2 & = \frac{1}{N_{ST}} \sum_{k=-N_{ST}/2}^{N_{ST}/2} |\hat{Y}_k - X_k|^2 \\
& = \frac{2}{N_{ST}} \sum_{k=-N_{ST}/2}^{N_{ST}/2} |X_k|^2 (1 - \cos(k\beta_2 L \omega_c \Delta \omega + \varphi_k)) \quad (2.9)
\end{aligned}$$

Using the following identities

$$\begin{aligned} \frac{1}{N} \sum_{k=-N}^N e^{jk\theta} &= \frac{1}{N} \frac{e^{jN\theta} - 1}{e^{j\theta} - 1} \\ &= \exp\left(j(N+1)\frac{\theta}{2}\right) \text{sinc}\left(N\frac{\theta}{2}\right) / \text{sinc}\left(\frac{\theta}{2}\right) \end{aligned} \quad (2.10)$$

and

$$\frac{1}{\sqrt{2\pi}\sigma_\varphi} \int_{-\infty}^{\infty} \cos \varphi_k \exp\left(-\frac{\varphi_k^2}{2\sigma_\varphi^2}\right) d\varphi_k = \exp\left(-\frac{\sigma_\varphi^2}{2}\right) \quad (2.11)$$

where $|X_k|$ and φ_k are independent random variables. Averaging EVM_0 we get

$$\langle EVM_0^2 \rangle = 2 \left(1 - \exp\left(-\frac{1}{2}\sigma_\varphi^2\right) \cos\left(\frac{1}{4}(N_{ST} + 2)\beta_2 L \omega_c \Delta\omega\right) \right) \times \text{sinc}\left(\frac{1}{4}N_{ST}\beta_2 L \omega_c \Delta\omega\right) / \text{sinc}\left(\frac{1}{2}\beta_2 L \omega_c \Delta\omega\right) \quad (2.12)$$

The expression given by equation (2.12) is the EVM induced by phase distortion. Both RF carrier phase noise and fiber dispersion will introduce relative phase shift between the OFDM subcarriers. Thus inter-carrier interference (ICI) will be induced and OFDM orthogonality will be lost.

Accounting for other sources of noise such as thermal, RIN, optical amplifier and shot noise, the total EVM can be expressed as [25]

$$EVM^2 = \langle EVM_0^2 \rangle + 1/SNR \quad (2.13)$$

where $SNR = \sigma_s^2 / \sigma_n^2$ is the received signal to noise ratio, with σ_s^2 as the received UWB signal power and σ_n^2 as the noise power as explained in Appendix B. Fiber dispersion not only induces relative phase shift between OFDM subcarriers but also converts the laser phase noise to RIN. Therefore, SNR in equation (2.13) also includes the converted RIN that depends on fiber dispersion. In Appendix B, the converted RIN is analyzed.

2.2.2 Wireless Transmission of UWB

The performance will depend on two factors. First, the multi-path reception from the adjacent objects can affect the performance, but UWB signal has an ultra-short duration in time domain, so the number of multi-path components that arrives at the receiver within the period is small and will not have a serious effect as it would have in a narrowband channel [26]. The analysis of the

effect of multi-path is rather complex and highly dependent on the environment. As a rule of thumb, the loss increases due to multi-path when the distance between the transmitting and receiving antennas is increased. Secondly, the path loss is of an important issue, which at a distance d is given by [27]

$$P_L(d) = [P_{L0} + 10\gamma \log_{10}(d/d_0)] + S(d) \quad (2.14)$$

here $P_{L0} = 20 \log_{10}(4\pi f_c d / c) \approx 44$ dB is the path loss for $d_0 = 1$ m, $f_c = \sqrt{f_{\min} f_{\max}} = 3.88$ GHz where $f_{\min} = 3.168$ GHz and $f_{\max} = 4.752$ GHz being the lower and upper -10 dB cutoff frequencies of the power spectrum of band group 1 for MB-OFDM UWB system, $10\gamma \log_{10}(d/d_0)$ is the mean path-loss referenced to 1 m, $\gamma \approx 2$ is the path-loss exponent and $S(d)$ represents the lognormal shadowing [26-27] and can be approximated from transmitted and received RF power measurement to 1.85 dB with a standard deviation of 0.3. All the values stated are empirical values for a line of sight (LOS) model with omnidirectional transmit and receive antennas and can vary from location to location. Then the RF power at the receiver (P_{rec}) in terms of transmitted UWB power (P_{uwb}), transmit antenna gain (G_T) and receive antenna gain (G_R) can be expressed by

$$P_{rec} = P_{uwb} + G_T + G_R - P_L(d) \quad (2.15)$$

In the experiment, we used pair of In4Tel antennas with gain $G_T = G_R = 2$ dBi. Therefore, from the above equation it is seen that the received power will depend mainly on the mean path-loss referenced to 1 m.

2.3 Experimental System Configuration

The considered system setup for the performance evaluation of UWB over fiber is shown in Figure 2.1. A commercially available evaluation board, DV 9110M TX (point A in Figure 2.1), from WisAir, providing MB-OFDM compliant modulation with three WiMedia sub-bands allocated at center frequency of 3.432, 3.96 and 4.488 GHz, is used for MB-UWB generation.

For the performance evaluation of UWB wireless systems with fiber distribution, the UWB signal after 20km of fiber transmission is launched to air by an antenna and received by a receiver module DV 9110M RX (point E in Figure 2.1). A laptop is used to run the built-in

WisMan software provided with the DV 9110M modules to configure and control the transmitter and receiver modules. Number of transmitted packets is fixed at 10^6 and each packet has 1024 octets. The PER is evaluated from number of the transmitted and received packets.

An arbitrary waveform generator, AWG 7122B (point B in Figure 2.1), from Tektronix with 9.6 GHz effective RF bandwidth is used for UWB signal generation. First the MB-OFDM UWB signals compliant with WiMedia standard [5] and the narrow band interferers are generated using MATLAB. For the MB-OFDM UWB signal each generated sub-band has an RF bandwidth of 528 MHz with 128 OFDM subcarriers and bit rate of 200 Mb/s with QPSK modulation. Among the subcarriers, 100 subcarriers carry data and the rest are null, pilot and guard tones. The separation between subcarriers is 4.125 MHz. The signal also has a cyclic prefix and guard interval of 60.61 and 9.47 ns, respectively. The generated WiMedia sub-band follows a simple hopping sequence as f_1 , f_2 , and f_3 according to Time Frequency Code (TFC) 1, defined in WiMedia standard [5], so that only one channel exists at any particular time.

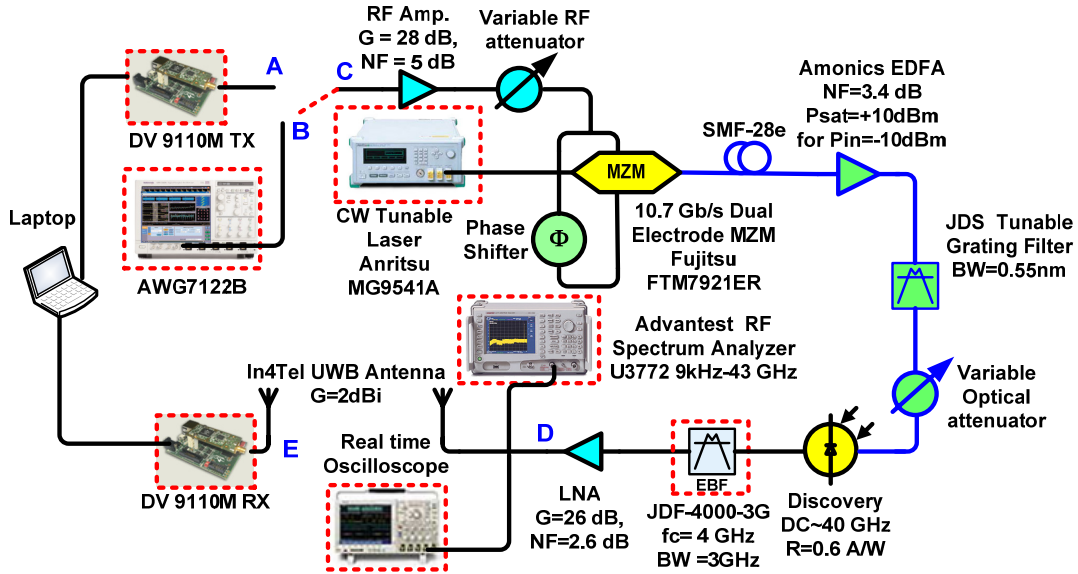


Figure 2.1 Experimental setup for externally modulated MB-OFDM UWB over fiber system (BW: bandwidth, G: gain, NF: noise figure, R: responsivity)

The RF signal is amplified and variable RF attenuator is used to vary the RF power. A CW light from tunable laser source (Anritsu MG9541A) have a wavelength of 1550 nm, linewidth of 800 KHz, intrinsic RIN of -155 dB/Hz and output power of 0 dBm. The CW light is injected into a 10.7 Gb/s DE-MZM from Fujitsu, driven by the RF signal from the output of the DV 9110M Tx module (point A in Figure 2.1) or from the output of the AWG7122B (point B in Figure 2.1). The MZM has 6 dB insertion loss, half-wave switching voltage of 3.8V and an extinction ratio of 28.5 dB.

To obtain OSSB modulation the UWB signal is applied to both branches of the DE-MZM through a hybrid electrical coupler (HEC) and bias-T with a $\Phi=90^\circ$ phase shifter in one branch. On the contrary, to generate optical double side band (ODSB), the same signal is directly applied to both electrodes of the MZM with $\Phi=0$ degree phase shift. The modulated lightwave is sent through SMF, with fiber loss of $\alpha = 0.21$ dB/km and chromatic dispersion of 17 ps/ (nm.km). We consider UWB over fiber with back-to-back, 20 and 40 km of fiber transmission. After fiber transmission, the UWB signal is optically amplified by an erbium doped fiber amplifier (EDFA) and then a JDS tunable grating filter with bandwidth of 0.55 nm and insertion loss of 2 dB is used before being detected by a high speed PD (Discovery DSC-740 with 3-dB bandwidth of 35 GHz and responsivity of 0.62 A/W). The EDFA gain is controlled in such a way that the insertion loss of all optical components and fiber is compensated. A variable optical attenuator is used to vary the received optical power at the photodetector. After photodetection the UWB signal is electrically filtered by a JDF EBF of bandwidth of 3 GHz and then amplified by a broadband RF amplifier from SHF (SHF-810) (>30 GHz) as shown in Figure 2.1. The broadband photodetector combined with the broadband RF amplifier is referred to “ideal” optical receiver. Here the “ideal” optical receiver means that it does not introduce amplitude and phase distortion to the OFDM signal.

The received signal is evaluated with a high speed real time oscilloscope DSO 91204 from Agilent Technologies. At the real time oscilloscope the received signal is first internally amplified using a low noise amplifier (LNA) and down-converted to the complex baseband using I and Q mixers. The complex baseband signal passes a low-pass band filter to reject out of band interferers. The signal is then sampled and quantized using an analog to digital converter (ADC) to obtain the complex digital baseband signal. The real time oscilloscope has a large memory that

stores about 5 million samples of the signal for processing. Baseband processing begins with the packet detection followed by Fast Fourier transform (FFT) operation. The output signal from the FFT is equalized using a frequency domain equalizer. A phase correction is applied to the output of the equalizer to undo the effect of carrier and timing mismatch between transmitter and receiver according to ECMA-368 standard [7]. The pilot tones in each OFDM symbol are used to drive the digital phase-locked-loop (PLL). The output of the equalizer is de-mapped and de-interleaved before passing to a Viterbi decoder. The error corrected bit sequence is descrambled and passed on to the media access control (MAC) layer for further processing.

EVM or relative constellation root mean square (RMS) error is the PHY performance and it contains information about both phase and amplitude errors that are more useful for assessing microwave properties of the signal like the random noise, phase noise, Amplitude/Amplitude (AM/AM) distortion, Amplitude/Phase (AM/PM) distortion, delay distortion and interference effects. Average EVM in WiMedia PHY 1.2 standard [7] is computed as follows

$$EVM = \frac{1}{N_f} \sum_{i=1}^{N_f} \sqrt{\sum_{n=1+N_{sync}+N_{hdr}}^{N_{packet}} \left[\frac{\sum_{k=1}^{N_D} |R_{D,n}[k] - C_{D,n}[k]|^2 + \sum_{k=1}^{N_P} |R_{P,n}[k] - C_{P,n}[k]|^2}{(N_D + N_P) N_{frame} P_0} \right]} \quad (2.16)$$

where N_f is the number of packets under test, N_{packet} is the number of symbols in the packet, N_{sync} is the number of symbols in the preamble, N_{hdr} is the number of symbols in the header, $N_{frame} = N_{packet} - N_{sync} - N_{hdr}$ is the number of symbols in the frame, N_D is the number of data subcarriers, N_P is the number of pilot subcarriers, P_0 is the average power over all payload symbols of the data and pilot constellations, $C_{D,n}[k]$ and $C_{P,n}[k]$ are the transmitted k^{th} data subcarrier and k^{th} pilot subcarrier for the n^{th} OFDM symbol, respectively, and $R_{D,n}[k]$ and $R_{P,n}[k]$ are the observed k^{th} data subcarrier and k^{th} pilot subcarrier for the n^{th} OFDM symbol, respectively.

The EVM required at the transmitter for bit rates of up to 200 Mb/s is -17dB and above 200 Mb/s it is -19.5 dB respectively with no transmitter attenuation [7]. For conformance testing -16 dB is the EVM limit for 200 Mb/s. The EVM is analyzed on the payload portion of the packet only, over a minimum of 100 packets generated from random data. The payload of each packet has to be at least 30 symbols in length. In our experiment each packet consists of 60 symbols.

For experiments concerning RIN a CW light from multi-channel fiber optic source module ILX Lightwave FOM-7900B is set to have a wavelength of 1553.3 nm and output power from -6 to 5 dBm. The linewidth of the laser can be tuned to either 30 MHz or 1 GHz.

2.4 Simulation Setup

Figure 2.2 shows simulation setup for MB OFDM UWB with VPI Transmission Maker and MATLAB. First a pseudo random bit sequence (PRBS) is generated which is scrambled into a bit sequence that is free from long strings of simple patterns such as mark and spaces. Then a mother convolutional encoder with coding rate of 1/3 was used. The convolutionally encoded bits were punctured to achieve coding rate of 5/8. The data was bit interleaved and converted into complex valued QPSK sequence according to gray coded constellation. Then for each 100 data, 12 pilots, 10 guard and also 6 null-tones are added to satisfy the 2^N condition for radix butterfly algorithm for IFFT [6]. The data is passed through a Saleh-Valenzuela channel for UWB [7]. Then from this data real and imaginary part are separated and written to different text files. All the wireless signal processing is done using MATLAB™.

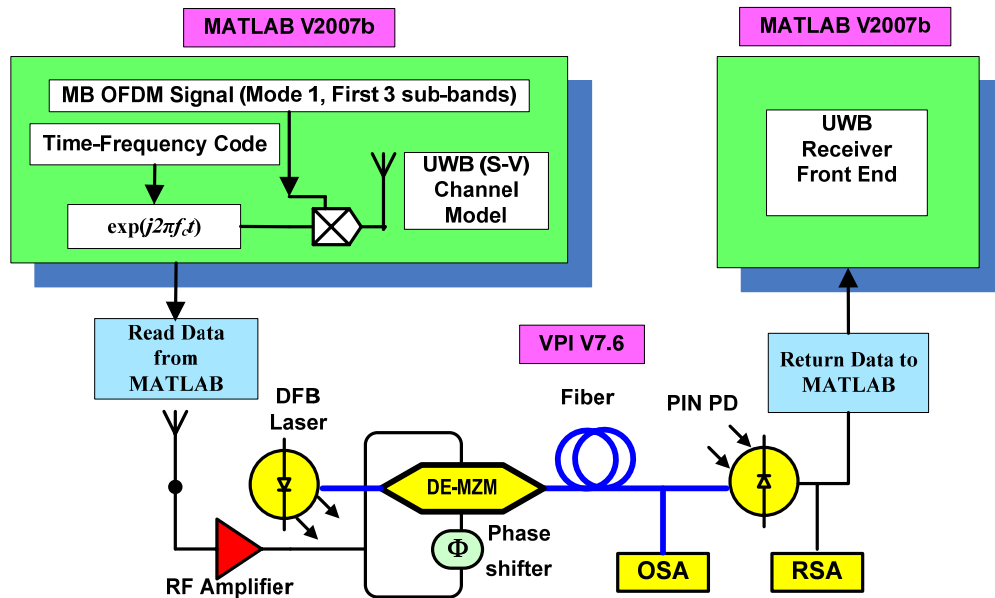


Figure 2.2 Simulation setup for MB OFDM UWB.

This data is read by using file reader of the software VPI7.6 from VPIphotonics™. A distributed feed-back (DFB) laser and a DE-MZM are used to externally modulate the signal. The laser has RIN of -155dB/Hz. The DE-MZM has an extinction ratio of 28.5dB, insertion loss of 6 dB and half-wave switching voltage of 5V. The fiber used is an SMF with dispersion of $17 \times 10^{-6} \text{ s/m}^2$, dispersion slope of $0.086 \times 10^3 \text{ s/m}^3$ and nonlinear refractive index of $2.6 \times 10^{-20} \text{ m}^2$. A PIN PD with responsivity of 0.62A/W was used as a photo-detector.

2.5 Single Channel UWB over Fiber System

It is well known that there are two optical SCM techniques, i.e. OSSB and ODSB. In Appendix C, we experimentally compare the performance of the two modulation techniques in the system. It is shown that the ODSB modulation cannot be used in the MB-OFDM UWB wireless system with fiber distribution. Therefore we only consider the OSSB modulation technique in the following investigation and the optical spectrum is shown in Figure 2.3 (a).

To make sure that UWB wireless with fiber distribution as shown in Figure 2.1 satisfies the FCC's spectral requirement, the received signal is tested using the data analyzer and it is found that the UWB signal passed the spectral mask test and measured adjacent channel power ratio (ACPR) was higher than 20 dB for RF modulation index of up to 8% at the MZM as shown in Figure 2.3 (b). Thus RF modulation index of up to 8% is only considered in the following investigation to abide by the FCC regulation. Figure 2.3 (c) shows RF spectrum for the first three bands are centered at frequency of $f_1=3.432$, $f_2=3.96$ and $f_3=4.488$ GHz. The signal follows simple frequency hopping sequences like f_1 , f_2 and f_3 as shown in Figure 2.3(d) that is the spectrogram. The bit rate of 200 Mb/s is used for each band with QPSK modulations shown from the constellation of Figure 2.3(e). (Figure 2.3(d) and (e) were measured with a Lecroy serial data analyzer SDA11000).

In this section we will analyze the impact of optical modulation and fiber transmission, and investigate the impact of optical demodulation, effect of optical receiver noise and received optical power.

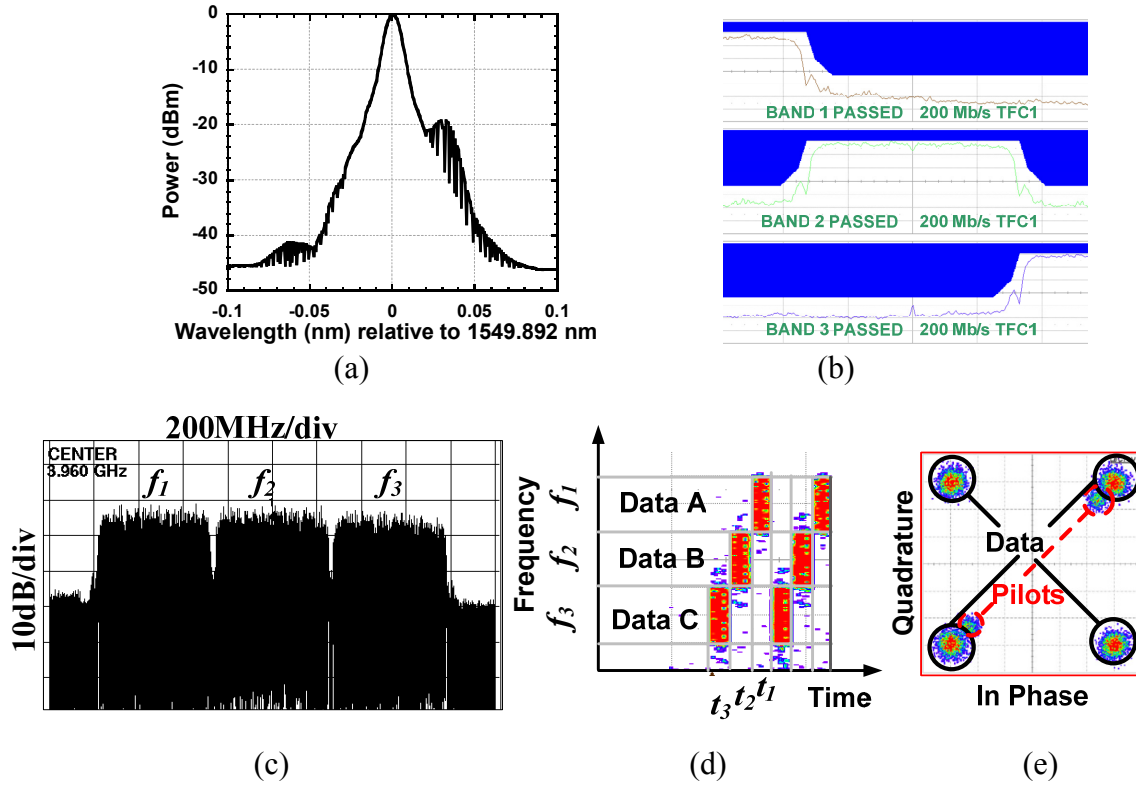


Figure 2.3 First three bands of MB-OFDM UWB wireless in (a) Optical spectrum, (b) spectral mask test according to FCC, (c) frequency domain, (d) frequency-time domain and (e) received constellation.

2.5.1 Impact of Optical Modulation and Fiber Transmission

Using the setup as shown in Figure 2.1, we experimentally characterize the impact of optical modulation and fiber transmission using measured EVM. For different fiber lengths, we adjust the gain of the EDFA to fully compensate for all loss and keep the same input power to the PD. The ideal optical receiver used has broadband response with flat magnitude and linear delay over the considered signal bandwidth. Figure 2.4 shows measured EVM with RF modulation index for UWB over fiber with fiber length of 0, 20 and 40 km, considering bit rate of 53.3 and 200 Mb/s. It is apparent that the minimum EVM is obtained at RF modulation index of 3~4 % for both 53.3 and 200 Mb/s, almost independent of the bit rate, as shown in Figure 2.4 (a) and (b). At the low RF power the EVM is high due to low SNR. On the other hand, at the high power level the EVM increases due to DE-MZM nonlinearities and fiber dispersion induced nonlinear distortion mainly.

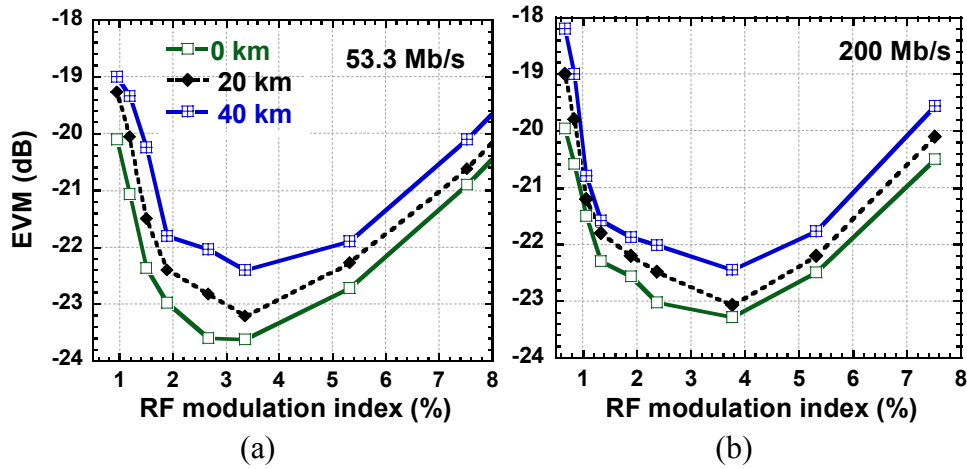


Figure 2.4 Measured EVM with RF modulation index with a parameter of fiber length for bit rate of (a) 53.3Mb/s and (b) 200Mb/s.

To fully understand the behaviors in Figure 2.4, it is required to have a full understanding of nonlinear distortion. It is well known that the OFDM signal has a high peak to average power ratio (PAPR). The measured PAPR for the UWB signal is about 14~17 dB from the DV9110 module. Nonlinear distortion for the UWB signal can be induced by RF amplifier due to large PAPR, phase noise of the RF carrier local oscillator due to Phase/ Amplitude (PM/AM) conversion and nonlinear response of the DE-MZM. However, RF amplifier can induce nonlinear distortion only at higher RF power level. But for OFDM UWB, the RF amplifier is operated in the linear region for most of the time owing to low power spectral density of the UWB. The phase noise may induce nonlinear distortion due to PM/AM conversion and created PM/AM modulation is imposed onto the complex waveform. Nonlinear distortion induced by the nonlinearities of the DE-MZM due to AM/AM modulation and fiber dispersion due to PM/AM conversion is the most important. Equation (2.6) reveals that the DE-MZM nonlinearities combined with fiber dispersion will induce both AM/AM and PM/AM distortion within one symbol.

To distinguish the impact of the DE-MZM response nonlinearities and fiber dispersion, we first consider the back to back UWB over fiber, i.e. without fiber. If the response nonlinearities of the DE-MZM are only considered, equation (2.6) is reduced to

$$i_r(t) = P_{in} t_{ff} G e^{-\alpha L} J_1(\pi m_{RF}) [J_0(\pi m_{RF})]^{N_{ST}-1} \times \exp\left\{j\left[\omega_r t - r \Delta \omega T_{CP} - \frac{\pi}{4} + \theta_r\right]\right\} \quad (2.17)$$

where the ideal optical receiver response is assumed.

It can be noted from equation (2.17), that the received constellation is rotated by 45° . It is also shown that there is a pure AM/AM conversion induced distortion due to the term of $J_1(\pi m_{RF}) [J_0(\pi m_{RF})]^{N_{ST}-1}$, which depends only on the total transmitted RF power level at the DE-MZM. Figure 2.5 shows the relative amplitude (i.e. $2J_1(\pi m_{RF}) [J_0(\pi m_{RF})]^{N_{ST}-1}$) of the 128 subcarriers versus RF modulation index for the second band. It is obvious that the amplitude of all the 128 subcarriers is the same for any modulation index, and almost linearly increases with modulation index at RF modulation index of up to 4%. However, RF modulation index of higher than 4% will decrease the amplitude, i.e. AM/AM compression. Consequently RF modulation index of 4% is found optimum theoretically. This optimum modulation index of 4% is almost in good agreement with the above experimental results as shown in Figure 2.4. However, there is a small discrepancy between the optimum modulation indexes found from Figure 2.4 and Figure 2.5. This small discrepancy is mainly due to our simplified approach used in theory where it is assumed that all subcarriers are carrying data, DE-MZM extinction ratio is infinite, and there is no dependence of transmitted power level on bit rate.

In order to investigate the combined effect of fiber dispersion and DE-MZM response nonlinearities on each of the 128 subcarriers, relative amplitude of the subcarriers at 1, 32, 64, 96, and 128 in the second band (centered at 3.96 GHz) after fiber transmission of 20 and 40 km is shown in Figure 2.6, calculated by equation (2.6). It is shown that all the subcarriers have identical relative amplitude that increases almost linearly with the RF modulation index of up to $\sim 4\%$. However, the subcarriers may not have the same amplitude if modulation index is more than 4%. For example, at the modulation index of 10%, the subcarriers have different amplitudes as shown in Figure 2.6(a) and (b). This is contrary to the back-to-back transmission as shown in Figure 2.5. Any amplitude mismatch between subcarriers will distort the received constellation and degrade the EVM. For the back-to-back UWB over fiber system, the relative phase of the 128 subcarriers is constant and -45° for any modulation index. Because fiber dispersion will

induce different phase shifts for different subcarriers, the subcarrier phase will depend on fiber length and modulation index.

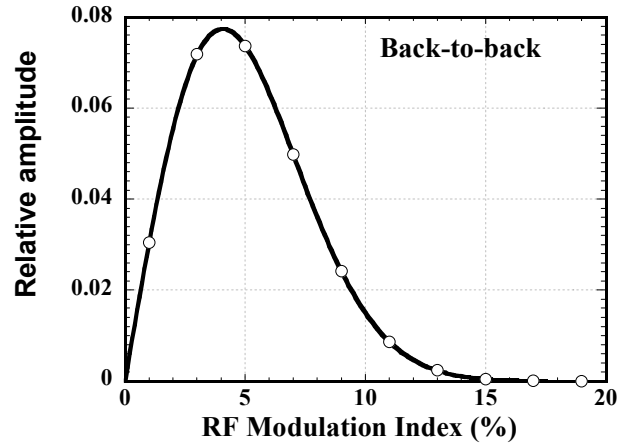


Figure 2.5 Relative amplitude of subcarriers in second band versus RF modulation index for back-to-back UWB over fiber.

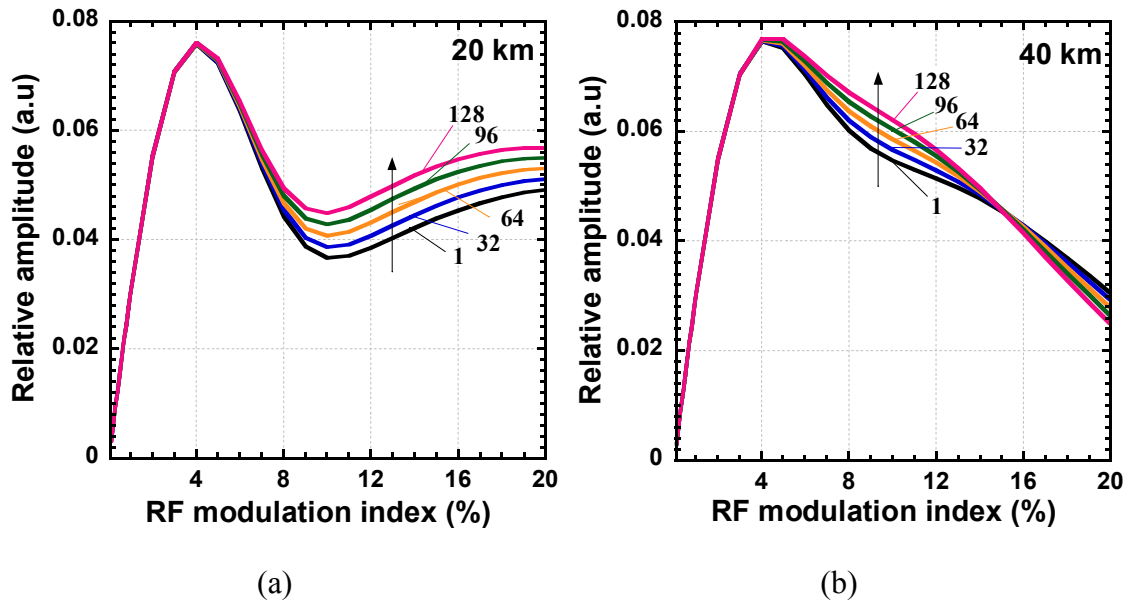


Figure 2.6 Calculated relative amplitude of subcarriers at 1, 32, 64, 96 and 128 in band 2 versus RF modulation index for UWB over fiber at (a) 20 and (b) 40 km of fiber.

Corresponding to Figure 2.6, Figure 2.7 shows the relative phase shift of the subcarriers mentioned above with modulation index. It is seen that the relative phase shift is changed from -40° to 45° and -30° to 45° for 20 and 40 km of fiber transmission, respectively. Also as expected, different subcarriers have different phase shifts for the same modulation index. In fact, fiber dispersion induces frequency dependent group delay at each subcarrier. Using equation (2.6), the calculated group delay over the band-two varies by ~ 0.8 and ~ 1.2 ps for 20 and 40 km of fiber, respectively. Relative phase shift between subcarriers will induce intercarrier interference and result in loss of orthogonality. We then investigate the impact of phase mismatch between subcarriers on the EVM of the system versus fiber dispersion. For RF modulation index of 4%, the amplitude mismatch between subcarriers is negligible.

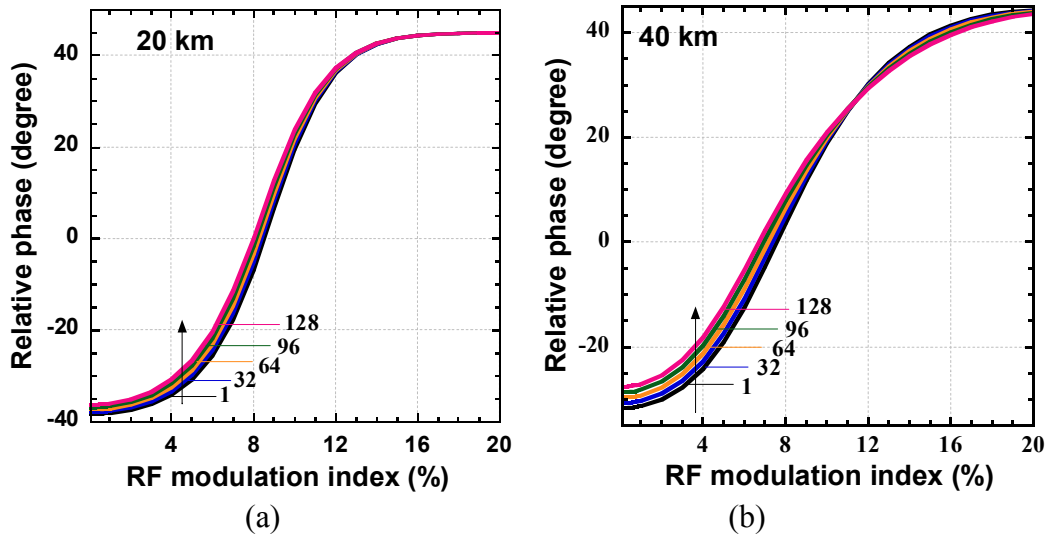


Figure 2.7 Calculated phase distortion of subcarriers (1, 32, 64, 96 and 128) in band-two versus RF modulation index at (a) 20 and (b) 40 km of fiber transmission.

In the EVM computation, we assume that any constant delay can be compensated by cyclic prefix, and the received complex baseband symbol is normalized. Calculated EVM degradation of the system versus fiber length using equation (2.13) is shown in Figure 2.8. In the calculation we used measured EVM of -24.4 dB without fiber link directly from UWB generator and SNR computed due to thermal noise only, which gives a phase noise power of $\sigma_\phi^2 \sim 0.0036$. The EVM

degradation is obtained with respect to the back to back at modulation index of 4%. Compared to the back to back, it is clearly shown that the EVM degradation of ~ 0.36 and ~ 1.1 dB is expected after 20 and 40 km of fiber transmission, respectively. This is in good agreement with the measurement in Figure 2.4. However the experimental EVM is slightly better because of the complex demodulation and error correction schemes used at the UWB receiver. The EVM degradation shown in Figure 2.8 is due to increased RIN due to the interaction of the laser phase noise and chromatic dispersion as shown in Appendix B, and the phase distortion induced by fiber dispersion as given in equation (2.12). Note that for Figure 2.8, a UWB over fiber system only with a single optical amplifier is considered in order to show the impact of fiber dispersion related penalty. By the above analysis, we conclude that RF modulation index of $\sim 4\%$ is optimum. For modulation index of above 4%, it was found above that DE-MZM response nonlinearities and fiber dispersion induced nonlinear distortion degrades the UWB wireless system performance. This is the reason why the EVM in Figure 2.4 is increased with modulation index if more than 4%.

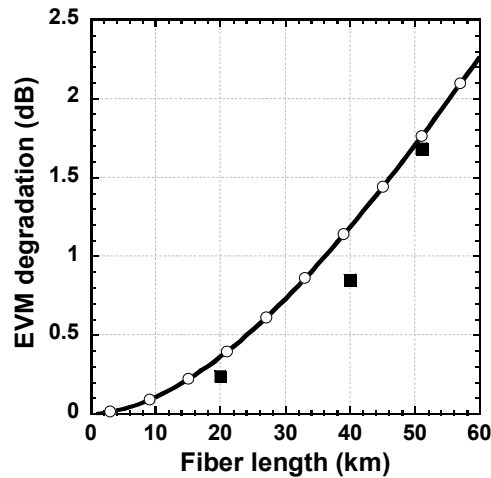


Figure 2.8 Calculated EVM degradation versus fiber length with respect to back to back and 0 dBm received optical power. Black square: experimental results for 20, 40 and 52 km.

2.5.2 Impact of Optical Demodulation

In this subsection, we will analyze the impact of optical demodulation. We consider two cases: one is the “ideal” optical receiver and the other is bandwidth-limited and has variation of magnitude and time delay over the OFDM signal bandwidth. The bandwidth-limited optical receiver is obtained by inserting a bandwidth-limited electrical filter in the “ideal” optical receiver. Equation (2.6) shows that the band limited optical receiver response will have great impact on overall performance.

We used a Chebyshev-I bandpass filter (BPF) centered at frequency, $f_c = 4$ GHz with a 3 dB bandwidth of 3 GHz. The magnitude and phase response measured are shown in Figure 2.9. It is clearly seen from Figure 2.9(a) that the magnitude response of filter has a ripple of ± 0.5 dB over the passband. It is expected that the magnitude ripple will induce distortion for the subcarriers of the OFDM signal. We measured EVM for the system with fiber transmission of 20 km, where the two receivers are used. Figure 2.10 shows measured EVM with RF modulation index. We also simulate the UWB over fiber system using VPI-Transmission Maker™ and MATLAB as described in Section 2.4. The simulated EVM is also shown in Figure 2.10. It is seen that a good agreement between the simulated and measured is obtained for using the two optical receivers. However, with ideal receiver response there is a discrepancy in EVM performance at higher modulation index due to nonlinearity of the RF amplifier and harmonic distortion effects arising from the A/D converters of the real time oscilloscope. It is found that the EVM is degraded by more than 2 dB at modulation index of 4% because of using the optical receiver with Chebyshev-I response. Due to the in-band ripples of the Chebyshev-I response, some of the sub-carriers of the OFDM signal are distorted in amplitude. Also, the filter’s phase or group delay response may cause a slow varying decay trail and can smear the signal at the edges [28]. Smearing will increase the delay spread resulting in inter symbol interference.

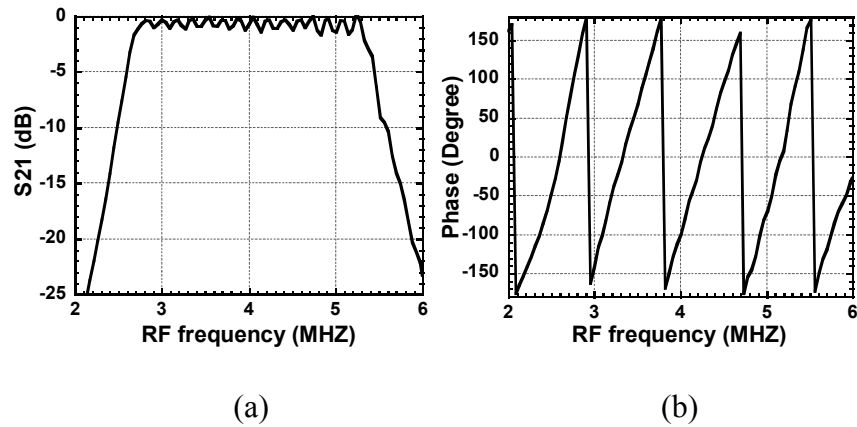


Figure 2.9 (a) Measured magnitude $|S_{21}|$ and (b) measured phase response of the experimental filter measured with a HP 8720 vector network analyzer.

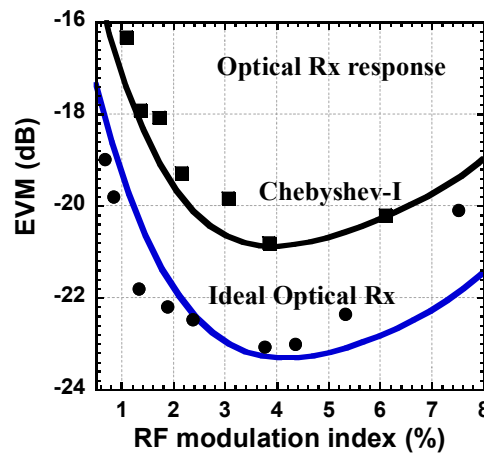


Figure 2.10 Measured (symbol) and simulated (line) EVM using two receivers. Black square: experimental results using optical Rx with Chebyshev-I response, Black circle: experimental results using the “ideal” optical Rx.

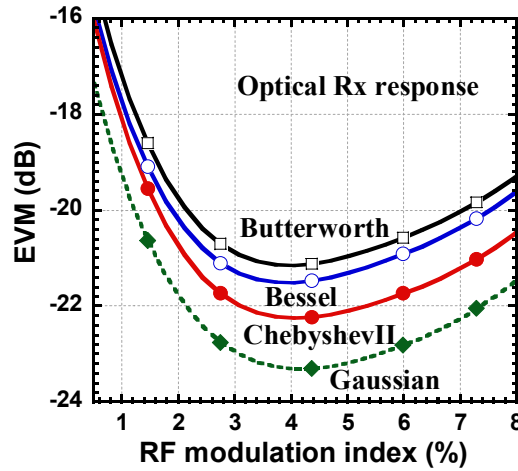


Figure 2.11 Simulated EVM using optical receiver with different responses. The used filters are fifth order centered at frequency $f_c = 4\text{GHz}$ with a 3dB bandwidth of 3GHz.

To further understand the impact of optical receiver response, we consider optical receiver with fifth order Butterworth, Bessel, Chebyshev-II, and Gaussian responses, respectively. Simulated EVM using the above optical receivers is shown in Figure 2.11. The bandwidth is 3 GHz for all the optical receivers. It is seen that the optical receiver with Gaussian response leads to the best performance. A Gaussian filter with fifth order has flat magnitude and zero delay response in the passband. So, the performance using the optical receiver with Gaussian response will be similar to the ideal receiver. But a Gaussian response is not physically realizable. In Figure 2.11, the EVM using Butterworth response is -21.2 dB compared to -20.7 dB using Chebyshev-I in Figure 2.10 at modulation index of 4% and it is evident that Butterworth response performs slightly better than Chebyshev-I response of the same order because Butterworth has a flat magnitude response and better delay characteristics than Chebyshev-I filter. To achieve a sharp cutoff, a higher order Butterworth filter is required. But, higher order Butterworth filter will have high overshoot and instability in response compared to Bessel and Chebyshev-II filter [29] and lower order Butterworth filter does not fulfill filtering requirements due to its wide passband. Bessel filter's performance is in between Butterworth and Chebyshev-II response since Bessel filter has a linear phase response and excellent impulse response with minimal overshoot within its passband. For a given order, its magnitude response is not as flat as Butterworth and other filters. Also, a Bessel filter requires more complex design and is difficult

to integrate with a receiver front end. Consequently it may not be appropriate. In Figure 2.11, it is clear that EVM performance using optical receiver with Chebyshev-II response is better than using optical receiver with Chebyshev-I, Butterworth and Bessel response. The response of a Chebyshev-II filter is equiripple in the stopband and monotonic in the passband. Also Chebyshev-II's delay response is moderate. In OFDM signal all the subcarriers are independent of each other. As a result, the subcarriers can be added constructively or destructively, resulting in a very large or weak signal, respectively. This is why the OFDM signal has a large PAPR and will suffer badly from nonlinearity. Since OFDM signals are highly sensitive to amplitude distortion, Chebyshev-II response at the receiver front end gives better EVM because the filter will introduce hardly any amplitude distortion. Therefore, Chebyshev-II response is the best choice for optical receiver in UWB over fiber system.

Now, to find out the optimum order and bandwidth, we carry out simulations using Chebyshev-II response with different order and bandwidth. Only odd-orders are considered since even-order Chebyshev filter requires an extra impedance matching network [30]. Simulated EVM with modulation index is presented in Figure 2.12 for 20 km of fiber transmission and bit rate of 200 Mb/s. The BPF was centered at 4 GHz and the bandwidth was varied. Figure 2.12 shows that EVM performance is greatly dependent on filter order and bandwidth. The change in EVM can be explained from the magnitude and delay response of the filter which is presented in Appendix D. It is seen that Chebyshev-II has a flat magnitude response in the passband. So, only delay response may degrade EVM performance.

If the delay fluctuates within the passband, the OFDM subcarriers undergo different phase shift. The effect of delay fluctuation due to filter response is similar to the effect of phase shift introduced by fiber dispersion. A filter's group delay and overshoot are nearly proportional to the filter order and inversely proportional to the filter bandwidth. So, for a higher order filter if the bandwidth is increased the delay response gets better. It is seen that if the bandwidth is low, e.g. 2 GHz, the EVM degrades because the OFDM subcarriers near the edges experience a slight attenuation and high group delay fluctuation. The delay within the signal bandwidth varies from 80 to 250 ps for fifth order Chebyshev-II response with 2 GHz bandwidth. In contrast, the average delay fluctuation is 57, 80 and 62 ps for third order filter with 2.5 GHz, fifth order filter with 2.5 GHz and seventh order filter with 3 GHz, respectively. Consequently, the EVM

performance using seventh order filter with 3 GHz is in between fifth order filter with 2.5 GHz and third order filter with 2.5 GHz. For the 3 GHz bandwidth a seventh order filter has a very sharp cutoff but its delay response is not as good as third and fifth order filter. Also microwave filter with higher than fifth order is complex to be implemented and is expensive.

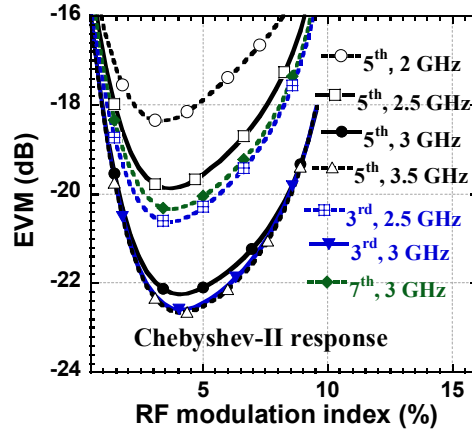


Figure 2.12 Simulated EVM with Chebyshev-II filter order and bandwidth for 200 Mb/s UWB signal transmitted over 20 km of fiber.

Figure 2.12 shows the EVM performance using third order 3 GHz, fifth order 3 and 3.5 GHz filter's response is alike since their average delay fluctuation is close (42, 47 and 40 ps respectively). On the other hand, the best filter order and bandwidth of the optical receiver in uplink UWB over fiber system may also depend on environment, because an UWB antenna may be placed close to some narrow band interferers like GSM at 0.8~0.9 GHz and microwave ovens at 1.5~2 GHz. So, for uplink when the data is received by a base station from a user with an antenna under the presence of such narrow band interferers, optical receiver with third order filter response can perform poorly due to its slowly decaying stopband and the large magnitude of out of band ripples. From magnitude response in Appendix D it is seen third order 3 GHz filter will not satisfy the required 20 dB suppression of the sidebands. So, optical receiver with fifth order filter response is a better choice than third order filter response for filtering of MB OFDM UWB signals.

As stated before, increasing the filter bandwidth for a given order improves its delay response, and therefore reduces the EVM. But, the receiver noise increases if the electrical bandwidth of optical receiver is increased which is explained in Appendix B. Consequently, an optical receiver with bandwidth as narrow as possible should be selected without introducing amplitude and delay distortion. It is also seen from Figure 2.12 that the EVM performance using the fifth order filter response was improved by only 0.29 dB at RF modulation index of 4% when the bandwidth is increased from 3 GHz to 3.5 GHz. Therefore, 3 GHz is considered the optimum bandwidth, which is roughly two times of the bandwidth ($3.168 \text{ GHz} = 2 \times 3 \times 528 \text{ MHz}$) of the band.

2.5.3 Effect of Receiver Noise and Received Optical Power

Until now, we have assumed all the losses due to fiber and optical components are compensated using an EDFA. To see the effect of the received optical power, we first operate the system for the best EVM at data rate of 200 Mb/s by setting the RF modulation index to 4% and received optical power to 0 dBm at the photodetector. Then we insert a precision variable optical attenuator Agilent 8156A before the photodetector to vary the received optical power.

Figure 2.13 shows measured EVM at 200 Mb/s considering back-to-back and after 20 km of fiber. The EVM performance is degraded as the received optical power decreases. To understand the behavior in Figure 2.13, we study the impairment of noise. In Appendix B, each contribution of thermal noise, shot noise, RIN, signal-ASE beat and ASE-ASE beat noise is studied. It is found that signal-ASE beat noise is dominant in additive noise. Therefore, EVM decrease with the increase of the received optical power is due to the fact that UWB RF power is increased with the increase of received optical power. The total EVM dependency on the optical power (given by equation (2.13) is of the form $A/P_{opt} + \langle EVM_0^2 \rangle$, A-constant, and EVM_0 does not depend on optical power. It is clear that EVM degradation is inversely proportional to received optical power. Another important finding from Figure 2.13 is that the required optical power at optical receiver in UWB over fiber is reasonably higher than that in radio over fiber with other modulation schemes which can work with optical power of as low as -40 dBm [1]. The higher optical power requirement is due to the low RF modulation index and the low power spectral density (-41.3 dBm/MHz) of the UWB RF signal.

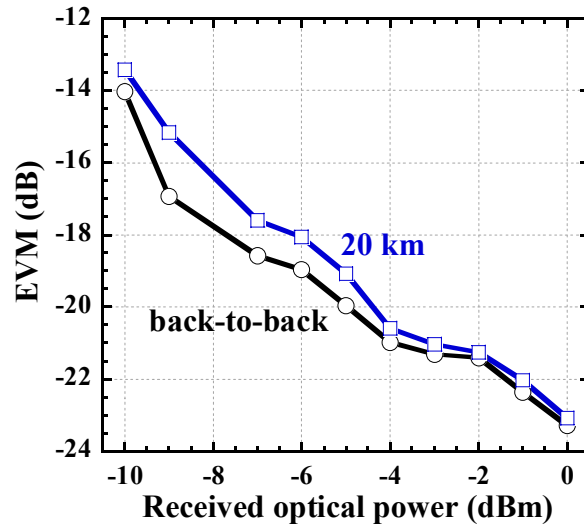


Figure 2.13 Measured EVM versus received optical power at photodetector.

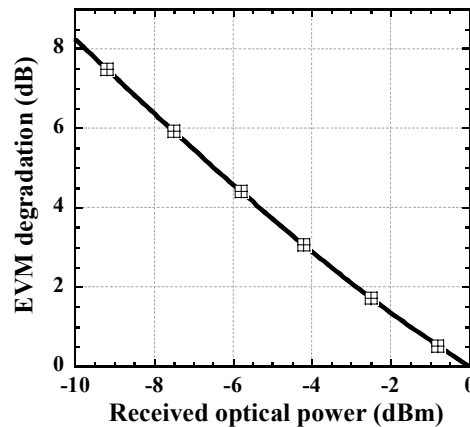


Figure 2.14 Calculated EVM degradation versus received optical power for back-to-back transmission with respect to 0 dBm received optical power.

We calculate the EVM degradation versus received optical power as shown in Figure 2.14. It is evident by Figure 2.14 that the EVM degrades almost linearly with the received optical power. Experimental results in Figure 2.13 are in good agreement with calculated EVM from 0 up to -9 dBm. However there is a small discrepancy at low optical power and it is due to the limited sensitivity of the real time oscilloscope that has difficulty in triggering at low RF power level. As

shown in Figure 2.13, there is a difference in EVM performance between back-to-back and 20 km of fiber, which is explained in Figure 2.8.

2.6 Single Channel Wireless UWB over Fiber System

In this Section, using the setup described above in Section 2.3, here also, our system passed the spectral mask requirement set by US Federal Communications Commission (FCC) and measured ACPR was higher than 20 dB for maximum transmitted UWB power.

2.6.1 Transmitted UWB signal power and Receiver Sensitivity

The PER depends on the received SNR and receiver sensitivity. As the power level of the input UWB signal to the DE-MZM increases the transmitted output power increases up to a certain value corresponding to a modulation index $m_{RF} = 4\%$ then starts decreasing due to AM/AM compression of the DE-MZM as found in Section 2.5.1. If the SNR increases the packet error rate will decrease. We vary the transmitted UWB power level from -46.5 dBm up to -11.13 dBm by changing the UWB input power to the DE-MZM from -32.5 to 3.17 dBm and measure transmitted, received RF power and the corresponding PER at the receiver after 1 m distance of wireless link, shown in Figure 2.15.

From Figure 2.15 we find out that for maximum allowable PER of 8% and for 53.3, 200 and 480 Mb/s the receiver sensitivity is -82, -76.7 and -72.3 dBm, respectively, which meet the required receiver sensitivity of -80.8, -74.5 and -70.4 dBm specified by WiMedia physical (PHY) layer [7] as shown in

Table A. 5 (Appendix A). Because the measured UWB receiver sensitivity determines the minimum transmitted power before the transmitting antenna, the required minimum power as shown in Figure 6.16 is -30.7, -35 and -40.5 dBm for 480, 200 and 53.3 Mb/s, respectively. In addition, it is clear that the receiver sensitivity is worst for the 480 Mb/s. This will limit the dynamic range and wireless transmission range for high bit rates. This is why for 480 Mb/s the PER performance is poor at low transmitted power levels.

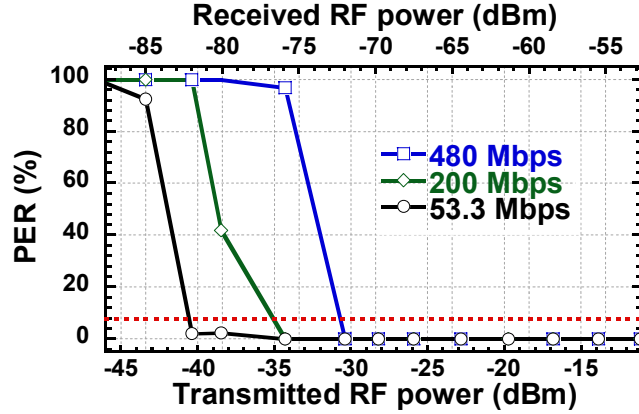


Figure 2.15 PER versus UWB power and data rate for 20 km optical link and 1 m wireless link.

2.6.2 Effect of Wireless Link

It is seen from equation (2.15) that the received power will depend mainly on the mean path-loss referenced to 1 m. To show the performance under a wireless channel, we vary the distance between two UWB antennas in Figure 2.1 from 1 to 4 m and observe the corresponding PER at the UWB receiver as shown in Figure 2.16. From equation (2.14) mean path-loss referenced to 1 m is 6, 9.6 and 12 dB for 2, 3 and 4 m, respectively. As the distance between two antennas increases the packet error rate will aggravate, and this is because the losses are increased and the received signal is attenuated.

From Figure 2.16 it is found that PER is almost zero for up to 2 m wireless at bit rates of up to 480 Mb/s and input power level of more than -12.5 dBm ($m_{RF} = 2\%$) at the DE-MZM which corresponds to average transmitted power before the antenna of $P_{uwb} = -26$ dBm. It is also found that the highest bit rate 480 Mb/s is the most degraded one by the wireless link length. This is primarily due to the fact that the receiver sensitivity is the worst for this bit rate. After 4 m wireless transmission and for typical average transmitted power of -20 and -26 dBm (corresponding to RF modulation index of 4% and 2%, respectively) the received RF power using equation (2.15) is -73.85 and -79.85 dBm, respectively, which is below the receiver sensitivity at 480 and 200 Mb/s, respectively. The corresponding PER can be easily deduced from Figure 2.15, for example for received RF power of -73.85 dBm ($m_{RF} = 4\%$) the PER is $\sim 45\%$ and $\sim 0\%$ for 480 and 200 Mb/s, respectively, while for received RF power of -79.85 dBm

($m_{RF} = 2\%$) the PER is almost 100% and 38% at 480 and 200 Mb/s, respectively. Conversely, at 53.3 Mb/s the PER is almost 0% at RF modulation index of 2% and 4%. This is because the corresponding received RF power is higher than the receiver sensitivity at this data rate. The above calculated results agree well with the measured values in Figure 2.16. Therefore the PER performance can be predicted using equation (2.15) to compute the received RF power and compare it to measured receiver sensitivity.

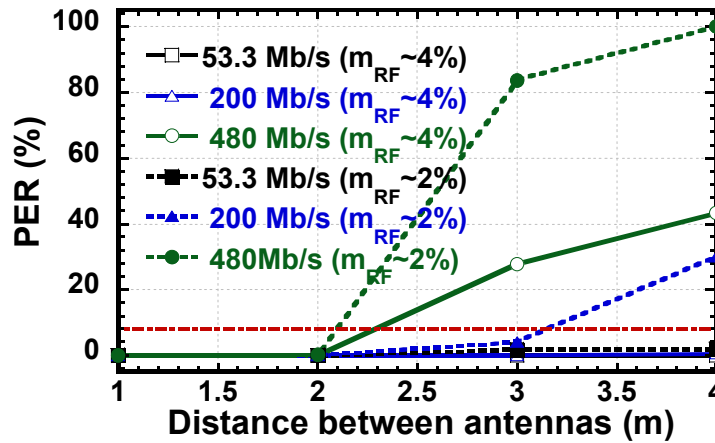


Figure 2.16 PER versus wireless range and data rate for 20 km of optical link.

2.6.3 Impact of Optical Received Power and Receiver Response

Measured PER versus RF modulation index of the DE-MZM is shown in Figure 2.17, for 200 Mb/s with antenna separation of 1m and transmission through 20 km of SMF at different received optical power levels to the photodetector. It is clearly seen that for any received optical power level the modified optical receiver response degrades PER (similar results are found at other bit rates: 53.3 and 480 Mb/s). This is because the inband ripples from the filter response introduce unequal attenuation in each subcarrier within the same symbol which may result in loss of orthogonality between the OFDM subcarriers.

On the other hand, the received optical power level will impact the PER differently. For the system with ideal (modified) optical receiver, 8% PER is obtained at RF modulation index of 2% (2.63%), 0.55% (0.84%) and 0.29% (0.48%) for the received optical power of -4, 1 and 4 dBm,

respectively. It can be seen that the PER can be decreased by increasing the RF modulation index m_{RF} or the received optical power P_{opt} . This is because the received UWB signal power is proportional to the receiver optical power square and to the UWB input power at the DE-MZM ($P_{rec} \propto (P_{opt}m_{RF})^2$) for low m_{RF} of up to 4% without introducing any AM/AM compression at the DE-MZM.

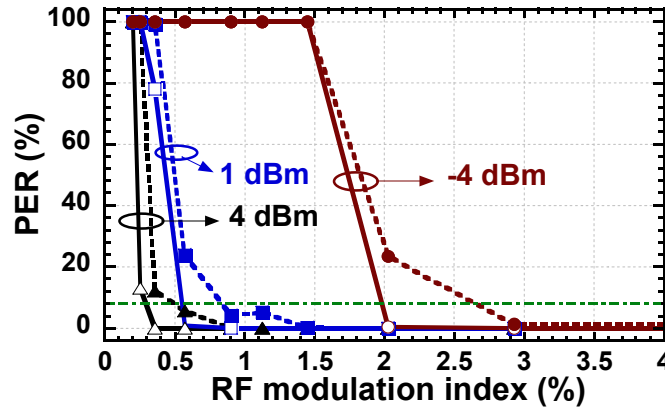


Figure 2.17 Effect of receiver response and received optical power on PER for 200 Mb/s with modified optical response (dashed) and with ideal receiver response (solid) after 20km of fiber and 1m wireless transmission.

2.7 Impact of Relative Intensity Noise

In this section we will discuss the impact of various physical parameters that control laser RIN and fiber transmission with focus on MB UWB technology. Laser RIN depends on many quantities, the most important of which are power at laser output, relaxation frequency, frequency of RF signal, magnitude of the optical feedback, mode suppression ratio and temperature.

2.7.1 Laser Intrinsic RIN, Resonant Frequency and Laser Output Power

Ultra wide band systems are adversely affected by the RIN in two ways. Since the transmitted RF signal has a wide bandwidth the total noise over signal bandwidth is large. On the other hand most of the low cost diode lasers' relaxation frequency coincides with the frequency spectrum of

the MB UWB signal. We will first investigate how laser intrinsic RIN affects the system performance and how we can improve system performance by reducing intrinsic laser RIN. Using the setup as shown in Figure 2.1, we experimentally characterize the impact of RIN and fiber transmission using measured EVM. We adjust the gain of the EDFA to fully compensate for all loss and keep the same input power to the PD.

Measured RIN spectrum versus frequency is presented in Figure 2.18 at the laser output for the laser module (shown in Figure 2.1) with linewidth of 30 MHz. It is observable that RIN frequency spectrum is not flat. The RIN spectral density is small at low frequencies and peaks at the relaxation resonance frequency and then falls to the shot noise level. Measured RIN peak frequency and corresponding intensity noise spectral density is presented in Figure 2.19.

It is evident from Figure 2.19 that as the laser output power increases, the RIN peak shifts to higher frequency and the RIN magnitude is decreased. System's EVM performance as a function of laser output power for back to back transmission is presented in Figure 2.20. We found that EVM performance depends highly on the RIN of the laser.

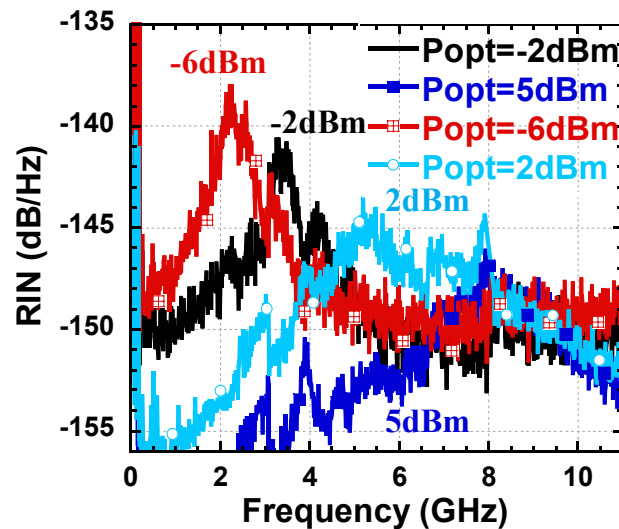


Figure 2.18 Measured spectral density of RIN as a function of frequency for back to back transmission.

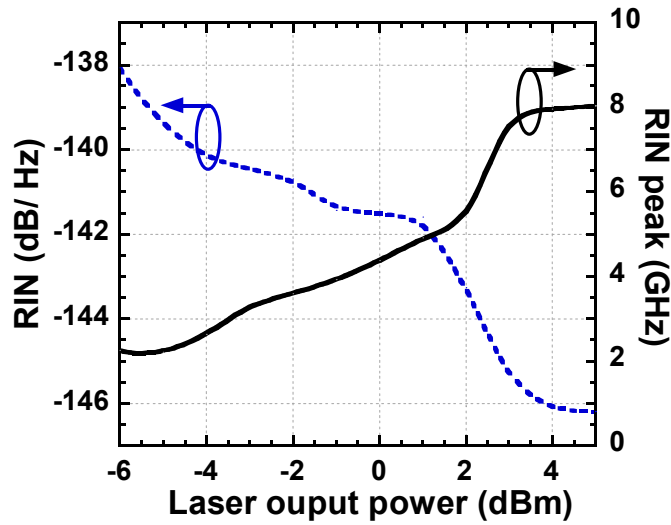


Figure 2.19 Measured RIN peak frequency and corresponding spectral density of RIN for back to back transmission.

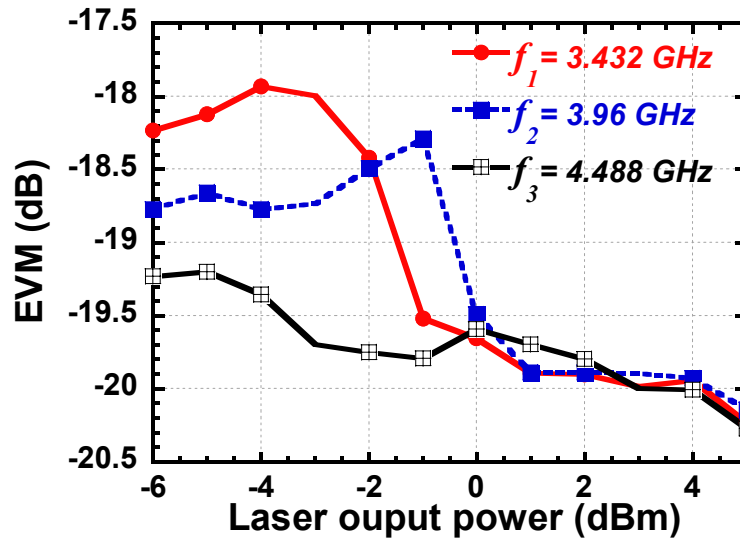


Figure 2.20 Measured EVM with laser output power for back to back transmission at bit rate of 200Mb/s.

At low power levels, i.e. from -6 to -2 dBm, EVM performance of all three bands is poor due to high RIN of the laser. Also at low power the RIN peak resides at low frequencies. That is why the first band (3.432 GHz) of MB UWB suffers most at low power and has poor EVM performance. We see that EVM peaks at around -3 dBm which makes perfect sense since at around -3 dBm the RIN peak exactly coincides with the first band. As the laser output power

increases from -2 to 0 dBm the relaxation peak shifts to the second band and worst EVM performance for second band (3.96 GHz) is observed at -1 dBm. After -1 dBm with the increase of laser power the RIN begins to decrease and falls below -142 dB/Hz. That is why EVM performance of all the bands improves considerably after 0 dBm. The RIN peak eventually shifts to the third band (4.488 GHz) at around 1 dBm so its EVM performance is worse than the other bands. However, it is notable that since this peak occurs at higher power with low RIN, overall EVM performance of all the bands is satisfactory after 1 dBm.

Therefore, the choice of laser output power is a critical factor in minimizing system's intrinsic RIN and avoiding operation exactly at the RIN peak frequency. Since, most of the low cost commercial diode lasers have an output power of 2~3 dBm and relaxation peak at around 5 GHz. Therefore, we choose the laser output power of 2 dBm in the rest of the chapter.

2.7.2 Laser Linewidth, Fiber Dispersion and RF frequency

It is well known that laser RIN can be enhanced by GVD in optical fiber. In addition, previous work shows that laser RIN due to phase to intensity noise conversion by fiber dispersion is directly proportional to the laser linewidth [31-32]. The calculated power spectral density of RIN as a parameter of frequency for the laser source, depicted in Figure 2.1, is shown in Figure 2.21 for two different linewidths of 30 MHz and 1 GHz, and for fiber transmission of 20, 40 and 60 km, respectively. To understand the effect of laser linewidth on RIN and EVM performance, we choose the second band centered at 3.96 GHz and bandwidth of 528 MHz. Calculated EVM degradation of the system versus fiber length, using equation (2.13), is shown in Figure 2.22 for three different laser linewidths. The laser depicted in Figure 2.1 has an intrinsic RIN of -145dB/Hz with linewidth of 30 MHz and 1 GHz. The other laser has linewidth of 800 kHz and intrinsic RIN of -155dB/Hz. The experimental EVM degradation is also shown in Figure 2.22. Calculated results are in good agreement with the measurement in Figure 2.22. However, the experimental EVM degradation is slightly better than the calculated one because of the complex demodulation and error correction schemes used at the UWB receiver. Compared to the back to back, it is clearly shown that EVM degradation of ~0.36 and ~1.1 dB is expected for laser with linewidth of 800 kHz, whereas it is ~0.58 and ~1.95 dB for 30 MHz laser, after 20 and 40 km of fiber transmission, respectively. For the laser with linewidth of 1 GHz, the EVM

degradation is ~ 1 and ~ 3 dB for the two fiber lengths. The EVM degradation shown in Figure 2.22 is due to increased RIN due to the interaction of the laser phase noise and chromatic dispersion as shown in Figure 2.21.

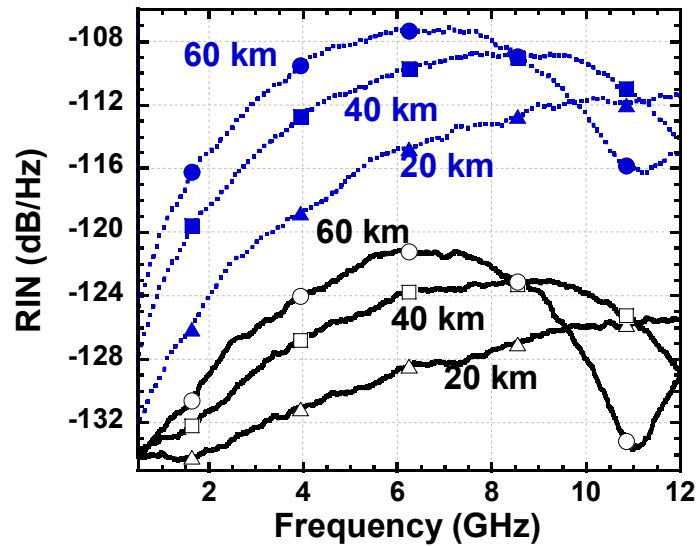


Figure 2.21 Calculated RIN versus frequency for 20, 40 and 60 km (Solid: linewidth of 30 MHz. Dotted: linewidth of 1 GHz).

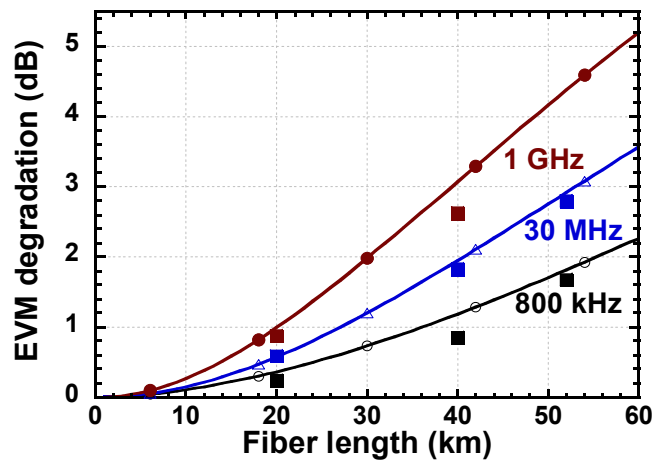


Figure 2.22 Calculated EVM degradation versus fiber length with respect to back-to-back. Square: experimental results for 20, 40 and 52 km.

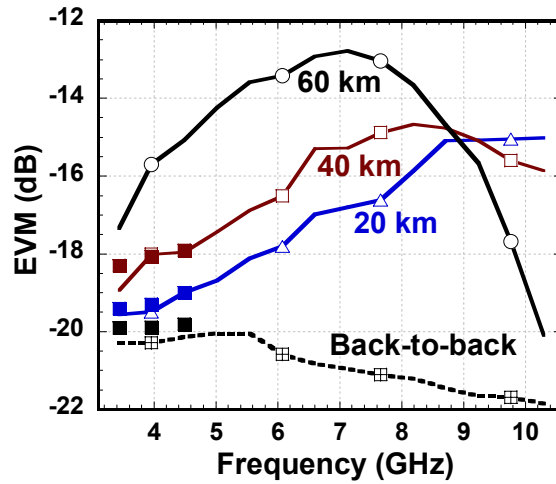


Figure 2.23 Simulated (line) EVM versus bands in an MB UWB over fiber system. Square: experimental results for 0, 20 and 40 km centered at 3.432, 3.96 and 4.488 GHz band.

At last one of the most important factors is the UWB carrier frequency of the UWB system. MB UWB has 14 bands with center frequency $f_c(\text{MHz}) = 2904 + 528n_b$, $n_b = 1, 2, \dots, 14$. We perform simulation for all the 14 bands of MB OFDM using VPI TransmissionMaker software. Figure 2.23 shows simulated EVM for 14 bands UWB over fiber with fiber length of back-to-back, 20, 40 and 60 km, considering bit rate of 200 Mb/s and laser linewidth of 30 MHz. The experimentally measured EVM is also shown in Figure 2.23 for 20 and 40 km for bands centered at 3.432, 3.96 and 4.488 GHz. The results from Figure 2.23 show that for back to back as the frequency increases, EVM initially degrades up to the RIN peak, then it is improved after 5.544 GHz band. However, with fiber dispersion the scenario is completely different. For 20 km of fiber, dispersion shifts the peak of RIN to lower frequency bands as shown in Figure 2.21 and as frequency increases the EVM also increases for all the frequency bands. Also for 20 km of fiber, from Figure 2.21 we see the RIN becomes almost constant after 9.768 GHz band and so does the EVM. With fiber transmission link of 40 km the EVM initially increases until 8.184 GHz band than gradually decreases as the RIN drops in value. The result for 60 km fiber transmission link is quite interesting. Due to sinusoidal behavior of the dispersion induced phase noise to intensity noise conversion the RIN begins to decrease considerably after 7.656 GHz band and EVM is improved rapidly.

2.8 Performance of Multi-band OFDM Ultra-Wideband over Fiber Transmission under the Presence of In Band Interferers

For real world applications UWB receivers face jamming scenarios from multiple in-band and out of band interferers. Some of the typical interferers at the input of a MB OFDM receiver are shown in Figure 2.24. IEEE 802.11b/g, Bluetooth and microwave ovens act as out of band interferers. WiMAX at 3.5 GHz interferes with band group 1, IEEE 802.11a/n interferes with band group 2 and radar signal interferes with band group 4, respectively.

We used the experimental setup of Figure 2.1. The MB-OFDM UWB signal with 200Mb/s is generated by the AWG 7122B. The generated WiMedia sub-bands are presented in Table 2.1. The sub-bands follow a simple hopping sequence as f_1 , f_2 , f_3 according to TFC 1, defined in WiMedia standard so that only one channel exists at any particular time.

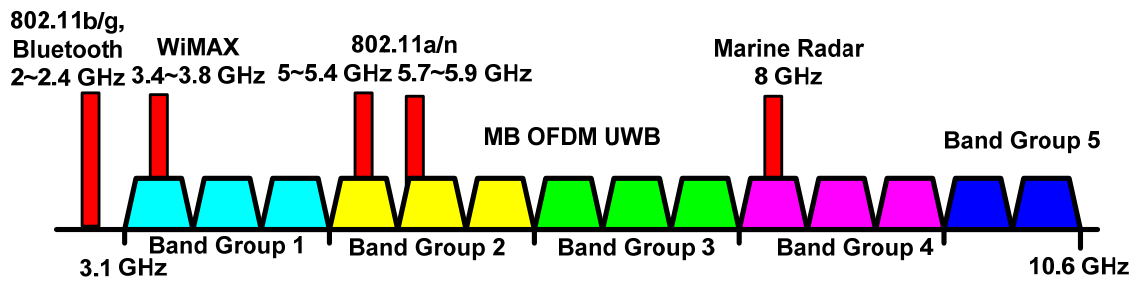


Figure 2.24 Spectrum of UWB signal with narrow band interferers.

The generated UWB signal has a low power spectral density (PSD) and small footprint. As a result, the UWB signal appears to be very low level background noise to an unintended narrowband receiver. The PSD of the generated signal and interferers (for interferer to UWB peak power ratio of 20 dB) at point B in Figure 2.1 is given in

Table 2.2 that shows the PSD level difference between UWB and interferer is roughly 20 dB. This difference gives a rough estimation of signal to noise ratio at the narrowband receiver.

The received power at the photodetector is fixed at 4 dBm in all cases. After the photodetection the UWB signal is amplified by a broadband RF amplifier from MiniCircuits (ZVA-213) with gain of 26 dB as shown in Figure 2.1. The received signal (at point D) is evaluated with a high speed real time oscilloscope DPO 72004B from Tektronix.

Table 2.1 Generated UWB sub-bands and corresponding interferers.

Band Group	Corresponding in band interferer
Band group 1, 3 sub-bands centered at $f_1=3.432$, $f_2=3.96$ and $f_3=4.488$ GHz	IEEE 802.16-2004, WiMAX at 3.5 GHz
Band group 2, 3 sub-bands centered at $f_1=5.016$, $f_2=5.544$ and $f_3=6.072$ GHz	IEEE 802.11n, MIMO at 5 GHz and IEEE 802.11a, WLAN at 5.8 GHz
Band group 4, 3 sub-bands centered at $f_1=8.184$, $f_2=8.712$ and $f_3=9.240$ GHz	Marine radar at 8 GHz

Table 2.2 Generated UWB sub-bands, interferers and their corresponding PSD.

Band Group	UWB PSD (dBm/Hz)	Interferer PSD (dBm/Hz)
Band group 1	-111.48	-91.53
Band group 2	-112.35	-92.19/ -92.29
Band group 4	-118.19	-98.07

In this section we will analyze EVM performance of MB UWB over fiber under different in-band interference scenarios. We first investigate the system performance without any in-band interference and use the information to compare degradation under interference conditions. To emulate 1 m transmission over air under real antenna scenarios we added two multipath version of our generated signal with delay of 1 symbol and 2 symbols, relative amplitude of -35 dB and -40 dB and phase of 5 and 10 degree, respectively from the arbitrary waveform generator before transmission through the fiber. We tried to make our results independent of the amplification at the receiver front end so we present the results as a parameter of interferer to UWB peak power ratio rather than the power of interferer. For example free space path loss for 1 m can be emulated by inserting a 40 dB attenuator between points B and C in Figure 2.1. In that case, extra RF amplification has to be provided to keep the RF modulation index at the electro optic modulator constant. It should be noted that EVM is the ratio of the distortion in the received constellation with respect to transmitted constellation. So, theoretically fixed gain or attenuation

at the front end is a common multiplication factor both for the numerator and denominator and does not have any impact on EVM performance.

2.8.1 UWB over Single Mode Fiber Stand Alone Operation

We turn off the interferers from arbitrary waveform generator and transmit only MB UWB signal of band group 1, band group 2 and band group 4 according to WiMedia specification as described in Table 2.1 through the fiber one by one and measure the EVM at point D in Figure 2.1. We also measure the intrinsic EVM of the generator, where the output of generator at point B is directly connected to point D in Figure 2.1 using a coaxial cable. Results from our measurement are enlisted in Table 2.3. The results show that EVM degradation due to electrical to optical conversion is usually 2~3 dB. EVM performance for back-to-back (B-B), i.e. no actual fiber transmission is around -24 dB for all the band groups. This value increases by 1.4~2 dB for 20 km fiber transmission. At high frequencies there is a higher degradation in EVM performance for 20 km fiber transmission compared to back-to-back due to fiber chromatic dispersion induced laser phase to intensity noise conversion or RIN [31]. The results obtained are still much better than the WiMedia defined -16 dB limit of EVM [7] and for lower band groups and the fiber link can be easily extended up to 60~80 km of single mode fiber depending on the quality of the devices used for electrical to optical and optical to electrical conversion.

Table 2.3 Measured EVM Performance for Stand Alone UWB Transmission.

Band Group	Intrinsic	B-B	20 km of SMF
Band group 1	-27.32 dB	-24.50 dB	-23.12 dB
Band group 2	-26.21 dB	-24.25 dB	-22.65 dB
Band group 4	-25.52 dB	-23.44 dB	-21.30 dB

2.8.2 Performance of Band Group 1 of MB OFDM UWB under the presence of WiMAX with Fiber Distribution

Recently (21/5/2008) European Commission has opened the radio spectrum 3.4~3.8 GHz for WiMAX applications [33]. This notion raised many concerns among the UWB communities because WiMAX will interfere with band group 1. Band group 1 of UWB was thought to have the most potential because of mature CMOS technology in this frequency range and absence of other interferers. Subsequently, how WiMAX will affect UWB over fiber transmission has become a cause of apprehension among researchers. We study the performance of UWB over fiber transmission under the presence of WiMAX. We generate a 20 MHz wide WiMAX signal centered at 3.5 GHz with 64 Quadrature Amplitude Modulation (QAM) and a bit rate of 54 Mb/s based on IEEE 802.16-2004 technology [33]. The signal has 256 OFDM subcarriers among which 56 are null and guard tones, 8 are pilots and the rest 192 are data tones. Transmitted RF spectrum of UWB and WiMAX at point B and received spectrum after 20 km at point D in Figure 2.1 is showed in Figure 2.25 (a) and (b), respectively.

The results from EVM measurement presented in Figure 2.26 show that EVM performance of UWB over fiber transmission is severely degraded under presence of WiMAX. If the WiMAX to UWB peak power ratio is more than ~14 dB the transmission performance quickly falls below WiMedia defined limit of -16 dB. The performance degradation is mainly due to large number of subcarriers present in WiMAX within a small bandwidth so the sub-carriers interact with each other and the OFDM subcarriers in MB OFDM UWB signal resulting in a high carrier leakage and inter carrier interference.

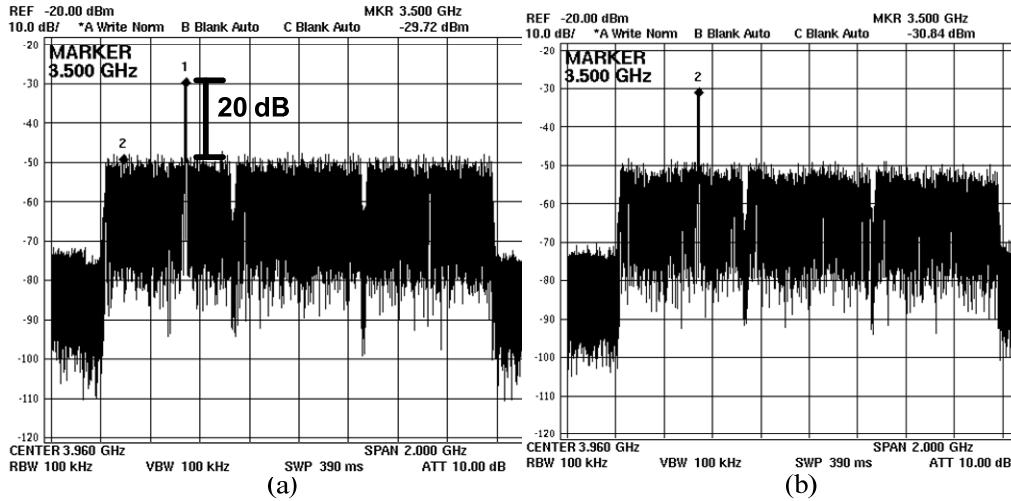


Figure 2.25 RF spectrum of UWB band group 1 and WiMAX (a) transmitted at point B (b) received at point D in Figure 2.1 for bit rate of 200 Mb/s with 20 km fiber transmission (Interferer to UWB peak power ratio is 20 dB).

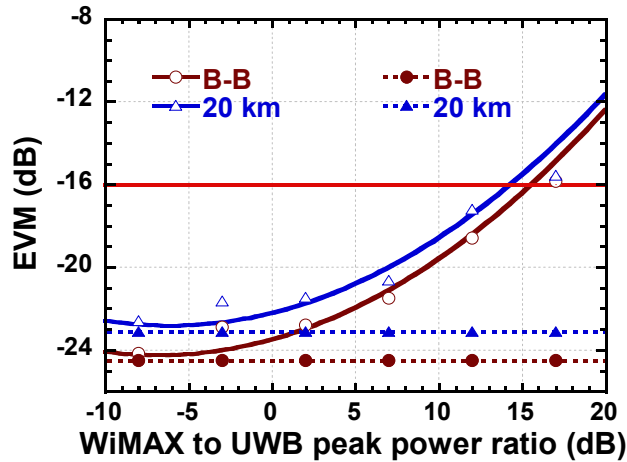


Figure 2.26 EVM performance of UWB over fiber transmission under the presence of WiMAX as a function of WiMAX to UWB peak power ratio (Solid lines: best fitted curves, dotted lines: without interference).

2.8.3 Performance of Band Group 2 of MB OFDM UWB under the presence of WLAN MIMO and WLAN with Fiber Distribution

IEEE 802.11n MIMO is an emerging technology that can provide throughput higher than 100 Mb/s for access network applications. The standard has been ratified in September 2009 [34]. So interference from MIMO to UWB is an interesting research topic. We generate a 54 Mb/s WLAN MIMO signal according to IEEE 802.11n standard. The signal uses OFDM modulation of 64 subcarriers each modulated with 64 QAM. The signal also uses space time block coding (STBC) which makes the power distribution and spectral density in the RF signal different from conventional WLAN. Transmitted RF spectrum of UWB and WLAN MIMO at point A and received spectrum after 20 km at point D in Figure 2.1 is showed in Figure 2.27 (a) and (b), respectively. Measured EVM is shown in Figure 2.28 and it is found that EVM of the transmitted UWB signal degrades as the WLAN MIMO's power is increased but acceptable performance is found if the WLAN MIMO's peak power level is not higher than UWB peak power level by more than ~ 17.5 dB.

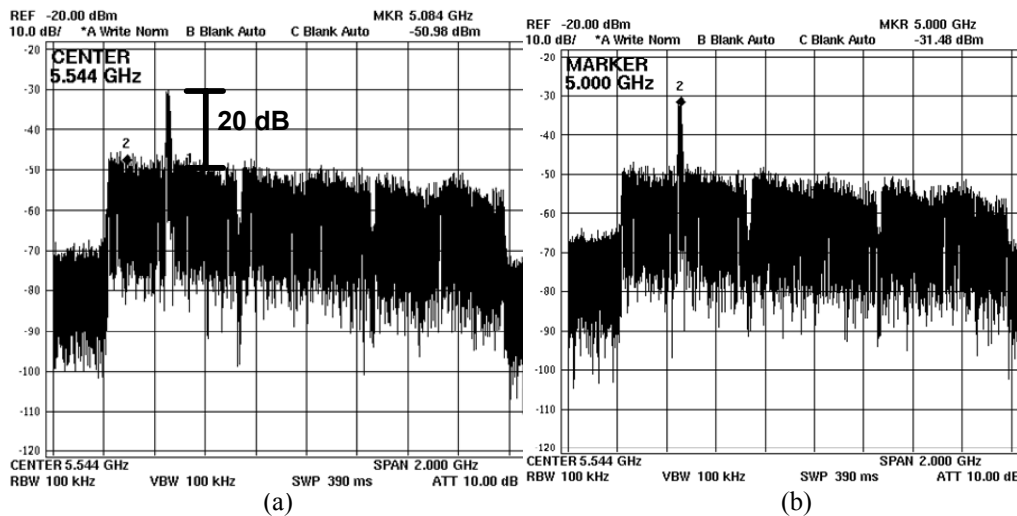


Figure 2.27 RF spectrum of UWB band group 2 and WLAN MIMO (a) transmitted at point B (b) received at point D in Figure 2.1 for bit rate of 200 Mb/s with 20 km fiber transmission (Interferer to UWB peak power ratio is 20 dB).

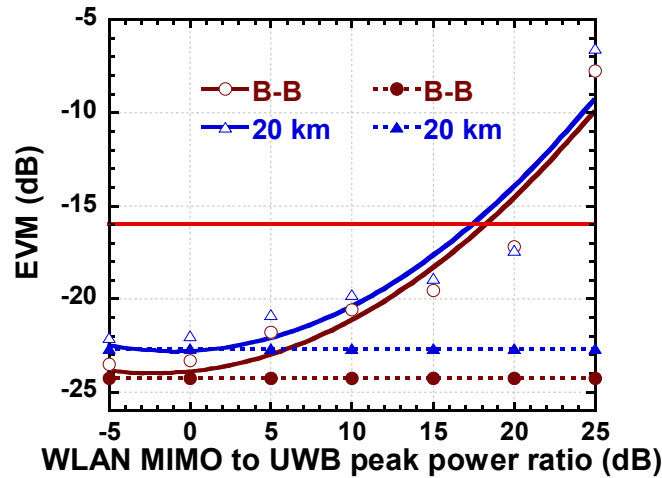


Figure 2.28 EVM performance of UWB over fiber transmission under the presence of WLAN MIMO as a function of WLAN MIMO to UWB peak power ratio (Solid lines: best fitted curves, dotted lines: without interference).

IEEE 802.11a, conventional WLAN is a widely used technology. WLAN signal consists of a 20 MHz channel with center frequency 5.8 GHz comprising of 64 subcarriers of which 52 are effective subcarriers, 48 carrying data and 4 pilots [35]. The modulation scheme is 64 QAM OFDM with bit rate of 54 Mb/s. Transmitted RF spectrum of UWB and WLAN at point B and received spectrum after 20 km at point D in Figure 2.1 is showed in Figure 2.29 (a) and (b), respectively. Our experimental results from EVM measurement of UWB over fiber transmission is shown in Figure 2.30. The EVM is almost constant for back-to-back and 20 km fiber transmission until WLAN to MB UWB peak power level ratio reaches 10 dB. After that the EVM begins to decrease slowly in both cases. The EVM falls below -16 dB limit if the peak power ratio is more than 21 dB and 20 dB, respectively for back-to-back and 20 km fiber distribution.

It should be noted that WLAN signals interfere with UWB signals much less than WiMAX due to the fact that the number of subcarriers carrying data in WLAN is only one fourth of that in WiMAX. As a result, WLAN will disrupt smaller numbers of subcarriers in UWB when compared to WiMAX.

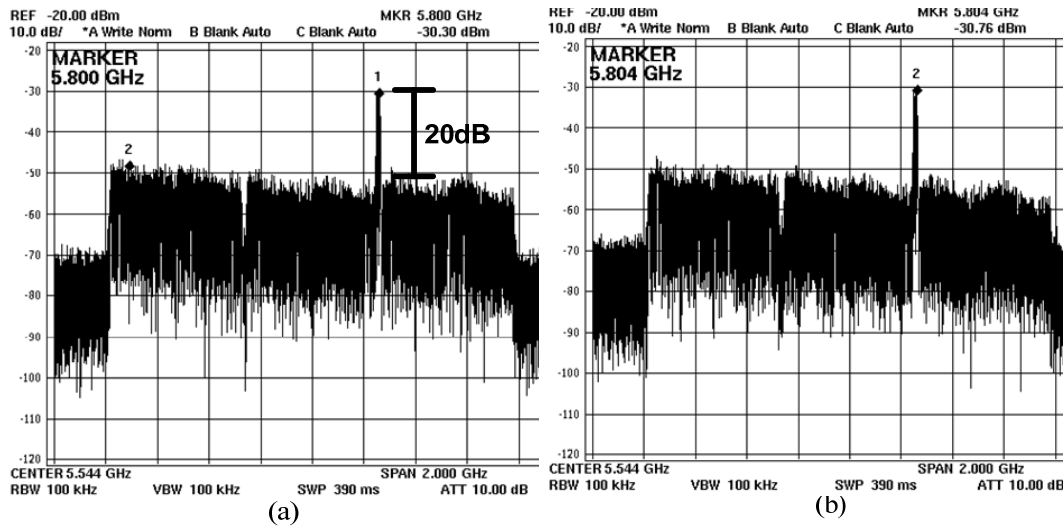


Figure 2.29 RF spectrum of UWB band group 2 and WLAN (a) transmitted at point B (b) received at point D in Figure 2.1 for bit rate of 200 Mb/s with 20 km fiber transmission (Interferer to UWB peak power ratio is 20 dB).

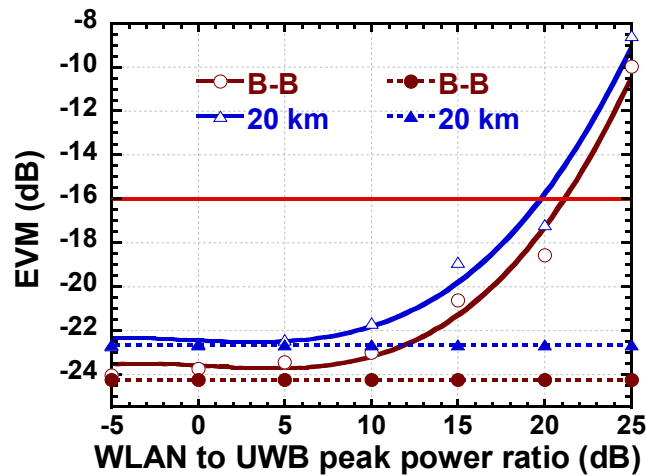


Figure 2.30 EVM performance of UWB over fiber transmission under the presence of WLAN as a function of WLAN to UWB peak power ratio (Solid lines: best fitted curves, dotted lines: without interference).

2.8.4 Performance of Band Group 4 of MB OFDM UWB under the presence of Marine Radar with Fiber Distribution

Radar signals at high frequency can also interfere with MB UWB signals. We used a linear frequency modulated pulse (LFM) centered at 8 GHz with pulse width of 5 μ s and frequency sweep of 20 MHz as a radar source and combined with band group 4 of UWB signal. Transmitted RF spectrum of UWB and marine radar and received spectrum after 20 km is showed in Figure 2.31(a) and (b), respectively. The EVM performance of UWB as a parameter of radar peak power to UWB peak power is shown in Figure 2.32. The EVM degrades quickly if the radar peak power is increased for both back-to-back and 20 km fiber transmission. Referring to Figure 2.32, EVM value of -16 dB is found for radar to UWB peak power ratio of 17 dB and 15 dB for back-to-back and 20 km fiber transmission, respectively. Large difference between back-to-back and 20 km fiber distribution is due to laser RIN as explained in Section 2.7. Experiments with C band military radar in the frequency range of 5.250~5.925 GHz and band group 2 (4.752~6.336 GHz) give similar results.

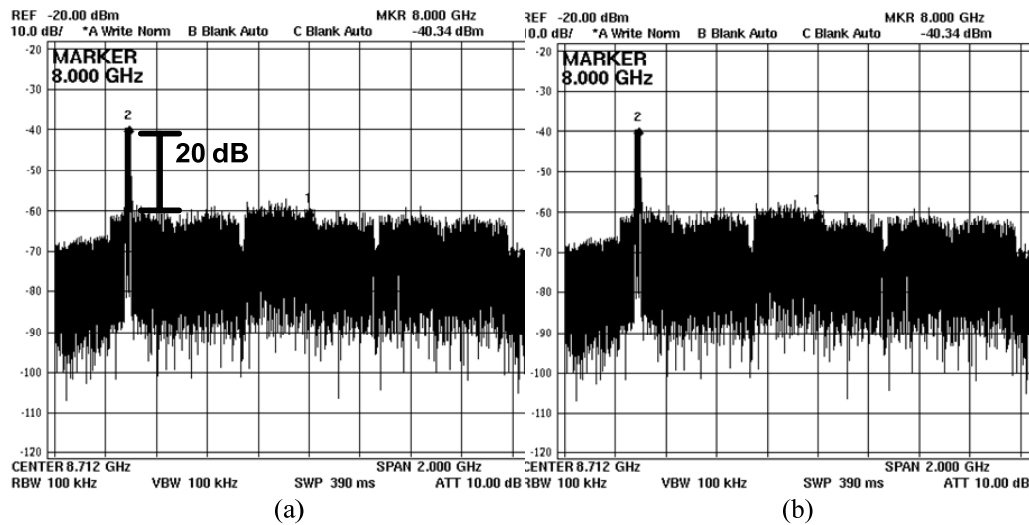


Figure 2.31 RF spectrum of UWB band group 4 and marine radar (a) transmitted at point B (b) received at point D in Figure 2.1 for bit rate of 200 Mb/s with 20 km fiber transmission (Interferer to UWB peak power ratio is 20 dB).

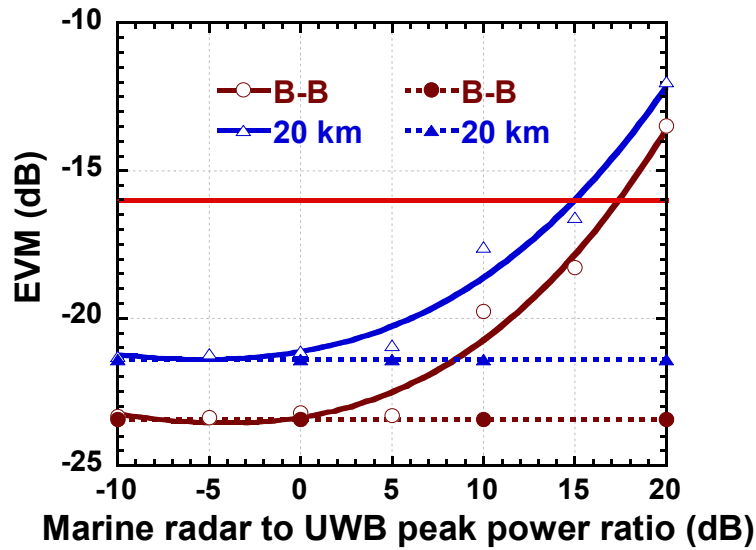


Figure 2.32 EVM performance of UWB over fiber transmission under the presence of WLAN as a function of WLAN to UWB peak power ratio (Solid lines: best fitted curves, dotted lines: without interference).

Low duty cycle pulses from radar signal interact and disrupt the subcarriers in UWB signal. Time domain waveforms after 20 km of fiber transmission without and with radar signal as interferer are presented in Figure 2.33 and Figure 2.34, respectively. It is clearly visible that radar signal distorts the waveform at the edges. It should be noted that in UWB receivers most of the signal processing is performed in time domain. Therefore, any short pulse like radar in time domain jams the UWB signal at UWB receiver input and causes the degradation of EVM.

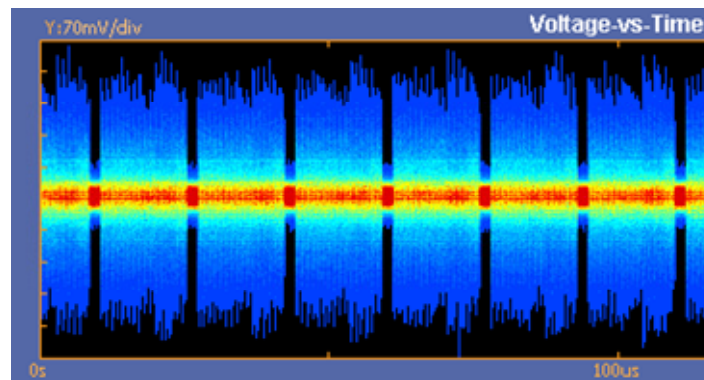


Figure 2.33 Received time domain waveform for band group 4 after 20 Km of fiber transmission with bit rate of 200Mb/s without any signal interferer.

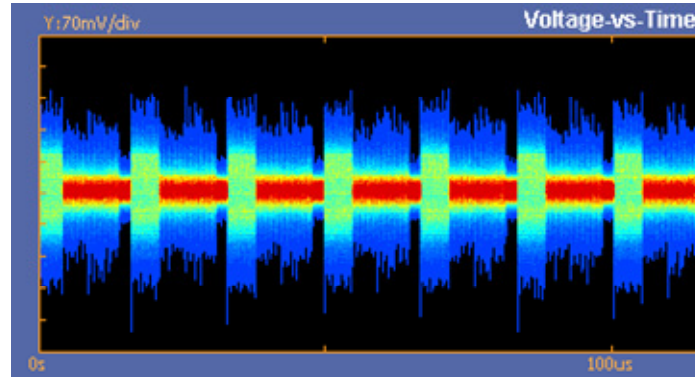


Figure 2.34 Received time domain waveform for band group 4 after 20 Km of fiber transmission with bit rate of 200Mb/s with radar signal as interferer (Interferer to UWB peak power ratio is 20 dB).

2.9 Chapter Summary

In this chapter, first, we have experimentally investigated and theoretically analyzed the performance of MB-OFDM UWB when transmitted over fiber. EVM is employed to evaluate the system quality of UWB signal considering system's parameters such as RF modulation index of DE-MZM, fiber transmission and received optical power. Performance degradation of MB-OFDM UWB caused by various impairments including DE-MZM nonlinearities, fiber dispersion and optical receiver response are also comprehensively investigated.

It is found that for RF modulation index of up to $\sim 4\%$ OFDM subcarriers suffer from relative phase shift due to fiber dispersion and are immune to amplitude distortion that could be induced by the combined effect of DE-MZM response nonlinearities and fiber dispersion. However, if modulation index is more than 4% the OFDM subcarriers suffer from both amplitude and phase distortion due to the combined effect of DE-MZM response nonlinearities and fiber dispersion. Therefore modulation index of 4% is optimum to achieve the best EVM. Moreover, when the optimum modulation index is used fiber transmission is further limited by laser phase noise converted RIN due to fiber dispersion and phase distortion induced by fiber dispersion in addition to increase of optical amplifier noise due to fiber loss, compared to back to back UWB over fiber. Also, it has been found that the optical receiver response has significant impact on

EVM performance. It is found that Chebyshev-II response with 3 GHz bandwidth and fifth order is the best for MB OFDM UWB over fiber. This is due to low amplitude and phase distortion within the passband. Since the UWB over fiber is operated at a low RF modulation index and multiband UWB has a low power spectral density, it is found that required optical power at optical receiver in UWB over fiber is reasonably higher than that in radio over fiber with other modulation schemes. Furthermore, we have found that EVM in UWB over fiber is degraded almost linearly with the decrease of receiver optical power.

Next, we have investigated experimentally the performance of MB-OFDM wireless UWB in terms of PER when transmitted over 20 km of SMF. PER was measured at different bit rates to evaluate the receiver sensitivity, required minimum transmitted UWB power, effect of wireless distance, DE-MZM modulation index, received optical power and optical receiver response. It is found that for 20 km of fiber and 1 m wireless range transmission, the minimum transmitted UWB power to achieve the allowable 8% PER is -40.5, -35 and -30.7 dBm at 53.3, 200 and 480 Mb/s, respectively, and is limited by the measured receiver sensitivity of -82, -76.7 and -72.3 dBm, respectively, which is better than the required sensitivity specified by the Wimedia PHY layer. In addition, we found that increasing the received optical power will improve PER and increase RF dynamic range suggesting that an optical amplification is better than RF counterpart. Also an optical receiver with flat magnitude response in the passband performs better with a MB-OFDM UWB over fiber. The results show that radio over fiber is very promising technology for increasing the coverage distance for the emerging and future ultra wideband systems operating at higher bit rates.

The performance of MB OFDM UWB was investigated when transmitted over fiber under the effect of RIN considering system's parameters such as laser output power, linewidth and fiber transmission length. It is found that the system should be operated at a high laser output power to avoid RIN degradation. It is shown using a narrow linewidth laser with low RIN will significantly improve system performance. Also simulations were performed for all the 14 bands of MB UWB to show performance dependence of RF carrier frequency. The results show that bands higher than 7.656 GHz are critically affected depending on fiber dispersion induced phase to intensity noise conversion.

It is found that different in-band interferers can affect the performance of MB-OFDM UWB severely if certain interferer to UWB peak power ratio is not maintained. For WiMax/ marine radar and UWB devices that are co-located this ratio is only ~ 14 and ~ 15 dB, respectively, for WiMAX and radar signals if distributed over 20 km of single mode fiber. MB UWB over fiber is more resistant to interference from WLAN MIMO and conventional WLAN. The interferer to MB UWB peak power ratio is ~ 17.5 and ~ 20 dB for 20 km fiber transmission for WLAN MIMO and conventional WLAN, respectively for satisfying the EVM requirement of -16 dB, which is the EVM threshold specified for conformance testing according to the recent WiMedia standard for UWB. Our results will allow the future researchers in the field of MB UWB over fiber transmission to optimize performance UWB over fiber transmission under the presence of all possible in-band interferers.

CHAPTER 3 PROPOSED LINEARIZATION TECHNIQUE FOR MZM

3.1 Introduction

Many techniques for reducing nonlinear distortion have been described in literature, such as analog predistortion techniques [36-45], the adaptive pre-distortion method [46], the feed forward linearization technique [47], dual-parallel modulation techniques [48], serially cascaded modulation techniques [49], and balanced detection [50-51]. Each devised with its advantages and disadvantages. A linearization technique called the dual parallel linearized modulator, which consists of two MZMs placed in parallel, was also proposed. The upper MZM is biased at positive quadrature with modulation index set high and the lower is biased at negative quadrature with modulation index set low, where the two resulting inverted optical powers are combined to cancel IMD along with some RF carrier power [52-53]. This linearization technique may become impractical, because of the optical combining of two independent MZM transfer responses and the required accuracy in the relative phase shift between the two MZMs, which need to be within a few degrees for satisfactory IMD cancellation.

Recently, a simple technique that suppresses IMD was proposed, which consists of two linear polarizers placed before and after an optical phase modulator [54]. Because this technique transmits phase modulated light, it uses an acousto-optic frequency shifter for coherent heterodyne detection, which limits the RF bandwidth of the system and increases the cost and complexity. A linear optical phase demodulation has also been proposed in coherent receivers [55]. It is based on optical phase-locked loop and additional components, which will add cost to the receiver.

The objective in this chapter is to design a linearized modulator whose performance does not depend on modulation index, RF bandwidth limitation is removed and complexity is reduced, so that it may be incorporated into one silicon substrate or module for practical purposes. A linearized MZM that consists of two linear polarizers and a DE-MZM is proposed in this chapter. Using this modulator, OSSB modulation can be realized with the cancellation of third-order IMD (3IMD). This modulator utilizes both TE and TM polarization states. Therefore, this modulator is referred to as the mixed polarization OSSB MZM. However, when multiple RF tones are applied to the modulator and particularly with high modulation index, many harmonics and

intermodulation products are generated due to optical modulation and may lead to dispersion induced power fading and crosstalk even for OSSB modulation. This is because higher order distortion components beat with one another and generated component products that may overlap with or land very close to RF carriers. The proposed mixed-polarization OSSB MZM will be compared to the conventional MZM in terms of spurious free dynamic range (SFDR), 3IMD suppression and overall reduction of nonlinear distortion components.

This chapter is organized as follows; Section 3.2 will describe the proposed mixed-polarization OSSB MZM, Section 3.3 will provide the equation development for the SFDR and report on the sensitivity analysis due to polarization angle and electro-optic coefficient ratio errors, Section 3.4 will provide simulated third order suppression results, SFDR results and a comparison analysis to the conventional MZM, Section 3.5 will explore experimental SFDR and a comparison analysis to the conventional MZM. Section 3.6 will demonstrate the application of the proposed modulator to a MB-OFDM UWB signal and Section 3.7 will finally provide concluding remarks.

3.2 Proposed Mixed-Polarization OSSB Mach-Zehnder Modulator

Figure 3.1 shows the proposed mixed-polarization OSSB MZM, which consists of a linear polarizer adjusted to an angle of α , a z-cut Lithium Niobate Oxide (LiNbO_3) DE-MZM and a second linear polarizer adjusted to an angle of β . It is well known that the z-cut LiNbO_3 MZM exhibits an electro-optic coefficient r_{31} along the x-(TE) axis, which is approximately 1/3 of r_{33} coefficient of the z- (TM) axis [56]. The anisotropy will allow different amounts of modulation depth in the two polarized states. The optical signal entering the modulator passes through a linear polarizer set to an angle α with respect to the z-axis, this will excite a superposition of TE and TM modes that will be modulated to different modulation depths. This will have the effect of allowing the z-(TM) axis carry more IMD, while the x-(TE) axis will carry less IMD. The optical signal is then passed through a second linear polarizer that is angled to β with respect to the z-axis. The two angles are related to one another, but a unique solution does not exist, so they will be selected in such a fashion as to maximize the RF carriers and minimize IMD. By carefully selecting α and β of the two linear polarizers, the combined IMD from the two arms of the DE-MZM can be suppressed.

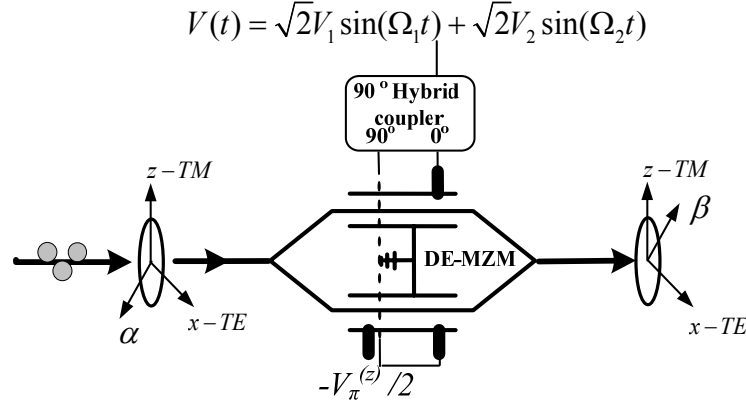


Figure 3.1 The mixed polarization OSSB MZM considered.

Two RF sinusoidal tones are applied to the z-cut LiNbO₃ MZM electrodes, where the RF tones are phase shifted by 90° from each other. The DE-MZM is biased at quadrature and for this case it is assumed that the quadrature biasing is on a downward slope of the MZM response. The normalized voltages applied to the two electrodes are represented by $V_u(t) = m_1 \sin(\Omega_1 t) + m_2 \sin(\Omega_2 t)$ and $V_l(t) = m_1 \cos(\Omega_1 t) + m_2 \cos(\Omega_2 t) - \pi/2$ for the upper and lower electrodes, respectively, where Ω_1 and Ω_2 are the angular frequencies of the two RF tones.

Here $m_{1,2} = \frac{\pi}{V_{\pi}^{(z)}} V_{1,2}$ are the modulation indexes for the z-polarized component of the electric field, where $V_{\pi}^{(z)}$ is the half-wave switching voltage of the MZM in the z-(TM) axis. The electric field exiting the first linear polarizer and entering the z-cut LiNbO₃ MZM is represented by $\bar{\mathbf{E}}_{in}(t) = \sqrt{P_{in}} (\hat{\mathbf{z}} \cos(\alpha) + \hat{\mathbf{x}} \sin(\alpha)) e^{j\omega t}$, where P_{in} is the input optical power to the MZM. If birefringence is considered and defined as $\Delta\tau = d \Delta n / c$, the time delay between the two orthogonal polarization components, TE and TM, where d is the distance traveled by the light, c is the speed of light in a vacuum and Δn is the birefringence or the difference between the highest and lowest refractive indices in the MZM. Thus, the electric field vectors of the upper and lower electrodes are represented, respectively by

$$\bar{\mathbf{E}}_{u,\alpha}(t) = \sqrt{\frac{P_{in}}{1+\delta^2}} \begin{pmatrix} \hat{\mathbf{z}} \cos(\alpha) e^{j(m_1 \sin[\Omega_1(t+\Delta\tau)] + m_2 \sin[\Omega_2(t+\Delta\tau)])} e^{j\omega\Delta\tau} \\ + \hat{\mathbf{x}} \sin(\alpha) e^{j\gamma(m_1 \sin(\Omega_1 t) + m_2 \sin(\Omega_2 t))} \end{pmatrix} e^{j\omega t}$$

and

$$\bar{\mathbf{E}}_{l,\alpha}(t) = \sqrt{\frac{P_{in}}{1+\delta^2}} \begin{pmatrix} \hat{\mathbf{z}} \cos(\alpha) \delta e^{j(m_1 \cos[\Omega_1(t+\Delta\tau)] + m_2 \cos[\Omega_2(t+\Delta\tau)] - \pi/2)} e^{j\omega\Delta\tau} \\ + \hat{\mathbf{x}} \sin(\alpha) \delta e^{j(\gamma(m_1 \cos(\Omega_1 t) + m_2 \cos(\Omega_2 t)) - \pi/2)} \end{pmatrix} e^{j\omega t},$$

where $\delta = (\sqrt{ER} - 1)/(\sqrt{ER} + 1)$, ER is extinction ratio of the DE-MZM, γ is a dimensionless ratio of less than one, which describes the electro-optic coefficient ratio in the x-axis to that of the z-axis and ω is the optical angular frequency. The total electric field exiting the z-cut LiNbO₃ DE-MZM with insertion loss t_{ff} is given by

$$\bar{\mathbf{E}}_{out,\alpha}(t) = \sqrt{\frac{P_{in} t_{ff}}{1+\delta^2}} \begin{pmatrix} \hat{\mathbf{z}} \cos(\alpha) \begin{bmatrix} e^{j(m_1 \sin[\Omega_1(t+\Delta\tau)] + m_2 \sin[\Omega_2(t+\Delta\tau)])} \\ + \delta e^{j(m_1 \cos[\Omega_1(t+\Delta\tau)] + m_2 \cos[\Omega_2(t+\Delta\tau)] - \pi/2)} \end{bmatrix} e^{j\omega(t+\Delta\tau)} \\ + \hat{\mathbf{x}} \sin(\alpha) \begin{bmatrix} e^{j\gamma(m_1 \sin(\Omega_1 t) + m_2 \sin(\Omega_2 t))} \\ + \delta e^{j(\gamma(m_1 \cos(\Omega_1 t) + m_2 \cos(\Omega_2 t)) - \pi/2)} \end{bmatrix} e^{j\omega t} \end{pmatrix} \quad (3.1)$$

By using the Jacobi-Auger expansion $e^{jx \sin(\Omega t)} = \sum_{n=-\infty}^{\infty} J_n(x) e^{jn\Omega t}$ and $e^{jx \cos(\Omega t)} = \sum_{n=-\infty}^{\infty} j^n J_n(x) e^{jn\Omega t}$ in equation (3.1), one obtains the total electric field exiting the z-cut LiNbO₃ DE-MZM, just before the second linear polarizer as,

$$\bar{\mathbf{E}}_{out,\alpha}(t) = \sqrt{\frac{P_{in} t_{ff}}{1+\delta^2}} \sum_{n=-\infty}^{\infty} \sum_{m=-\infty}^{\infty} (1 - \delta j^{(n+m+1)}) \times \left\{ \begin{array}{l} \hat{\mathbf{z}} \cos(\alpha) J_n(m_1) J_m(m_2) e^{j(n\Omega_1 + m\Omega_2 + \omega)\Delta\tau} \\ + \hat{\mathbf{x}} \sin(\alpha) J_n(\gamma m_1) J_m(\gamma m_2) \end{array} \right\} \times e^{j(n\Omega_1 + m\Omega_2 + \omega)t} \quad (3.2)$$

It is seen that lower sidebands at frequencies of $-\Omega_1$ and $-\Omega_2$ are suppressed in equation (3.2) thus OSSB modulation is obtained.

After the second linear polarizer, which is set to the angle of β with respect to the z-axis, the electric field component exiting the second linear polarizer is given by,

$$E_{out,\beta}(t) = \sqrt{\frac{P_{in} t_{ff}}{1+\delta^2}} \sum_{n=-\infty}^{\infty} \sum_{m=-\infty}^{\infty} (1 - \delta j^{(n+m+1)}) \times \left\{ \begin{aligned} &\cos(\alpha) \cos(\beta) J_n(m_1) J_m(m_2) e^{j(n\Omega_1 + m\Omega_2 + \omega)\Delta\tau} \\ &+ \sin(\alpha) \sin(\beta) J_n(\gamma m_1) J_m(\gamma m_2) \end{aligned} \right\} \times e^{j(n\Omega_1 + m\Omega_2 + \omega)t} \quad (3.3)$$

Applying the Bessel series expansion, $J_n(x) \equiv \sum_{r=0}^{\infty} (-1)^r (x/2)^{2r+n} / (r!(n+r)!)$ to equation (3.3)

the output electric field is simplified into,

$$\begin{aligned} E_{out,\beta}(t) = & \sqrt{\frac{P_{in} t_{ff}}{1+\delta^2}} (1 - \delta j) \left(\begin{aligned} &\cos(\alpha) \cos(\beta) e^{j\omega\Delta\tau} + O(m_1^2) \\ &\sin(\alpha) \sin(\beta) + O(m_2^2) \end{aligned} \right) e^{j\omega t} \\ & + \frac{(1+\delta)}{2} \sqrt{\frac{P_{in} t_{ff}}{1+\delta^2}} \left(\begin{aligned} &\cos(\alpha) \cos(\beta) \left[m_1 - \frac{1}{8} m_1^3 \right] e^{j(\omega+\Omega_1)\Delta\tau} + \\ &\sin(\alpha) \sin(\beta) \left[\gamma m_1 - \frac{1}{8} \gamma^3 m_1^3 \right] + O(m_1^5) \end{aligned} \right) e^{j(\omega+\Omega_1)t} \\ & + \frac{(1+\delta)}{2} \sqrt{\frac{P_{in} t_{ff}}{1+\delta^2}} \left(\begin{aligned} &\cos(\alpha) \cos(\beta) \left[m_2 - \frac{1}{8} m_2^3 \right] e^{j(\omega+\Omega_2)\Delta\tau} + \\ &\sin(\alpha) \sin(\beta) \left[\gamma m_2 - \frac{1}{8} \gamma^3 m_2^3 \right] + O(m_2^5) \end{aligned} \right) e^{j(\omega+\Omega_2)t} \\ & - \frac{(1+\delta)}{2} \sqrt{\frac{P_{in} t_{ff}}{1+\delta^2}} \left(\begin{aligned} &\cos(\alpha) \cos(\beta) \frac{1}{8} m_1^2 m_2 e^{j(\omega+2\Omega_1-\Omega_2)\Delta\tau} + \\ &\sin(\alpha) \sin(\beta) \frac{1}{8} \gamma^3 m_1^2 m_2 + O(m_1^4 m_2^3) \end{aligned} \right) e^{j(\omega+2\Omega_1-\Omega_2)t} \\ & - \frac{(1+\delta)}{2} \sqrt{\frac{P_{in} t_{ff}}{1+\delta^2}} \left(\begin{aligned} &\cos(\alpha) \cos(\beta) \frac{1}{8} m_1 m_2^2 e^{j\omega\Delta\tau} + \\ &\sin(\alpha) \sin(\beta) \frac{1}{8} \gamma^3 m_1 m_2^2 + O(m_1^3 m_2^4) \end{aligned} \right) e^{j(\omega+2\Omega_2-\Omega_1)t} + \dots \quad (3.4) \end{aligned}$$

From equation (3.4) it can be seen that $e^{j(\omega+\Omega_i)\Delta\tau}$, $i=1,2$ is the differential phase delay between the two orthogonal polarization components for a given RF subcarrier. Third order IMD cannot be completely suppressed if this differential phase delay is not negligible. However, if it is negligible, i.e. $e^{j(\omega+\Omega_i)\Delta\tau} \approx 1 - ((\omega+\Omega_i)\Delta\tau)^2/2$, for $\omega\Delta\tau \ll 1$, which is usually the case as stated in [54] the differential phase delay is small for the MZM, $\sim 1\%$ and the condition for the complete suppression of third order IMD will depend on the differential group delay, as given in equation (3.5). It is seen from equation (3.4) that the IMD due to the characteristic of the MZM can be removed by eliminating the IMD components or the terms proportional to $m_{1,2}^3$ in electric field, if the following condition of

$$\cos(\alpha)\cos(\beta)\left[1 - \frac{(\omega\Delta\tau)^2}{2}\right] + \gamma^3 \sin(\alpha)\sin(\beta) = 0, \quad (3.5)$$

is satisfied, where the assumption of $\omega\Delta\tau \ll 1$ was used. We may see that equation (3.5) does not have a unique solution, so it would be ideal to choose a solution that maximizes the RF carriers that are proportional to $m_{1,2}$ in electric field. This yields $\alpha = -\beta = \pm \tan^{-1}\left(\gamma^{\frac{3}{2}}\sqrt{1 - (\omega\Delta\tau)^2/2}\right)$. Due to linearization, a decrease in optical RF signal subcarrier power is induced by a factor of

$\frac{\gamma(1-\gamma^2)}{(1 - (\omega\Delta\tau)^2/2 + \gamma^3)}\left(1 - (\omega\Delta\tau)^2/2\right)$, for $\omega\Delta\tau \ll 1$. If birefringence is neglected, i.e. $\omega\Delta\tau = 0$ and

$\gamma = 1/3$ for a typical z-cut LiNbO₃ MZM, this leads to $\alpha = -\beta = \pm 79^\circ$ and the above factor yields an 11 dB loss, which is the same as [54]. It is also noted from equation (3.5) that the suppression of 3IMD is not dependent on individual modulation depths, so a costly DC bias controller is not required for this proposed design.

3.3 SFDR and Sensitivity Analysis

A development for the expression of SFDR for a RoF system, where the considered mixed-polarization OSSB MZM is used. The IMD output power includes residual IMD and its higher orders components. Assuming equal modulation index, i.e. $m_1 = m_2 = m$, using equation (3.4) to obtain the photo-current $\frac{1}{2}\Re G_{opt}L_{opt}E_{out,\beta}(t)E_{out,\beta}^*(t)$, where \Re is the responsivity of the

photodetector, G_{opt} is the gain of the optical amplifier and L_{opt} is insertion loss of optical filter. The RF carrier and 3IMD output power are expressed as

$$P_{RF} = \frac{ER}{4(1+ER)} a_0^2 a_1^2 \left(\Re P_{in} L_{opt} G_{opt} t_{ff} \right)^2 G_{RF} L_{RF} m^2 R_L \quad (3.6)$$

and

$$P_{3IMD} = \left(\frac{5}{384} \right)^2 \frac{ER}{1+ER} a_0^2 a_5^2 \left(\Re P_{in} L_{opt} G_{opt} t_{ff} \right)^2 G_{RF} L_{RF} m^{10} R_L, \quad (3.7)$$

respectively, where

$$a_n = \cos(\alpha) \cos(\beta) + \gamma^n \sin(\alpha) \sin(\beta), \quad (3.8)$$

R_L is the receiver load, G_{RF} is the gain of the RF amplifier and L_{RF} is the loss of RF connectors used after the photodetector. Similarly for the conventional MZM, the RF carrier and 3IMD output power can be computed similar to the above and also by setting $\alpha = \beta = 0$ in equation (3.4), and can be expressed, respectively, as

$$P_{RF} = \frac{ER}{4(1+ER)} \left(\Re P_{in} L_{opt} G_{opt} t_{ff} \right)^2 G_{RF} L_{RF} m^2 R_L \quad (3.9)$$

and

$$P_{3IMD} = \frac{ER}{2^8(1+ER)} \left(\Re P_{in} L_{opt} G_{opt} t_{ff} \right)^2 G_{RF} L_{RF} m^6 R_L, \quad (3.10)$$

To obtain the expression of SFDR, one must solve the equation of $P_{3IMD} = N_0$, where N_0 is the receiver noise floor power, for m and use this m in P_{RF} to obtain the electrical RF carrier power then the SFDR is obtained by dividing the electrical RF carrier power by the noise power floor N_0 . The SFDR for using the linearized and conventional MZM can be easily computed, respectively as

$$SFDR = \left(\frac{3}{5} \right)^{2/5} \frac{a_0^{8/5} a_1^2}{a_5^{2/5}} \left(\frac{2ER}{1+ER} \left(\Re P_{in} L_{opt} G_{opt} t_{ff} \right)^2 G_{RF} L_{RF} R_L / N_0 \right)^{4/5} \quad (3.11)$$

and

$$SFDR_c = \left(\frac{2ER}{1+ER} \left(\Re P_{in} L_{opt} G_{opt} t_{ff} \right)^2 G_{RF} L_{RF} R_L / N_0 \right)^{2/3} \quad (3.12)$$

Setting $\beta = -\alpha + \Delta\phi$, where $\Delta\phi$ is the angular detuning from the “ideal” angle of $\pm 79^\circ$, and using equations (3.5) and (3.8) after some mathematical manipulations to obtain $a_n = \frac{\gamma^3 - \gamma^n}{1 + \gamma^3} \cos(\Delta\phi)$ and substitute it into equation (3.11) to obtain the SFDR by using the linearized MZM considering the impact of $\Delta\phi$ and γ as

$$SFDR = \left(\frac{3}{5}\right)^{2/5} \left(\frac{2ER}{1+ER} \left(\Re P_{in} L_{opt} G_{opt} t_{ff} \right)^2 G_{RF} L_{RF} R_L / N_0 \right)^{4/5} \times \left[\sqrt{\gamma(1-\gamma^2)} (1-\gamma^3) \cos^2(\Delta\phi) / (1+\gamma^3)^2 \right]^{8/5} \quad (3.13)$$

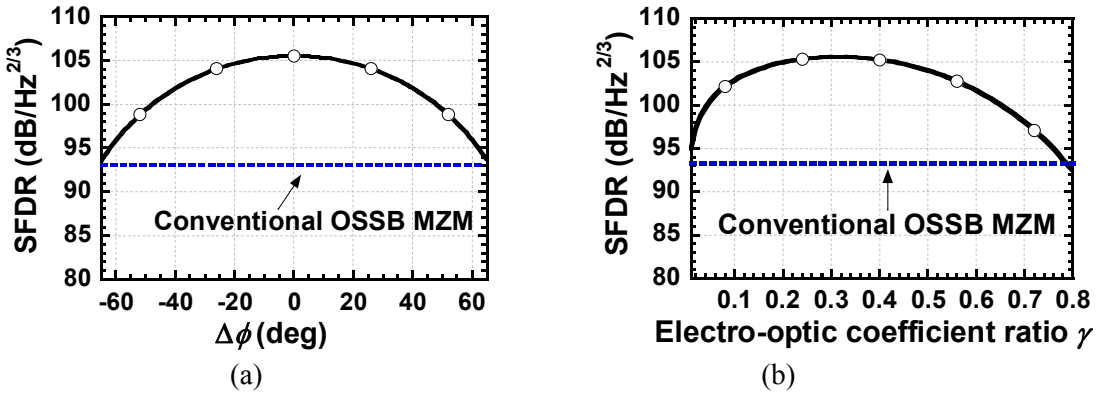


Figure 3.2 (a) Theoretical SFDR versus angular detuning $\Delta\phi$ with electro-optic coefficient ratio of $\gamma = 1/3$ and (b) theoretical SFDR versus electro-optic coefficient ratio γ with $\Delta\phi = 0$ for the mixed-polarization OSSB MZM.

Figure 3.2 shows the theoretical SFDR versus angular detuning and electro-optic coefficient ratio using equation (3.13) for the mixed-polarization OSSB MZM and (3.12) using the conventional MZM. In Figure 3.2 (a), the electro-optic coefficient ratio was set to $\gamma = 1/3$ and the angular detuning was varied from the “ideal” angle of $\beta = -\alpha = -79^\circ$. In Figure 3.2 (b) we set the phase difference to $\Delta\phi = 0$ and varied the electro-optic coefficient ratio. For the both figures, the same parameters were used as in the experiment in Section 3.5, for example $N_0 = -130$ dBm/Hz, $ER = 20$ dB, $P_{in} = 4$ mW, $t_{ff} = -6$ dB, $G_{opt} = 6$ dB, $L_{opt} = 3.5$ dB, $G_{RF} = 22$ dB, $L_{RF} = 3$ dB, $R_L = 50 \Omega$ and $\Re = 0.62$ A/W. It is seen from Figure 3.2 that the SFDR peaks at $\Delta\phi = 0$ and $\gamma = 1/3$. The mixed-polarization OSSB MZM improves the SFDR if detuning angle from the

optimum angle is within $-62^\circ < \Delta\phi < 62^\circ$ and electro-optic coefficient ratio is within $0.01 < \gamma < 0.75$. An improvement of SFDR of up to ~ 12 dB with less sensitivity to detuning angle and electro-optic coefficient ratio if within the range of $-26^\circ < \Delta\phi < 26^\circ$ and $0.15 < \gamma < 0.49$, respectively. This indicates that the mixed-polarization OSSB MZM is, to some extent, robust to polarizer angle and electrode material electro-optic coefficient instabilities.

3.4 Simulation Results and Analysis

As shown in Figure 3.1, two RF tones drive the electrodes of the z-cut LiNbO₃ MZM, but they are 90° phase shifted from each other and the MZM is biased at quadrature. The z-cut LiNbO₃ DE-MZM has a 6 dB insertion loss, 20 dB extinction ratio and a half wave switching voltage of 5 V. The CW laser is set to 1550 nm with linewidth of 800 KHz, optical power of 6 dBm and RIN of -150 dB/Hz. The angles of α and β of the two linear polarizers are set to $\pm 79^\circ$, respectively. The optical transmission is through 20 km of SMF with an attenuation of 0.2 dB/km and chromatic dispersion of 16 ps/nm-km. The fiber attenuation is compensated and an optical filter with a 68 GHz bandwidth is used to filter the optical signal before being detected by a PIN photodetector with responsivity of 0.62 A/W, and thermal noise of 10^{-12} A/ $\sqrt{\text{Hz}}$. Simulation was carried out with the commercial software ©VPI-TransmissionMaker 7.6. We consider an optical carrier transporting two RF tones at frequencies $f_1 = 8$ GHz and $f_2 = 10$ GHz as to match the tones used in the experimental analysis in Section 3.5.

Figure 3.3 (a) and (b) show the simulated optical spectrum at the input of the photodetector for a RoF system through 20 km of SMF using the conventional MZM and mixed polarization MZM with the linear polarizer angles optimally set to $\pm 79^\circ$, respectively. The total RF input power for the two tones was set to 19 dBm in both the conventional and mixed polarization MZM. It is verified that the mixed polarization MZM leads to an OSSB modulation as shown in Figure 3.3 (b) (the residual RF signal subcarriers at -8 and -10 GHz are due to the finite extinction ratio of the MZM). Moreover, in the conventional MZM in Figure 3.3 (a), it is seen that two 3IMDs, which are located at frequencies of $2f_1 - f_2 = 6$ GHz and $2f_2 - f_1 = 12$ GHz, are close to the RF signal subcarriers and are most detrimental to them. Conversely, using the mixed polarization MZM the 3IMD components at 6 and 12 GHz are suppressed by more than 32 dBc

compared to using the conventional MZM. It is seen that there are many optical intermodulation components generated. However, their power levels are considerably reduced when using the mixed polarization MZM compared to using the conventional MZM as seen from Figure 3.3 (b). These intermodulation components will beat with one another at the photodetector, generating components that will overlap in frequency with the two RF carriers, so that power fading due to fiber chromatic dispersion and crosstalk may be caused. This suggests that the intermodulation component related beats induced power fading and crosstalk, which is significantly reduced for the mixed polarization MZM.

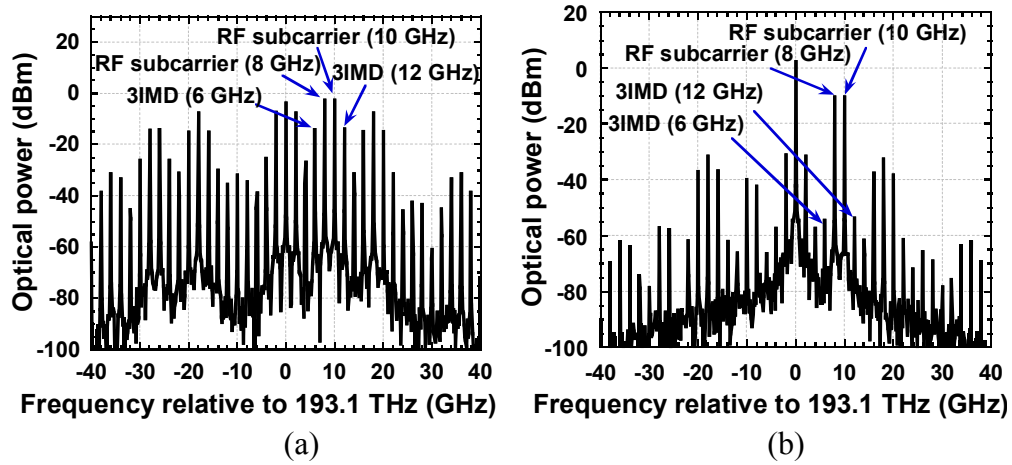


Figure 3.3 Simulated optical spectra at the input of the photodetector, for a RoF system through 20 km of SMF using (a) conventional OSSB MZM and (b) mixed polarization OSSB MZM with polarizer angles optimally set to $\pm 79^\circ$.

Corresponding to Figure 3.3, the RF output spectra are shown in Figure 3.4 (a) and (b). It is clearly shown that by using the conventional MZM the IMD components are comparable to the two RF carriers (~ 1 dB difference between the RF carriers and 3IMD components) as shown in Figure 3.4 (a). However, for the mixed polarization MZM, the magnitude of distortion components is significantly reduced and 3IMD is suppressed by more than 30 dBc below the two RF carriers. It is known that OSSB is not greatly affected by power fading when transmitted through dispersive fiber [12]. In order to investigate the effect of chromatic dispersion when using the mixed polarization MZM at high modulation index, we simulated and compared both

conventional and mixed polarization MZM with RF tones of 8 and 10 GHz, where the input RF power level was set to 19 dBm for both the conventional and mixed polarization MZM.

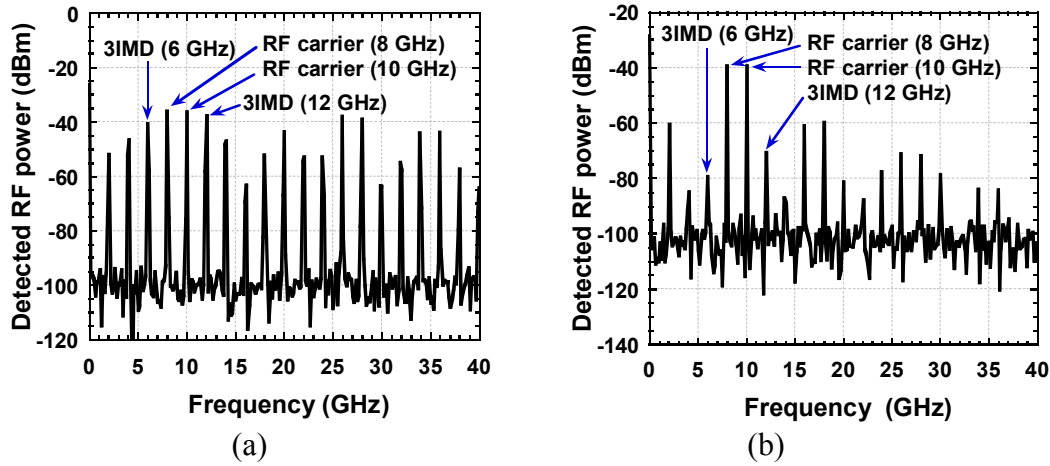


Figure 3.4 Simulated RF spectra corresponding to Figure 3.3 .

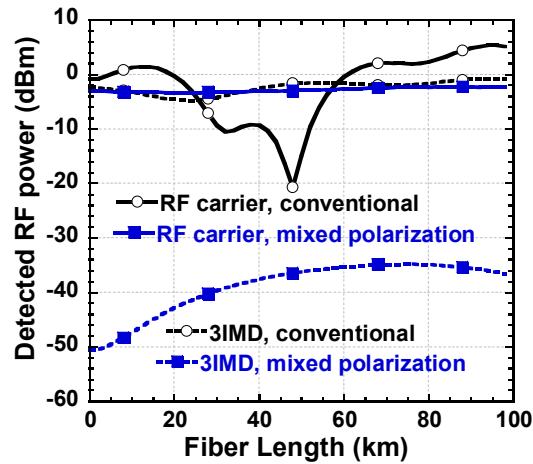


Figure 3.5 Simulated RF carrier and 3IMD power versus fiber length for a RoF system using the conventional and mixed polarization OSSB MZM, respectively, with compensated fiber loss.

Figure 3.5 compares the RF carrier and 3IMD powers for the conventional and mixed polarization MZM. Fiber loss is compensated in order to emphasize the effects of chromatic dispersion on the RF signal. We can see that the RF carrier power does not vary with changing

fiber length and thus there is no intermodulation component induced power fading and crosstalk, when using the mixed polarization MZM, while the RF carrier power fluctuates with changing fiber length and thus intermodulation component induced power fading and crosstalk must exist when using the conventional MZM. This is due to constructive and destructive interactions between many harmonic and intermodulation components for the conventional MZM as shown in Figure 3.4 (a). Thus the beats between distortion components are overlapped in frequency with the RF carriers, and then these beats interplay with the RF carriers. It is clearly shown that the mixed polarization MZM is immune to power fading and crosstalk caused by these interactions of intermodulation components and chromatic dispersion. It is shown that 3IMD is suppressed by more than 30 dBc as shown in Figure 3.4 (b). Therefore, not only is the mixed polarization OSSB transmission immune to power fading and crosstalk, but it also provides a greater suppression of 3IMD, which leads to an improvement in SFDR.

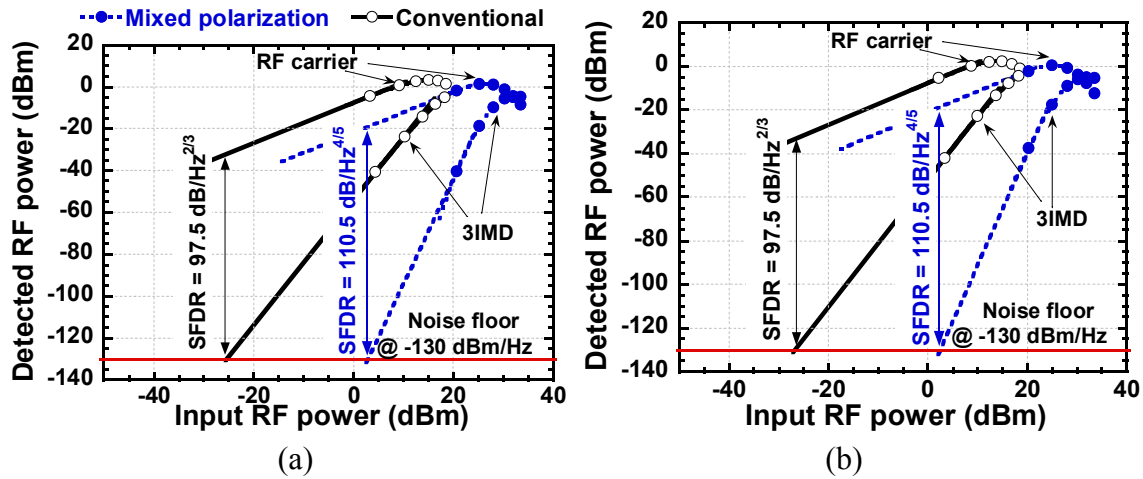


Figure 3.6 Simulated spurious free dynamic range for a RoF system using the mixed polarization and conventional OSSB MZM in (a) back-to-back and (b) through 20 km of single mode fiber.

In order to show the suppression of 3IMD by using the mixed polarization MZM over the conventional MZM, we compared the SFDR for a RoF system using a mixed polarization and conventional OSSB MZM as shown in Figure 3.6 (a) and (b) for back-to-back and through 20 km of SMF, respectively. From Figure 3.6 (a) and (b) it is shown that nonlinear distortion is 5th order limited (see the slope of 3IMD power) for the RoF system using the mixed polarization

MZM. But for the conventional MZM, it is 3rd order limited as seen in Figure 3.6. This shows that the 3IMD is cancelled for the mixed polarization MZM. Figure 3.6 shows that the SFDR improvement is 13 dB for both back-to-back and 20 km of fiber for the mixed polarization MZM.

3.5 Experimental Results with Two RF Tones

Figure 3.7 shows the experimental setup for a RoF system using the mixed polarization MZM. Two RF synthesizers are used to generate two tones at 8 and 10 GHz with equal power (at point B). The generated RF signal is amplified by an LNA of 22 dB gain and drive a DE-MZM using a 90° hybrid splitter for OSSB modulation. The photo-detected signal is amplified by another LNA of 22 dB gain. The RF power levels from the two synthesizers were varied from -20 to -5 dBm to operate the LNA in the linear regime. The tunable laser source delivers a linearly polarized light. One polarization controller (PC) was used to manually adjust the polarization angle α of the input lightwave to the DE-MZM. Another PC with a Chiral Photonics in-fiber linear polarizer is used to manually adjust the polarization angle β of the output lightwave from the DE-MZM. An optical amplifier was used to compensate for optical fiber losses and insertion loss of the DE-MZM. An optical filter with a bandwidth of 0.55 nm and insertion loss of 3.5 dB is used before the photodetector to reduce the amplified spontaneous emission noise (ASE). The RF signal is monitored by an RF spectrum for spectrum analysis Table 3.1 shows the physical parameters for the setup given in Figure 3.7.

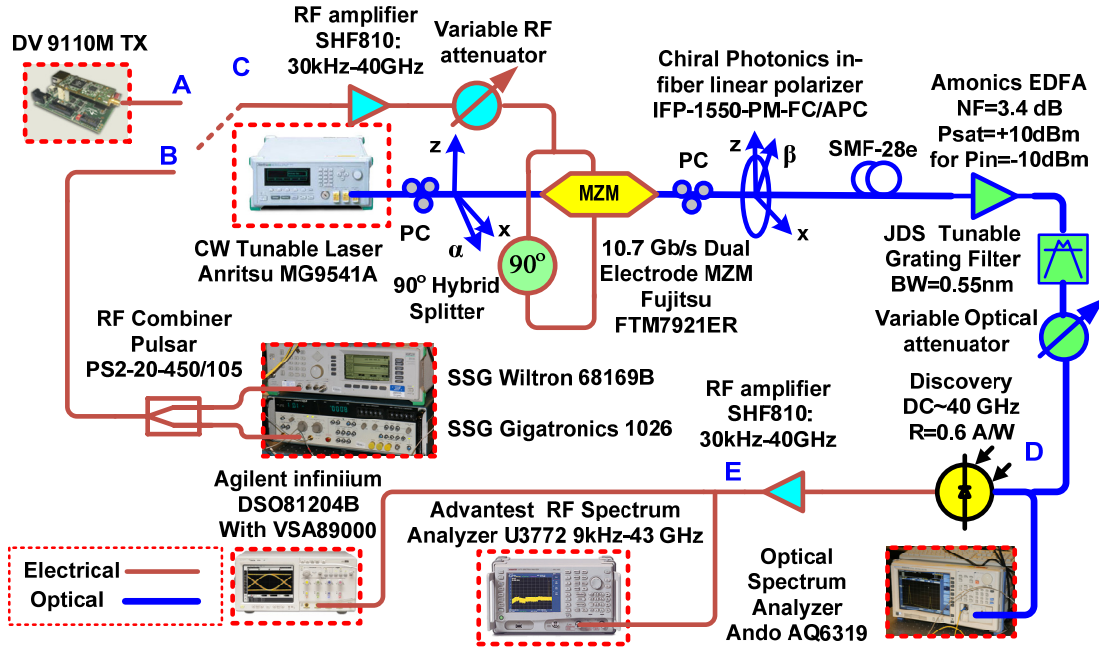


Figure 3.7 Experimental setup for a RoF system using the mixed polarization OSSB MZM. SSG: Synthesized Sweep Generator, PC: Polarization controller.

Table 3.1 Physical experimental parameters

Optical wavelength	λ	1549.8145 nm
Optical power	P_{in}	6 dBm
Optical amplifier gain	G_{opt}	6 dB
RF ₁ frequency	f_1	8 GHz
RF ₂ frequency	f_2	10 GHz
Elec. spectrum analyzer's resolution	RBW	100 Hz
Elec. spectrum analyzer's noise floor density	N_0	-130 dBm/Hz
Mach-Zehnder V_π	V_π	5 V
Mach-Zehnder insertion loss	t_{ff}	6 dB
Mach-Zehnder extinction ratio	ER	20 dB
Optical filter insertion loss	L_{opt}	3.5 dB
Photodetector responsivity	\mathfrak{R}	0.62 A/W
LNA gain	G_{RF}	22 dB
RF connectors loss	L_{RF}	3 dB
Load resistance of the optical receiver	R_L	50 Ω

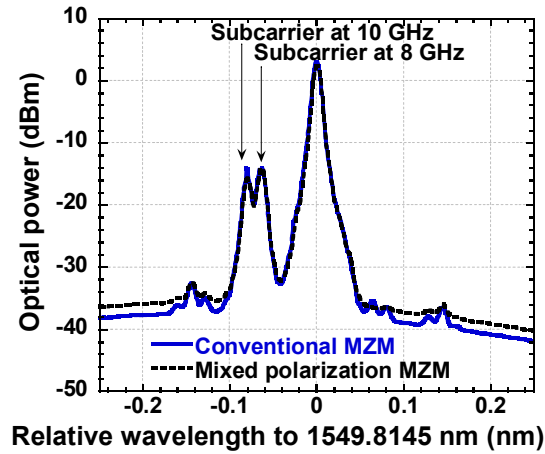


Figure 3.8 Experimentally measured optical spectrum for the conventional and mixed polarization OSSB MZM.

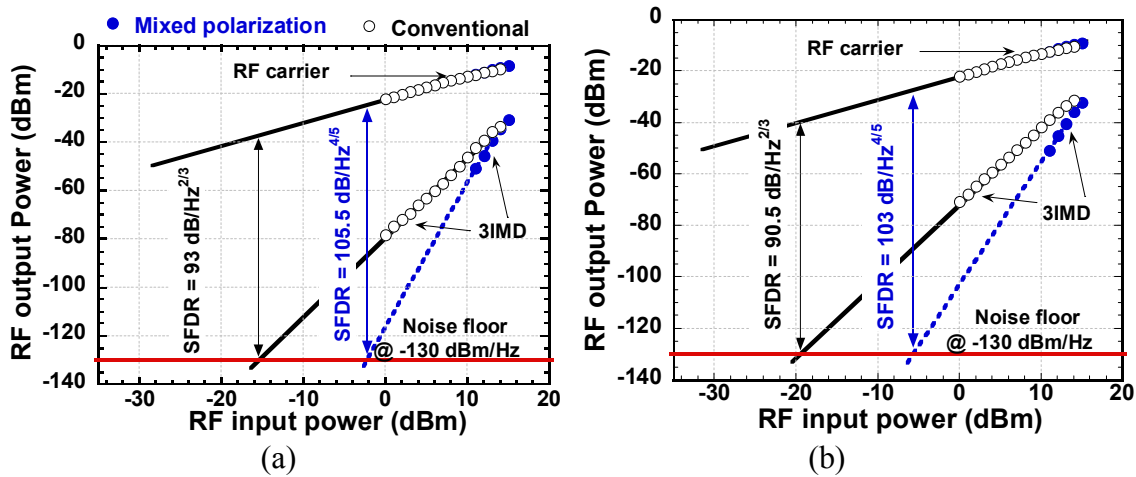


Figure 3.9 Measured SFDR in a normalized 1 Hz noise bandwidth for (a) back-to-back and (b) 20 km RoF system using the conventional and mixed polarization OSSB MZM.

Figure 3.8 shows the measured optical spectra from the output of the conventional and mixed-polarization modulator (at point D in Figure 3.7). It is seen that OSSB modulation is obtained in both cases. Figure 3.9 shows the measured SFDR for the conventional and mixed polarization MZM. It is seen that an improvement of ~ 12.5 dB in SFDR is obtained using the mixed polarization MZM over the conventional MZM, which matches closely with theoretical prediction and simulation results. This indicates that in the experiment the birefringence is

negligible in the MZM and the interconnection fiber between the MZM output and the second linear polarizer.

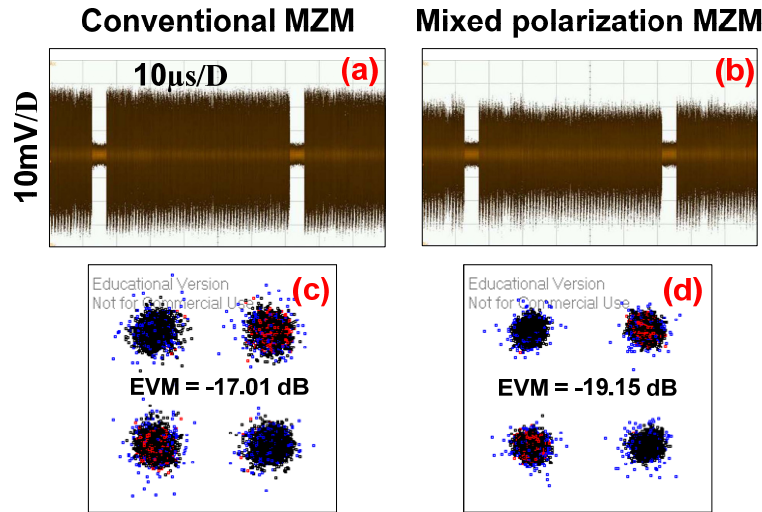


Figure 3.10 Measured waveform, constellation and EVM of received MB-OFDM UWB signal after 20 km of fibre transmission when using conventional MZM (a) and (c), and mixed polarization MZM (b) and (d), respectively. The RF modulation index is 6.54%.

3.6 Experimental Results with MB-OFDM UWB Signal

We used the same experimental setup, as shown in Figure 3.7, except we replaced the synthesized sweep generators by a MB-OFDM UWB source by connecting point A to point C. DV 9110M TX module from Wisair is used to generate an MB-OFDM UWB signal at band group 1 at bit rate of 200Mb/s with TFC1 compliant with Wimedia standard [5]. The input optical power to the DE-MZM was set to 4 dBm and the RF modulation index of the MB-OFDB UWB signal was set to 6.54 %. A variable optical attenuator is inserted before the photodetector to set the received optical power to -13 dBm after transmission over 20 km of fiber. A real time oscilloscope DSO81204B (from Agilent Technologies) is used for UWB signal analysis. Figure 3.10 (a-b) and (c-d) shows the waveform and constellation with measured EVM for conventional and mixed polarization MZM, respectively. It is observed that the signal power has been reduced from the waveform due to insertion loss from linearization technique while the constellation is

less distorted and the EVM is improved by more than 2 dB when using the mixed polarization MZM.

3.7 Chapter Summary

This chapter presented the mixed-polarization OSSB MZM, which alleviated most of the limitations incurred by the previous proposed linearization techniques. A comprehensive investigation was conducted for the mixed-polarization MZM in the suppression of IMD in theory, simulation and experiment. The suppression of third order IMD using the mixed-polarization MZM is independent of modulation index. Both theory and simulation predict a 13 dB improvement of SFDR for back-to-back and 20 km fiber RoF system using the mixed-polarization modulator. Moreover, power fading of the RF carrier and crosstalk due to intermodulation via fiber chromatic dispersion is significantly suppressed compared to using the conventional OSSB MZM. We experimentally verified the mixed-polarization modulation technique. It was shown that an improvement of ~ 12.5 dB in SFDR using discrete optical components was achieved and good agreement with theory and simulation is obtained. Also, an improvement of 2 dB in EVM is achieved when applying our proposed mixed polarization technique to MB-OFDM UWB signal after transmission over 20 km of fiber. Due to the linearization process an RF carrier power penalty is incurred, which will need to be compensated for with optical amplifiers or increasing the input optical power. It will remain as a future research to find a way to improve upon this technique by reducing the power penalty.

CHAPTER 4 PROPOSED PREDISTORTION CIRCUIT FOR EAM

4.1 Introduction

The mixed polarization technique proposed in Chapter 3 cannot be applied to the EAMs because they are designed and fabricated to be polarization independent. In [47], a feed-forward linearization technique of EAM was proposed. The basic idea of feed-forward linearization is as follows. Part of the output light from EAM is converted back to RF signal, and by subtracting this RF signal from the original RF signal, only the distortion generated by the EAM is left, then this distorted RF signal is applied to modulate a DFB-laser to cancel the distortion induced by the EAM. However, this method has a very rigorous requirement on the wavelength of the two lasers. If the wavelengths of the two lasers are not exactly the same, then, the linearization would not happen. Also, the feed-forward linearization method requires an extra laser and PD, which will increase the cost and the complexity of the whole system. In [48-49], two EAMs are used either in parallel or in series, and the reverse biases of the EAMs are adjusted to have third order intermodulation (IMD3) cancelled. These two methods gave a good suppression of IMD3, but using two EAMs will also increase cost.

In [40, 44], the analog predistortion circuits were used in narrowband system to linearize RF power amplifiers. In [36-37], it was successfully introduced the widely used predistortion circuit architecture in radio-over-fiber system with radio of below 1 GHz like CATV, GSM, and so on. In the traditional predistortion circuit, as shown in Figure 4.1, the input RF signal is first split into two paths, one path goes through the nonlinearity generation circuit, the other path goes through the time delay, and then these two paths are combined together by a power combiner. A phase shifter and an amplifier are used in the nonlinear path to adjust the phase and the magnitude of IMD3 of the pre-distorted signal, so that good cancellation of IMD3 can be achieved. In [36] the composite triple beat distortion (CTB) is reduced by 10 dB over 400-960 MHz, and in [37] the CTB is reduced by 22.6 dB over 55.25-535.25 MHz for CATV over fiber system. However, the drawback of the traditional predistortion circuit is the use of extra RF components, including phase shifter and amplifier, which may introduce new IMD that would be mixed with the original pre-distorted signal generated by the predistortion circuit, besides that the phase shifter is a narrow band RF component and cannot be used in UWB system. Another

drawback is the use of two RF paths, which require very precise time delay, several picoseconds extra time delay would cause the whole circuit to fail, and this would cause the difficulty for the real circuit implementation, especially in high frequency broadband system such as MB-OFDM UWB.

In this chapter a novel predistortion circuit which uses anti-parallel diodes in two paths with push-pull bias is proposed. The RF signal would go through the diodes, and the pre-distorted signal would be generated simultaneously in the two paths. This suggests that the predistortion circuit will not generate even order nonlinear products. However, third order nonlinearity generated from the two paths will be added together, which is used to cancel the third order nonlinearity of the EAM. In Section 4.2 the nonlinearity of EAM transfer function and the general relationship of transfer functions between predistortion circuit and EAM are presented. Then, a novel architecture of predistortion circuit is proposed. Following that, we present our theoretical analysis in Section 4.3. Experimental demonstration of predistortion circuit in a RoF system by using two RF tone test and MB-OFDM UWB signal is presented in Section 4.4. Finally, the conclusions are drawn in Section 4.5.

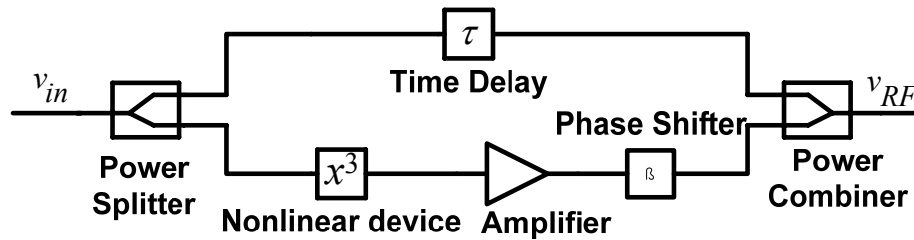


Figure 4.1 Traditional predistortion circuit

4.2 Principle and Theory

Figure 4.2 shows measured EAM transfer function for an EAM integrated with a DFB laser. The normalized transfer function of the EAM in Figure 4.2 can be represented as $P_{out}(V)/P_{in} = \exp(-\Gamma \alpha(V)L)$, where P_{in} is input optical power, Γ is the confinement factor, α is the absorption coefficient that varies with driving voltage V , and L is the waveguide length of the

EAM. The driving voltage is given by $V = V_b + v_{RF}$, where V_b is the bias voltage of the EAM, and v_{RF} is voltage of the RF signal. For the small signal approximation, i.e. $v_{RF} \ll V_b$, we can expand the normalized transfer function at a given bias into Taylor series

$$p_{out} = \frac{P_{out}(V)}{P_{in}} = k_1 v_{RF} + k_2 v_{RF}^2 + k_3 v_{RF}^3 + \dots \quad (4.1)$$

where k_i ($i=1, 2, 3, \dots$) are the coefficients related to the EAM transfer function and bias.

Figure 4.2 also shows measured power of IMD3 and fundamental RF carrier at different DC bias voltage when the input power of RF tones at 3.96 and 3.964 GHz is 3 dBm per RF tone. It is seen that power of fundamental carrier is the highest when the reversed bias is near 0 V, and the IMD3 is also the highest at 0 V bias due to the signal clipping but not to the transfer function nonlinearity of the EAM. While the reversed bias increases, the power of the fundamental carrier starts decreasing. For RoF system, it is desired to have higher power of the fundamental carrier. So in this work, we bias the EAM at 0.5 V to avoid clipping and also have higher power of the fundamental carrier.

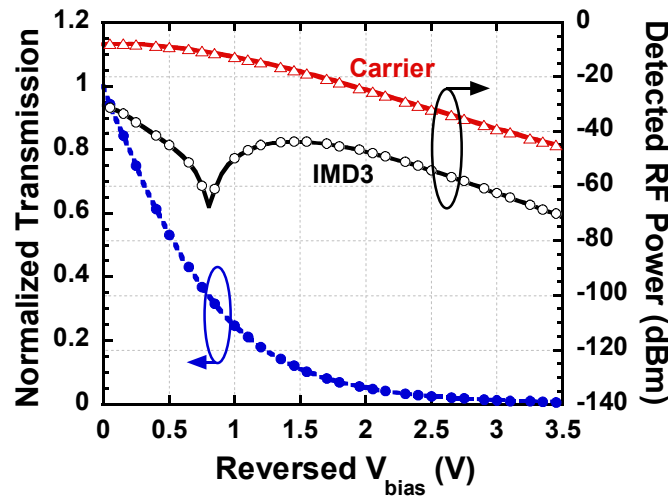


Figure 4.2 Normalized transfer function of EAM and the power of IMD3 and fundamental carrier versus EAM bias. Input power is 3 dBm per RF tone.

The block diagram of the predistortion circuit followed with an EAM is depicted in Figure 4.3. With the small signal assumption, we can only consider up to third order nonlinearity.

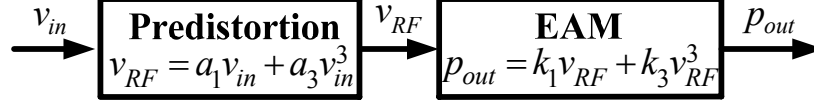


Figure 4.3 Block diagram of predistortion circuit and EAM.

The output of the predistortion circuit can be written as

$$v_{RF} = a_1 v_{in} + a_3 v_{in}^3 \quad (4.2)$$

where v_{in} denotes input RF signal voltage to the predistortion circuit, and a_i ($i=1$ and 3) are the coefficients related to the predistortion circuits. By considering the linear and third order nonlinear term in equation (4.1), the output after the EAM, by substituting (4.2) into (4.1), is given by

$$p_{out} = k_1 a_1 v_{in} + (k_1 a_3 + k_3 a_1^3) v_{in}^3 \quad (4.3)$$

where the rest of terms is ignored. To suppress third order nonlinear distortion at the output of EAM, the designed predistortion circuit must meet the condition of

$$\frac{k_1}{k_3} = -\frac{a_1^3}{a_3} \quad (4.4)$$

on the coefficients a_i and k_i ($i=1$, and 3). The condition provides the relationship of linear and third-order nonlinear coefficients between the EAM and predistortion circuit.

4.3 Proposed Predistortion Circuit

Figure 4.4 shows the basic configuration of the predistortion circuit. The input RF signal is equally split into two paths by a power splitter, and goes through a pair of anti-parallel diodes. The even order nonlinear products are cancelled due to the anti-parallel connection, and only odd-order nonlinear products are left. The $\lambda/4$ impedance transformer is used to 50 Ohm matching.

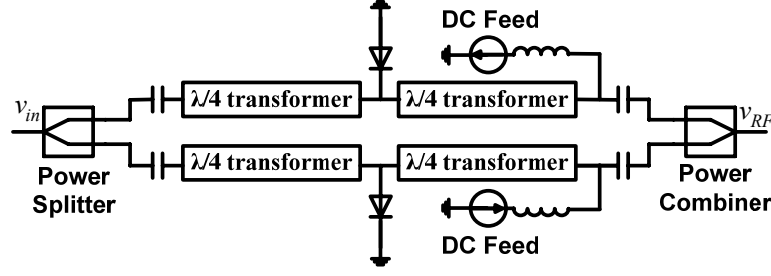


Figure 4.4 Schematic of predistortion circuit

By using the nonlinear current method, we obtain the Volterra series [57] for all the third order products at the circuit output, given in Appendix E. For two tones of RF signals at ω_1 and ω_2 , the expression of the voltage of the fundamental carrier ($V_{RF,fun}$) at ω_1 and ω_2 and of IMD3 ($V_{RF,IMD3}$) at each frequency of $2\omega_2 - \omega_1$ and $2\omega_1 - \omega_2$ at the circuit output is given, respectively, by (see Appendix E)

$$V_{RF,fun} = -\frac{(1 + g_1 R_b) Z_{load} V_s}{(Z_s + Z_{load})(1 + g_1 R_b) + g_1 Z_0^2} \quad (4.5)$$

$$V_{RF,IMD3} = -\frac{3}{4} \frac{Z_{load} Z_0^4 V_s^3}{\left[g_1 Z_0^2 + (1 + g_1 R_b)(Z_s + Z_{load}) \right]^5} \times \left[(g_1 g_3 - 2g_2^2) Z_0^2 + \left[g_3 (1 + g_1 R_b) - 2g_2^2 R_b \right] (Z_s + Z_{load}) \right]^3 \quad (4.6)$$

where V_s and Z_s is the source voltage and impedance, respectively, Z_{load} is the load impedance, R_b is the bulk resistance, g_1 , g_2 and g_3 are coefficient of the Taylor Series expansion of nonlinear conductance of the diode.

We can also express the coefficients for the predistortion circuit in equation (4.2) by (see Appendix E)

$$a_1 = -\frac{(1 + g_1 R_b) Z_{load}}{Z_{load} (1 + g_1 R_b) + g_1 Z_0^2} \quad (4.7)$$

$$a_3 = -\frac{Z_{load}Z_0^4}{\left[g_1Z_0^2 + (1+g_1R_b)(Z_s + Z_{load})\right]^2} \quad (4.8)$$

$$\times \frac{(g_1g_3 - 2g_2^2)Z_0^2 + [g_3(1+g_1R_b) - 2g_2^2R_b](Z_s + Z_{load})}{\left[Z_{load}(1+g_1R_b) + g_1Z_0^2\right]^3}$$

Equations (4.5) and (4.6) are used to calculate the fundamental carrier and IMD3 voltage at the circuit output, respectively. We carried out Harmonic Balance simulation in Advanced Design System (ADS) from Agilent Technologies for the diode with 50 Ohm load. Here we used two tones of input signal at 3960 and 3964.125MHz with equal power of -5 dBm. In Figure 4.5 (a)-(b), we compare calculated, simulated and measured RF power of fundamental carrier and IMD3, respectively, at different DC bias current from 0 to 9 mA. Figure 4.5 (a) shows very good agreement in RF carrier power between simulation and measurement for up to 6 mA, while the calculated results show a discrepancy of less than 0.5 dB. This is mainly due to the third order limited approximation used in the theory. At high bias current of the diode, higher order nonlinearity must be considered for the diode in theory. In Figure 4.5 (b) both simulation and calculation present some discrepancy in IMD3 power from the measured but follow similar trend as the measured IMD3. This discrepancy is mainly due to some residual IMD3 generated by the RF source and the RSA. However, a good prediction can be obtained from either simulation or calculation, and fine tuning of the bias current can set the right IMD3 magnitude and phase.

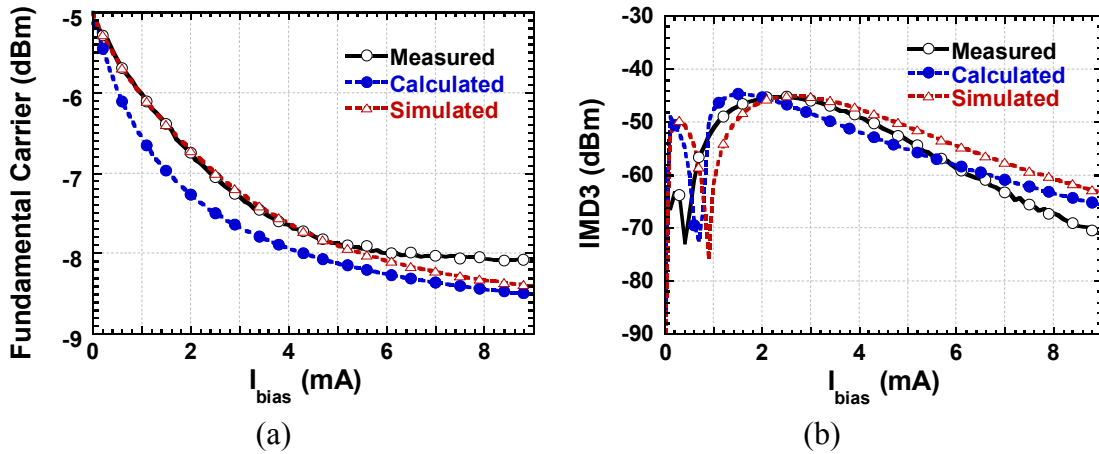


Figure 4.5 Measured, simulated and calculated RF power of (a) fundamental carrier and (b) IMD3. The input power is -5 dBm per RF tone.

4.4 Performance Evaluation in Back to Back RoF System with Two RF Tone Test

Figure 4.6 shows the experimental setup for a RoF system using the predistortion circuit. Two RF signal generators are used to generate two tone signals at 3960 and 3964.125 MHz with equal power (point A connected directly to point B). We keep the frequency spacing between two tones to be 4.125 MHz, which is the sub-carrier frequency spacing in MB-OFDM UWB system. The combined RF tones are applied to the predistortion circuit and then to a 10 Gb/s EAM integrated with laser diode. The modulated optical signal is directly detected by a high-speed PIN PD with a 3-dB bandwidth of 32 GHz and a responsivity of 0.62 A/W. The generated photocurrent is displayed on an RSA. The fabricated predistortion circuit is shown in Figure 4.7. Beam lead Schottky diodes are used, and biased by accurate current source. The optimum bias current for the pair diodes is 13.3 mA when the EAM is reversed bias at 0.5V.

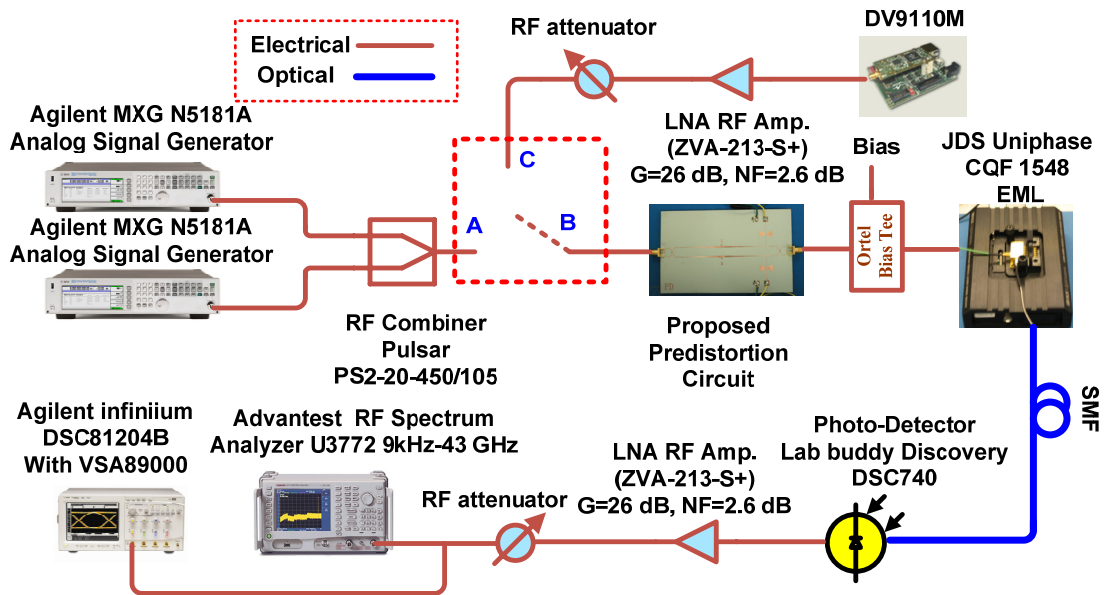


Figure 4.6 Experimental setup for a RoF system using predistortion circuit. Two tone test A connected to B, and MB-OFDM UWB test C connected to B.

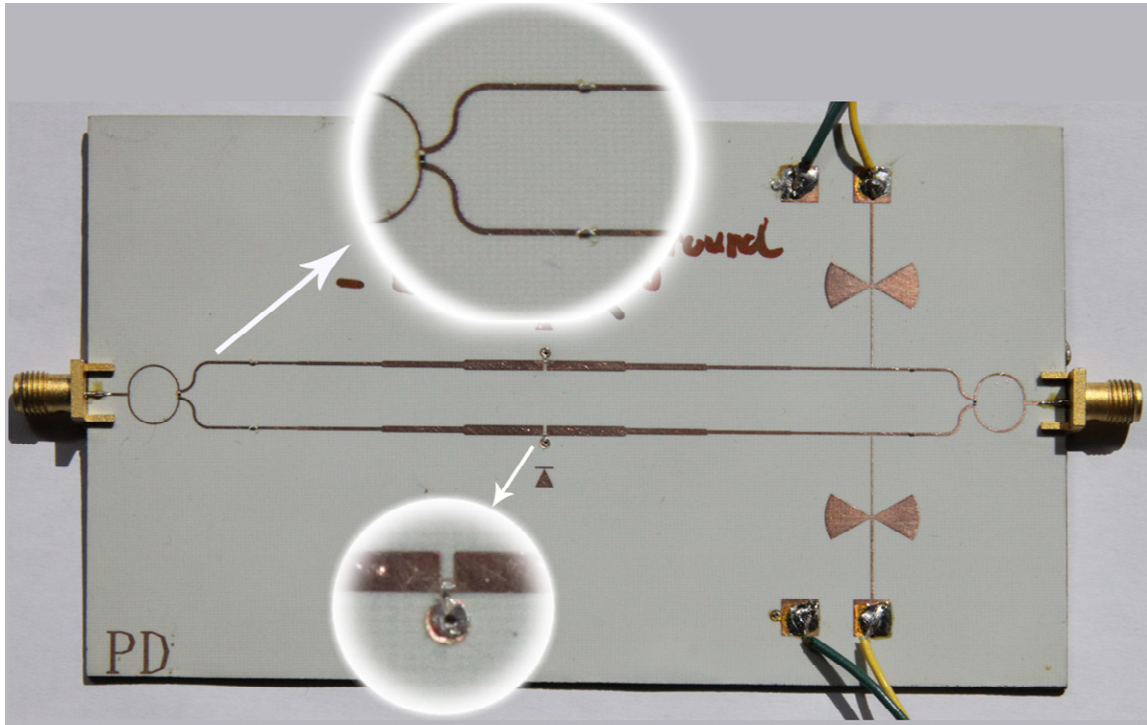


Figure 4.7 Fabricated predistortion circuit

Figure 4.8(a)-(b) shows measured RF spectra at the output of the photodetector, without and with the predistortion circuit, for 3.5 dBm input power of per RF tone and 0.5 V reverse bias of the EAM. After using the predistortion circuit, the IMD3 is suppressed by more than 18.5 dB while the fundamental carrier is reduced by 3 dB compared to without predistortion circuit. Thus the predistortion circuit introduces 3 dB insertion loss, and 3 dB back off in the input power would reduce the IMD3 by 9 dB. Thus the predistortion circuit gives an effective improvement of 9.5 dB in suppression of IMD3.

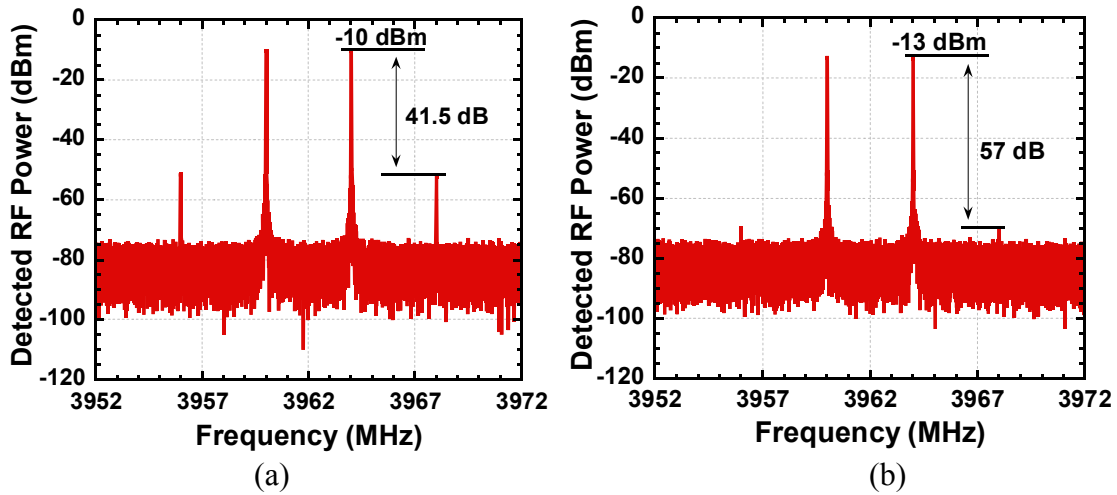
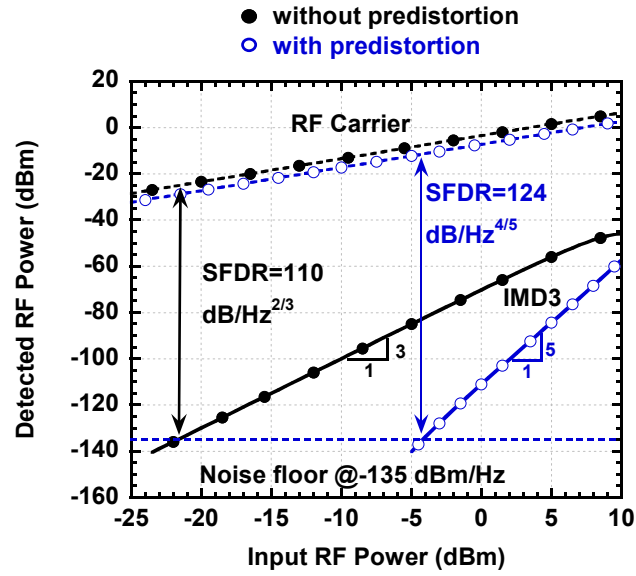
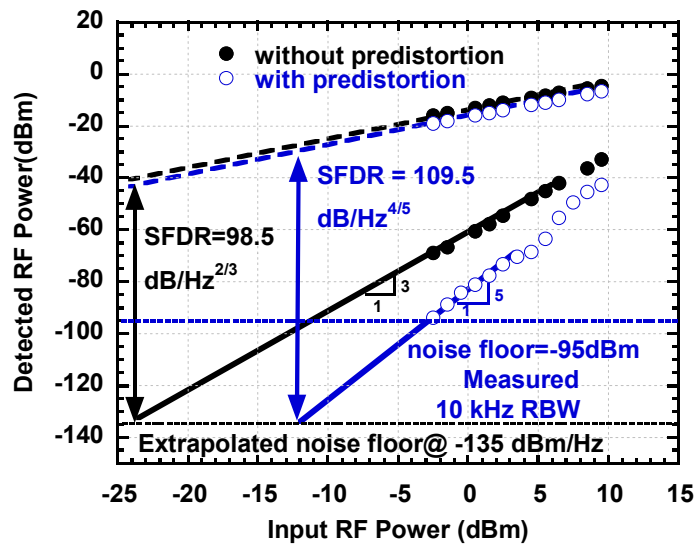


Figure 4.8 Measured spectra at the output of the EAM, (a) without and (b) with predistortion circuit. Input power is 3.5 dBm per RF tone and EAM reverse bias is 0.5 V.

Next, we vary the input power per RF tone from 3.5 to 9.5 dBm, and measure the RF power of the carrier and IMD3 with and without predistortion circuit. Figure 4.9 (a) shows simulated SFDR of $124 \text{ dB/Hz}^{4/5}$ and $110 \text{ dB/Hz}^{2/3}$ for the EAM with and without the predistortion circuit, respectively. Figure 4.9 (b) shows measured SFDR of $109.5 \text{ dB/Hz}^{4/5}$ and $98.5 \text{ dB/Hz}^{2/3}$ for the EAM with and without the predistortion circuit, respectively. Both simulation and measurement show that nonlinear distortion is 5th order limited (see the slope of IMD3 power) for the RoF system using the predistorted EAM. But without the predistortion circuit, it is 3rd order limited as seen in Figure 4.9. This shows that the IMD3 is cancelled from the predistorted EAM. Figure 4.9 (a) and (b) shows that the predistortion circuit leads to a SFDR improvement of ~ 14 and ~ 11 dB, in simulation and experiment, respectively. The difference is mainly due to PCB fabrication process.



(a)



(b)

Figure 4.9 Simulated (a) and measured (b) spurious free dynamic range. EAM reverse bias is 0.5 V.

We also investigated the performance of the predistortion circuit for broadband operation. For this, we vary the frequency of the two RF tones over band group 1 of MB-OFDM UWB and measure the power level of the RF carrier and IMD3. The input power was set to 3.5 dBm per RF tone. We swept frequency from 3.168 to 4.752 GHz to cover all frequency of bandgroup 1 in

MB-OFDM UWB and kept the two tones with 4.125MHz spacing. For fair comparison, we attenuate the RF input power to the EAM by 3 dB in order to keep the same RF output power of the carrier with and without predistortion circuit at the center frequency 3.96 GHz of band group 1. Figure 4.10 shows the frequency response with and without the predistortion circuit. It is observed that the improvement in IMD3 suppression reduces at lower frequencies. This is because at lower frequencies the insertion loss is lower and the input RF power is higher, then the nonlinearities are more pronounced in the EAM. However, the frequency response of the predistorted EAM is almost constant for up to 3.96 GHz and then decreases by almost 2 dB in the upper frequency band. The predistortion circuit achieves a suppression of IMD3 by more than 7 dB over the whole band group 1 of MB-OFDM UWB.

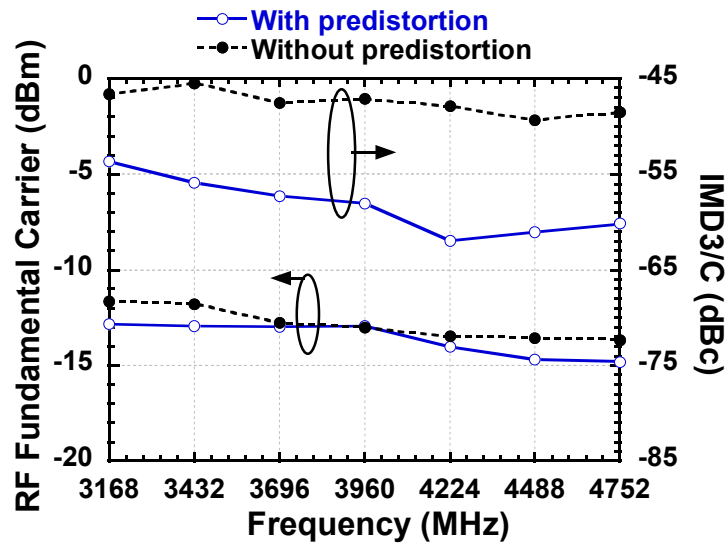


Figure 4.10 Measured frequency response of the EAM with and without predistortion circuit. Input power is 3.5 dBm per RF tone and EAM reverse bias is 0.5 V.

4.5 Performance Evaluation in MB-OFDM over Fiber System

We used the same experimental setup shown in Figure 4.6 for performance evaluation of UWB over fiber using our predistortion circuit (point C is connected to point B). To generate MB-OFDM UWB, we used a commercially available evaluation board, DV 9110M from WisAir,

which provides MB-OFDM compliant modulation with the first three WiMedia sub-bands of 528 MHz bandwidth allocated at center frequency of $f_1=3.432$, $f_2=3.96$ and $f_3=4.488$ GHz. The signal follows simple frequency hopping sequences like f_1 , f_2 and f_3 . The bit rate of 200 Mb/s is used for each band with QPSK modulations. The MB-OFDM UWB signal generated from DV 9110M module is applied to predistortion circuit and then to an EAM. The modulated optical signal was transmitted through an SMF. The EVM of the photodetected signal was measured by a 12 GHz high speed real time oscilloscope DSO81204B from Agilent Technologies. The optimum bias current for the pair diodes is 13.3 mA when the EAM was reversely biased at 0.5 V.

To show the improved performance of the transmitted MB-OFDM-UWB signal over fiber using our predistortion circuit, we have measured and compared EVM using EAM with and without predistortion circuit in back-to-back and after 20 km of fiber transmission, respectively. The transmitted power level from the DVM9110M is ~ 14 dBm, the loss from RF connections and Bias Tee is 4 dB, and the maximum losses from the RF attenuator are 16dB. By using a low-noise amplifier of 26 dB gain and attenuator, we are able to vary the input power to the predistortion circuit from ~ -8 to ~ 8 dBm. Because the predistortion circuit has 3- dB insertion loss, we insert 3-dB attenuator before the EAM for without predistortion circuit to make fair comparison between EAM with and without predistortion. Figure 4.11 (a)-(b) shows the measured EVM for back to back and after 20 km of fiber transmission for EAM with and without predistortion circuit.

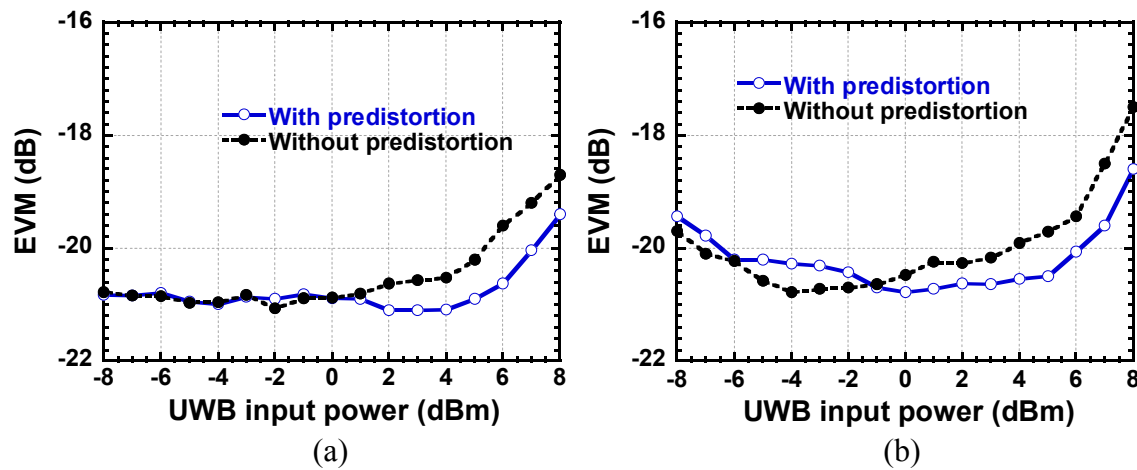


Figure 4.11 Measured EVM versus UWB input power for (a) back to back and (b) after 20 km of fiber transmission with and without predistortion circuit.

It is observed that the predistortion circuit leads to improvement of EVM at high input power levels, where the nonlinearity is the main limiting factor to the signal to noise ratio. However, at low power level of less than ~ 0 dBm, there is no improvement in the EVM by adding the predistortion circuit. This is because the RoF system is not limited by nonlinearity at these power levels. For back to back and after 20 km of fiber transmission, the EVM can be improved by up to 1 dB by using the predistortion circuit.

4.6 Chapter Summary

In this chapter, a predistortion circuit for linearization of EAM using reflective diodes pair has been designed for MB-OFDM UWB system at bandgroup 1 (3.1~ 4.8 GHz). It is found that the designed predistortion circuit leads to 11-dB improvement in the SFDR at the center frequency of bandgroup 1, and more than 7-dB improvement in suppression of IMD3 over the whole bandgroup 1. By evaluating the predistortion circuit with the MB-OFDM UWB signal, a 1-dB EVM improvement is obtained for first three band OFDM UWB over 20 km fiber. This suggests the proposed predistortion circuit is a cost effective broadband linearization technique for MB-OFDM UWB over fiber.

CHAPTER 5 PRE-COMPENSATED OPTICAL DOUBLE-SIDEBAND SUBCARRIER MODULATION IMMUNE TO FIBER CHROMATIC DISPERSION INDUCED RF POWER FADING

5.1 Introduction

We propose and demonstrate a new optical double-sideband modulation technique that is immune to fiber chromatic dispersion and thus free of dispersion induced RF power fading. The proposed modulation technique also provides a 3-dB improvement of RF power compared to OSSB modulation. The proposed modulation technique is analyzed in theory and simulation. It is shown that for a given fiber length an optimum electrical phase shift exists to completely cancel the dispersion induced RF power fading. We verify this proposed modulation technique experimentally for single tone RF signal and for a MB OFDM UWB signal.

In this chapter we will present a very simple and new modulation technique to overcome dispersion-induced power fading and increase the power efficiency by 3 dB. A DE-MZM which has been used for optical SCM [58-62] will be the key component in our proposed technique. The dispersion-induced phase difference between upper and lower sidebands is compensated by splitting the RF signal into two phase shifted RF signals. The resulting RF signals will drive a DE-MZM in a tandem single sideband (TSSB) modulation, i.e., each signal will generate different OSSB. The electrical phase difference between the two RF drives will be tuned to compensate for the dispersion-induced power fading. Simulation and theoretical analysis are carried out with experimental proof of concept to validate the potential of the proposed technique to overcome both power fading caused by chromatic dispersion in ODSB and 3 dB power loss experienced in OSSB modulation. This chapter is organized as follows; Section 5.2 will provide theoretical analysis and give a closed form expression of the electrical tuning phase shift between the two electrical drives, and of the power efficiency improvement as functions of system parameters namely DE-MZM extinction ratio, fiber transmission length and chromatic dispersion. Simulation analysis and verification of our theory is given in Section 5.3. In Section 5.4, the proposed technique is experimentally demonstrated for 12 GHz RF tone at back to back and 52 km fiber transmission. In Section 5.5, the proposed technique is also applied to MB-

OFDM UWB signal transmitted over 20 km of fiber and similar results were obtained. Finally, some conclusions will be drawn in Section 5.6.

5.2 Theoretical Analysis

A RoF link where the proposed modulator is used is shown in Figure 5.1. Suppose that a lightwave expressed by an electrical field with an optical carrier at ω_c is injected to a DE-MZM driven by a sinusoidal RF signal of $V_{RF}(t) = \sqrt{2}V_{RF} \sin(\omega_{RF}t + \theta)$, where $\sqrt{2}V_{RF}$, $\omega_{RF} = 2\pi f_{RF}$ and θ are modulation voltage, angular frequency and random phase of the RF input signal. ϕ is the phase difference between the two RF signals applied to the DE-MZM.

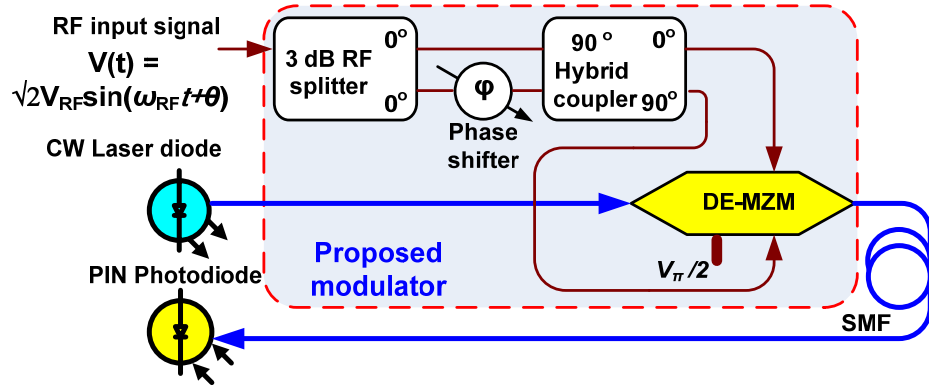


Figure 5.1 RoF link setup where the proposed modulator is used.

5.2.1 Optimum Phase Shift

In Appendix F, we derive the theoretical expression (5.1) for the required electrical phase shift ϕ to compensate for chromatic dispersion induced power fading and achieve maximum RF output power.

$$\phi = -2 \tan^{-1} \left[\frac{(1 + \delta^2)}{(1 - \delta^2 + 2\delta \tan \theta_2)} \right] \quad (5.1)$$

where $\delta = (\sqrt{ER} - 1) / (\sqrt{ER} + 1)$ is the splitting ratio, ER is the DE-MZM extinction ratio, and $\theta_2 = \pi \lambda_c^2 DL f_{RF}^2 / c$ represents the chromatic dispersion induced phase shift, $\lambda_c = 2\pi c / \omega_c$, c - the speed of light in vacuum, L and D - fiber length and chromatic dispersion, respectively.

Figure 5.2 shows the calculated optimum phase shift using equation (5.1) versus dispersion induced phase shift θ_2 for different MZM extinction ratios. It is seen that the electrical phase shift

depends on the MZM extinction ratio and increases linearly with the dispersion induced phase shift for high MZM extinction ratio. This is because for high extinction ratio, equation (5.1) can be simplified into $\varphi \sim 2\theta_2 - \pi$.

5.2.2 Power Efficiency Improvement

In order to show the improvement using the proposed electrical dispersion compensation technique compared to OSSB modulation, the improvement of RF power is derived in Appendix F by expressing the ratio of the RF output power of the proposed technique to that of the conventional OSSB as

$$\eta = \frac{\left(1 + \delta^2 + (1 - \delta^2) \sin \varphi\right)^2}{1 + \delta^4 + (1 - \delta^4) \sin \varphi} \quad (5.2)$$

Equation (5.2) indicates that the MZM extinction ratio has impact on the RF efficiency improvement of the proposed technique. Figure 5.3 shows the calculated improvement efficiency using equations (5.1) and (5.2) at different MZM extinction ratios. It is clearly shown that the improvement efficiency is almost 3 dB when high extinction ratio is used. This is because at high MZM extinction ratio, i.e. $\delta \sim 1$, equation (5.2) reduces to $\eta \sim 2$.

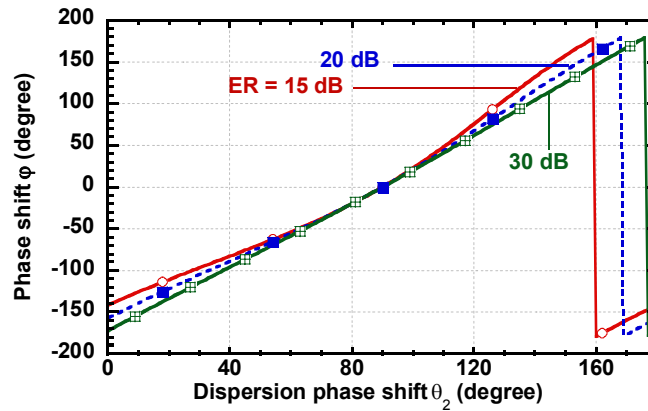


Figure 5.2 Calculated optimum electrical phase shift versus dispersion induced phase shift θ_2 for different MZM extinction ratios (ER): 15, 20 and 30 dB. A laser emitting at 1550 nm and fiber dispersion of 16 ps/(nm.km) are used.

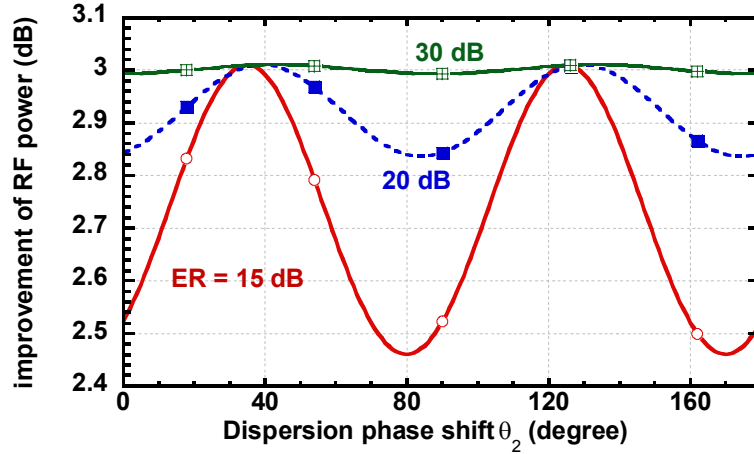


Figure 5.3 Calculated RF power efficiency improvement versus dispersion induced phase shift θ_2 for different MZM extinction ratios (ER): 15, 20 and 30 dB, and when using optimum electrical phase shift ϕ . A laser emitting at 1550 nm and fiber dispersion of 16 ps/(nm.km) are used.

5.3 Verification and Analysis by Simulation

In order to validate the theoretical analysis of dispersion compensation using our technique presented in Section 5.2, we simulated the system setup shown in Figure 5.1. Simulation was carried out with the commercial software VPItransmissionMaker 7.6. A continuous wave light from a laser source is assumed to have a wavelength of 1550 nm, output power of 0 dBm, and RIN of -155 dB/Hz. The CW light is injected into a DE-MZM, driven by an RF signal. The RF signal is split equally into two RF signals and one of them is phase shifted by a tunable phase shifter. The resulting two RF signals are applied to both electrodes of the DE-MZM through a double arrow 90° HEC. Low total RF modulation index $m_{RF} = \sqrt{2} V_{RF} / V_\pi$ is used, V_π the halfwave switching voltage of the DE-MZM. The output signal from the DE-MZM is injected into an SMF of length L , loss of $\alpha = 0.2$ dB/km and chromatic dispersion of $D = 16$ ps/(nm.km). The optical signal is detected by a high-speed PIN PD with a 3 dB bandwidth of 32 GHz and a responsivity of 0.62 A/W. In the simulation insertion loss from the DE-MZM and fiber are compensated using an EDFA that maintain a 0 dBm optical power at the photodetector.

We assume that the DE-MZM has an extinction ratio of 30 dB and is driven by an RF signal with an RF modulation index of $m_{RF} = \sqrt{2}/10$. We used an RF signal at 12 GHz and 3.96 GHz transmitted over 52 km and 20 km of fiber, as for the experimental analysis in Section 5.4 and

5.5, respectively. We sweep the electrical phase shift and measure the RF output power. Figure 5.4 shows the RF output power versus electrical phase shift at different fiber lengths and RF frequencies. For back to back transmission the maximum RF power is obtained at electrical phase shift of -173° . The maximum RF power is obtained at electrical phase shift of -158.5° and 174° after transmission of the RF signal at 3.96 GHz and 12 GHz over 20 km and 52 km of fiber, respectively. For back-to-back there is no dispersion induced phase shift, while after transmission of the RF signal at 12 GHz and 3.96 GHz over 52 km and 20 km of fiber, the dispersion induced phase shift is 173.5° and 7.5° , respectively. The corresponding optimum electrical phase shift displayed in Figure 5.2 using equation (5.1) agrees very well with the simulated values obtained at the maximum RF power shown in Figure 5.4.

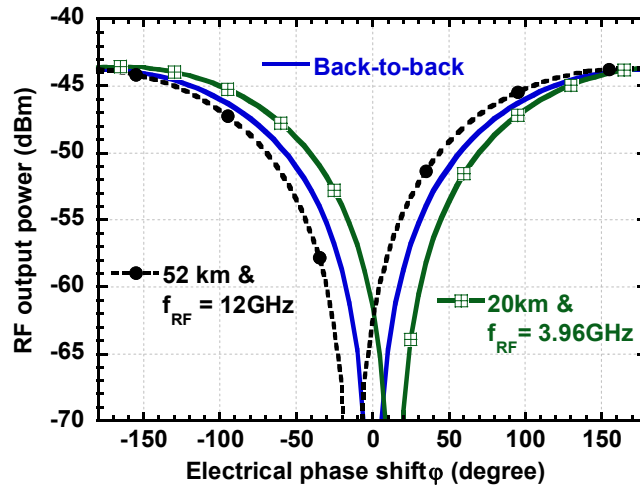


Figure 5.4 Simulated RF power versus electrical phase shift at different fiber length. A laser emitting at 1550 nm, $f_{RF}=12$ GHz, fiber dispersion of 16 ps/(nm.km), MZM extinction ratio of 30 dB and RF modulation index of $\sqrt{2}/10$ are used.

Then we simulated the improvement of RF power compared to OSSB versus MZM extinction ratio using the optimum electrical phase shift calculated by equation (5.1). Figure 5.5 depicts the simulated (lines) and calculated (marks) RF power efficiency improvement for back-to-back and after transmission of the RF signal at 12 GHz and 3.96 GHz over 52 km and 20 km of fiber, respectively. For the calculation we used equations (5.1) and (5.2). It is clearly shown

that the simulated and calculated improvements agree well. This verifies that our theory developed in Section 5.2 is accurate. Moreover, it is seen that almost 3 dB improvement in RF power is obtained if the MZM has an extinction ratio of more than 20 dB. The dependency on low extinction ratio is clear from equation (5.2) and the maximum and minimum improvement in RF power is 2 and $2\left(\frac{(ER-1)}{(ER+1)}\right)^2$, respectively.

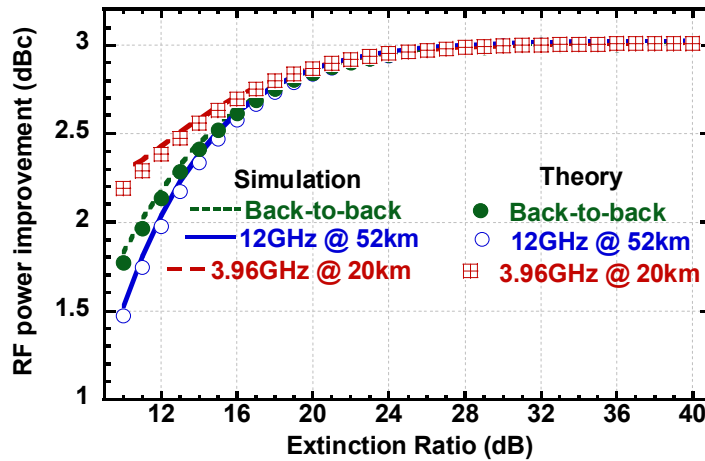


Figure 5.5 RF power improvement versus MZM extinction ratio at different fiber length obtained by using simulation (lines) and theory (marks).

The improvement in RF power may not clearly display the influence of fiber chromatic dispersion on the signal pulse when the RF signal is carrying data. For this case we investigated the performance of 12 GHz RF signal carrying non return to zero (NRZ) data at bit rate of 625 Mb/s. We used an optimum electrical phase shift of -173° and 174° for back to back and after 52 km of fiber transmission, respectively, and measured the Q factor versus received optical power and compare our proposed ODSB to OSSB. Simulation results in Figure 5.6 show no power penalty at $Q = 9$ for either OSSB or proposed ODSB after 52 km of fiber transmission. However, there is 1.5 dB improvement of optical receiver sensitivity in our proposed ODSB compared to OSSB. Figure 5.6 shows that $Q = 9$ can be achieved at -15.9 dBm of received optical power for OSSB whereas only -17.4 dBm is required for our proposed ODSB. The corresponding eye diagrams in Figure 5.7 show a good quality of the transmitted signal and suggest that at least

similar performance of OSSB could be achieved by using our proposed ODSB with 3 dB RF power improvement.

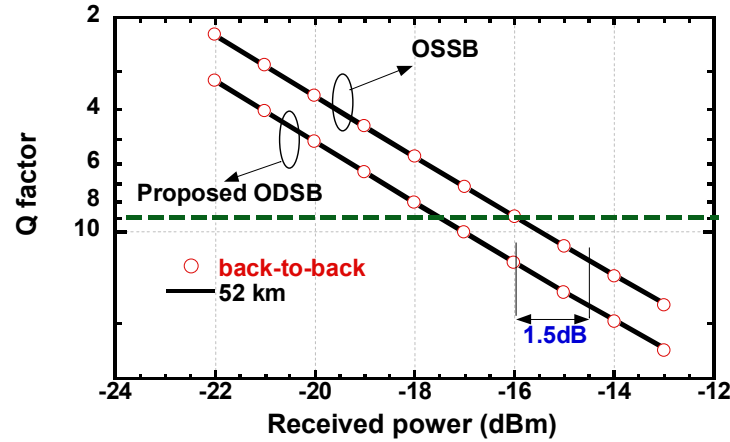


Figure 5.6 Q factor for OSSB and proposed ODSB versus received optical power for 12 GHz RF signal carrying NRZ data at 625Mb/s bit rate.

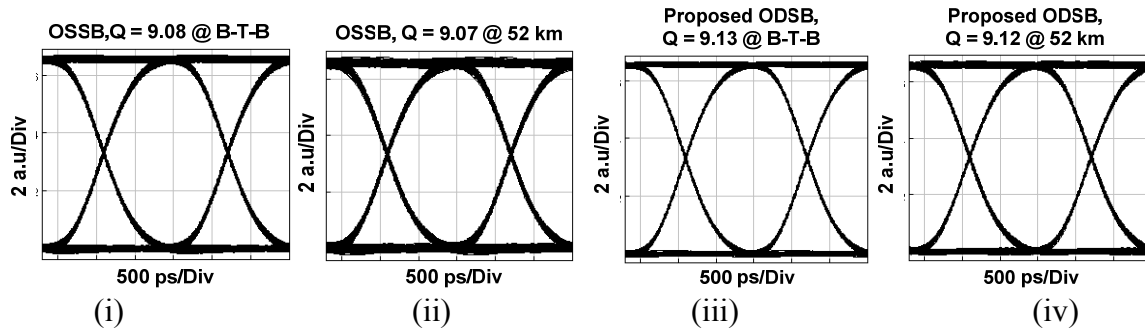


Figure 5.7 Eye diagram for OSSB: (i) back to back (B-T-B), (ii) 52 km, and for proposed ODSB: (iii) B-T-B, (iv) 52 km. The received optical power is -15.9 dBm and -17.4 dBm for OSSB and proposed ODSB, respectively.

Next, we will verify experimentally the performance of two different RF signals: one is a single RF tone without data modulation, and the other is MB-OFDM UWB transmitted over fiber using our proposed ODSB modulation technique.

5.4 Experimental Verification using One RF Tone

In order to experimentally validate our technique we demonstrate the conventional ODSB, OSSB and our proposed ODSB modulation in a back-to-back and 52 km RoF transmission.

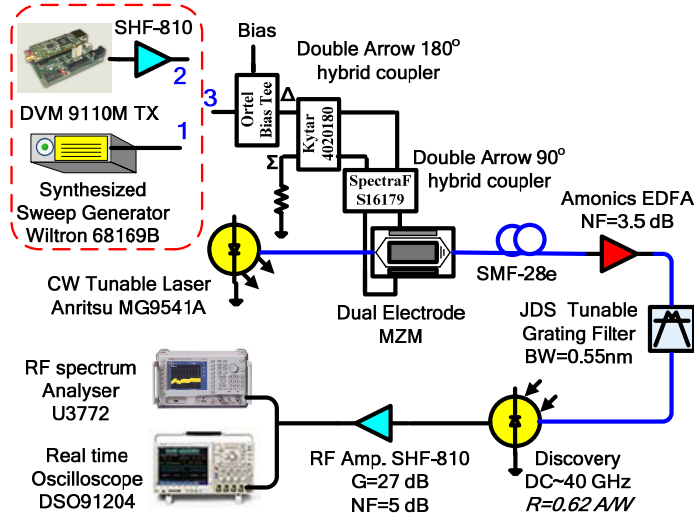


Figure 5.8 Experimental set up for proof of concept.

Figure 5.8 shows the experimental setup that was used for the proof of concept where point 3 is connected to point 1. A tunable laser source (Anritsu MG9541A) delivers a linearly polarized light at 1549.978 nm of 6 dBm optical power with a linewidth of 800 KHz and intrinsic RIN of -155 dB/Hz. The lightwave is injected into a DE-MZM (T. DEH. 5-40PD-ADC Sumitomo) of 6 dB insertion loss, 32 dB extinction ratio and 5 V half wave switching voltage. The DE-MZM was biased at quadrature bias and driven by a 12.1115 GHz RF source of 10 dBm output RF power. An EDFA has been used to compensate for fiber loss and insertion loss of the optical filter. A 0 dBm optical power has been maintained at the receiver. Due to unavailability of broadband tunable phase shifter we used a 180° HEC to introduce a phase shift of 180°. After the 180° HEC two output RF signals (one is 180° phase shifted) are fed to two input ports of 90° HEC in order to drive the DE-MZM in TSSB configuration. The modulated optical signal is directly detected by a high-speed PIN PD with a 3-dB bandwidth of 32 GHz and a responsivity of 0.62A/W. The generated photocurrent is amplified by 27 dB gain and displayed on an RSA.

We kept all components in the setup for all the three modulations, in order to have the same insertion loss. For OSSB modulation, one of the two outputs of the 180° HEC is injected to the 90° HEC. For the conventional ODSB modulation, the input RF signal is connected to the Σ input port of the 180° HEC, and for our proposed ODSB modulation the input RF signal is connected to the Δ input port of the 180° HEC to have 180° phase difference between the two output signals. Then two outputs are injected to the 90° HEC. Then the two outputs drive the MZM two electrodes.

Figure 5.9 shows the measured optical spectrum at the output of the DE-MZM for the OSSB, the conventional ODSB and our proposed ODSB modulation. Note that there is inherent 180° phase difference between the two sidebands using the conventional ODSB modulation. It is seen that our proposed technique results in an ODSB modulation and the optical spectrum is the same as that obtained using the conventional ODSB modulation. However, an additional 180° phase difference is applied to two driving voltages of the DE-MZM in our proposed ODSB modulation compared to the conventional ODSB modulation. This suggests that the two sidebands as shown in Figure 5.9 are in-phase when using our proposed ODSB modulation and have 180° phase difference if using the conventional ODSB modulation.

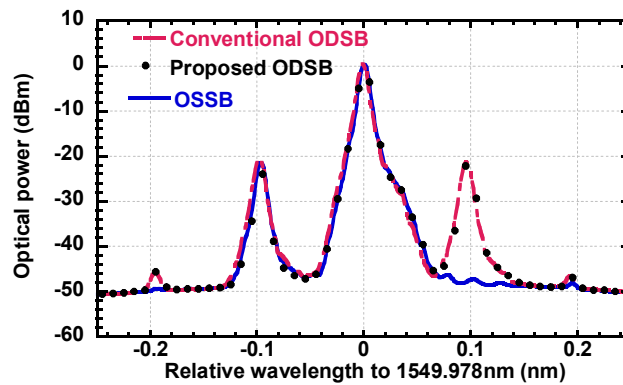


Figure 5.9 Measured optical spectrum using OSSB (solid line), conventional ODSB (dashed line) and our proposed ODSB (mark) modulation.

Corresponding to Figure 5.9, the measured RF spectrum is shown in Figure 5.10. It is seen that using conventional ODSB modulation the RF power is suppressed by more than 20 dB

compared to OSSB modulation. Due to inherent 180° phase difference between the two sidebands from the conventional ODSB modulation, the RF power is significantly suppressed. As seen in Figure 5.10, our proposed ODSB modulation avoids such a suppression of RF power by inserting additional 180° phase shift. It is well known that fiber chromatic dispersion will induce phase shift between the two sidebands and thus RF power fading is introduced. The above results imply that by changing the phase difference between the two driving voltages for a given fiber length we are able to obtain fiber chromatic dispersion free RoF transmission. Moreover, our proposed ODSB modulation results in an RF power of 6 dB higher than that using OSSB modulation. Note that there is a 3 dB loss from the 180° HEC. Thus our proposed ODSB modulation improves the RF power by 3 dB compared to OSSB, which is in good agreement with our theoretical predictions and simulation.

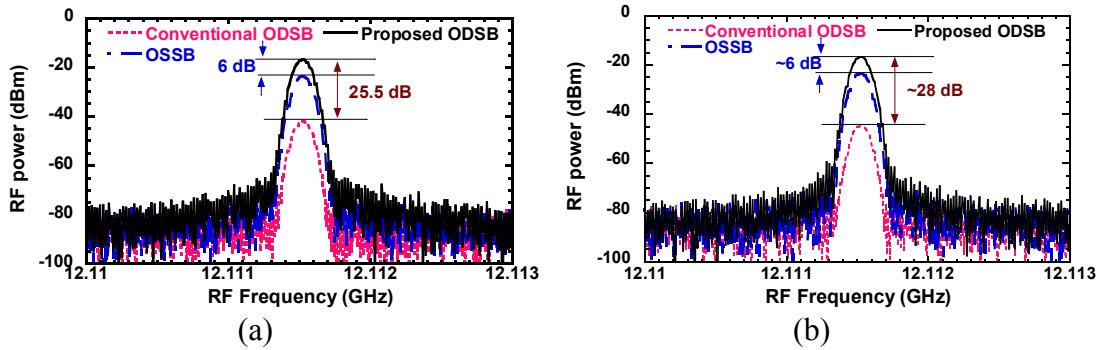


Figure 5.10 Measured electrical spectrum for (a) back-to-back and (b) after 52 km of fiber transmission.

5.5 Experimental Verification using MB-OFDM UWB Signal

We used the same experimental setup shown in Figure 5.8 for performance evaluation of UWB over fiber using our proposed ODSB modulation, where point 3 is connected to point 2. To generate MB-OFDM UWB we used a commercially available evaluation board, DV 9110M from WisAir, which provides MB-OFDM compliant modulation with the first three WiMedia sub-bands of 528 MHz bandwidth allocated at center frequency of $f_1=3.432$, $f_2=3.96$ and $f_3=4.488$ GHz. The signal follows TFC1. The bit rate of 200 Mb/s is used for each band with QPSK modulations.

The tunable laser source is set to wavelength of 1550 nm, and output power of 0 dBm. The CW light is injected into a 10.7 Gb/s DE-MZM from Fujitsu, driven by the UWB signal from the output of the DV 9110M Tx module. The MZM has 6 dB insertion loss, RF half wave switching voltage of 3.8 V and an extinction ratio of 28.5 dB. The modulated optical signal was transmitted through an SMF fiber. The EDFA compensates for all optical losses and maintains 0 dBm optical power at the receiver. The EVM of the photodetected signal was measured by a 12 GHz high speed real time oscilloscope DSO91204 from Agilent Technologies. The RF spectrum is also measured with 43 GHz RSA. For OSSB modulation, the 180° HEC is removed and the amplified UWB signal is directly injected to the 90° HEC.

To show the improved performance of the transmitted MB-OFDM-UWB signal over fiber using our proposed technique, we have measured and compared the EVM using OSSB, ODSB and our proposed ODSB modulation in back-to-back and after 20 km of fiber transmission, respectively. The total RF input power at the MZM was varied by changing the attenuation level of the transmitted power from 0 to 15 dB using the built-in WisMan software provided with the DV 9110M module. The maximum transmitted power level from the DV 9110M is ~ 18 dBm and the amplification of the LNA is ~ 27 dB with ~ 1.5 dB loss from RF connections and Bias Tee. This gives a transmitted power level range from ~ -6 to ~ 7.5 dBm.

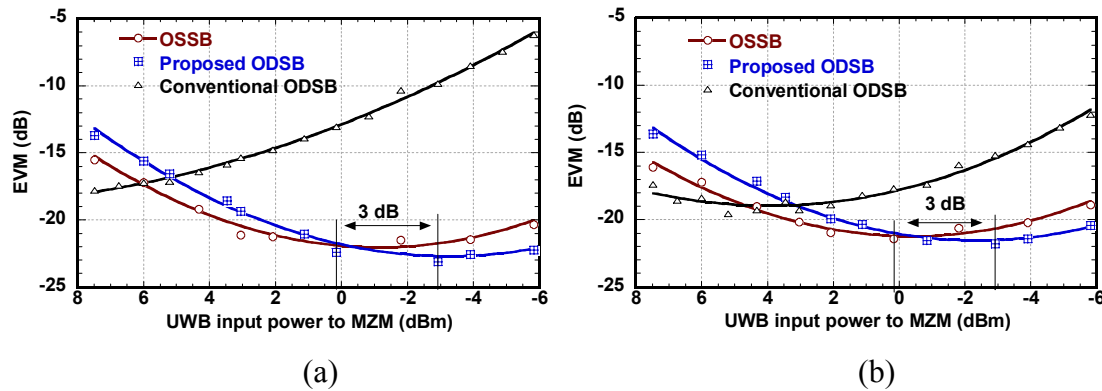


Figure 5.11 Measured EVM versus UWB input power for OSSB, conventional and proposed ODSB for (a) back to back and (b) 20 km of fiber transmission.

Figure 5.11 shows the EVM versus the total input power to the MZM modulator for OSSB, conventional and proposed ODSB in (a) back-to-back and (b) after 20 km of fiber transmission. It is clearly shown that conventional ODSB presents the worst EVM performance due to power fading caused chromatic dispersion effect. The EVM using ODSB is slightly improved with 20 km fiber length because the optical sidebands are not completely out of phase due to fiber dispersion. It can be also seen that our proposed ODSB technique compared to OSSB presents better EVM at low transmitted power level of less than ~ 0 dBm. For back-to-back a minimum EVM of -22.4, -23.1 and -17.8 dB is achieved at 0.16, -2.92 and 7.48 dBm for OSSB, proposed and conventional ODSB, respectively, and the corresponding constellations are shown in inset (i), (ii) and (iii) of Figure 5.12, respectively. While after 20 km of fiber transmission a minimum EVM of -21.4, -21.8 and -19.6 dB is obtained at 0.16, -2.92 and 5.21 dBm, and the corresponding constellations are shown in inset (iv), (v) and (vi) of Figure 5.12, respectively. It can be noticed that our proposed ODSB has ~ 3 dB improvement in power efficiency for optimum input power with slightly better EVM compared to OSSB.

Now, we set the power of transmitted UWB to 0.16 dBm and -2.92 dBm at the input to the MZM for OSSB and conventional/proposed ODSB, respectively, and measure the optical and RF spectrum before and after the photodetection, respectively, for back to back transmission. Figure 5.13 shows no difference in the optical spectrum of the conventional- and proposed- ODSB modulation.

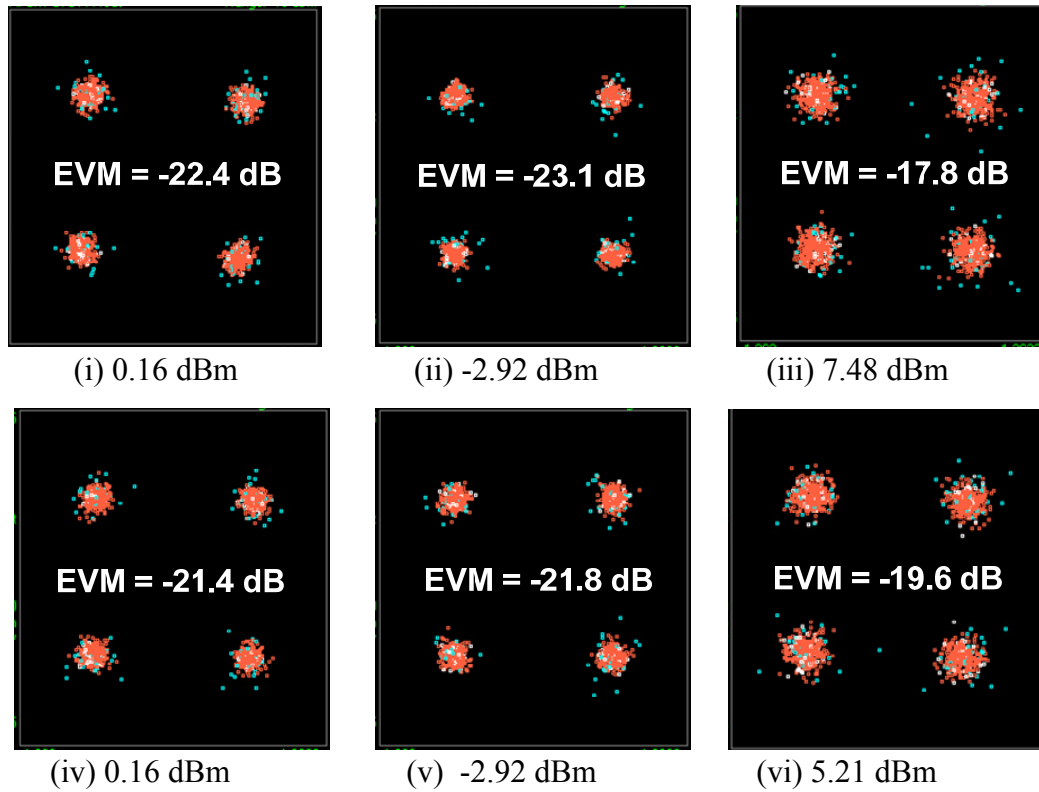


Figure 5.12 Measured constellation with minimum EVM at optimum input UWB power to MZM at back to back (B-T-B) for (i) OSSB, (ii) proposed ODSB and (iii) conventional ODSB, and after 20 km for (iv) OSSB, (v) proposed ODSB and (vi) conventional ODSB.

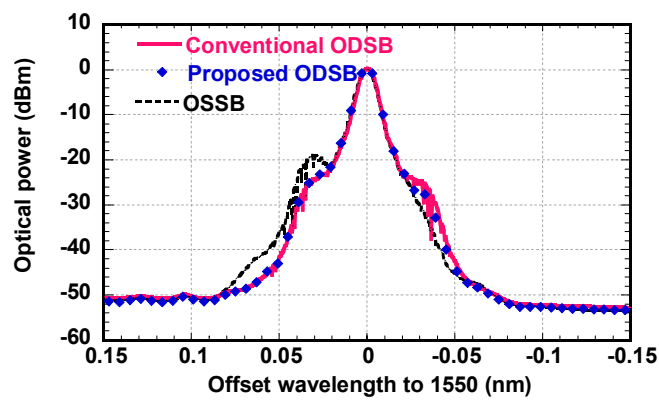


Figure 5.13 Measured optical spectrum using OSSB modulation (dashed line), and the conventional ODSB (solid line) and our proposed ODSB (mark) modulation.

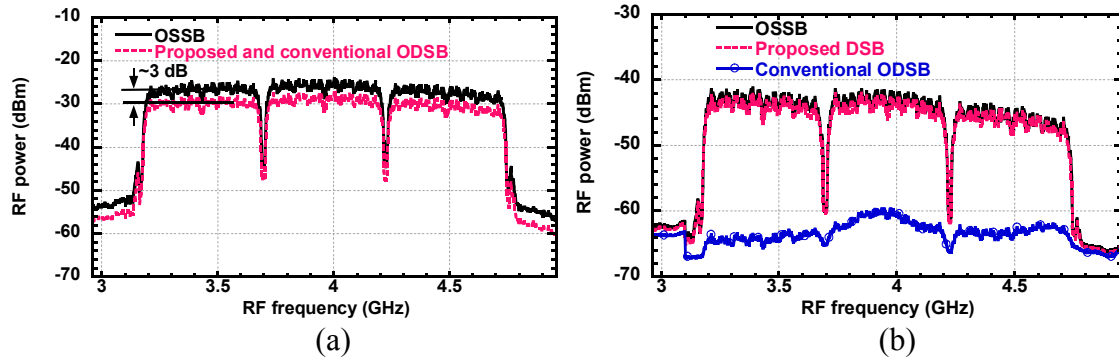


Figure 5.14 RF spectrum of the (a) transmitted and (b) received UWB signal for OSSB, conventional and proposed ODSB for back-to-back transmission.

Figure 5.14 shows measured electrical spectrum of transmitted and received three band UWB signals using the three modulation techniques. The effect of dispersion is apparent only after the photodetection as shown in Figure 5.14(b). Actually an 180° phase difference exists in back-to-back between the two optical subcarrier sidebands with respect to the optical carrier, resulting in maximum fading of the UWB signal after the photodetection in conventional ODSB modulation. However, in our proposed ODSB modulation an additional 180° phase difference is applied to two driving voltages of the DE-MZM to make the two sidebands in-phase, resulting in fully recovered UWB signal. The above results imply that by changing the phase difference between the two driving voltages for a given fiber length we are able to mitigate the fiber chromatic dispersion caused power fading in RoF transmission. Practically by tuning the electrical phase shift, the phase difference due to the chromatic dispersion between the upper and lower sidebands can be removed, resulting in fully recovered RF carrier. Figure 5.14 (a) and (b) also show power efficiency improvement of 3 dB in our proposed ODSB compared to OSSB.

Power efficiency improvement has been also measured for different input power levels as shown in Figure 5.15. It is clearly seen that almost the same received power level in OSSB can be obtained by reducing the transmitted power by 3 dB for using our proposed ODSB. Because EVM is inversely proportional to the square root of the received signal to noise ratio [25], this implies at least the same EVM performance as OSSB can be achieved using our proposed ODSB with 3 dB saving in the transmitted power, which is in good agreement with our theoretical prediction.

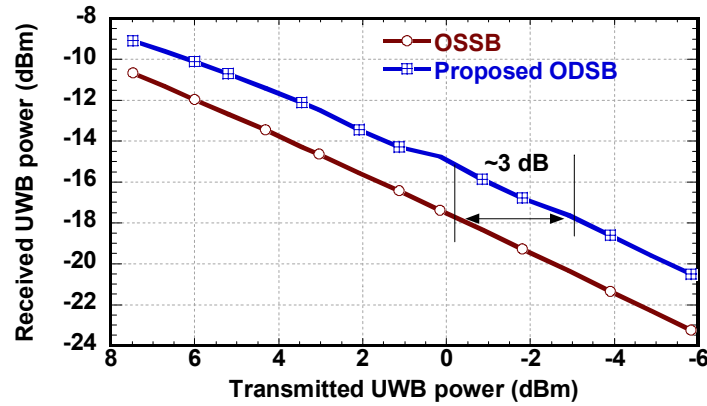


Figure 5.15 Received power versus transmitted power of the UWB MB-OFDM signal for OSSB and proposed ODSB at back to back transmission.

5.6 Chapter Summary

We have proposed a new modulation technique to overcome fiber chromatic dispersion caused power fading when ODSB modulation is used. This modulation technique also improves the RF power by up to 3 dB compared to OSSB modulation. The proposed technique is simple and implemented in electrical domain with phase shifting. Theoretical analysis was made to obtain the optimum conditions for optimum performance, such as optimum phase shift and impact of MZM extinction ratio. Then simulation was used to further analyze the proposed modulation and compared to the theory. Moreover, we present an experimental proof to validate our concept for RF signal consisting of single RF tone or of MB-OFDM UWB signal. By using our proposed modulation technique a 3-dB RF power improvement, compared to OSSB, was achieved experimentally without degradation of the signal quality. The proposed technique can be applied to any frequency band, especially to millimeter-wave band region where RF power resources are very limited.

CHAPTER 6 TUNABLE OPTICAL CARRIER SUPPRESSION SINGLE SIDE BAND TECHNIQUE FOR IMPROVED OPTICAL MODULATION EFFICIENCY OF RF AND MB-OFDM UWB SIGNAL OVER FIBER

6.1 Introduction

For an optical carrier used for distributing an optical subcarrier or sideband signal, it was found experimentally that the optimum optical power ratio of the optical carrier to sideband is 0 dB [18, 63]. One approach to alter the power ratio is to use an optical notch filter for reducing optical carrier power [18]. However carrier filtering needs tuning when the laser or carrier drifts (chirping effect). An optical carrier-suppressed single sideband modulation using a hyperfine blocking filter based on a virtually imaged phased-array has been reported in [19]. In this scheme the blocking filter can be tuned for simultaneous single sideband and strong carrier suppression up to 30 dB below the unsuppressed single sideband. However, this technique suffers from high insertion loss of more than 13 dB and power penalty caused by the blocking filtering effects such as sideband shaping and residual chromatic dispersion. Another technique [20] intentionally used stimulated Brillouin scattering as a carrier filter. An injected power above the SBS threshold into a length of optical fiber is used to reject the carrier while allowing the modulated sidebands to pass with low loss. However the system suffers from signal distortion and instabilities in the transmitted power attributed to the noise in the spontaneous scattering process that initiates SBS [22]. Later, a technique was proposed that a MZM is used and the power ratio can be tuned with the help of bias voltage [21]. However, this technique only enables to obtain ODSB modulation and OSSB modulation cannot be obtained without optical filtering.

In [64] an x-cut Lithium Niobate dual parallel Mach-Zhender modulator (dMZM) has been designed for OSSB modulation with carrier-suppression ratio over 25dB. The dMZM comprises a main MZM with an MZM inserted in each arm. Several applications are possible with this device: generation of optical mm-wave signals using frequency doubling [65], quadrupling [66] and octupling [67], and optical carrier suppressed-optical differential quadrature and phase-shift keying signals in radio over fiber systems [68].

Using the same modulator as in [64-68], this chapter will show that not only OSSB modulation but also tunability of the power ratio of optical carrier to sideband (OCSR) can be obtained

simultaneously. By changing bias voltage, the power ratio of optical carrier to sideband can be tuned continuously. The chapter is organized into five sections. In Section 6.2, the principle and theory of the proposed modulation technique are presented for both single and two RF tones signal. Simulations using commercial software are carried out and compared to theory in Section 6.3 considering tunability of OCSR, RF power and impact of extinction ratio and RF modulation index of the two integrated MZMs. In Section 6.4, the distortion effects are experimentally investigated and the performance improvement of using our proposed modulation technique is demonstrated for MB-OFDM UWB signal transmission over 20 km of single mode fiber. Finally, our conclusions are drawn in Section 6.5.

6.2 Principle and Theory of Tunable Optical Carrier Suppression Single Sideband Modulation Technique

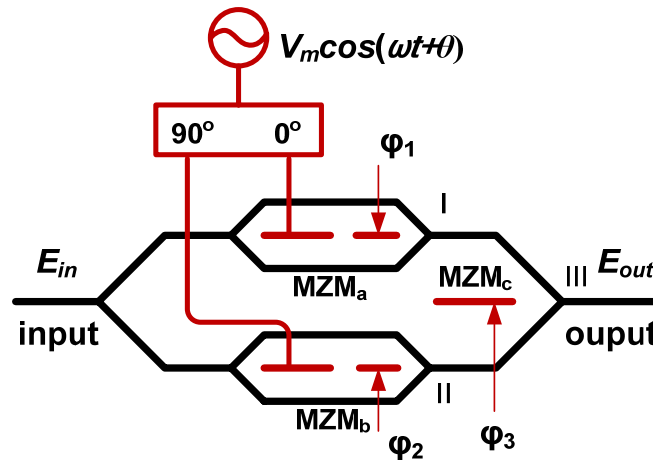


Figure 6.1 Dual parallel MZM used for OSSB modulation with tunability of optical carrier suppression

Figure 6.1 shows the schematic of the dMZM modulator. The dMZM is similar to the one used in [64-68]. As shown in Figure 6.1, the injected light is split into two branches i.e. I and II by a 3-dB optical splitter. In each branch there is a single-electrode MZM, i.e. MZM_a in branch I and MZM_b in branch II. The two MZMs are integrated in another principal MZM_c. Because of the x-cut design, the three MZMs are configured for push pull operation, and each has independent DC bias. It is assumed that the two parallel MZMs are identical.

To obtain OSSB modulation, it is required that the optical phase difference between path-I and path-II be $\pi/2$, and the two RF signals driving MZM_a and MZM_b must have same amplitude but in quadrature phase. Thus MZM_a and MZM_b must have identical bias voltage ($\varphi_1 = \varphi_2 = \varphi$), and the applied bias voltage to MZM_c port must be $\pm V_\pi/4$ ($\varphi_3 = \pm\pi/4$), where V_π is the π -shift voltage assumed to be the same for the three MZMs without loss of generality. The applied bias voltage φ to MZM_a and MZM_b will be controlled to tune the suppression of the optical carrier.

6.2.1 Theoretical Analysis for Single RF Tone

The theory of the mechanics of the modulator is given as follows. Considering one RF signal with $V_m \cos(\omega t + \theta)$, at a frequency of $\omega/2\pi$, phase θ and an amplitude of V_m , driving the modulator, we obtain the output electric field in branch I and II, at the output of MZM_a and MZM_b, respectively,

$$E_I(t) = \sqrt{t_{ff}/2} E_{in} \left\{ a e^{j\varphi_1} \exp[j\pi/\sqrt{2} m \cos(\omega t + \theta)] + r e^{-j\varphi_1} \exp[-j\pi/\sqrt{2} m \cos(\omega t + \theta)] \right\} \quad (6.1)$$

$$E_{II}(t) = \sqrt{t_{ff}/2} E_{in} \left\{ a e^{j\varphi_2} \exp[j\pi/\sqrt{2} m \sin(\omega t + \theta)] + r e^{-j\varphi_2} \exp[-j\pi/\sqrt{2} m \sin(\omega t + \theta)] \right\} \quad (6.2)$$

where t_{ff} represents insertion loss of each parallel MZM, $a = \sqrt{0.5 + \varepsilon}$, $r = \sqrt{1 - a^2}$ with $\varepsilon = \sqrt{ER}/(ER + 1)$ represents the difference in the power split ratio of their Y-junctions and ER is the MZM extinction ratio. E_{in} is amplitude of input electric field. The power splitting and coupling ratios of the Y-junctions of MZM_c are assumed to be 3-dB. The parameter $m = V_m/V_\pi$ defined modulation index (MI), $\varphi_k = \pi V_{kDC}/(2V_\pi)$ and V_{kDC} are the applied bias voltage at each port to each of the MZMs as shown in Figure 6.1.

The output electric field from the dMZM at III is

$$\begin{aligned} E_{III}(t) &= 1/\sqrt{2} [E_I(t) e^{j\varphi_3} + E_{II}(t) e^{-j\varphi_3}] \\ &= \frac{1}{2} \sqrt{t_{ff}} E_{in} \sum_{n=-\infty}^{\infty} a_n J_n(\pi/\sqrt{2} m) \exp[jn(\omega t + \theta)] \end{aligned} \quad (6.3)$$

where

$$a_n = j^n \left[a e^{j\varphi_1} + (-1)^n r e^{-j\varphi_1} \right] e^{j\varphi_3} + \left[a e^{j\varphi_2} + (-1)^n r e^{-j\varphi_2} \right] e^{-j\varphi_3} \quad (6.4)$$

From the above it is clear that lower (upper) single sideband can be obtained by setting $a_1 = 0$ ($a_{-1} = 0$). For that we must have $\varphi_1 = \varphi_2$ and $\varphi_3 = \pi/4$ ($\varphi_3 = -\pi/4$). In the following and the rest of the chapter we will consider upper sideband $\varphi_1 = \varphi_2 = \varphi$, $\varphi_3 = -\pi/4$, and thus equation (6.4) becomes

$$a_n = \left[a e^{j\varphi} + (-1)^n r e^{-j\varphi} \right] \left(j^n e^{-j\pi/4} + e^{j\pi/4} \right) \quad (6.5)$$

Optical carrier to sideband ratio (OCSR) is defined by the optical power ratio of the optical carrier P_0 to that of the optical sub-carrier or sideband P_ω . From equations (6.3) and (6.5), the OCSR can be expressed by

$$\begin{aligned} OCSR &= \frac{|a_0|^2 J_0^2(\pi/\sqrt{2} m)}{|a_1|^2 J_1^2(\pi/\sqrt{2} m)} \\ &= \frac{1}{2} \frac{1 + \sqrt{1 - (2\varepsilon)^2} \cos 2\varphi}{1 - \sqrt{1 - (2\varepsilon)^2} \cos 2\varphi} \frac{J_0^2(\pi/\sqrt{2} m)}{J_1^2(\pi/\sqrt{2} m)} \\ &= \frac{1}{2} \frac{ER + 1 + (ER - 1) \cos 2\varphi}{ER + 1 - (ER - 1) \cos 2\varphi} \frac{J_0^2(\pi/\sqrt{2} m)}{J_1^2(\pi/\sqrt{2} m)} \end{aligned} \quad (6.6)$$

Considering only optical components up to third order harmonic, the optical power ratio of second harmonic to the carrier $2P_{2\omega}/P_0$ and third harmonic to the fundamental $P_{-3\omega}/P_\omega$, can be expressed respectively, by

$$\frac{2P_{2\omega}}{P_0} = \frac{2J_2^2(\pi/\sqrt{2} m)}{J_0^2(\pi/\sqrt{2} m)} \quad (6.7)$$

$$\frac{P_{-3\omega}}{P_\omega} = \frac{J_3^2(\pi/\sqrt{2} m)}{J_1^2(\pi/\sqrt{2} m)} \quad (6.8)$$

and are plotted versus modulation index m on Figure 6.2. As shown in Figure 6.2 for a modulation index less than 52% the optical carrier and subcarrier are more than 10 and 24 dBc higher in optical power than optical components at $\pm 2\omega$ and -3ω , respectively.

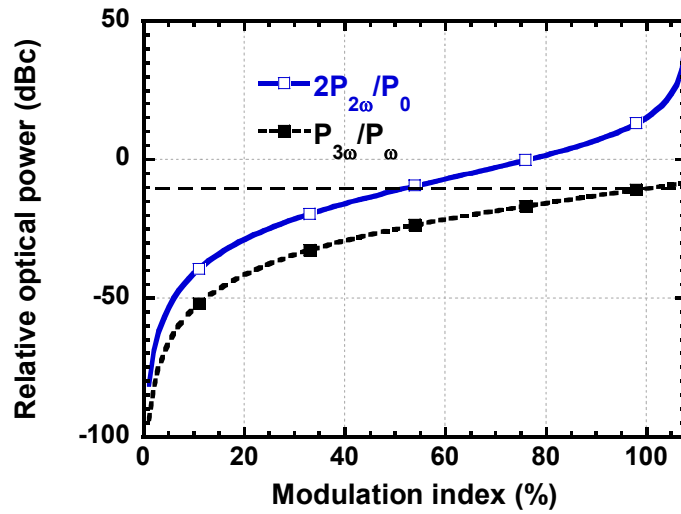


Figure 6.2 Optical power ratio of second harmonic to the carrier $2P_{2\omega}/P_0$ and third harmonic to the fundamental $P_{3\omega}/P_{\omega}$.

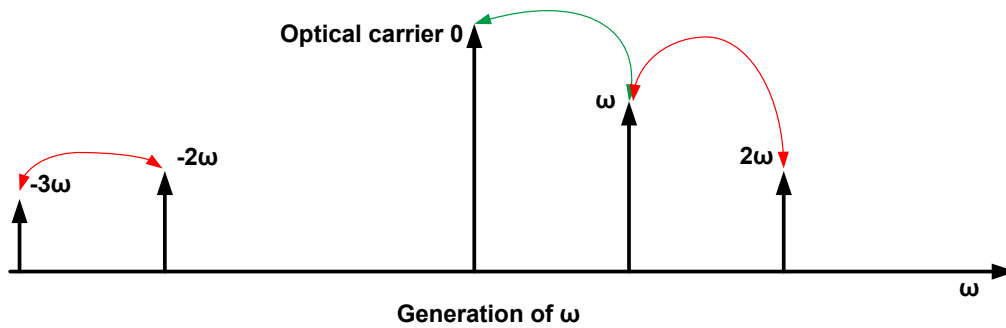


Figure 6.3 Optical spectrum at the output of the dMZM showing the generation of the RF signal from the contribution of different optical components.

Because of the beating of these optical components at the photodetector, there will be some distortion induced into the RF output signal at ω . For example the optical component at 2ω and -2ω will beat with that at ω and -3ω , respectively, to generate an RF component at ω as shown in Figure 6.3. The RF power ratio of the resulting distortion term to that of the RF output signal can be expressed by

$$\begin{aligned}
\frac{P_{dis}}{P_{RF}} &= \frac{|E_{2\omega}E_{\omega}^* + E_{-2\omega}E_{-3\omega}^*|^2}{|E_{\omega}E_0^*|^2} \\
&= \frac{|a_2a_1^*J_2(\pi/\sqrt{2}m)J_1(\pi/\sqrt{2}m) - a_{-2}a_{-3}^*J_2(\pi/\sqrt{2}m)J_3(\pi/\sqrt{2}m)|^2}{|a_1a_0^*J_1(\pi/\sqrt{2}m)J_0(\pi/\sqrt{2}m)|^2} \quad (6.9) \\
&= \frac{J_2^2(\pi/\sqrt{2}m)}{J_0^2(\pi/\sqrt{2}m)} \left[1 - \frac{J_3(\pi/\sqrt{2}m)}{J_1(\pi/\sqrt{2}m)} \right]^2
\end{aligned}$$

Figure 6.4 shows that distortion power level relative to the RF carrier versus modulation index. It is clear that the in-band distortion level is suppressed by more than 14 dB if the modulation index is kept below 52%.

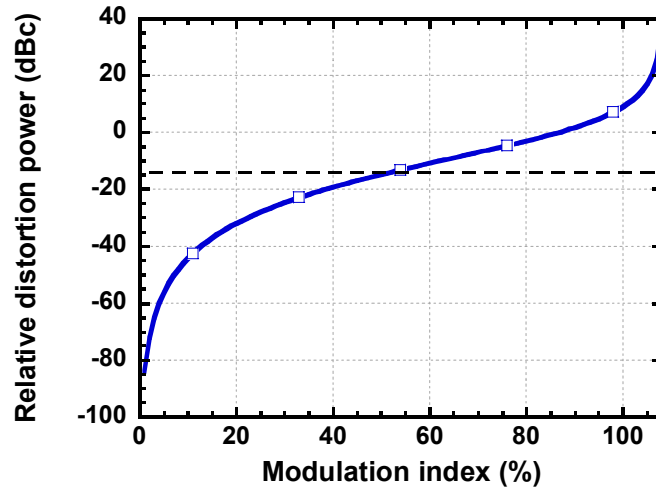


Figure 6.4 Distortion power level relative to the RF output carrier versus modulation index.

In the following we assume the modulation index is less than 52% then we can ignore the optical power from all high-order harmonics and IMD. The total output optical power from the modulator can be written $P_{out} = P_0 + P_{\omega}$, and then $P_{out} = (1 + OCSR)P_{\omega}$. When the light with al field given by equation (6.3) is injected to a photodetector with responsivity of \mathfrak{R} , the detected RF power at ω can be given by

$$\begin{aligned}
P_{RF} &= \frac{1}{2} \Re^2 \left| E_0 E_{\omega_1} \right|^2 \\
&= 2 \Re^2 P_0 P_{\omega} \\
&= 2 \Re^2 P_{out}^2 \frac{OCSR}{(OCSR+1)^2}
\end{aligned} \tag{6.10}$$

Figure 6.5 shows the relative RF power versus OCSR and that maximum RF power can be obtained when the OCSR=1.

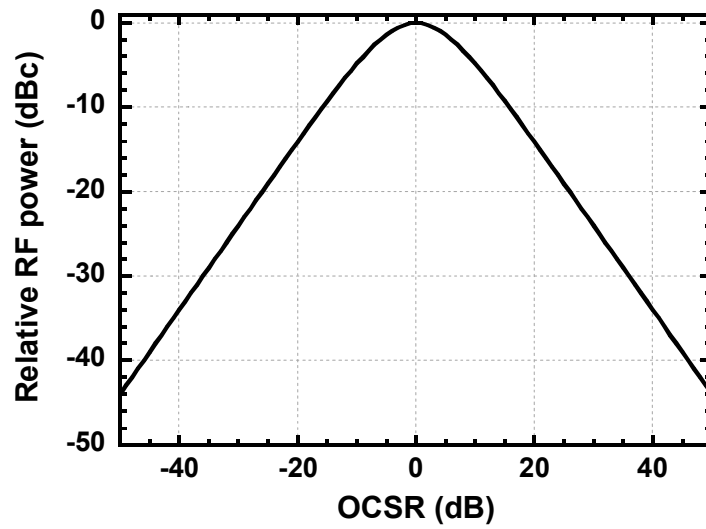


Figure 6.5 Relative RF power versus OCSR for constant received optical power.

It is clear from equation (6.6) that by tuning the phase shift φ the OCSR will swing between maximum and minimum values given, respectively, by

$$OCSR_{\max} = \frac{1}{2} ER J_0^2 \left(\pi / \sqrt{2} m \right) / J_1^2 \left(\pi / \sqrt{2} m \right) \tag{6.11}$$

$$OCSR_{\min} = \frac{1}{2} ER^{-1} J_0^2 \left(\pi / \sqrt{2} m \right) / J_1^2 \left(\pi / \sqrt{2} m \right) \tag{6.12}$$

Then tunability range of OCSR is ER^2 ($= OCSR_{\max} / OCSR_{\min}$) and the maximum achievable P_{RF} will depend on the extinction ratio and modulation index, and three cases can arise.

Case 1: if $OCSR_{\min} \leq 1 \leq OCSR_{\max}$, i.e

$$1/ER \leq J_0^2(\pi/\sqrt{2}m) / \left[2J_1^2(\pi/\sqrt{2}m) \right] \leq ER \quad (6.13)$$

then maximum P_{RF} is obtained at $OCSR = 1$ by tuning the phase shift to an optimum value directly expressed from (6.6) by

$$\varphi = \pm \frac{1}{2} \arccos \left[\frac{ER+1}{ER-1} \frac{1 - \frac{1}{2} J_0^2(\pi/\sqrt{2}m) / J_1^2(\pi/\sqrt{2}m)}{1 + \frac{1}{2} J_0^2(\pi/\sqrt{2}m) / J_1^2(\pi/\sqrt{2}m)} \right] \quad (6.14)$$

and the RF power is expressed by

$$P_{RF} = \frac{1}{2} \Re^2 P_{out}^2 \quad (6.15)$$

Case 2: if $OCSR_{\min} > 1$, i.e

$$ER < J_0^2(\pi/\sqrt{2}m) / \left[2J_1^2(\pi/\sqrt{2}m) \right] \quad (6.16)$$

then maximum P_{RF} is obtained at $OCSR = OCSR_{\min}$ by tuning the phase shift to $\pm\pi/2$, and the RF power is expressed by

$$\begin{aligned} P_{RF} &= 2\Re^2 P_{out}^2 \frac{OCSR_{\min}}{(1 + OCSR_{\min})^2} \\ &= 2\Re^2 P_{out}^2 ER \frac{J_0^2(\pi/\sqrt{2}m) J_1^2(\pi/\sqrt{2}m)}{\left[J_0^2(\pi/\sqrt{2}m) + 2ER J_1^2(\pi/\sqrt{2}m) \right]^2} \end{aligned} \quad (6.17)$$

Case 3: if $OCSR_{\max} < 1$, i.e

$$J_0^2(\pi/\sqrt{2}m) / \left[2J_1^2(\pi/\sqrt{2}m) \right] < 1/ER \quad (6.18)$$

then maximum P_{RF} is obtained at $OCSR = OCSR_{\max}$ by tuning the phase shift to 0, and the RF power is expressed by

$$\begin{aligned}
P_{RF} &= 2\Re^2 P_{out}^2 \frac{OCSR_{\max}}{(1 + OCSR_{\max})^2} \\
&= 4\Re^2 P_{out}^2 ER \frac{J_0^2(\pi/\sqrt{2}m) J_1^2(\pi/\sqrt{2}m)}{\left[2J_1^2(\pi/\sqrt{2}m) + ER J_0^2(\pi/\sqrt{2}m)\right]^2}
\end{aligned} \tag{6.19}$$

Figure 6.6 shows optimum OCSR and corresponding phase shift versus modulation index for different extinction ratio (ER): 15, 20, 28.5 and 35 dB. It is clear that higher extinction ratio allows to achieve an OCSR=1 for maximum RF power at lower modulation index. For example OCSR=1 is achieved at modulation index of 11, 7, 3 and 2% for an ER of 15, 20, 28.5 and 35 dB, respectively. Also for high extinction ratios of greater than 20 dB the required optimum phase bias is almost independent on ER and varies linearly with the modulation index. This is because at high extinction ratio $ER \gg 1$ the optimal phase shift expressed by equation (6.14) reduces to

$$\varphi \sim \pi/2 - \arctan \left[\sqrt{2} J_1(\pi/\sqrt{2}m) / J_0(\pi/\sqrt{2}m) \right] \tag{6.20}$$

and is almost linear with the modulation index as shown from the plot of Figure 6.7.

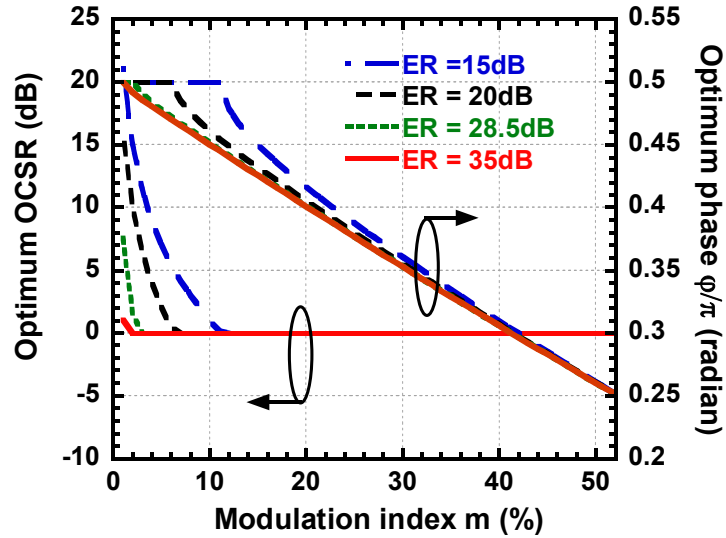


Figure 6.6 Optimum OCSR and corresponding phase shift versus modulation index for different extinction ratio (ER): 15, 20, 28.5 and 35 dB.

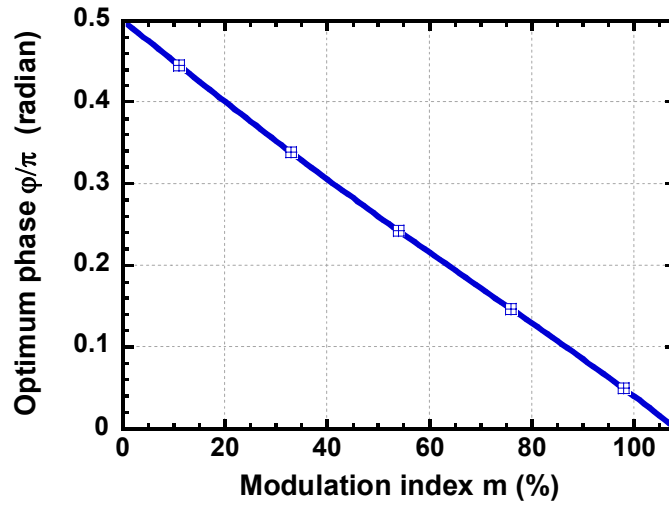


Figure 6.7 Approximated phase shift versus modulation index for high extinction ratio.

Figure 6.8 shows the impact of extinction ratio on the optimum OCSR at different modulation index. It can be seen that by increasing the modulation index or extinction ratio the optimum OCSR decreases up to an OCSR = 1. To achieve an optimum OCSR = 1 the minimum required ER is 37, 23, 17, 11 and 10 for modulation index of 1, 5, 10, 19 and 20%, respectively. For modulation index less than 52%, the minimum required extinction ratio to achieve an OCSR = 1, is given by (see equation (6.13))

$$ER_{\min} = J_0^2 \left(\pi / \sqrt{2} m \right) / \left[2J_1^2 \left(\pi / \sqrt{2} m \right) \right] \quad (6.21)$$

and it decreases with the increase of the modulation index as shown in Figure 6.9.

Optimum phase shift versus extinction ratio is depicted in Figure 6.10 for different modulation index. It is shown that the optimum phase shift is almost independent on extinction ratios of greater than 20 dB. For modulation index of 1, 5, 10, 19, 30, 40 and 50%, the optimum phase shift ϕ is $\sim 0.5\pi$, 0.48π , 0.45π , 0.4π , 0.35π , 0.3π and 0.26π , respectively. This is also confirmed by equation (6.21) and Figure 6.7. It is then advantageous to have very high extinction ratio to improve both the efficiency and linearity of the modulator.

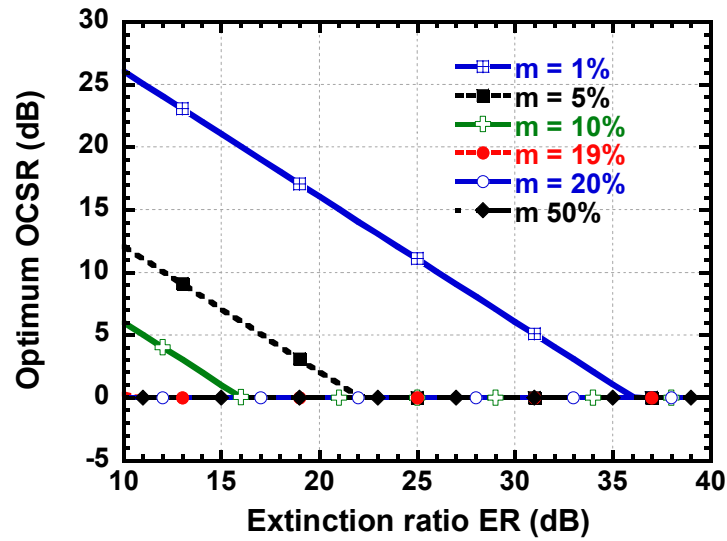


Figure 6.8 Optimum OCSR versus extinction ratio (ER) for different modulation index: 1, 5, 10, 19, 20 and 50%.

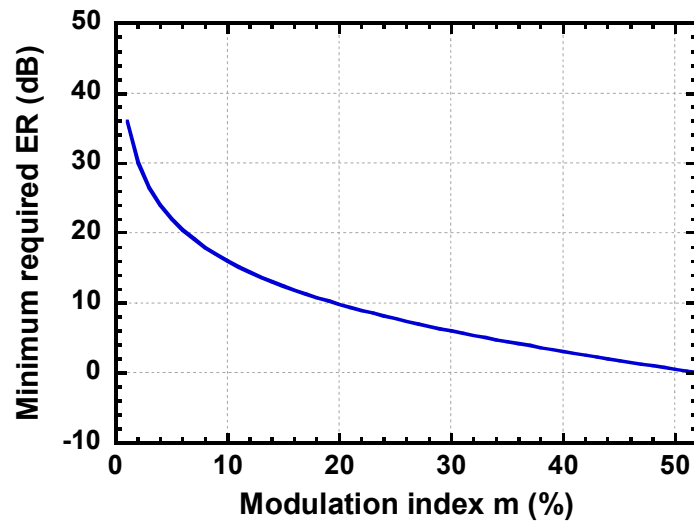


Figure 6.9 Minimum required ER to achieve an OCSR=1 versus modulation index.

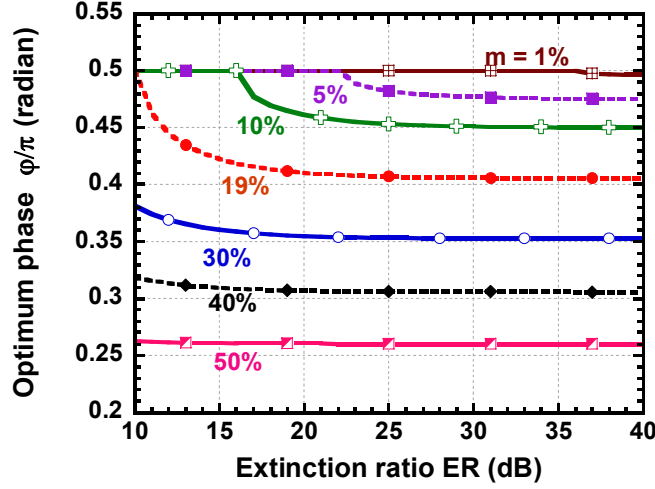


Figure 6.10 Optimum phase shift versus extinction ratio (ER) for different modulation index: 1, 5, 10, 19, 30, 40 and 50%.

6.2.2 Theoretical Analysis for Two RF Tones

In this section, we investigate the situation in which one optical carrier carries two sub-carriers. Considering two RF signals: $V_m \cos(\omega_1 t + \theta_1)$ and $V_m \cos(\omega_2 t + \theta_2)$ with frequencies of $\omega_1/2\pi$ and $\omega_2/2\pi$, arbitrary phase θ_1 and θ_2 , and amplitude of V_m driving the modulator, after mathematical manipulations, we obtain the output electric field from the dMZM modulator at III in Figure 6.1,

$$E_{III}(t) = \frac{1}{2} \sqrt{t_{ff}} E_{in} \sum_{n_1, n_2 = -\infty}^{\infty} a_{n_1 + n_2} J_{n_1} \left(\frac{\pi}{\sqrt{2}} m \right) J_{n_2} \left(\frac{\pi}{\sqrt{2}} m \right) \times \exp \left\{ j \left[(n_1 \omega_1 + n_2 \omega_2) t + n_1 \theta_1 + n_2 \theta_2 \right] \right\} \quad (6.22)$$

where a_n is given by equation (6.5) and other parameters are defined above. Here also the OCSR can be expressed by equation (6.6).

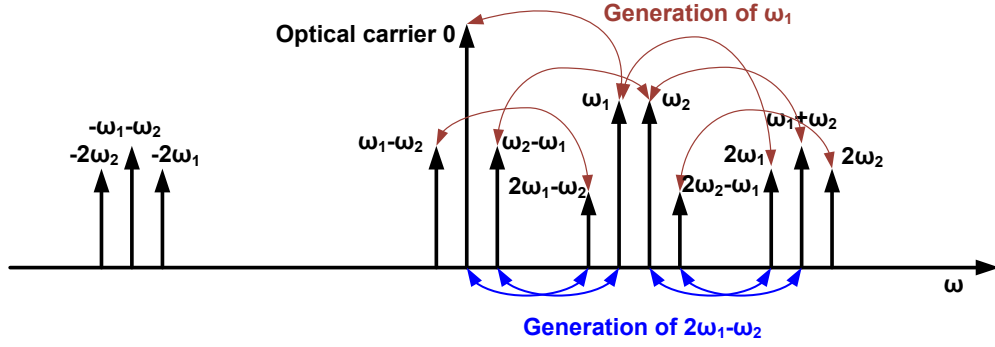


Figure 6.11 Optical spectrum showing the generation of the RF component at ω_1 and 3IMD at $2\omega_1 - \omega_2$ after beating at the photodetector.

We consider only optical components up to 3IMDs and second order harmonics as shown in Figure 6.11. Note that the optical components at $\omega_2 - 2\omega_1$ and $\omega_1 - 2\omega_2$ are also eliminated with subcarriers at $-\omega_1$ and $-\omega_2$. This will improve the linearity of the dMZM by at least 3dB compared to OSSB using DE-MZM. The optical power ratio of the optical components at second harmonics ($\pm 2\omega_1, \pm 2\omega_2$) and 2nd IMDs frequencies ($\pm(\omega_1 + \omega_2), \pm(\omega_1 - \omega_2)$) to the optical carrier, and of the optical component at 3rd IMDs frequencies ($2\omega_1 - \omega_2, 2\omega_2 - \omega_1$) to the optical subcarriers at fundamental frequencies (ω_1, ω_2) can be expressed respectively, by

$$\frac{1}{P_0} \left(P_{2\omega_1} + P_{2\omega_2} + P_{-2\omega_1} + P_{-2\omega_2} + P_{\omega_1 - \omega_2} + P_{\omega_2 - \omega_1} + P_{\omega_1 + \omega_2} + P_{-\omega_1 - \omega_2} \right) = \frac{4}{P_0} (P_{2\omega_1} + P_{\omega_1 + \omega_2})$$

$$= \left[\frac{2J_2(\pi/\sqrt{2}m)}{J_0(\pi/\sqrt{2}m)} \right]^2 + \left[\frac{\sqrt{2}J_1(\pi/\sqrt{2}m)}{J_0(\pi/\sqrt{2}m)} \right]^4 \quad (6.23)$$

$$\frac{P_{2\omega_1 - \omega_2} + P_{2\omega_2 - \omega_1}}{P_{\omega_1} + P_{\omega_2}} = \frac{P_{2\omega_1 - \omega_2}}{P_{\omega_1}}$$

$$= \left[\frac{J_2(\pi/\sqrt{2}m)}{J_0(\pi/\sqrt{2}m)} \right]^2 \quad (6.24)$$

and are plotted versus modulation index m on Figure 6.12. As shown in Figure 6.12, for a

modulation index less than 31% , the optical power of the carrier is more than $\sim 10\text{dB}$ higher than the sum of optical power of components at $\pm 2\omega_1, \pm 2\omega_2$ and $\pm(\omega_1 + \omega_2)$, whereas the optical power of the fundamental is more than $\sim 24\text{dB}$ higher than the total optical power of components at $2\omega_1 - \omega_2$ and $2\omega_2 - \omega_1$.

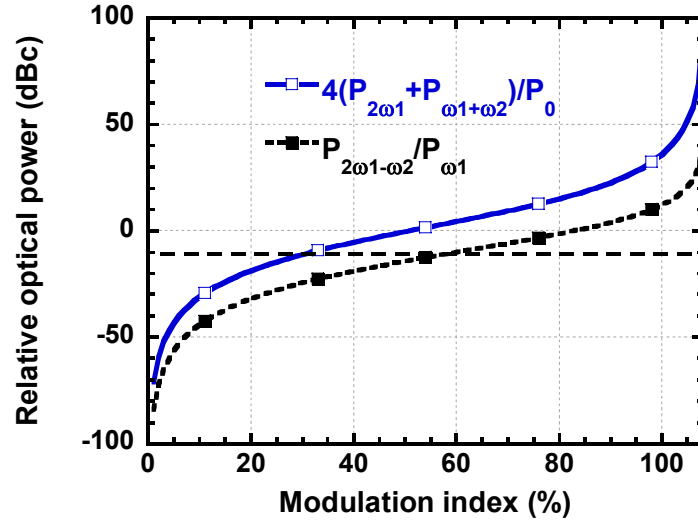


Figure 6.12 Optical power ratio of optical components at second harmonics and 2nd IMDs frequencies to the optical carrier ($4(P_{2\omega_1} + P_{\omega_2 - \omega_1})/P_0$), and the optical components at 3rd IMD to the optical subcarriers at fundamental frequencies ($P_{2\omega_1 - \omega_2}/P_{\omega_1}$) versus modulation index.

In addition, the beating of these optical components at the photodetector will generate in-band distortion induced into the RF output signal at ω_1 . For example, as shown in Figure 6.11, the optical components at ω_1 , $\omega_2 - \omega_1$, $\omega_1 - \omega_2$, ω_2 and $2\omega_2$ will beat with those at $2\omega_1$, ω_2 , $2\omega_1 - \omega_2$, $\omega_1 + \omega_2$, and $2\omega_2 - \omega_1$, respectively, to generate an RF component at ω_1 . The RF power ratio of the resulting distortion term to that of the RF output signal can be expressed by

$$\frac{P_{dis}}{P_{RF}} = \frac{|E_{2\omega_1} E_{\omega_1}^* + E_{\omega_2} E_{\omega_2 - \omega_1}^* + E_{2\omega_1 - \omega_2} E_{\omega_1 - \omega_2}^* + E_{\omega_1 + \omega_2} E_{\omega_2}^* + E_{2\omega_2} E_{2\omega_2 - \omega_1}^*|^2}{|E_{\omega_1} E_0^*|^2} \quad (6.25)$$

$$\begin{aligned}
& \left| \frac{a_2 a_1^*}{a_1 a_0^*} \left[\left(\frac{J_1(\pi/\sqrt{2}m)}{J_0(\pi/\sqrt{2}m)} \right)^2 - \left(\frac{J_2(\pi/\sqrt{2}m)}{J_0(\pi/\sqrt{2}m)} \right)^2 + \frac{J_2(\pi/\sqrt{2}m)}{J_0(\pi/\sqrt{2}m)} \right] \right|^2 \\
&= \left| - \left(\frac{J_1(\pi/\sqrt{2}m)}{J_0(\pi/\sqrt{2}m)} \right)^2 \left[1 - \frac{J_2(\pi/\sqrt{2}m)}{J_0(\pi/\sqrt{2}m)} \right] \right|^2 \\
&= \left| \frac{2\sqrt{ER} - j(ER-1)\sin 2\varphi}{2\sqrt{ER} + j(ER-1)\sin 2\varphi} \left[\left(\frac{J_1(\pi/\sqrt{2}m)}{J_0(\pi/\sqrt{2}m)} \right)^2 - \left(\frac{J_2(\pi/\sqrt{2}m)}{J_0(\pi/\sqrt{2}m)} \right)^2 + \frac{J_2(\pi/\sqrt{2}m)}{J_0(\pi/\sqrt{2}m)} \right] \right|^2 \\
&= \left| - \left(\frac{J_1(\pi/\sqrt{2}m)}{J_0(\pi/\sqrt{2}m)} \right)^2 \left[1 - \frac{J_2(\pi/\sqrt{2}m)}{J_0(\pi/\sqrt{2}m)} \right] \right|^2
\end{aligned}$$

The above expression will vary between upper and lower limits as

$$\begin{aligned}
& \left| \left(\frac{J_1(\pi/\sqrt{2}m)}{J_0(\pi/\sqrt{2}m)} \right)^2 - \left(\frac{J_2(\pi/\sqrt{2}m)}{J_0(\pi/\sqrt{2}m)} \right)^2 + \frac{J_2(\pi/\sqrt{2}m)}{J_0(\pi/\sqrt{2}m)} \right| \leq \frac{P_{dis}}{P_{RF}} \\
& \left| - \left(\frac{J_1(\pi/\sqrt{2}m)}{J_0(\pi/\sqrt{2}m)} \right)^2 \left[1 - \frac{J_2(\pi/\sqrt{2}m)}{J_0(\pi/\sqrt{2}m)} \right] \right| \\
& \leq \left| \left(\frac{J_1(\pi/\sqrt{2}m)}{J_0(\pi/\sqrt{2}m)} \right)^2 - \left(\frac{J_2(\pi/\sqrt{2}m)}{J_0(\pi/\sqrt{2}m)} \right)^2 + \frac{J_2(\pi/\sqrt{2}m)}{J_0(\pi/\sqrt{2}m)} \right|^2 \\
& \left| + \left(\frac{J_1(\pi/\sqrt{2}m)}{J_0(\pi/\sqrt{2}m)} \right)^2 \left[1 - \frac{J_2(\pi/\sqrt{2}m)}{J_0(\pi/\sqrt{2}m)} \right] \right|^2
\end{aligned} \tag{6.26}$$

Figure 6.13 shows the lower and upper bound of P_{dis}/P_{RF} using equation (6.26) versus modulation index. It is clear that for modulation index less than 31%, the power of the fundamental RF is at least 10 dB greater than that of the in band distortion.

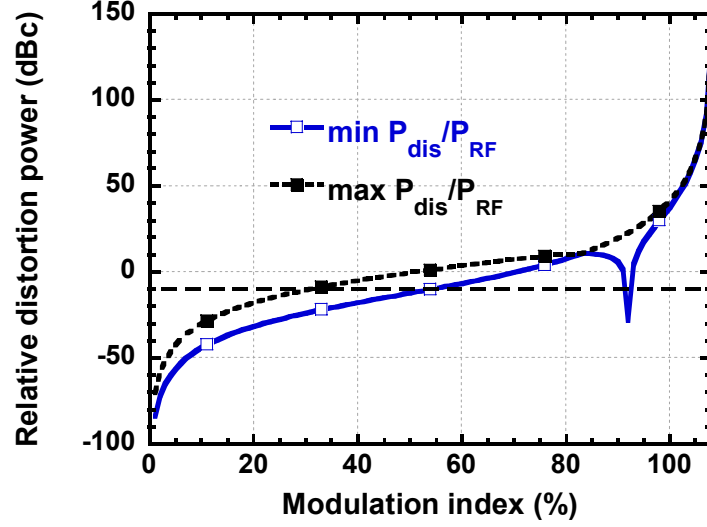


Figure 6.13 Power level of in-band distortion relative to the RF output power in the carrier versus modulation index.

In the following, we assume that the modulation index is less than 31%, therefore we can neglect the optical power from all optical components at high-order harmonic and IMD frequencies compared to the optical carrier and optical subcarriers at fundamental frequencies, respectively. The total output optical power from the modulator can be written $P_{out} = P_0 + 2P_{\omega_1}$, and then $P_{out} = (2 + OCSR)P_{\omega_1}$. When the light with optical field expressed by equation (6.22) is injected to a photodetector with responsivity of \mathfrak{R} , the detected RF power at ω_1 can be given by

$$\begin{aligned}
 P_{RF} &= \frac{1}{2} \mathfrak{R}^2 |E_0 E_{\omega_1}|^2 \\
 &= 2 \mathfrak{R}^2 P_0 P_{\omega_1} \\
 &= 2 \mathfrak{R}^2 P_{out}^2 \frac{OCSR}{(OCSR + 2)^2}
 \end{aligned} \tag{6.27}$$

Figure 6.14 shows the relative RF power versus OCSR and that maximum RF power can be obtained when the OCSR=2.

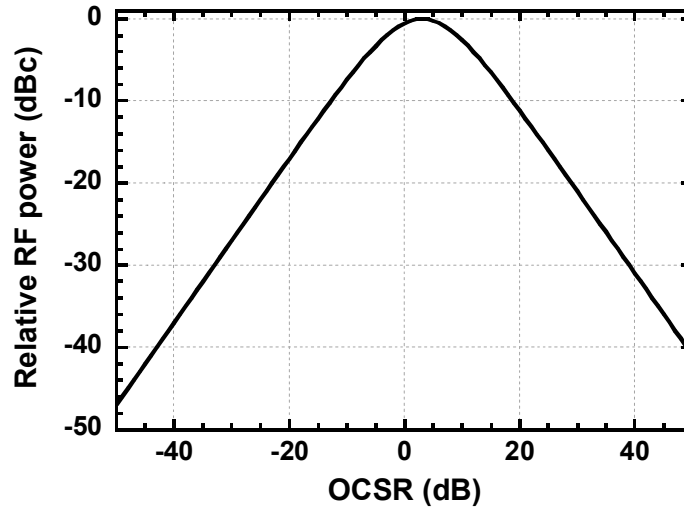


Figure 6.14 Relative RF power versus OCSR for constant received optical power.

As stated before by tuning the phase shift ϕ the OCSR will swing between maximum and minimum values given, respectively, by equation (6.11) and (6.12). Thus here also the maximum achievable P_{RF} will depend on the extinction ratio and modulation index, and three cases arise.

Case 1: if $OCSR_{\min} \leq 2 \leq OCSR_{\max}$, i.e

$$1/ER \leq J_0^2\left(\pi/\sqrt{2}m\right)/\left[4J_1^2\left(\pi/\sqrt{2}m\right)\right] \leq ER \quad (6.28)$$

then maximum P_{RF} is obtained at $OCSR = 2$ by tuning the phase shift to an optimum value directly expressed from equation (6.6) by

$$\phi = \pm \frac{1}{2} \arccos \left[\frac{ER+1}{ER-1} \frac{1 - \frac{1}{4} J_0^2\left(\pi/\sqrt{2}m\right)/J_1^2\left(\pi/\sqrt{2}m\right)}{1 + \frac{1}{4} J_0^2\left(\pi/\sqrt{2}m\right)/J_1^2\left(\pi/\sqrt{2}m\right)} \right] \quad (6.29)$$

and the RF power is expressed by

$$P_{RF} = \frac{1}{4} \Re^2 P_{out}^2 \quad (6.30)$$

Case 2: if $OCSR_{\min} > 2$, i.e

$$ER < J_0^2(\pi/\sqrt{2}m) / \left[4J_1^2(\pi/\sqrt{2}m) \right] \quad (6.31)$$

then maximum P_{RF} is obtained at $OCSR = OCSR_{\min}$ by tuning the phase shift to $\pm\pi/2$, and the RF power is expressed by

$$\begin{aligned} P_{RF} &= 2\Re^2 P_{out}^2 \frac{OCSR_{\min}}{(2 + OCSR_{\min})^2} \\ &= 4\Re^2 P_{out}^2 ER \frac{J_0^2(\pi/\sqrt{2}m) J_1^2(\pi/\sqrt{2}m)}{\left[J_0^2(\pi/\sqrt{2}m) + 4ERJ_1^2(\pi/\sqrt{2}m) \right]^2} \end{aligned} \quad (6.32)$$

Case 3: if $OCSR_{\max} < 2$, i.e

$$J_0^2(\pi/\sqrt{2}m) / \left[4J_1^2(\pi/\sqrt{2}m) \right] < 1/ER \quad (6.33)$$

then maximum P_{RF} is obtained at $OCSR = OCSR_{\max}$ by tuning the phase shift to 0, and the RF power is expressed by

$$\begin{aligned} P_{RF} &= 2\Re^2 P_{out}^2 \frac{OCSR_{\max}}{(2 + OCSR_{\max})^2} \\ &= 4\Re^2 P_{out}^2 ER \frac{J_0^2(\pi/\sqrt{2}m) J_1^2(\pi/\sqrt{2}m)}{\left[4J_1^2(\pi/\sqrt{2}m) + ERJ_0^2(\pi/\sqrt{2}m) \right]^2} \end{aligned} \quad (6.34)$$

Figure 6.15 shows optimum OCSR and corresponding phase shift versus modulation index for different extinction ratio (ER): 15, 20, 28.5 and 35 dB. It is clear that higher extinction ratio allows to achieve an $OCSR=2$ for maximum RF power at lower modulation index. For example $OCSR=2$ is achieved at modulation index of 8, 5, 2 and 1% for an ER of 15, 20, 28.5 and 35 dB, respectively. Also for high extinction ratios of greater than 20 dB the required optimum phase bias is almost independent on ER and varies linearly with the modulation index. This is because

at high extinction ratio $ER \gg 1$ the optimal phase shift given by equation (6.29) reduces to

$$\varphi \sim \pi/2 - \arctan \left[2J_1 \left(\pi/\sqrt{2} m \right) / J_0 \left(\pi/\sqrt{2} m \right) \right] \quad (6.35)$$

and is almost linear with the modulation index as shown from the plot of Figure 6.16.

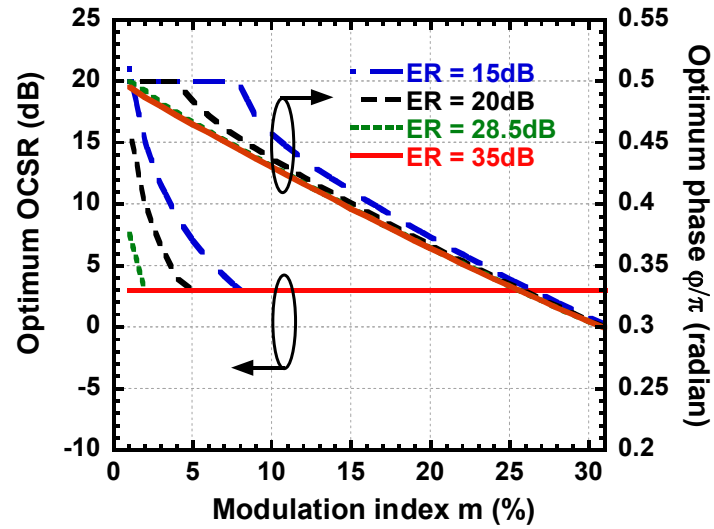


Figure 6.15 Optimum OCSR and corresponding phase shift versus modulation index for different extinction ratio (ER): 15, 20, 28.5 and 35 dB.

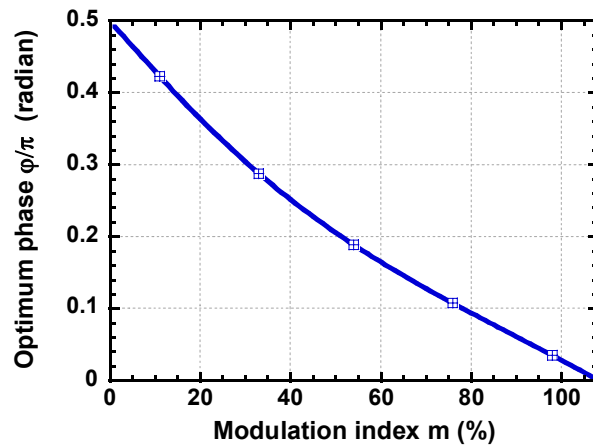


Figure 6.16 Approximated phase shift versus modulation index for high extinction ratio in two tone case.

Figure 6.17 shows the impact of extinction ratio on the optimum OCSR at different modulation index. It can be seen that by increasing the modulation index or extinction ratio the optimum OCSR decreases up to an OCSR = 2. To achieve an optimum OCSR = 2 the minimum required ER is 34, 28, 20, 15, 14, 11 and 10 for modulation index of 1, 2, 5, 8, 10, 14 and 15%, respectively. For modulation index less than 31%, the minimum required extinction ratio to achieve an OCSR = 2, is given by (see equation (6.28))

$$ER_{\min} = J_0^2\left(\pi/\sqrt{2}m\right)/\left[4J_1^2\left(\pi/\sqrt{2}m\right)\right] \quad (6.36)$$

and it decreases with the increase of the modulation index as shown in Figure 6.18.

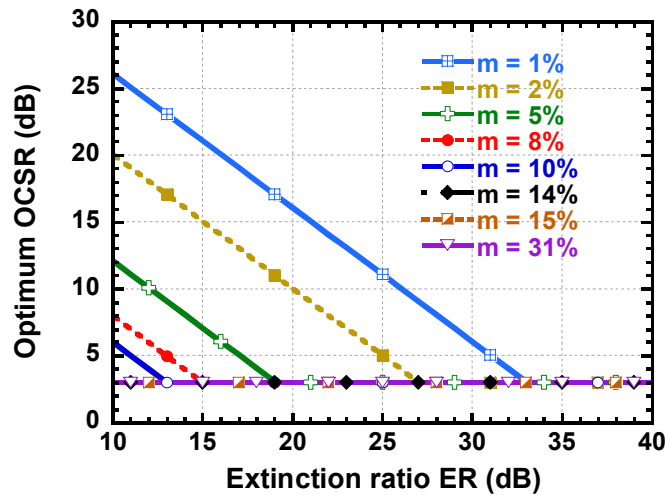


Figure 6.17 Optimum OCSR versus extinction ratio (ER) for different modulation index: 1, 2, 5, 8, 10, 14, 15 and 31%.

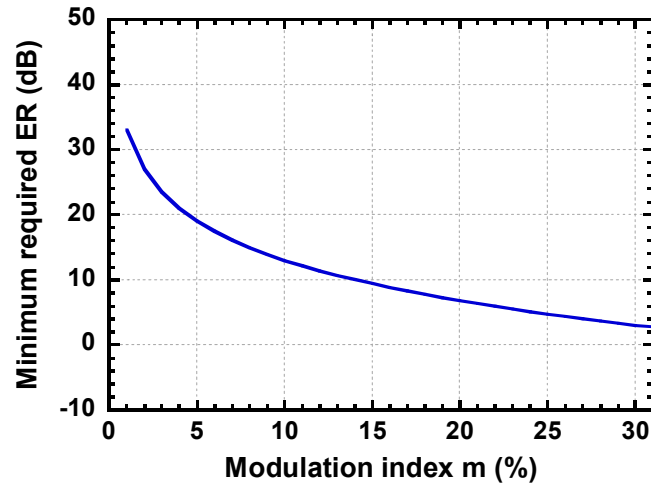


Figure 6.18 Minimum required ER to achieve an OCSR=2 versus modulation index.

Optimum phase shift versus extinction ratio is depicted in Figure 6.19 for different modulation index. It is shown that the optimum phase shift is almost independent on extinction ratios of greater than 23 dB. For modulation index of 1, 2, 5, 8, 10, 14, 15 and 31%, the optimum phase shift ϕ is $\sim 0.5\pi$, 0.5π , 0.46π , 0.45π , 0.43π , 0.4π , 0.4π and 0.3π , respectively. This is also confirmed by equation (6.35) and Figure 6.16.

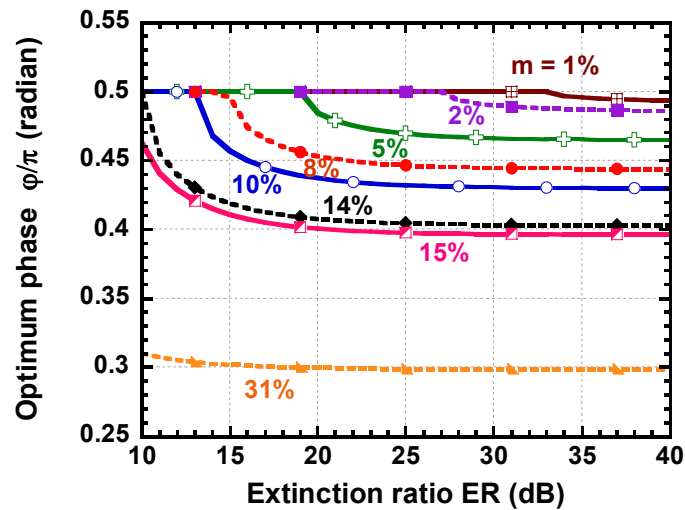


Figure 6.19 Optimum phase shift versus extinction ratio (ER) for different modulation index: 1, 2, 5, 8, 10, 14, 15 and 31%.

6.3 Simulation using Commercial Software and Comparison to Theory

To verify that not only OSSB modulation but also tunability of OCSR can be obtained simultaneously using dMZM modulator, we simulate this modulator using VPI-TransmissionMaker. In the simulation, it is assumed that a laser has a wavelength of 1550.57nm, linewidth of 800 KHz and power of 6 dBm. Each inner MZM modulator has π -phase shifted voltage of 6.5 V, insertion loss of 5.5 dB and Y-junction has extinction ratio of 28.5 dB.

First the modulation index was set to 28.28% and the case of single and two RF tones are studied. Figure 6.20 shows the optical and RF spectrum for single RF tone at 3.96 GHz and for different OCSR: (a-d) -20 dB, (b-e) 0 dB and (c-f) 20 dB. Figure 6.21 shows the optical and RF spectrum for two RF tones at 3.96 and 4.46 GHz and for different OCSR: (a-d) -20 dB, (b-e) 0 dB and (c-f) 23 dB. It is clear that OSSB is obtained with tunable OCSR for both single and two RF tones.

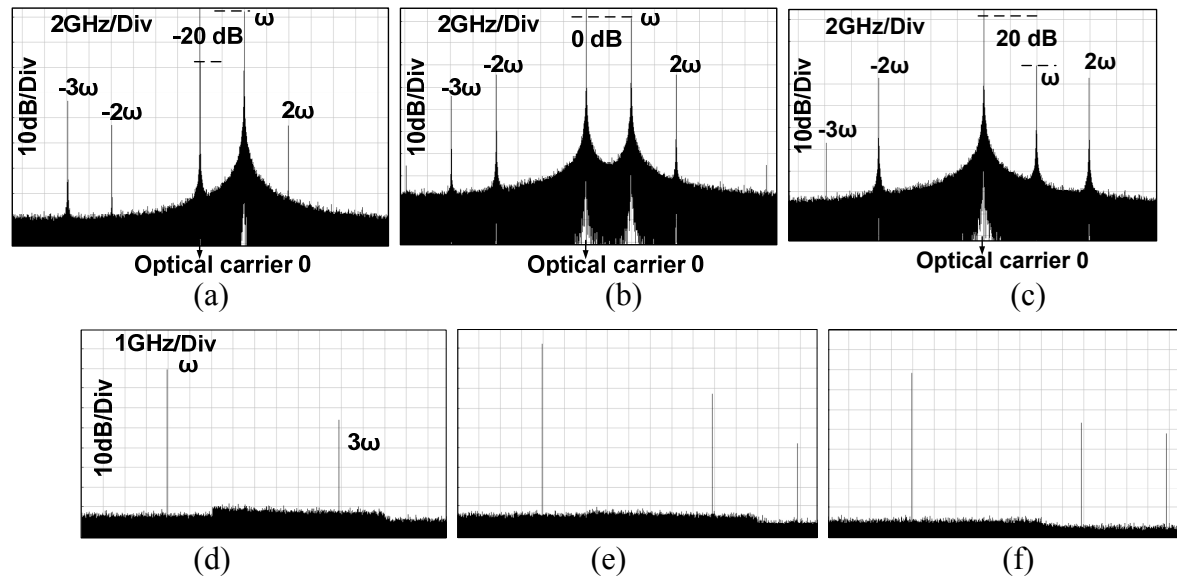


Figure 6.20 Optical and RF spectrum for one RF tone (3.96 GHz) at OCSR (a-d) -20 dB, (b-e) 0 dB and (c-f) 20 dB. The extinction ratio is 28.5dB and the modulation index is 28.28 %.

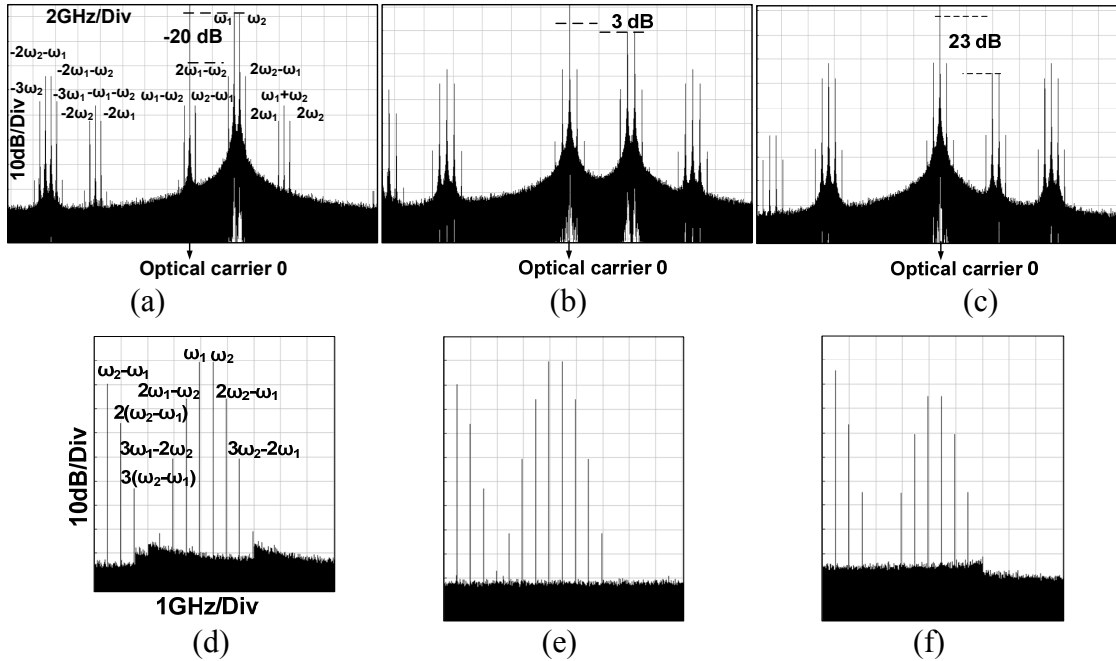


Figure 6.21 Optical and RF spectrum for two RF tones (3.96 and 4.46GHz) at OCSR of (a-d) -20 dB, (b-e) 3 dB and (c-f) 23 dB, respectively. The extinction ratio is 28.5dB and the modulation index is 28.28 %.

Next we vary the modulation index and study the optimum OCSR to achieve maximum RF power and the results are depicted in Figure 6.22(a) and (b) for single and two RF tones. It is clear that for a modulation index greater than 2%, the optimum OCSR to achieve a maximum RF power is 0 and 3 dB for single and two RF tones, respectively. A good agreement between theory and simulation is obtained with small discrepancy at high modulation index of less than 1 dB in RF power is attributed to contribution from high order harmonics and intermodulation products, as shown in Figure 6.20 and Figure 6.21, which has not been taken into account in our calculations.

To further show the accuracy of our theoretical prediction we vary the DC bias of the MZM_a and MZM_b and compute the OCSR and the relative RF power by simulation and theory at different modulation index for both single and two RF tones. Figure 6.23(a) and (b) shows the OCSR and relative RF power versus bias phase shift ϕ for one and two RF tones, respectively, and at different modulation indices: 14.14, 22.63 and 28.28%, and very good agreement are obtained between theory (lines) and simulation (marks). It is also found that maximum RF power

is achieved at an OCSR of 0 and 3 dB for single and two RF tones independently on the RF modulation index of less than 31% as depicted from Figure 6.24(a) and (b), respectively.

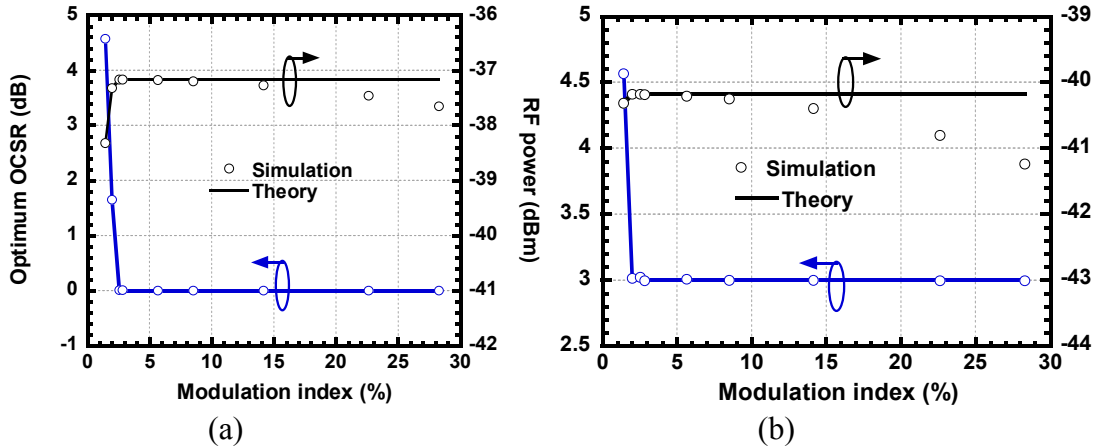


Figure 6.22 Optimum OCSR and RF power versus modulation index for 28.5dB extinction ratio. Simulation (mark) and theory (line). (a) One RF tone and (b) two RF tones.

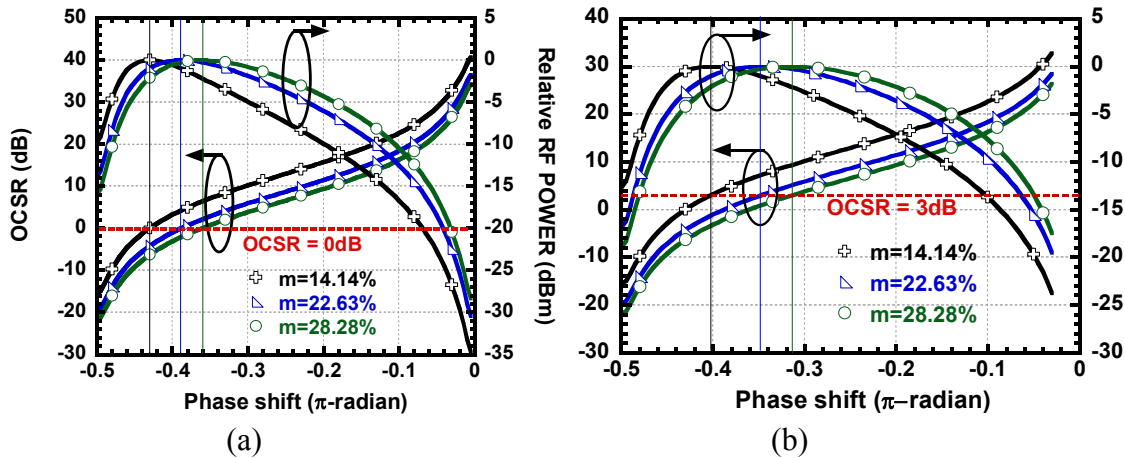


Figure 6.23. Compared theory (lines) and simulation (marks) of OCSR and RF power versus phase shift at different modulation index: 14.14, 22.63 and 28.28%. (a) One RF tone and (b) two RF tones. an extinction ratio of 28.5dB are used. The extinction ratio is 28.5 dB.

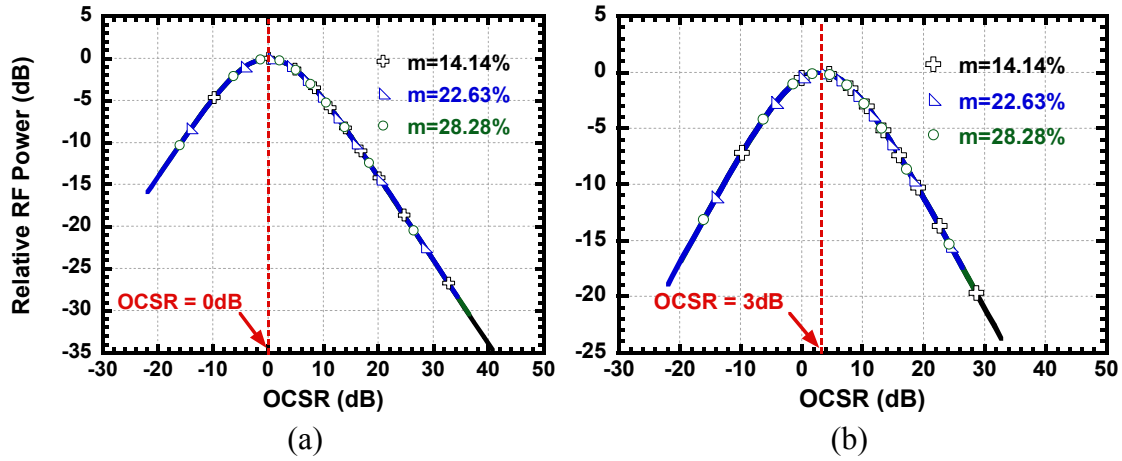


Figure 6.24 Compared theory (lines) and simulation (marks) of RF power versus OCSR for (a) one and (b) two RF tones and at different modulation indices: 14.14, 22.63 and 28.28%. The extinction ratio is 28.5dB.

6.4 Experimental Results and Discussion using Commercial dMZM

6.4.1 Experimental Setup

Figure 6.25 shows the experimental setup for the measurement of the performance of the proposed OSSB with tunable OCSR using a dMZM from Covega (Mach-10TM060). The used dMZM is integrated on a single x-cut lithium niobate chip, has insertion loss of 5.5 dB, extinction ratio of more than 20 dB, RF and DC half-wave switching voltage of 6.5 V and 4.5 V, respectively. A tunable laser source (Anritsu MG9541A) delivers a linearly polarized light at 1550.57nm of 6 dBm optical power with a linewidth of 800 KHz and intrinsic RIN of -155 dB/Hz. The lightwave source is injected into the dMZM driven by an RF source. The bias voltages V_1 and V_2 are tuned to change the OCSR while V_c is tuned to achieve OSSB modulation. The externally modulated signal passed through a single mode fiber, amplified with an EDFA and filtered by a tunable optical filter with 0.55nm bandwidth. A variable optical attenuator is used to control and set the received optical power to 0 dBm at the photodetector. An optical splitter is used to monitor the received optical signal by an OSA of 0.01nm resolution. After photo-detection the received RF signal is amplified with an LNA of 26dB gain and 2.6dB noise figure. The received signal is analyzed in the frequency domain by a 43 GHz RSA. A 12

GHz reel time oscilloscope (Agilent infiniiium DSO81204B) with a sampling rate of 40 GSa/s is used to analyze the received RF signal in time domain.

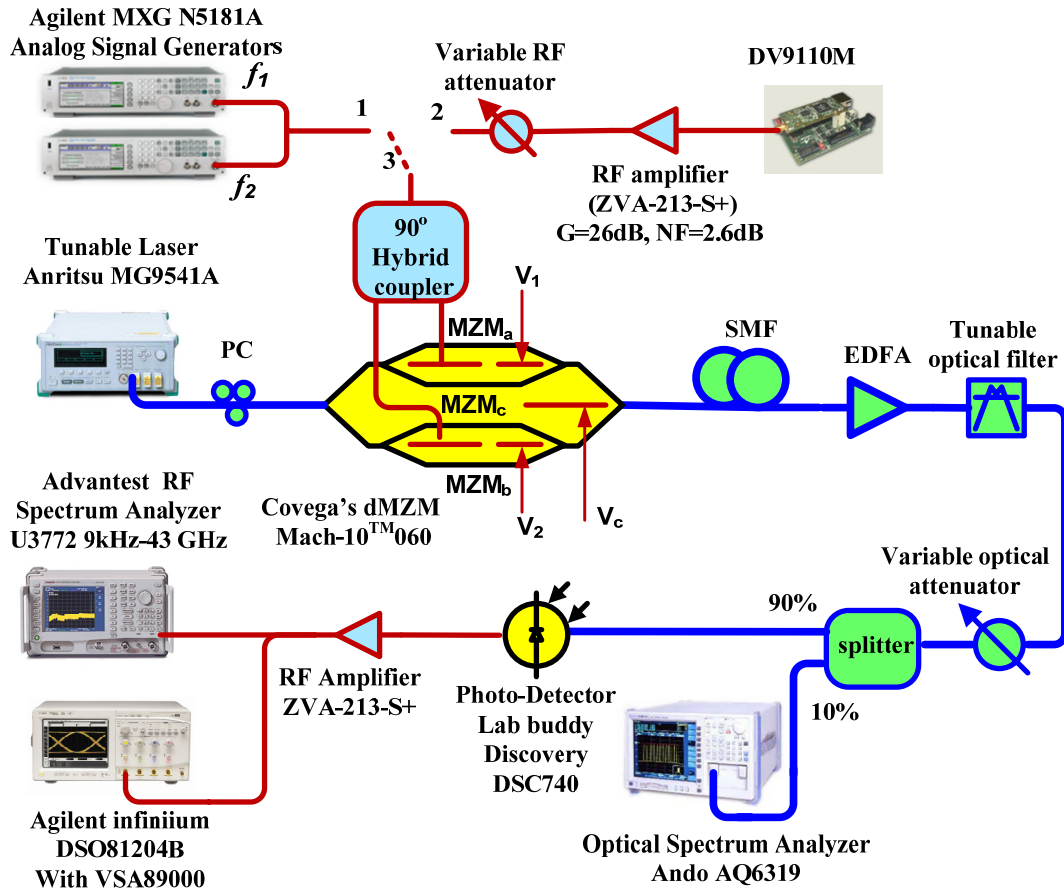


Figure 6.25 Experimental setup for the proposed OSSB with tunable OCSR using dual-parallel MZM modulator. PC: Polarization controller.

6.4.2 Distortion Effects using Two RF Tone Test

In order to assess the distortion effects of the RF signal for the proposed OSSB with tunable OCSR technique, we measure the IMD using two RF tones test with respect to OCSR. Two analog signal generators (Agilent MXG N5181A) were used to provide two RF tones at 3.96GHz and 3.964GHz with fixed power level at 12 dBm. We connected point 3 to point 1 in the experimental setup shown in Figure 6.25.

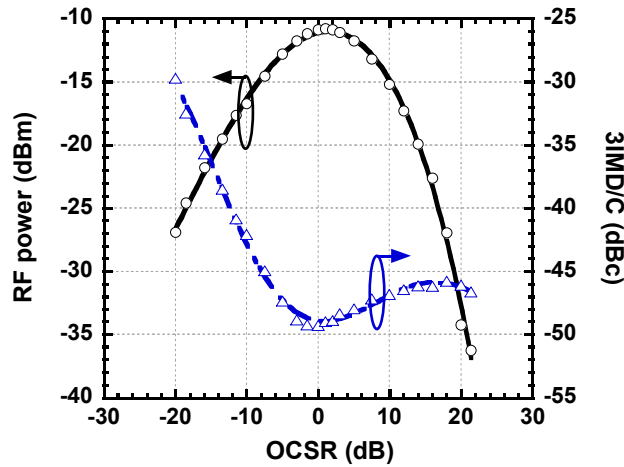


Figure 6.26 RF power and power ratio of 3rd order intermodulation distortion to carrier (3IMD/C) versus OCSR for two tones. Two RF tones at 3.96 and 3.964GHz with 12 dBm RF power per RF tone are used.

Figure 6.26 shows the measured received RF power of the carrier and the power ratio of third-order intermodulation distortion to the RF carrier (3IMD/C) versus the OCSR. It was observed that OCSR can be varied over a wide range from -20dB up to 21.4dB and maximum RF power of -10.79 dBm and minimum 3IMD/C of -49 dBc is obtained at an optimum OCSR of ~ 0 -1 dB as shown in Figure 6.27(a). Because of the limited resolution bandwidth ~ 1.2 GHz (0.01nm) of the OSA the two RF tones (3.96 and 3.964GHz) are indistinguishable. Then the power level read in the OSA is for the total power of two RF tones and the actual OCSR is 3 dB per RF tone as computed by theory and simulation. By increasing the OCSR from 0 to 21.4 dB, the 3IMD/C is increased by 2.7 dBc while the RF power is dropped drastically by more than 25 dB as shown in Figure 6.27(c). This is due to the low modulation efficiency of typical OSSB modulation that wastes most of the power in the useless optical carrier. It can be also seen that when the OCSR becomes negative and is decreased down to -20 dB, the 3IMD/C is increased up to -30 dBc as shown in Figure 6.27(b). This is mainly due to the clipping of the intensity modulated signal due to the strong suppression of the optical carrier that results in strong nonlinearity and RF power loss.

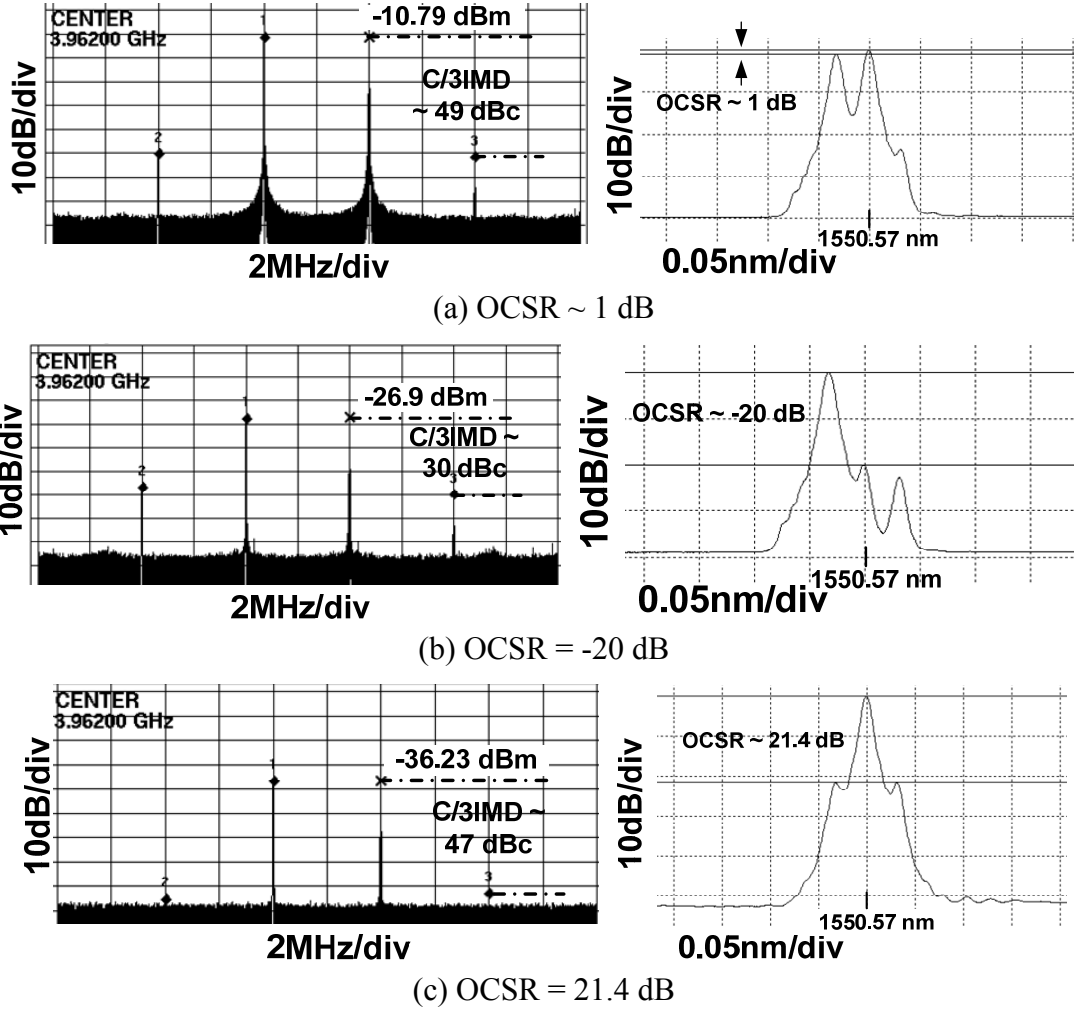


Figure 6.27 RF and optical spectrum at different OCSR (a) OCSR = 1 dB, (b) OCSR = -20 dB and (c) OCSR = 21.4 dB. An RF input power of 12 dBm per RF tone is used.

6.4.3 Performance of MB-OFDM UWB using the Proposed Technique

Next we used the same experimental setup shown in Figure 6.25 for performance evaluation of UWB over fiber using our proposed OSSB modulation with tunable OCSR, where point 3 is connected to point 2. To generate MB-OFDM UWB we used a commercially available evaluation board, DV 9110M from WisAir, which provides MB-OFDM compliant modulation with the first three WiMedia sub-bands of 528 MHz bandwidth allocated at center frequency of $f_1=3.432$, $f_2=3.96$ and $f_3=4.488$ GHz, as shown in Figure 6.28(a). The signal follows simple frequency hopping sequences like f_1 , f_2 and f_3 . The bit rate of 200 Mb/s is used for each band with QPSK modulations shown from the constellation of Figure 6.28(b). The UWB power input to the dMZM is set to -6.14dBm and the bias voltage applied to MZM_c was set to obtain OSSB

modulation. The OCSR was tuned by changing the applied bias voltages to MZM_a and MZM_b and the received optical power at the photo-detector was maintained to be 0 dBm. We used the real time oscilloscope DSO81204B to measure the EVM and received UWB power versus OCSR for back to back and after 20km of fiber transmission and the results are shown in Figure 6.29(a) and (b), respectively. It can be seen that maximum RF power is obtained at 0 dB OCSR, while minimum EVM of -21.8 dB is obtained around 5.4 dB OCSR. This is due to the high PAPR which is inherent to OFDM signal. The measured PAPR of the transmitted signal was around 11 dB, then by setting the OCSR to 5.4 dB, optical intensity clipping is avoided and better EVM performance is obtained. It is also seen that the system is compliant with the maximum required EVM of -17dB [7] when the OCSR is ranging between \sim -8dB and 20dB.

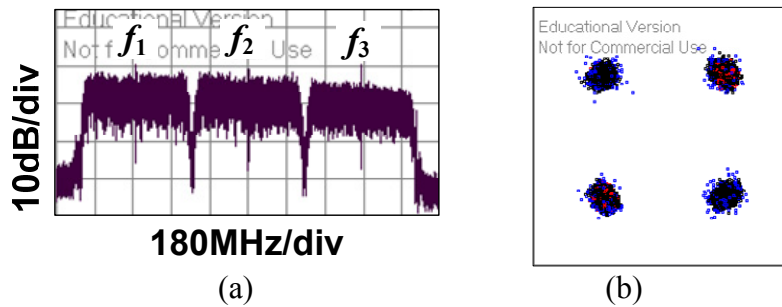


Figure 6.28 First three bands of MB-OFDM UWB wireless in (a) frequency domain and (b) received constellation.

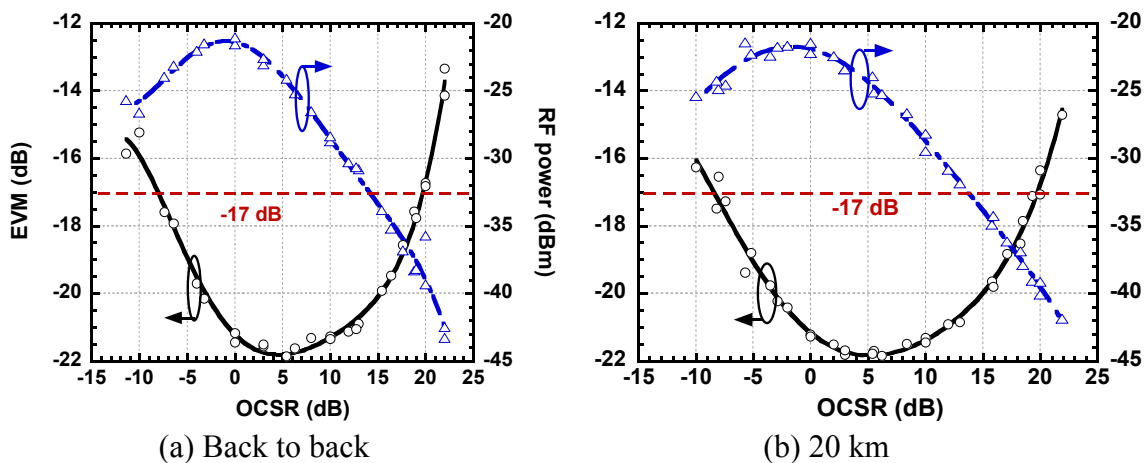


Figure 6.29 Measured EVM and RF output power versus OCSR for (a) back to back and (b) after 20 km of fiber transmission. The UWB input power to the dMZM is -6.14 dBm.

Figure 6.30 shows that an EVM of -17.9, -21.8 and -17.3 is obtained for an OCSR of 18.8, 5.4 and -7.4 dB, respectively. For high OCSR the modulation efficiency is very low and most of the power is in the optical carrier rather than in the optically subcarrier modulated sideband resulting in weak power of the received RF signal and higher DC power which increases the noise floor and reduces the signal to noise ratio as shown in the waveform of Figure 6.30(g). Conversely at very low OCSR the optical carrier is strongly suppressed below the optical sideband and clipping occurs in the optical intensity modulated signal at the photodetection. This will results in strong nonlinearity and severe IMD as depicted in the waveform of Figure 6.30(i).

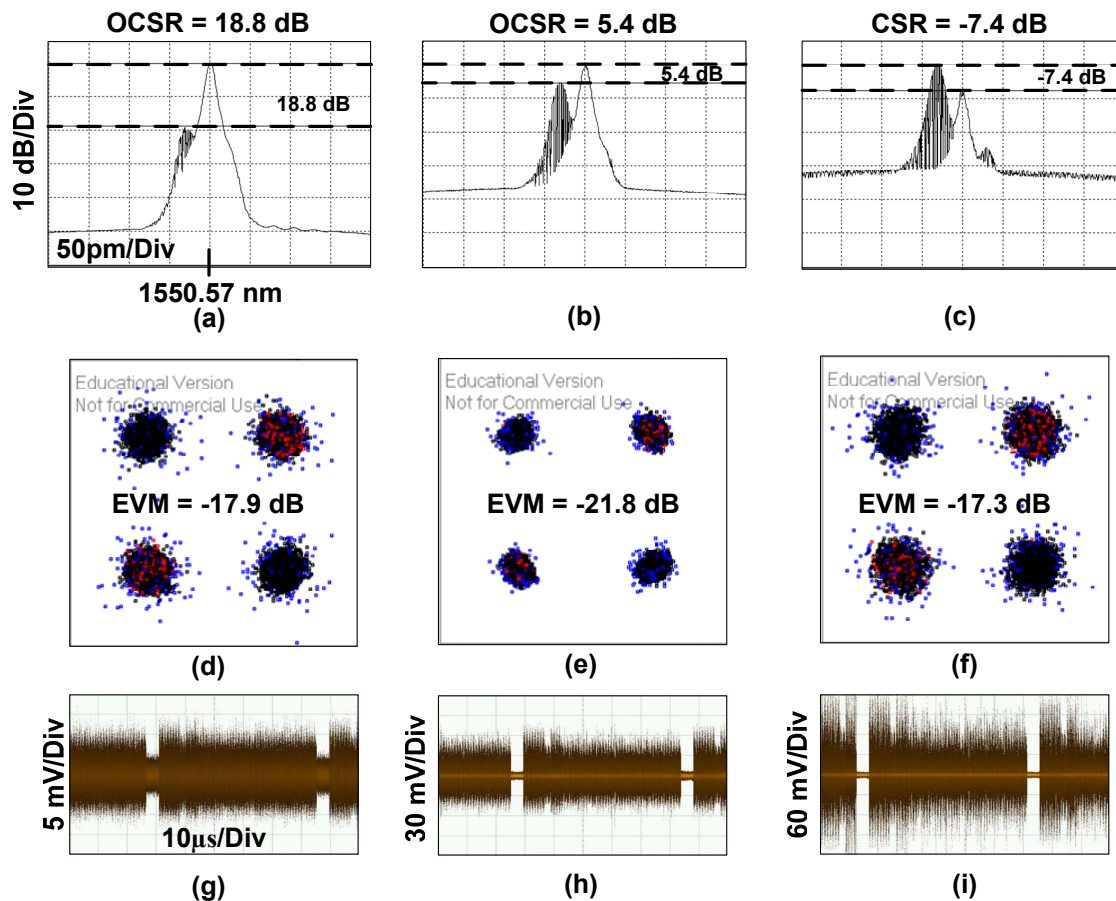


Figure 6.30 Optical spectrum, constellation and waveform for 20 km at different OCSR: 18.8, 5.4 and -7.4 dB.

6.5 Chapter Conclusion

We have shown that a dual parallel MZM modulator can be used for obtaining not only OSSB modulation but also tunability of OCSR. The dMZM is integrated in a single x-cut Lithium Niobate chip and consists of an outer MZM with an inner MZM inserted in each arm. To the best of our knowledge the function of OCSR tunability using this modulator is proposed and investigated for the first time. It is shown that a wide dynamic range of OCSR tunability can be obtained by varying the bias voltage applied to the inner MZMs. It is found that the optimum OCSR to obtain maximum RF output power depends on the modulation index and the extinction ratio of the dMZM. To achieve an OCSR of 0 dB there is a minimum required extinction ratio at a given modulation index. Moreover, we have investigated the impact of OCSR on the performance of MB-OFDM UWB signal. It is found that maximum received RF power is obtained at 0 dB OCSR while minimum EVM of the received MB-OFDM UWB constellation is achieved at 5.4dB OCSR. The proposed technique has been proven to be effective solution to improve the modulation efficiency of OSSB modulation.

CHAPTER 7 PHOTONIC UP/DOWN CONVERSION AND DISTRIBUTION OF MILLIMETER WAVE MB-OFDM UWB WIRELESS SIGNAL OVER FIBER SYSTEMS

7.1 Introduction

In this chapter, we first used our proposed technique [61] for MMW signal generation and transmission of MB-OFDM UWB signal over fiber. This technique used only one dual drive MZM biased at maximum transmission point (MATB) for MMW signal generation. Then, two second-order optical sidebands are generated with a frequency spacing of four times of the driving RF to the MZM. As proof of concept a 30 GHz MMW with three sub-bands of MB-OFDM UWB signals is experimentally generated and transmitted over 20 km of an SMF. The performance of the system is evaluated in terms of EVM versus RF and local oscillator (LO) modulation index of the MZM and fiber length. Performance degradation due to bias drift and extinction ratio are also investigated. Experimental results agree well with simulation and theoretical analysis.

Next, we proposed and demonstrated an alternative technique for photonic MMW down-conversion using four wave mixing (FWM) in an EAM. In this technique, dual lights from a CS transmitting over downlink fiber are used as two pumps and injected to an EAM, instead of using three lights [69]. Thanks to FWM, two lights are generated besides the dual pump lights. An MMW MB OFDM UWB signal also drives the EAM for optical SCM. In other words, each of the dual pump lights has double sideband subcarriers which carry the MMW MB OFDM UWB signal (i.e. four subcarriers for the dual pump lights). One of the sideband subcarriers is very close to one of the two FWM lights. By optical filtering, the desired FWM light (i.e. used for uplink optical carrier) with a sideband subcarrier (i.e. OSSB) is transmitted over uplink fiber to a CS. Thus, an MMW signal at a BS is optically down-converted to IF. In [70], also dual lights are only used, but the down-conversion is obtained by optical mixing (2nd order nonlinearity) instead of FWM (3rd order nonlinearity). We experimentally investigate the efficiency of the FWM versus EAM reverse bias and input optical power. Both proposed techniques are demonstrated for 30 GHz band but can be applied to 57-64 GHz MMW.

The chapter is organized into three sections. Section 7.2 presents the principle of photonic MMW up-conversion using DE-MZM. The performance of the generated MMW MB-OFDM UWB signal is also numerically and experimentally evaluated in terms of EVM versus RF and LO modulation index for back to back and after 20km of fiber transmission. Section 7.3 explains the principle and gives the experimental characterization of photonic MMW down-conversion using FWM in an EAM. FWM efficiency is studied versus input optical power and applied reverse bias to the EAM. Also, the performance of the down-converted MMW MB-OFDM UWB signal is experimentally evaluated in terms of EVM versus EAM, LO modulation index and received optical power after 20km of fiber. Finally summary is drawn in Section 7.4.

7.2 Photonic UP-Conversion of MMW MB-OFDM UWB Signal Using MZM

7.2.1 Proposed Technique

The proposed modulation technique for MMW MB-OFDM UWB signal is shown schematically in Figure 7.1. A CW laser is assumed to have a wavelength of $\lambda=1548.5$ nm, an output optical power of $P=7.5$ dBm, a linewidth of 800 KHz, and RIN of -150 dB/Hz. A sinusoidal LO signal has a frequency of $f_{LO}=6.51$ GHz and voltage of $V_{LO}(t)=V_{LO} \sin(\omega_{LO}t+\phi_{LO})$, where $\omega_{LO}=2\pi f_{LO}$, ϕ_{LO} - random phase noise of the LO. The total LO modulation index for the MMW generation is defined by $m_{LO}=V_{LO}/V_{\pi}$, where V_{π} is the modulator's switching voltage. The CW light is injected to the first DE-MZM, biased at maximum transmission. This DE-MZM has a switching voltage of 3.8 V, an extinction ratio of 28.5 dB and insertion loss of 6 dB. The dual electrodes are driven by the same LO sinusoid with 180 degree phase shift. Thus, only even-order optical harmonics are generated whereas all odd-order optical harmonics are suppressed ideally. Following the optical MMW generation, a second DE-MZM is driven by an MB-OFDM UWB signal and generates OSSB modulation. This DE-MZM has an extinction ratio of 32 dB, half wave switching voltage of 5 V, and insertion loss of 7 dB. The bit rate of 200 Mbps is used for each band of the MB-OFDM UWB signal with QPSK modulation.

Following the second DE-MZM an EDFA with a noise figure (NF) of 5 dB is used to compensate for optical losses. To reduce optical amplifier noise, an optical BPF is used after the

EDFA. The filter has a 3th order Gaussian transfer function with a bandwidth of 0.55 nm and a central wavelength of 1548.5 nm.

Distribution of MMW MB-OFDM UWB signals to remote antennas is realized over an SMF with fiber loss of $\alpha=0.22$ dB/km and chromatic dispersion of $16 \text{ ps}/(\text{nm} \cdot \text{km})$. At the base station, the transmitted MMW MB-OFDM UWB signal is detected by a PD (with responsivity of $\mathfrak{R} = 0.65 \text{ A/W}$ at 1548.5-nm, thermal noise of $2 \times 10^{-11} \text{ A}/\sqrt{\text{Hz}}$ and dark current of 2 nA). In practice, this MMW is launched into air by using an antenna.

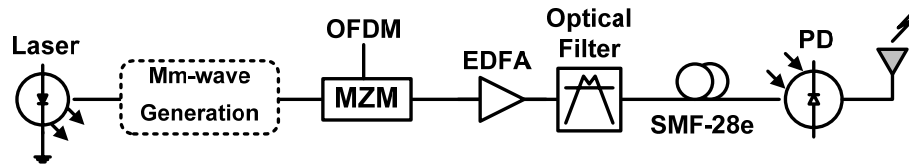


Figure 7.1 Schematic of the proposed MMW MB-OFDM RoF link.

7.2.2 Simulation Results and Discussion

Using commercial software VPI-TransmissionMaker and the parameters given in previous section, we simulate the system using one DE-MZM [61] as shown in Figure 7.1. Figure 7.2 and Figure 7.3 show simulated EVM versus RF and LO modulation index, respectively. First we set the LO modulation index m_{LO} to 67.5%, vary the RF modulation index m_{RF} and measure the EVM at back-to-back and after 20 km of fiber transmission. Figure 7.2 shows a minimum EVM of -19.8 and -19.3 dB is achieved at an optimum RF modulation index of $\sim 4\%$ for back-to-back and 20 km of fiber transmission, respectively. For RF modulation index of up to $\sim 4\%$, OFDM subcarriers suffer from relative phase shift due to fiber dispersion. For RF modulation index of more than 4% the OFDM subcarriers suffer from both amplitude and phase distortion due to the combined effect of MZM response nonlinearities and fiber dispersion. Same results have been found in Chapter 2 and [71]. Compared to back to back MMW UWB transmission over fiber is further limited by laser phase noise converted RIN due to fiber dispersion and phase distortion induced by fiber dispersion in addition to increased optical amplifier noise due to fiber loss as found in Chapter 2 and [71]. This explains the 0.5 dB in the EVM degradation at 4% RF modulation index after transmission over 20 km of fiber compared to back-to-back.

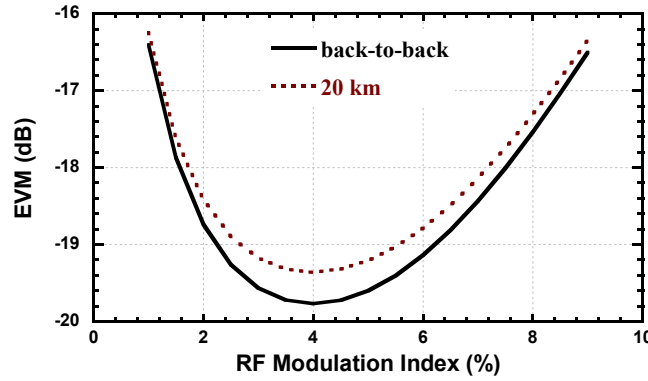


Figure 7.2 Simulated EVM versus RF modulation index of second MZM. LO modulation index of 67.5 % is used.

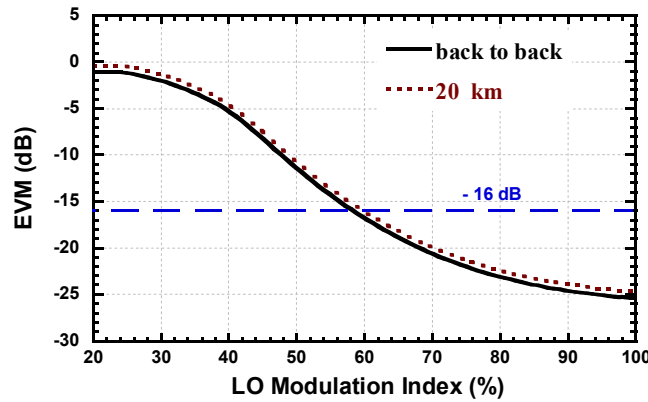


Figure 7.3 Simulated EVM versus LO modulation index of first DE-MZM for MMW generation. RF modulation index of 4% is used.

Next, we fixed the RF modulation index at optimum $\sim 4\%$ and investigate the impact of the LO modulation index. We vary the LO modulation index from 20% to 100% and measure the EVM for back to back and after transmission over 20 km of fiber. Figure 7.3 shows that by increasing the LO modulation index from 20 to $\sim 100\%$ the EVM decreases from -0.5 dB to -25 dB after 20 km of fiber transmission. It is also seen that for 20 km of fiber transmission an LO modulation index of more than 60% is necessary to achieve the minimum required EVM of -16 dB [7]. Compared to back-to-back transmission, the EVM is degraded by 0.5 dB after transmission through 20 km of fiber. The EVM is inversely proportional to the signal to noise

ratio [25], therefore EVM will decrease by increasing the power of the generated MMW MB-OFDM UWB signal which is theoretically proportional to $J_2^2(\pi m_{LO}/\sqrt{2})$ [61].

Figure 7.4 shows that by increasing the LO modulation index from 20% to 100% the power of the generated MMW MB-OFDM UWB signal increases and thus the EVM decreases as shown in Figure 7.3.

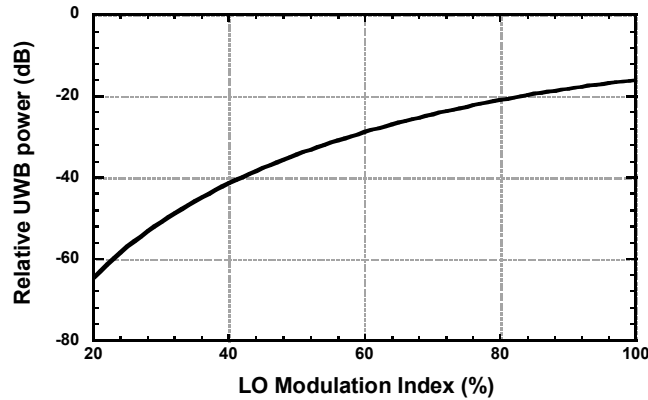


Figure 7.4 Calculated relative power of the generated MMW MB-OFDM UWB signal vs. LO modulation index for proposed technique.

Finally, we investigate the performance degradation due to bias drift and extinction ratio of the MZM used in the proposed technique. The fiber length was set to 20 km, and the RF and LO modulation index of the DE-MZM is fixed at ~4 % and 70%, respectively. The bias voltage drift ratio is defined as $(\Delta V/V\pi) 100\%$, where ΔV is the bias voltage drift. We found that the EVM is degraded by less than 1 dB for bias voltage drifts within $\pm 20\%$, however less than -18.9 dB of EVM can still be obtained as shown in Figure 7.5.

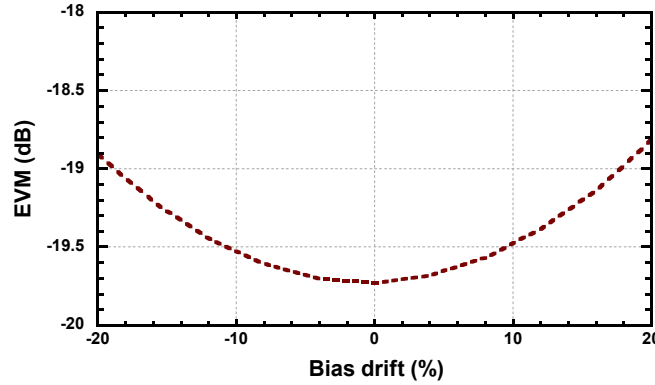


Figure 7.5 EVM vs. bias drift of the DE-MZM used in the proposed technique for MMW generation after transmission over 20 km of SMF. RF and LO modulation index of 4% and 70% is used, respectively.

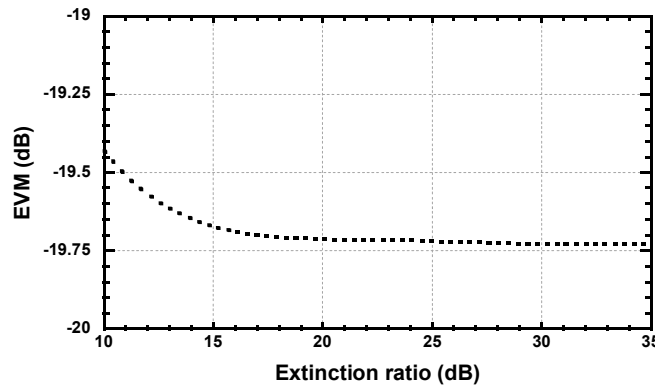


Figure 7.6 Simulated EVM versus extinction ratio of the MZM used in the proposed technique for MMW generation after transmission over 20 km of SMF. RF and LO modulation index of 4% and 70% is used, respectively.

It is known that the quality of MMW generation is impacted by MZM extinction ratio [61]. Thus, to further show the performance of the proposed modulation technique, impacted by the extinction ratio of the MZMs, we consider an MZM with an extinction ratio varying from 10 to 35 dB. The LO, RF modulation index and fiber length are fixed at 70%, 4% and 20 km, respectively. Figure 7.6 shows the simulated EVM as a function of extinction ratio. It is seen that the EVM is almost independent on extinction ratios of more than ~ 20 dB, which is the case in most commercially available MZMs. The EVM is degraded by only 0.25 dB if an MZM of 10 dB extinction ratio is used.

7.2.3 Experimental Results and Discussion

The experimental setup is shown in Figure 7.7. A CW light from a tunable laser source (Anritsu MG9541A) has a wavelength of 1548.5 nm, linewidth of 800 KHz, output power of 7.5 dBm and RIN of -150 dB/Hz. A local oscillator sinusoidal signal of frequency 6.51 GHz is amplified by an amplifier with 2.6-dB noise figure and 26-dB gain, and drives the DE-MZM (dashed box in Figure 7.7). The DE-MZM have switching voltage of 3.8 V, an extinction ratio of 28.5 dB and insertion loss of 6 dB. The CW light is injected to the first DE-MZM, biased at MATB. Thus, two strong second-order optical sidebands are generated and have a frequency spacing that is four times the frequency of the driving LO signal, i.e. a frequency quadrupling. Following the optical MMW generation, OSSB modulation with MB-OFDM wireless signals is implemented. Here we use a DE-MZM to obtain optical SCM with MB-OFDM UWB wireless signal. This MZM has an extinction ratio of 32 dB, half wave switching voltage of 5 V, and insertion loss of 7 dB, and is driven by an MB-OFDM UWB signal. An arbitrary waveform generator, AWG 7122B, is used to generate a MB-OFDM UWB signal at bandgroup 1 with bit rate of 200 Mb/s and frequency hopping TFC1 as defined in WiMedia standard [5]. The UWB signal is amplified by a power amplifier of 26 dB gain. A variable attenuator (VA) is used to vary the UWB power input to the MZM. Optical subcarriers carrying UWB wireless signals are present on both second-order optical sidebands that are generated by the first MZM as shown in Figure 7.8.

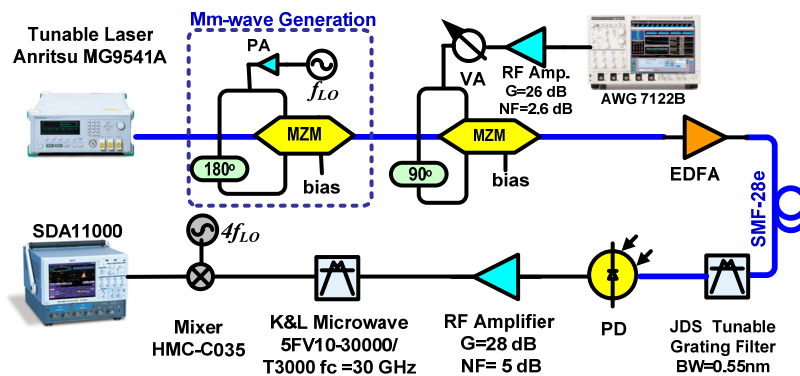


Figure 7.7 Experimental setup for the MMW MB-OFDM UWB over fiber system using proposed MMW generation (dashed box).

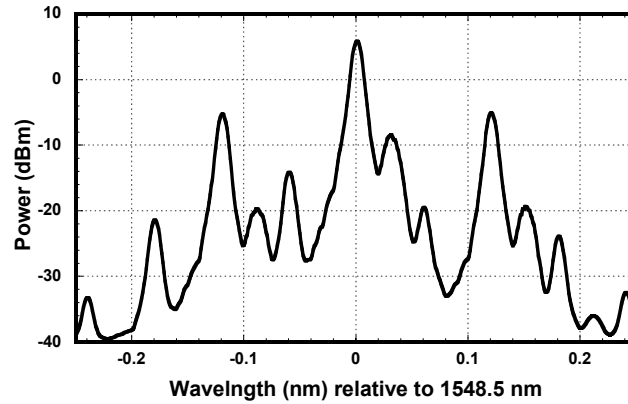


Figure 7.8 Measured optical spectrum after transmission over 20-km of fiber.

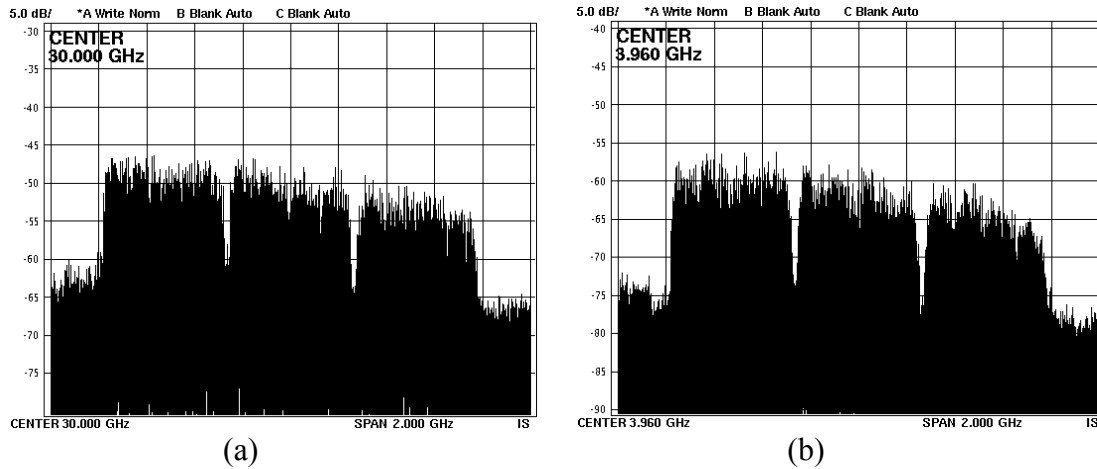


Figure 7.9 Measured electrical spectrum of MB-OFDM UWB wireless system. (a) before and (b) after electrical frequency down-conversion.

The generated optical signals are transmitted over 20 km of an SMF, with fiber loss of 0.22 dB/km and chromatic dispersion of 16 ps/(nm.km). An EDFA with NF of 5 dB is used to compensate for all optical loss and maintain an optical power of 6 mW at the photodetector. At the optical receiver, the optical signal is filtered by a JDS tunable optical filter, with bandwidth of 0.55 nm to reduce optical amplifier noise, and detected by a PD (Discovery DSC-740 with 3-dB bandwidth of 35 GHz and responsivity of 0.65 A/W). By photodetection MMW MB-OFDM UWB signal centered at 29.472, 30, and 30.528 GHz are generated as shown in Figure 7.9(a). The generated MMW MB-OFDM UWB signals are amplified by an RF amplifier ($NF=5$ dB and $G=28$ dB), and electrically filtered by a K&L BPF with a 3 dB bandwidth and center frequency of 30 GHz. Then, the MMW MB-OFDM UWB signal is down-converted to 3.432, 3.96 and

4.488 GHz, as shown in Figure 7.9(b), using a HMC-Co35 electrical mixer driven by a sinusoidal RF at $4f_{LO} = 26.04$ GHz (9 dBm). Both Figure 7.9(a) and (b) show an SNR greater than 15 dB. Finally the EVM of the down-converted MB-OFDM UWB signal was measured by a high speed real-time oscilloscope SDA 11000 from LeCroy.

To validate our simulation results, we set the LO modulation index to $\sim 83.5\%$, change the RF modulation index from 1% to 9% by varying the UWB input power to the second MZM, and measure the EVM at back-to-back and after transmission over 20 km of fiber. Figure 7.10 shows a minimum EVM of -19.2 dB and -18.7 dB is obtained at RF modulation index of $\sim 4\%$ for back to back and 20 km of fiber transmission, respectively. This 0.5 dB degradation in EVM after transmission over 20 km of fiber is in good agreements with simulation results shown in Figure 7.2 and Figure 7.3. However, there is a 3 dB discrepancy between simulated and measured EVM which is mainly due to the added phase noise and frequency shift between the two different LO sources used for frequency quadrupling and down-conversion at the MZM and RF mixer, respectively, as shown in the experimental setup of Figure 7.7. Figure 7.11(a) and (b) show the QPSK constellation diagram for the back-to-back and after 20 km of fiber transmission, respectively. The LO and RF modulation index are fixed at 83.5% and 4%, respectively. The good quality of the constellation is an indication of suitability of the radio over fiber technique for MMW MB-OFDM UWB generation and distribution.

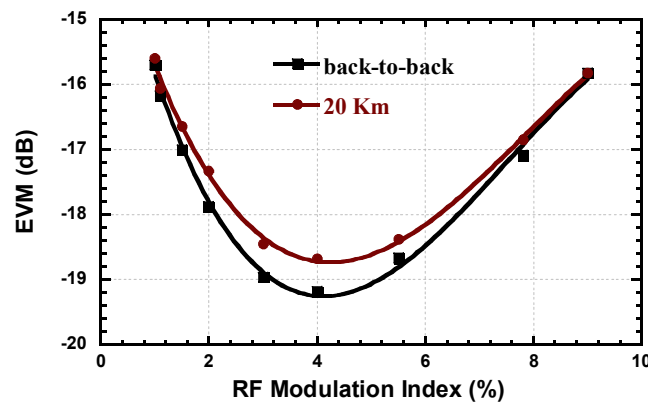


Figure 7.10 Measured EVM versus RF modulation index for back-to-back, and after 20-km of fiber transmission. LO modulation index of 83.5% is used.

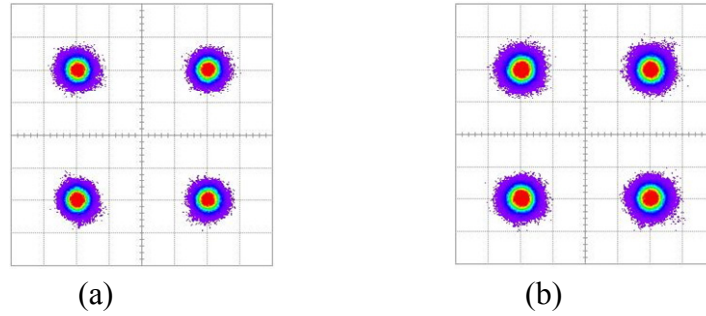


Figure 7.11 Measured constellation of QPSK MMW MB-OFDM for (a) back-to-back and (b) after 20-km of fiber transmission. RF and LO modulation index of 4% and 83.5% is used, respectively.

After that, we increase the LO modulation index from $\sim 70\%$ to 83.5% by varying the power level from the LO driving source. The RF modulation index of the second MZM is fixed at $\sim 4\%$, the fiber length was set to 20 km and we observe the EVM at different LO power levels and the EVM decreases from ~ -16.4 to -18.7 dB as shown in Figure 7.12. Experimental and simulation results show similar trend. As stated before a discrepancy of ~ 3 dB is mainly due to the added phase noise and frequency shift between the two different LO sources used for frequency quadrupling and down-conversion at the MZM and RF mixer, respectively.

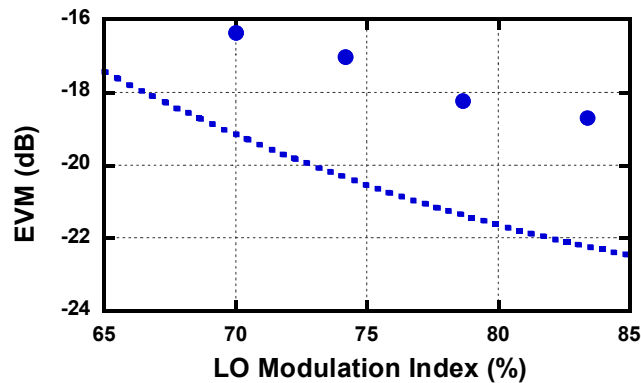


Figure 7.12 EVM vs. LO modulation index of first MZM for MMW generation after transmission over 20 km of SMF. Marks: measured EVM. Dashed line: simulated EVM. RF modulation index of 4% is used.

7.3 Photonic Down-Conversion of MMW MB-OFDM UWB Signal using FWM in an EAM

For downlinks, we have already investigated cost-effective techniques for the generation and distribution of MMW signals using optical frequency up-conversion [61-62], including MMW MB-OFDM UWB signal generation and transmission over fiber as presented in Section 7.2. For uplinks, it is preferable to use an EAM because it presents a low power consumption, compact size, polarization insensitivity, easy integration with other devices, and higher speed operation in photodetection, mixing and optical modulation due to the EAM inherent characteristics. It was demonstrated that an EAM can be used for frequency down-conversion from an MMW to an intermediate frequency (IF) signal [72-73] using cross-absorption modulation in an EAM for uplinks. Instead of using both a CW light for uplink and dual pump lights for down-conversion [72], a simpler technique [73] was proposed for MMW down-conversion in an EAM, in which only the dual lights are used for both uplink transmission and down-conversion.

7.3.1 Proposed Technique

The proposed technique is illustrated in Figure 7.13 using an EAM for frequency down-conversion, and optical modulation. In a CS, the downlink lightwave at frequency f_c is modulated in a MZM driven by an RF signal at a frequency $f_{lo}/2$ with optical carrier suppression. Thus the two optical subcarriers are generated with a frequency separation of f_{lo} , and the two optical subcarriers are referred to dual pump lights. This is one way to obtain dual pump lights with a given spacing. These dual pump lights are transmitted over downlink fiber to a BS. At a BS, the dual pump lights are injected into an EAM that is also driven by an MMW radio signal at f_{mm} . Due to FWM process in the EAM [74-75], two FWM lights separated by $3f_{lo}$ are generated besides the dual-pump lights. In the same time, an MMW signal is applied to the EAM which leads to ODSB SCM, and thus two optical subcarriers are generated for each pump light. The optical sidebands carry the modulation data, and the FWM lights can serve as uplink optical carriers. Then with proper optical filtering as shown in Figure 7.13, an OSSB together with the optical carrier (one FWM light) can be extracted for further transmission. After the photodetection, an IF signal will be generated at $f_{mm} - f_{lo}$.

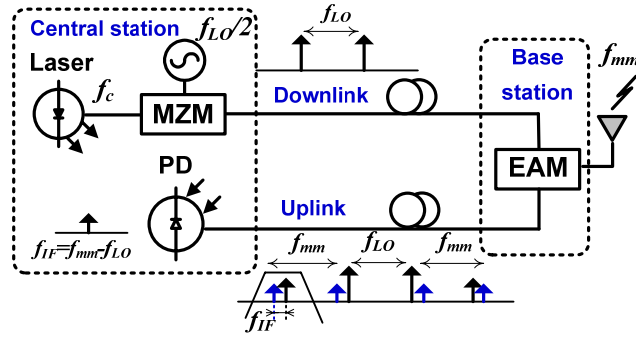


Figure 7.13 Schematic of MMW over fiber uplink using an EAM for frequency down-conversion.

On the other hand, down-conversion can be obtained by extracting one pump light (at $f_c \pm f_{lo}/2$) and nearby one sideband (at $f_c \pm (f_{mm} - f_{lo}/2)$). Then by photodetection, an IF signal at $f_{mm} - f_{lo}$ is obtained [76]. However, the optical carrier to subcarrier power ratio is high which degrades the optical signal to noise ratio and receiver sensitivity. Moreover, optical spurious components are generated from the second order nonlinearity of the EAM around each pump light and thus carrier to interference ratio is decreased [77]. Conversely, if one optical subcarrier at $f_c \pm (f_{lo}/2 + f_{mm})$ together with one FWM light at $f_c \pm 3f_{lo}/2$ is extracted out, OSSB modulation with tunable optical carrier suppression can be obtained by controlling the input optical power to the EAM or/and the power of the MMW driving signal. Therefore signal to noise ratio can be optimized due to tunability of optical carrier to subcarrier power ratio. Compared to [73], this technique leads to a better signal to noise ratio of down-converted IF signal, and a higher receiver sensitivity.

7.3.2 Experimental Setup

The considered system setup shown in Figure 7.14 is used to investigate the FWM efficiency in an EAM and to evaluate the performance of the down-converted MMW MB-OFDM UWB in MMW over fiber uplink. A tunable laser source delivers a light at 1548.823 nm of 0 dBm optical power with a linewidth of 800 KHz and intrinsic RIN of -155 dB/Hz. The light is injected into a dual-electrode MZM (DE-MZM) of 6 dB insertion loss, 32 dB extinction ratio and 5 V half wave switching voltage. The DE-MZM is biased at minimum transmission point and driven by a $f_{lo}/2 = 13.02$ GHz sinusoidal LO source. An 180° HEC is used to insert 180° phase shift between the two electrodes of the DE-MZM. ODSB with carrier suppression is obtained at the output of the DE-MZM. Thus, two optical sidebands, separated by 0.208 nm ($f_{lo}=26.04$ GHz), are generated and referred to dual pump lights as shown in Figure 7.15(a), together with some high-order nonlinear distortion products. The lights are launched into 20 km of standard SMF and amplified by an EDFA before being injected into an EAM. We use a commercial EAM from OKI with a 3 dB bandwidth of 32 GHz. The measured characteristic transmission of the EAM at 1548.823 nm and the calculated relative third intermodulation distortion are shown in Figure 7.16.

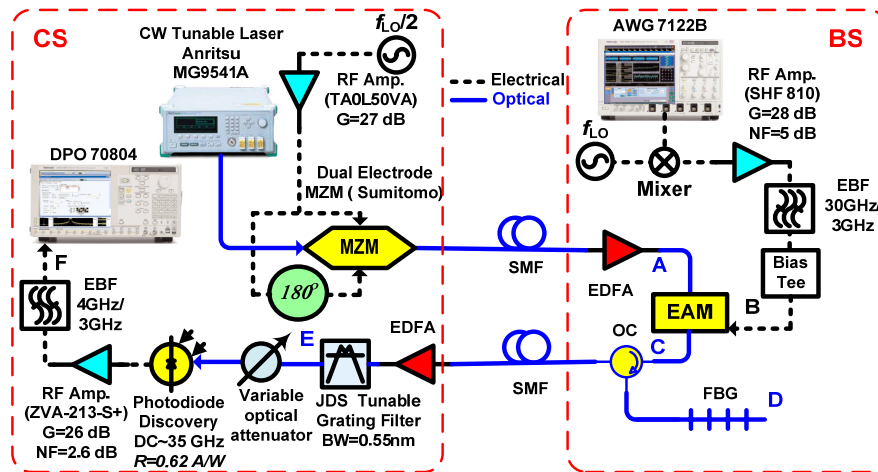
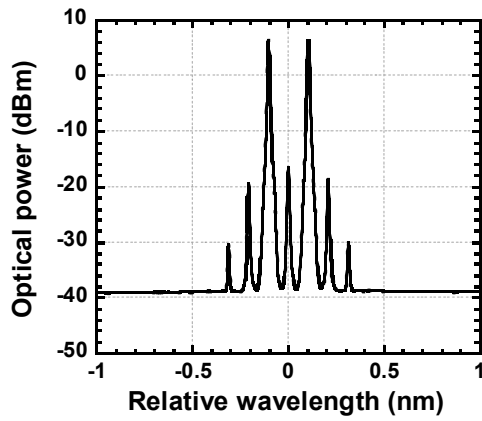
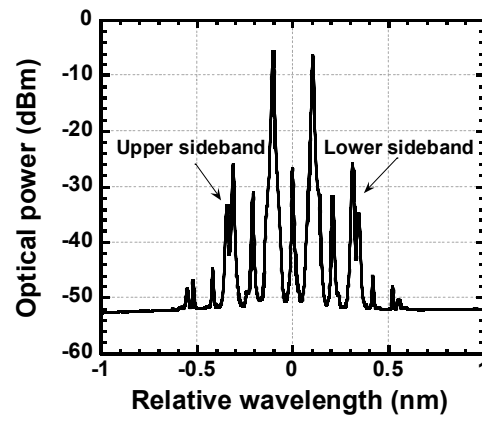


Figure 7.14 Experimental setup for photonic MMW down-conversion using FWM in an EAM. OC: optical circulator.

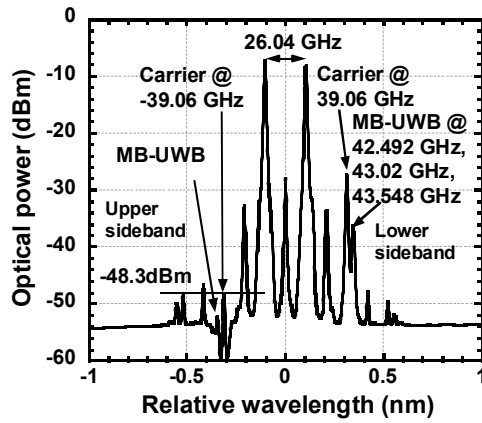
The AWG 7122B provides MB-OFDM compliant modulation with three WiMedia bands allocated at the center frequency of 3.432, 3.96 and 4.488 GHz. This MB OFDM UWB signal is mixed with an LO signal at 26.04 GHz, amplified and passes an EBF of 3 GHz bandwidth centered at 30 GHz. An MMW MB OFDM UWB signal hopping at 29.472, 30, and 30.528 GHz is generated as shown in Figure 7.15(e) and drives the EAM. The optical spectrum at the output of the EAM is shown in Figure 7.15(b). It is seen that there are two sidebands which both carry the MB OFDM UWB MMW signal, and they are close to the FWM lights (the other two sidebands are overlapped with the two pump lights and invisible). We use a reflective fiber Bragg grating (FBG) of 7.5 GHz 3-dB bandwidth with a circulator to extract the optical upper sideband for uplink transmission. The optical spectrum at point D in Figure 7.14 is shown in Figure 7.15(c). The extracted upper sideband consists of the FWM light (at -39.06 GHz) and MB OFDM UWB subcarrier (with signal hopping at -42.492, -43.02, and -43.548 GHz), together with some residual optical spectral components. After transmission over SMF of 20 km, amplification and optical filtering (for reducing ASE noise), the optical spectrum at the photodetector is shown in Figure 7.15(d). A variable optical attenuator is used to control the received optical power at the photodetector. After photodetection, the UWB signal is amplified by a broadband RF amplifier with gain of 26 dB and noise figure of 2.6 dB, and passes an EBF centered at 4 GHz with a 3 GHz bandwidth as shown in Figure 7.14. The received MB-OFDM UWB signal is shown in Figure 7.15(f) and evaluated with a high speed real-time oscilloscope DPO 70804 from Tektronix.



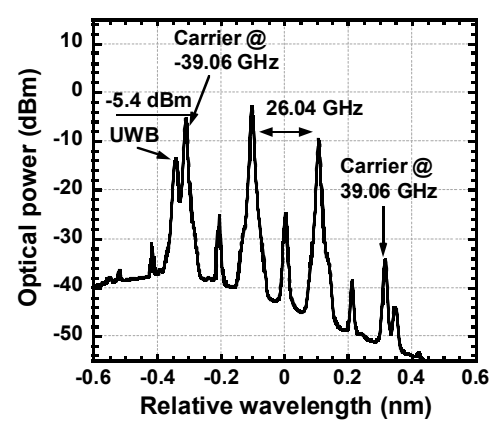
(a)



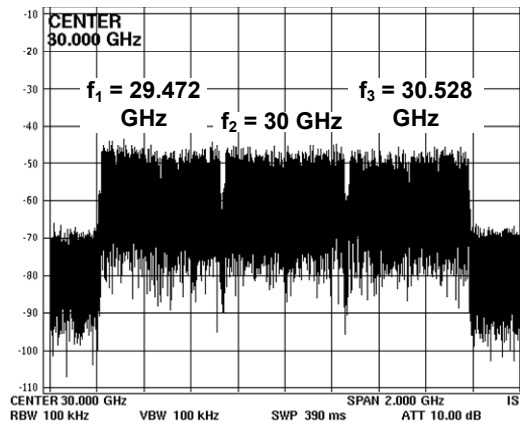
(b)



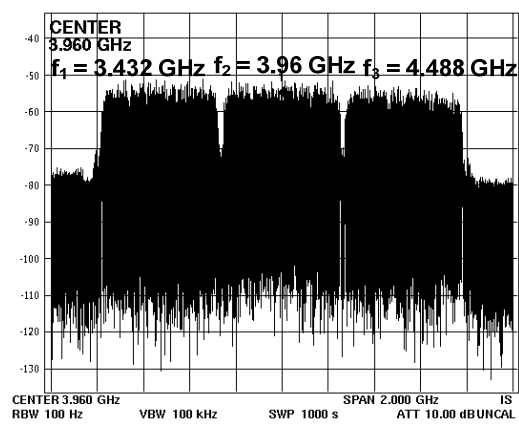
(c)



(d)



(e)



(f)

Figure 7.15 (a), (b), (c) and (d) represents the measured optical spectrum at point A, C, D and E, and (e) and (f) shows the RF spectrum of the transmitted MMW and received IF MB-OFDM UWB signal at point B and F, respectively in Figure 7.14.

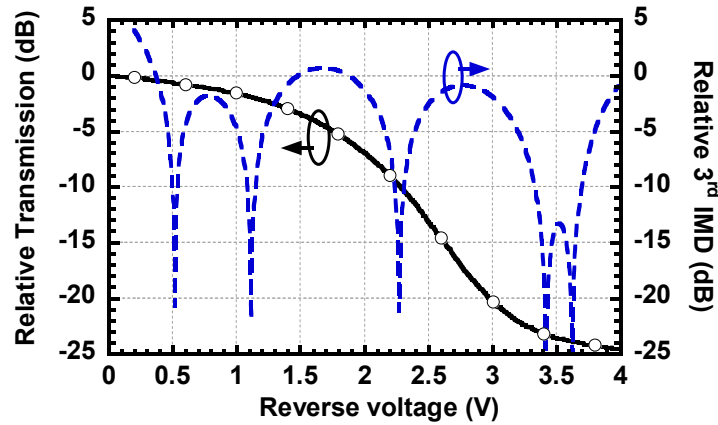


Figure 7.16 Measured relative transmission of the EAM at optical wavelength of 1548.823 nm and calculated relative third intermodulation distortion (3rd IMD).

7.3.3 Characterization of Four Wave Mixing in EAM

In the following, we define the FWM efficiency as the power ratio of the output FWM to the input pump. The electrical power of the LO signal driving the DE-MZM was set to 16.5 dBm. The total input optical power of the dual pump lights to the EDFA was ~ -17 dBm. The injected optical power into the EAM was set by the EDFA to 6.5 dBm per pump light. The MMW MB-OFDM UWB signal was not applied to the EAM. We vary the reverse bias voltage applied to the EAM and measure the FWM efficiency. Figure 7.16 shows the effect of reversed bias voltage on the efficiency of FWM in the EAM. It is clearly shown that the FWM efficiency increases with the applied reverse voltage of up to 2.3 V and starts decreasing after 2.3 V. This is because the absorption coefficient inside the EAM waveguide, responsible for the FWM, is enhanced with the increase of the reverse bias of up to 2.3 V. However, the FWM efficiency decreases for reverse bias of more than 2.3 V. This is because the slower FWM mechanisms [74], which are present for small wavelength spacing between the two optical pumps, reduce the third order susceptibility inside the EAM. Similar results have been found in [74-75] which confirms our experimental results. A maximum FWM efficiency is obtained at 2.3 V reverse bias, which happens to also minimize the 3IMD as shown in Figure 7.16.

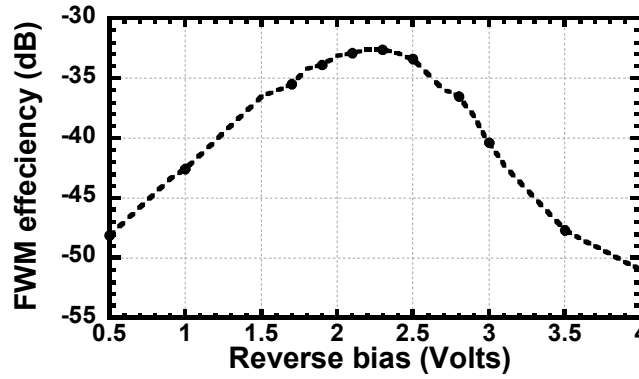


Figure 7.17 Measured FWM efficiency at the output of the EAM as a function of the reverse bias voltage. Pump and Probe input optical power is 6.5 dBm.

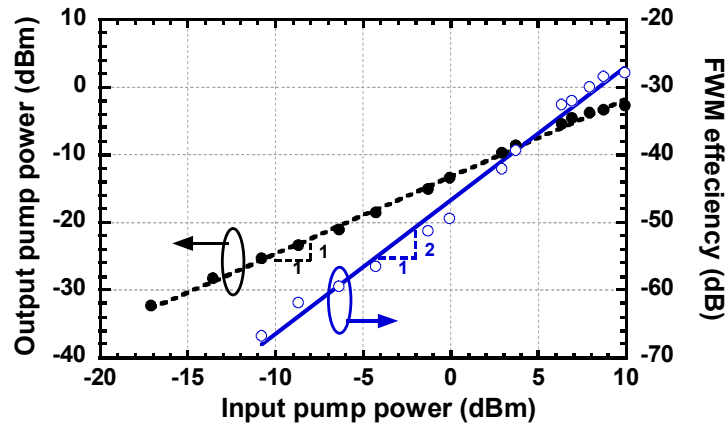


Figure 7.18 Measured FWM efficiency and output pump power at the output of the EAM as a function of the input pump power. Reverse bias voltage of the EAM is 2.3 V.

Next we set the reverse bias voltage of the EAM to 2.3 V for maximum FWM, and investigate how the FWM efficiency is impacted by the input pump power to the EAM. The injected optical power of the pump lights into the EAM was controlled by the EDFA. Figure 7.18 shows the FWM efficiency and the dependency of output pump power on the input pump power. It is clearly shown that the FWM efficiency in dB scale has a slope of 2, which was also found in [75]. This is because the FWM is generated through the third order nonlinearity, i.e. $P_{FWM} \propto P_{in}^3$, where P_{FWM} and P_{in} are power of the FWM and input pump, respectively. This suggests that high order nonlinearity is negligible for the input pump power ranged from -17 to +10 dBm. Figure

7.18 also shows that the output power of the pump varies linearly with the input pump power, showing no saturation within this input power range.

7.3.4 Application to MMW MB-OFDM UWB

The MMW MB OFDM UWB signals centered at 29.472, 30, and 30.528 GHz are applied to the EAM. The reverse bias voltage is set to 2.3 V for maximum FWM efficiency and the input pump power to the EAM is set to 6.5 dBm. Here we will investigate the performance of the down-converted MMW MB OFDM UWB signal in terms of RF modulation index of EAM, received optical power and LO modulation index of the MZM. The RF modulation index of the EAM is defined by $m_{RF} = V_{eff}/V_b$, where V_{eff} is the root mean square of the average applied RF power and V_b is the applied reverse bias voltage. The LO modulation index of the MZM is defined by $m_{lo} = V_{lo}/V_{\pi}$, where V_{π} is the half-wave switching voltage of the MZM.

First we set the received optical power at the photodetector to 0 dBm by the EDFA. We vary the RF modulation index of the EAM by changing the peak to peak voltage of the generated UWB signal from the AWG7122B. The measured EVM versus modulation index is shown in Figure 7.19. It is clear that the EVM degrades at low and high modulation index where noise at the low index and nonlinear distortion at the high index become dominant. Therefore, there is an optimum RF modulation index of around 7.5% to achieve the maximum SNR and minimum EVM. The good quality of the down-converted MMW MB-OFDM UWB signal is seen from the measured constellation (Figure 7.19 inset (a) and (b)).

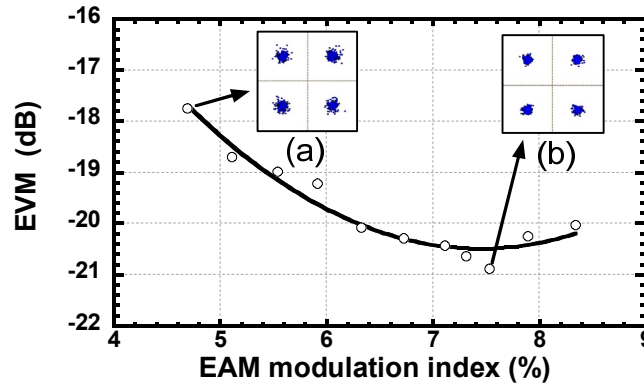


Figure 7.19 EVM versus RF modulation index of the EAM. Received optical power is 0 dBm and the LO power to the DE-MZM is 16.5 dBm.

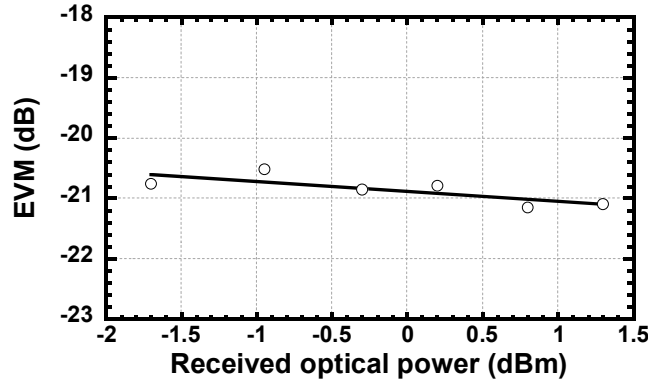


Figure 7.20 EVM performance versus received optical power. RF modulation index is 7.5 % and LO signal power to the DE-MZM is 16.5 dBm ($m_{lo} = 42\%$).

Next, we set the RF modulation index to 7.5 % and vary the received optical power at the photodetector. The EAM is operated in the linear region (minimum 3rd IMD) as shown in Figure 7.16. Measured EVM versus received optical power is shown in Figure 7.20. It is clearly seen that the EVM decreases slowly and linearly with the increase of the received optical power. This indicates that this down-conversion technique is less sensitive to the received optical power, to some extent. In the absence of other imperfections such as gain and phase imbalance of the transmitter's IQ modulator and phase noise from the MMW and/or RF sources, the minimum EVM can be expressed as [25] $EVM_{\min} = 1/\sqrt{SNR}$, in which the shot noise and signal-ASE beat noise are assumed dominant. Therefore, Figure 7.20 can be understood by the fact that optical receiver is limited by signal-ASE beat noise.

We also investigate the EVM performance versus LO modulation index, as shown in Figure 7.21. To obtain this, we fix the peak to peak voltage of the generated UWB signal to 0.85 V, which corresponds to the optimum RF modulation index of the EAM of 7.5%, and vary the power of the LO signal to the MZM from 16.5 to 23.5 dBm. The received optical power at the photodetector is set to 0 dBm. It is clearly seen from Figure 7.21 that the EVM is almost unchanged with the change of LO signal power. The best EVM is obtained at the LO modulation index of $m_{lo} \approx 84\%$. In fact the FWM light is proportional to $J_1^6(\pi m_{lo}/\sqrt{2})$ in optical power, where $J_1(\cdot)$ is the first order Bessel function of the first kind, and the MMW MB-OFDM UWB

modulated optical sideband is proportional to $J_1^2(\pi m_{lo}/\sqrt{2})$ in optical power, thus the power of photodetected MB-OFDM UWB signal at IF frequency is proportional to $J_1^8(\pi m_{lo}/\sqrt{2})$. Assumed that the shot noise and signal-ASE beat noise are dominant at the receiver, the total noise will be proportional $J_1^2(\pi m_{lo}/\sqrt{2})$ in optical power, and therefore the SNR will be proportional to $J_1^6(\pi m_{lo}/\sqrt{2})$. Hence the SNR is maximized and the EVM is minimized when the modulation index maximizes $J_1(\pi m_{lo}/\sqrt{2})$ at $m_{lo} = \sim 84\%$. The good quality of the down-converted MMW MB-OFDM UWB is clearly observed from the measured constellation after 20 km of fiber transmission for LO modulation index of 42.3% and 84.4% as shown in Figure 7.21 inset (a) and (b), respectively. This suggests that this down-conversion technique is less sensitive to LO RF input power.

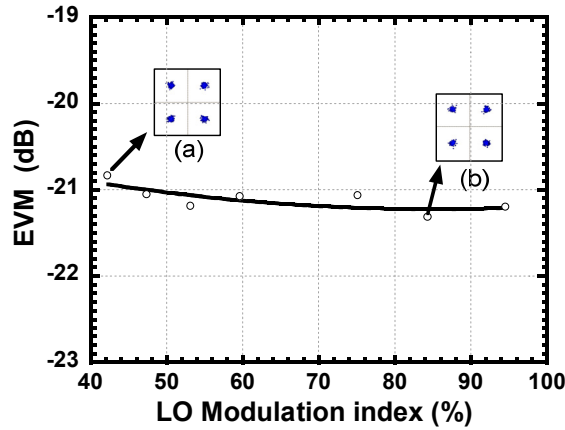


Figure 7.21 EVM versus LO modulation index. RF modulation index of the EAM is 7.5%. Received optical power is 0 dBm.

7.4 Chapter Summary

In this chapter, we first have experimentally investigated the performance of MMW MB-OFDM UWB signal generation and transmission over fiber using an optical frequency quadrupling technique. It is found that $\sim 4\%$ is the optimum RF modulation index of the MZM driven by the MB-OFDM UWB and an LO modulation index of 60% (theoretically) and 70% (experimentally)

is needed to achieve the minimum required EVM of -16 dB after 20 km of fiber transmission. It is also found that typical extinction ratio does not have significant impact on the EVM, whereas bias drift of 20% may degrade the EVM by up to 1 dB. Simulations, theoretical analysis and experiment have been carried out to evaluate the performance of the proposed system and obtained results are in good agreements.

Then, we have experimentally investigated and demonstrated a new technique using FWM in an EAM to down-convert the MMW to IF for MMW over fiber uplinks. FWM efficiency has been studied versus reverse bias voltage and input pump power to the EAM. It is found that maximum FWM efficiency is obtained at 2.3 V reverse bias and increases by a slope of 2 in dB scale with respect to the input pump power. We also have investigated the performance of an MMW MB-OFDM UWB signal down-conversion in an EAM with FWM. It is found that the optimum RF modulation index to the EAM driven by the MB-OFDM UWB, is $\sim 7.5\%$, and the down-conversion is almost insensitive to LO RF input power. It is found that signal to noise ratio can be optimized due to tunability of optical carrier to subcarrier power ratio. Compared to [73], this technique leads to a better signal to noise ratio of down-converted IF signal, and a higher receiver sensitivity. Furthermore, an experimental investigation was conducted with 30 GHz MMW MB-OFDM signal over fiber as an example, considering RF modulation index to EAM, the dual-light power, and receiver sensitivity.

This investigation shows a potential possibility for the proposed photonic up/down-conversion technique to be used for MMW MB-OFDM UWB signal over fiber down/uplinks. In addition, this proposed technique can be applied to 57-64 GHz MMW band.

CHAPTER 8 CONCLUSION

8.1 Concluding Remarks

In this thesis work, we have investigated first of all, in terms of error vector magnitude (EVM), the performance degradation of MB-OFDM UWB transmission over fiber caused by various impairments including MZM nonlinearities, fiber dispersion, receiver optical power and optical receiver response. Also, the performance of MB-OFDM wireless UWB has been experimentally investigated in terms of packet error rate (PER) when transmitted over 20 km of SMF. PER was measured at different bit rates to evaluate the receiver sensitivity, required minimum transmitted UWB power, effect of wireless distance, MZM modulation index, and received optical power etc. In addition, the performance of MB-OFDM UWB has been studied when transmitted over fiber under the influence of relative intensity noise (RIN) considering system parameters such as laser output power, linewidth and fiber transmission length. The performance of MB-OFDM UWB over fiber transmission system has been also assessed considering the effect of in-band jammers such as WiMAX, WLAN MIMO, WLAN and marine radar.

Based on this research it is found that:

- For OSSB modulated MZM, RF modulation index of ~4% is optimum to obtain the best possible EVM performance of MB-OFDM UWB over fiber.
- The optical receiver with fifth order Chebyshev-II response and 3 GHz bandwidth is the best for MB OFDM UWB over fiber in our work.
- Optical receiver sensitivity in UWB over fiber is reasonably low and the performance degrades almost linearly with the decrease of receiver optical power.
- Fiber transmission is further limited by laser phase noise converted RIN due to fiber dispersion and phase distortion induced by fiber dispersion.
- The system should be operated at a high laser output power to avoid RIN degradation.
- A narrow linewidth laser with low RIN will significantly improve system performance.
- Wireless range transmission of MB-OFDM UWB is limited by the receiver sensitivity.

- The performance of MB-OFDM UWB is severely affected by different in-band interferers if certain interferer to UWB peak power ratio is not maintained:

For satisfying the EVM requirement of -16 dB, which is the EVM threshold specified for conformance testing according to the recent WiMedia standard for UWB, this ratio is ~14, ~15, ~17.5 and ~20 dB for WiMAX, Radar, WLAN MIMO and WLAN signals, respectively, for distribution over 20 km of single mode fiber.

Our results will allow future researchers in the field of MB UWB over fiber transmission to optimize performance of UWB over fiber transmission versus systems parameters and under the presence of all possible in-band interferers.

In this work, we have proposed, developed and extensively investigated by theory, simulation and experiment, novel enabling technologies and design techniques for broadband linearization, compensation of chromatic dispersion induced power fading, improving optical modulation efficiency, and MMW up/down conversion for RoF down/up-links. We have also verified and evaluated experimentally the performance of using our proposed techniques for MB-OFDM ultra-wideband (UWB) signal transmission over fiber.

For broadband linearization, we have proposed a mixed polarization for MZM and analog predistortion for EAM. It is found that the 3IMD is suppressed independent of the modulation index. In the mixed polarization technique, the power fading of the RF carrier and crosstalk due to intermodulation via fiber chromatic dispersion are significantly suppressed compared to the case of using the conventional OSSB MZM. SFDR is improved by ~12.5 dB in experiment with good agreement with theory and simulation. Moreover, the proposed technique shows an improvement of 2dB in EVM when applied to MB-OFDM UWB system. A predistortion circuit for linearization of EAM using reflective diode pair has been designed for MB-OFDM UWB system at bandgroup 1 (3.1~ 4.8 GHz). It is found that the designed predistortion circuit leads to 11 dB improvements in the SFDR at the center frequency of bandgroup 1, and more than 7 dB improvements in suppression of IMD3 over the whole bandgroup 1. By evaluating the predistortion circuit with the MB-OFDM UWB signal, a 1-dB EVM improvement is obtained for the first three bands OFDM UWB over 20 km fiber. This suggests that the proposed designs are cost effective broadband linearization technique for MB-OFDM UWB over fiber.

To overcome the fiber chromatic dispersion that causes power fading when ODSB modulation is used, a novel modulation technique has been proposed. This modulation technique also improves the RF power by up to 3 dB compared to OSSB modulation. The main advantage of the proposed technique is simple and implemented in electrical domain with phase shifting. Theoretical analysis was made to obtain the optimum conditions for optimum performance, such as optimum phase shift and impact of MZM extinction ratio. Then simulation was used to further analyze the proposed modulation and compared to the theory. Moreover, we have presented an experimental proof to validate our concept for RF signal consisting of single RF tone or of MB-OFDM UWB signal. By using our proposed modulation technique, a 3-dB RF power improvement, compared to OSSB, was achieved experimentally without degradation of the signal quality.

We have proposed a modulation technique to improve the modulation efficiency in radio over fiber transmission. We have shown that a dMZM modulator can be used for obtaining not only OSSB modulation but also tunability of OCSR. To our knowledge, the function of OCSR tunability using this modulator was proposed and investigated for the first time. It has been shown that a wide dynamic range of OCSR tunability can be obtained by varying the bias voltage applied to the inner MZMs. It was found that the optimum OCSR to obtain maximum RF output power depends on the modulation index and the extinction ratio of the dMZM. To achieve an OCSR of 0 dB there is a minimum required extinction ratio that decreases with the increase of the modulation index. Moreover, we have investigated the impact of OCSR on the performance of MB-OFDM UWB signal. It was found that maximum received RF power is obtained at 0 dB OCSR while minimum EVM of the received MB-OFDM UWB constellation is achieved at 5.4dB OCSR.

The performance of MMW MB-OFDM UWB signal generation and transmission over fiber using an optical frequency up-conversion technique was experimentally demonstrated. It was found that ~4% is the optimum RF modulation index of the MZM driven by the MB-OFDM UWB and an LO modulation index of 60% (theoretically) and 70% (experimentally) is needed to achieve the minimum required EVM of -16 dB after 20 km of fiber transmission. It was also found that typical extinction ratio does not have significant impact on the EVM, whereas bias drift of 20% may degrade the EVM by up to 1 dB.

Table 8. 1 Main Contributions and Comments.

Contributions	Advantages	Drawbacks
Mixed-polarization MZM	<ul style="list-style-type: none"> ▪ 3rd order suppression ▪ Independent of individual modulation indexes ▪ Improved SFDR ▪ Optical single sideband transmission ▪ Broadband, low cost and less complexity 	<ul style="list-style-type: none"> ▪ 10 dB RF power penalty ▪ Applied only to polarization dependent components
Analog predistortion circuit using reflective diodes pair	<ul style="list-style-type: none"> ▪ 3rd order suppression ▪ Independent of individual modulation indexes ▪ Improved SFDR ▪ Applied to any nonlinear components ▪ Broadband, low cost and less complex 	<ul style="list-style-type: none"> ▪ 3 dB RF power penalty
Electrical compensation of power fading due to Fiber chromatic dispersion in ODSB	<ul style="list-style-type: none"> ▪ 3 dB RF power improvement compared to OSSB ▪ Simple implementation in electrical domain 	<ul style="list-style-type: none"> ▪ Require tunable electrical phase shifting
OSSB & Tunable OCSR using dMZM	<ul style="list-style-type: none"> ▪ Wide dynamic of OCSR tunability ▪ Improved modulation efficiency ▪ Optical single sideband transmission ▪ Broadband, low cost and less complex 	<ul style="list-style-type: none"> ▪ DC bias dependent
MMW down-conversion using FWM in EAM	<ul style="list-style-type: none"> ▪ Decrease required LO frequency by four times ▪ Optical single sideband transmission ▪ Broadband, low cost and less complex 	<ul style="list-style-type: none"> ▪ Low efficiency

Finally, we have experimentally investigated and demonstrated a new technique using FWM in an EAM to down-convert the MMW to IF for MMW over fiber uplinks. It was found that FWM efficiency can be maximized by tuning the reverse bias (2.3V) voltage and is increased by a slope of 2 in dB scale with respect to the input pump power. We have also investigated the performance of an MMW MB-OFDM UWB signal down-conversion in an EAM with FWM. It was found that there is an optimum RF modulation index (~7.5%) to the EAM driven by the

MB-OFDM UWB, and the down-conversion is almost insensitive to LO RF input power. This investigation shows a potential for the proposed photonic up/down-conversion technique to be used for MMW MB-OFDM UWB signal over fiber up/downlinks.

Since this work is concerned with a multitude of RoF aspects and many subjects are discussed and studied in detail, Table 8. 1 summarizes the main contributions described in this thesis along with comments on each proposed technique.

8.2 Future Work

The research contributions presented in this thesis may be extended in several ways.

First, MB-OFDM UWB over fiber is a fast emerging technology. However, many areas of UWB over fiber are yet to be explored.

- MB-OFDM UWB over optical wavelength division multiplexing (WDM) WDM is an open research challenge.
- Bi-directional transmission over fiber is another important issue that needs to be addressed. Bi-directional MB-OFDM UWB has great prospect for future access network applications. If the same optical wavelength is used, the study of Rayleigh back scattering (RBS) and stimulated Brillouin scattering (SBS) will be an interesting research topic.
- Investigation of performance of optical transmission by using a low cost EAM or EAM integrated distributed feedback laser (EML) can be done.
- Also, the effect of cross interference from narrowband jammers is not studied in this thesis. Practically two in-band jammers can exist simultaneously i.e. IEEE 802.11b/g at 2.4 GHz and 802.11a at 5.8 GHz can beat together to create harmonics at 3.4 GHz which will interfere with sub-band 1 Band Group 1.
- Besides, MB-OFDM UWB over fiber technology will benefit from studies on MAC layer protocols for optimum transmission performance.

Second, there is a need to investigate if there is a way to further improve the mixed-polarization OSSB MZM by reducing or removing the RF carrier power penalty of ~10 dB.

Also, since the mixed-polarization OSSB MZM was realized with discrete optical components, the next important practical experiment required would be to incorporate the mixed-polarization OSSB MZM on one silicon substrate or module to further investigate its performance.

Third, a further improvement of the predistortion circuit design can be investigated:

- Reduce the size of the predistortion circuit. In this thesis, the broadband impedance matching (from 3.1-4.8 GHz) was achieved by using the three section quarter-wave impedance transformer. However the size of circuit can be reduced by using hard substrate or other impedance matching techniques, for example using hybrid lumped elements and transmission line in the matching circuit or increasing the internal resistor of the diode by inserting a resistor or cascading many diodes in series. In this way, not only the size will be reduced but also the bandwidth will be broadened. After making its size smaller, the predistortion circuit can be fabricated by the Hybrid Microwave Integrated Circuit (HMIC) method, and wrapped into a commercialized microwave IC package.
- The predistortion circuit can also be modified to linearize DFB lasers or MZM. The predistortion circuit and the DFB laser or MZM can be soldered on the same printed circuit board (PCB), and after being packaged, the linearized DFB laser or MZM could be commercialized.
- Instead of using the diode, the transistors could also be used in the push-pull bias to generate the predistortion signal. In this way, the predistortion circuit can not only work as linearizer but also as a low noise amplifier.

Fourth, the pre-compensated ODSB SCM immune to fiber chromatic dispersion induced RF power fading can be very attractive if a broadband and tunable electrical phase shifter is available. This can be made possible by using photonic microwave techniques.

Fifth, in the proposed photonic MMW up-conversion, a balanced MZM with a single drive could be used instead of a DE-MZM to reduce cost.

Sixth, in the proposed photonic MMW down-conversion, it is interesting to investigate the possibility of substituting the EDFA used prior to the EAM, by a semiconductor optical amplifier in order to reduce cost.

Last but not the least, the possibility of integrating all proposed technique in one system with the use of WDM can be investigated.

8.3 List of Publications

1. **B. Hraimel**, X. Zhang, and K. Wu, "Optical Single-Sideband Modulation with Tunable Optical Carrier to Sideband Ratio in Radio over Fiber Systems," *Journal of Lightwave Technology*, submitted.
2. C. Sui, **B. Hraimel**, X. Zhang, L. Wu, Y. Shen, K. Wu, T. Liu, T. Xu and Q. Nie, "Impact of Electro-Absorption Modulator Integrated Laser on MB-OFDM Ultra-Wideband Signals over Fiber Systems," *Journal of Lightwave Technology*, under review.
3. Y. Pei, Xiupu Zhang , K. Xu, X. Sun, **B. Hraimel**, J. Wu and J. Lin, "Power Control for Radio-over-Fiber Downlinks in Frequency Division Multiplexing Cellular Communication Systems," *IEEE/OSA J. Optical Communications and Networking*, accepted 2010.
4. M. N. Sakib, **B. Hraimel**, X. Zhang, K. Wu, T. Liu, T. Xu, and Q. Nie, "Impact of Laser Relative Intensity Noise on Multiband OFDM Ultra Wideband Wireless Signal over Fiber System," *OSA/IEEE J. Optical Communications and Networking*, vol. 2, no. 10 , 2010.
5. **B. Hraimel**, W. Jiang, X. Zhang, K. Wu, T. Liu, T. Xu, Q. Nie, and K. Xu, "Experimental Demonstration of a Mixed-Polarization to Linearize Electro-Absorption Modulators in Radio-over-Fiber Links," *Photonics Technology Letters*, submitted.
6. L. Wu, **B. Hraimel** , X. Zhang, K. Wu, M. Mohamed, and C. Sui, "Photonic Generation of Millimeter-Waves Using Two Cascaded Electro-Absorption Modulators in Radio-over-Fiber Systems," *2010 International Topical Meeting Microwave Photonics, 5-9 Oct. 2010*, accepted.
7. Y. Pei, **B. Hraimel**, Y. Shen, Kun Xu, X. Zhang, X. Sun, J. Wu, and J. Lin, "Performance Characterization and Limitation of Coherence Multiplexing Technique in Radio over Fiber Systems," *2010 International Topical Meeting Microwave Photonics, 5-9 Oct. 2010*, accepted.
8. C. Sui, **B. Hraimel**, X. Zhang, and K. Wu, "Performance Evaluation of MB-OFDM Ultra-Wideband Over Fiber Transmission Using a Low Cost Electro-Absorption Modulator Integrated Laser," *2010 International Topical Meeting Microwave Photonics, 5-9 Oct. 2010*, accepted.
9. Y. Shen, **B. Hraimel**, X. Zhang, G. Cowan, K. Wu, and T. Liu, "A Novel Analog Broadband RF Predistortion Circuit to Linearize Electroabsorption Modulator in Multiband OFDM Ultra-Wideband Radio over Fiber System," *IEEE Transaction on Microwave Theory and Technique, special issue on Microwave Photonics*, accepted 2010.
10. **B. Hraimel**, X. Zhang, and K. Wu, "Photonic Down-Conversion of Millimeter Wave Multiband Orthogonal Frequency Division Multiplexing Ultra-Wideband Using Four

- Wave Mixing in an Electro-Absorption Modulator,” *IEEE/OSA Journal of Lightwave Technology*, vol. 28, no. 13, pp. 1987-1993, July 2010.
11. M. Mohamed, **B. Hraimel**, and X. Zhang, “Optical Generation of Millimeter Wave Multiband OFDM UWB Wireless Signal and Distribution over Fiber,” *Photonics Technology Letters*, vol. 22, no. 15, pp. 1180-1182, Aug. 2010.
 12. **B. Hraimel**, X. Zhang, M. Mohamed, and K. Wu, “Precompensated Optical Double-Sideband Subcarrier Modulation Immune to Fiber Chromatic Dispersion Induced RF Power Fading,” *OSA/IEEE J. Optical Communications and Networking*, vol. 1, no. 4, pp. 331–342, 2009.
 13. **B. Hraimel**, X. Zhang, M. Mohamed, M. Sakib, and K. Wu “Performance Improvement of Multiband OFDM Ultra-Wideband over Fiber Link using a Novel Optical Double Sideband Subcarrier Modulation Scheme,” *International Microwave Symposium*, paper TUPF-2, Boston, USA, June 2009.
 14. **B. Hraimel**, X. Zhang, M. Mohamed, and K. Wu, “Electrical Compensation of Fiber Chromatic Dispersion Induced RF Power Fading in Optical Double-Sideband Subcarrier Modulation,” *OFC/NFOEC*, paper JWA55, USA, Mar. 2009
 15. **B. Hraimel**, M. Mohamed, X. Zhang, and K. Wu, “Transmission performance of multiband orthogonal frequency division multiplexing ultra-wideband wireless systems with fiber distribution,” *Asia-Pacific Microwave Photonics Conference 2009 (APMP)*, paper C06, Beijing, April 2009.
 16. B. Masella, **B. Hraimel**, and X. Zhang, "Mixed-polarization to improve dynamic range of optical single sideband in a Mach-Zehnder modulator," in *2009 Conference on Optical Fiber Communication - OFC 2009, 22-26 March 2009*, Piscataway, NJ, USA, 2009, pp. 1-3.
 17. M. Mohamed, **B. Hraimel**, X. Zhang, M. N. Sakib, and K. Wu, “Performance of millimeter wave MB-OFDM ultra wideband signal generation using optical frequency up-conversion and transmission over fiber,” *Asia-Pacific Microwave Photonics Conference 2009*.
 18. M. Sakib, **B. Hraimel**, X. Zhang, M. Mohamed, and K. Wu, “Effect of Relative Intensity Noise Induced Distortion on Multiband OFDM Ultra-Wideband over Fiber System,” *APMP*, paper J03, Beijing, April 2009.
 19. B. Masella, **B. Hraimel**, and X. Zhang , "Enhanced Spurious-Free Dynamic Range Using Mixed Polarization in Optical Single Sideband Mach–Zehnder Modulator," *Journal of Lightwave Technology*, vol. 27, pp. 3034-3041, 2009.
 20. X. Zhang, M. Sakib, **B. Hraimel**, K. Wu, M. Mohamed, and Dongya Shen, “Multiband OFDM Ultra-Wideband wireless communication systems with Fiber distribution,” *IEEE Communications Magazine*, December 2009.
 21. M. N. Sakib, **B. Hraimel**, X. Zhang, and K. Wu, “Investigation of the performance of multiband orthogonal frequency division multiplexing ultrawideband over fiber transmission under the presence of in-band interferers,” *IEEE/OSA Journal of Optical Communications and Networking*, vol. 1, pp. 235-44, 2009.

22. M. Mohamed, **B. Hraimel**, X. Zhang, and M. Sakib, "Optical Generation of Millimeter Wave Multiband OFDM Ultra-Wideband Wireless Signal and Transmission over Fiber," *International Conference on Advanced Infocomm Technology*, Xi'an, China, July 2009.
23. M. Sakib, **B. Hraimel**, X. Zhang, M. Mohamed, W. Jiang, K. Wu, and Dongya Shen "Impact of Optical Transmission on Multiband OFDM Ultra-Wideband Wireless System with Fiber Distribution," *IEEE/OSA Journal of Lightwave Technology*, vol. 27, pp. 4112-4123, 2009.
24. M. Mohamed, **B. Hraimel**, X. Zhang, M. N. Sakib, and Ke, Wu, "Frequency quadrupler for millimeter-wave multiband OFDM ultrawideband wireless signals and distribution over fiber systems," *IEEE/OSA Journal of Optical Communications and Networking*, vol. 1, pp. 428-38, 2009.
25. M. Mohamed, **B. Hraimel**, X. Zhang, and M. Sakib, "Performance of Optical Frequency Multiplication for Millimeter Wave MB-OFDM Ultrawideband Signal Generation and Distribution in RoF Systems," *IEEE International Conference on Broadband Network and Multimedia Technology*, China, October 2009.
26. M. Mohamed, **B. Hraimel**, X. Zhang, and K. Wu, "Efficient photonic generation of millimeter-waves using optical frequency multiplication in radio-over-fiber systems," in *2007 International Topical Meeting Microwave Photonics, 3-5 Oct. 2007*, Piscataway, NJ, USA, 2007, pp. 179-82.
27. M. Mohamed, **B. Hraimel**, X. Zhang, and K. Wu, "Frequency sixupler for millimeter-wave signal generation and transmission in radio-over-fiber systems," *Proceeding of ICAIT*, paper conf189a16, Da Meisha, China, July 2008.
28. M. Mohamed, **B. Hraimel**, X. Zhang, and K. Wu, "Frequency sixupler for millimeter-wave over fiber systems," *Optics Express*, vol. 16, pp. 10141-51, 2008.
29. M. Mohamed, **B. Hraimel**, X. Zhang, and K. Wu, "Analysis of frequency quadrupling using a single Mach-Zehnder modulator for millimeter-wave generation and distribution over fiber systems," *Optics Express*, vol. 16, pp. 10786-10802, 2008.
30. **B. Hraimel**, R. Kashyap, X. Zhang, J. Yao, and K. Wu, "Large signal analysis of fiber dispersion effect on photonic up-conversion in radio over fiber link using dual electrode Mach-Zehnder external modulator," in *Photonics North 2006, 5-8 June 2006*, USA, 2006, pp. 63432-1.
31. **B. Hraimel**, M. O. Twati, and K. Wu, "Closed-form dynamic range expression of dual-electrode Mach-Zehnder modulator in radio-over-fiber WDM system," *Journal of Lightwave Technology*, vol. 24, pp. 2380-7, 2006.

REFERENCES

- [1] H. Al-Raweshidy and S. Komaki, *Radio over fiber technologies for mobile communications networks*, 1st ed. ed.: Artech House Boston, MA, 2002.
- [2] B. Dang and I. Niemegeers, "Analysis of IEEE 802.11 in radio over fiber home networks," 2005, pp. 744-747.
- [3] P. Tang, *et al.*, "PER and EVM measurements of a radio-over-fiber network for cellular and WLAN system applications," *Lightwave Technology, Journal of*, vol. 22, pp. 2370-2376, 2004.
- [4] http://www.naic.edu/~astro/RXstatus/Lnarrow/fcc_UWB.pdf [Online].
- [5] http://www.ieee802.org/15/pub/2003/Jul03/03268r2P802-15_TG3a-Multi-band-CFP-Documents.pdf [Online].
- [6] G. Heidari, *WiMedia UWB: technology of choice for wireless USB and Bluetooth*: Wiley Publishing, 2008.
- [7] <http://www.ecma-international.org/publications/files/ECMA-ST/ECMA-368.pdf> [Online].
- [8] M. Welborn, "System considerations for ultra-wideband wireless networks," 2001.
- [9] <http://www.vpiphotonics.com/> [Online].
- [10] U. Gliese, *et al.*, "Chromatic dispersion in fiber-optic microwave and millimeter-wave links," *Microwave Theory and Techniques, IEEE Transactions on*, vol. 44, pp. 1716-1724, 1996.
- [11] J. Yu, *et al.*, "Centralized lightwave WDM-PON employing 16-QAM intensity modulated OFDM downstream and OOK modulated upstream signals," *IEEE Photonics Technology Letters*, vol. 20, pp. 1545-1547, 2008.
- [12] G. Smith, *et al.*, "Technique for optical SSB generation to overcome dispersion penalties in fibre-radio systems," *Electronics Letters*, vol. 33, p. 74, 1997.
- [13] V. Urick and F. Bucholtz, "Compensation of arbitrary chromatic dispersion in analog links using a modulation-diversity receiver," *IEEE Photonics Technology Letters*, vol. 17, pp. 893-895, 2005.
- [14] H. Sun, *et al.*, "Tunable RF-power-fading compensation of multiple-channel double-sideband SCM transmission using a nonlinearly chirped FBG," *IEEE Photonics Technology Letters*, vol. 12, pp. 546-548, 2000.
- [15] H. Sotobayashi and K. Kitayama, "Cancellation of the signal fading for 60 GHz subcarrier multiplexed optical DSB signal transmission in nondispersion shifted fiber using midway optical phase conjugation," *Journal of Lightwave Technology*, vol. 17, p. 2488, 1999.
- [16] H. Sotobayashi and K. Kitayama, "Effects of asymmetric power change on BER performance using midway optical phase conjugation for fading cancellation in 60 GHz

- millimetre-wave optical DSB signal transmission over 100 km non-dispersion-shifted fibre," *Electronics Letters*, vol. 35, pp. 992-993, 1999.
- [17] M. Attygalle, *et al.*, "Extending optical transmission distance in fiber wireless links using passive filtering in conjunction with optimized modulation," *Journal of Lightwave Technology*, vol. 24, p. 1703, 2006.
 - [18] M. Attygalle, *et al.*, "Transmission improvement in fiber wireless links using fiber Bragg gratings," *IEEE Photonics Technology Letters*, vol. 17, pp. 190-192, 2005.
 - [19] S. Xiao and A. Weiner, "Optical carrier-suppressed single sideband (O-CS-SSB) modulation using a hyperfine blocking filter based on a virtually imaged phased-array (VIPA)," *IEEE Photonics Technology Letters*, vol. 17, pp. 1522-1524, 2005.
 - [20] K. Williams and R. Esman, "Stimulated Brillouin scattering for improvement of microwave fibre-optic link efficiency," *Electronics Letters*, vol. 30, p. 1965, 1994.
 - [21] W. Hu, *et al.*, "High SNR 50 GHz radio-over-fibre uplink system by use of low biased Mach-Zehnder modulator technique," *Electronics Letters*, vol. 42, pp. 550-552, 2006.
 - [22] A. Gaeta and R. Boyd, "Stochastic dynamics of stimulated Brillouin scattering in an optical fiber," *Physical Review A*, vol. 44, pp. 3205-3209, 1991.
 - [23] K. Mandke, *et al.*, "The evolution of ultra wide band radio for wireless personal area networks," *Spectrum*, vol. 3, p. 10.6, 2003.
 - [24] C. Zhao and R. Baxley, "Error vector magnitude analysis for OFDM systems," 2006, pp. 1830-1834.
 - [25] A. Georgiadis, "Gain, phase imbalance, and phase noise effects on error vector magnitude," *IEEE Transactions on Vehicular Technology*, vol. 53, pp. 443-449, 2004.
 - [26] W. Siriwongpairat and K. Liu, *Ultra-wideband communications systems: multiband OFDM approach*: Wiley-IEEE Press, 2007.
 - [27] S. Ghassemzadeh and V. Tarokh, "UWB path loss characterization in residential environments," 2003, pp. 501-504.
 - [28] X. Li and L. Cimini Jr, "Effects of clipping and filtering on the performance of OFDM," 1997.
 - [29] L. Paarmann, *Design and analysis of analog filters*: Kluwer Academic Publishers, 2001.
 - [30] D. Pozar, "Microwave Engineering, 3rd," ed: John Wiley & Sons, Hoboken, NJ, USA, 2007, pp. 77-78.
 - [31] W. Marshall, *et al.*, "Laser phase noise to intensity noise conversion by lowest-order group-velocity dispersion in optical fiber: exact theory," *Optics Letters*, vol. 25, pp. 165-167, 2000.
 - [32] P. Laurencio and M. Medeiros, "Relative Intensity Noise in Optical Single Side Band Systems with Multiple In-Line Amplifiers: Analysis and Validation," *Fiber and Integrated Optics*, vol. 27, pp. 78-88, 2008.
 - [33] <http://eurlex.europa.eu/LexUriServ/LexUriServ.do?uri=OJ:L:2008:144:0077:008>

- 1:EN:PDF, "European Commission's decision of 21:5:2008 on the harmonization of 3400~3800 MHz frequency band for terrestrial system capable of providing electronic communication services in the community."
- [34] http://standards.ieee.org/announcements/ieee802.11n_2009amendment_ratified.html, 2009.
- [35] <http://easy.intranet.gr/IEEE80211a.pdf> [Online].
- [36] L. Roselli, *et al.*, "Analog laser predistortion for multiservice radio-over-fiber systems," *Journal of Lightwave Technology*, vol. 21, p. 1211, 2003.
- [37] G. Wilson, *et al.*, "Predistortion of electroabsorption modulators for analog CATV systems at 1.55 μm ," *Lightwave Technology, Journal of*, vol. 15, pp. 1654-1662, 1997.
- [38] H. Lu, *et al.*, "Intermodulation distortion suppression in a full-duplex radio-on-fiber ring network," *IEEE Photonics Technology Letters*, vol. 16, pp. 602-604, 2004.
- [39] V. Urick, *et al.*, "Wide-band predistortion linearization for externally modulated long-haul analog fiber-optic links," *IEEE Transactions on Microwave Theory and Techniques*, vol. 54, pp. 1458-1463, 2006.
- [40] N. Imai, *et al.*, "Novel linearizer using balanced circulators and its application to multilevel digital radio systems," *IEEE Transactions on Microwave Theory and Techniques*, vol. 37, pp. 1237-1243, 1989.
- [41] S. C. Bera, *et al.*, "Diode-based predistortion lineariser for power amplifiers," *Electronics Letters*, vol. 44, pp. 125-127, 2008.
- [42] H. Jeong, *et al.*, "A design of K-band predistortion linearizer using reflective Schottky diode for satellite TWTAs," 2005, pp. 597-600.
- [43] L. Roselli, *et al.*, "An active cubic circuit for power amplifier analog predistortion," 2003.
- [44] H. Park, *et al.*, "Analysis and design of compact third-order intermodulation generation circuits," *Microwave and Optical Technology Letters*, vol. 51, 2009.
- [45] L. Roselli, *et al.*, "Predistortion circuit design for II and III order simultaneous linearization in multiservice telecommunications apparatuses," in *Microwave Symposium Digest, 2002 IEEE MTT-S International*, 2002, pp. 1711-1714.
- [46] S. P. Stapleton, "Amplifier linearization using adaptive digital predistortion," *Applied Microwave & Wireless*, vol. 13, pp. 72-74, 2001.
- [47] T. Iwai, *et al.*, "Signal distortion and noise in AM-SCM transmission system employing the feedforward linearized MQW-EA external modulator," *Lightwave Technology, Journal of*, vol. 13, pp. 1606-1612, 1995.
- [48] W. Choi, "Nonlinearity suppression of electroabsorption modulator through dual-parallel modulation," *Microwave and Optical Technology Letters*, vol. 29, p. 2, 2001.
- [49] S. Sohn and S. Han, "Linear optical modulation in a serially cascaded electroabsorption modulator," *Microwave and Optical Technology Letters*, vol. 27, pp. 447-450, 2000.

- [50] S. Mathai, *et al.*, "Experimental demonstration of a balanced electroabsorption modulated microwave photonic link," *IEEE Transactions on Microwave Theory and Techniques*, vol. 49, pp. 1956-61, 2001.
- [51] Y. Wu, "Optical heterodyned radio over fiber link design using electro-absorption and electro-optic modulators," PHD, University of California, San Diego, Chapter 6, 2004.
- [52] J. Brooks, *et al.*, "Implementation and evaluation of a dual parallel linearizationsystem for AM-SCM video transmission," *Journal of Lightwave Technology*, vol. 11, pp. 34-41, 1993.
- [53] T. Cho and K. Kim, "Effect of third-order intermodulation on radio-over-fiber systems by a dual-electrode Mach-Zehnder modulator with ODSB and OSSB signals," *Journal of Lightwave Technology*, vol. 24, p. 2052, 2006.
- [54] B. M. Haas and T. E. Murphy, "A simple, linearized, phase-modulated analog optical transmission system," *IEEE Photonics Technology Letters*, vol. 19, pp. 729-31, 2007.
- [55] A. Ramaswamy, *et al.*, "Coherent receiver based on a broadband optical phase-lock loop," 2007.
- [56] L. Johnson and H. Roussel, "Reduction intermodulation distortion in interferometric optical modulators," *Optics Letters*, vol. 13, pp. 928-930, 1988.
- [57] S. Maas, *Nonlinear microwave and RF circuits*, 2nd Edition ed.: Artech House Publishers, 2003.
- [58] B. Hraimel, *et al.*, "Closed-form dynamic range expression of dual-electrode Mach-Zehnder modulator in radio-over-fiber WDM system," *Journal of Lightwave Technology*, vol. 24, pp. 2380-2387, 2006.
- [59] B. Hraimel, *et al.*, "Large signal analysis of fiber dispersion effect on photonic up-conversion in radio over fiber link using dual electrode Mach-Zehnder external modulator," 2006, p. 63432L.
- [60] M. Mohamed, *et al.*, "Efficient photonic generation of millimeter-waves using optical frequency multiplication in radio-over-fiber systems," 2007, pp. 179-182.
- [61] M. Mohamed, *et al.*, "Analysis of frequency quadrupling using a single Mach-Zehnder modulator for millimeter-wave generation and distribution over fiber systems," *Opt. Express*, vol. 16, pp. 10786-10802, 2008.
- [62] M. Mohamed, *et al.*, "Frequency sixupler for millimeter-wave over fiber systems," *Opt. Express*, vol. 16, pp. 10141-10151, 2008.
- [63] C. Lim, *et al.*, "Analysis of optical carrier-to-sideband ratio for improving transmission performance in fiber-radio links," *IEEE Transactions on Microwave Theory and Techniques*, vol. 54, pp. 2181-2187, 2006.
- [64] K. Higuma, *et al.*, "X-cut lithium niobate optical single-sideband modulator," *Electronics Letters*, vol. 37, pp. 515-16, 2001.
- [65] P.-T. Shih, *et al.*, "Hybrid access network integrated with wireless multilevel vector and wired baseband signals using frequency doubling and no optical filtering," *IEEE Photonics Technology Letters*, vol. 21, pp. 857-859, 2009.

- [66] C. Lin, *et al.*, "Generation of Carrier Suppressed Optical mm-wave Signals using Frequency Quadrupling and no Optical Filtering," 2008.
- [67] J. Ma, *et al.*, "64GHz optical millimeter-wave generation by octupling 8GHz local oscillator via a nested LiNbO₃ modulator," *Optics and Laser Technology*, 2009.
- [68] Q. Chang, *et al.*, "Generation and Transmission of Optical Carrier Suppressed-Optical Differential (Quadrature) Phase-Shift Keying (OCS-OD (Q) PSK) Signals in Radio Over Fiber Systems," *Journal of Lightwave Technology*, vol. 26, pp. 2611-2618, 2008.
- [69] H. Chi and J. Yao, "Frequency quadrupling and upconversion in a radio over fiber link," *Lightwave Technology, Journal of*, vol. 26, pp. 2706-2711, 2008.
- [70] J. Yu, *et al.*, "Optical millimeter-wave generation or up-conversion using external modulators," *IEEE Photonics Technology Letters*, vol. 18, pp. 265-267, 2006.
- [71] M. Sakib, *et al.*, "Impact of optical transmission on multiband OFDM ultra-wideband wireless system with fiber distribution," *J. Lightwave Technol*, vol. 27, pp. 4112-4123, 2009.
- [72] J. Seo, *et al.*, "Remote optoelectronic frequency down-conversion using 60-GHz optical heterodyne signals and an electroabsorption modulator," *IEEE Photonics Technology Letters*, vol. 17, pp. 1073-1075, 2005.
- [73] Z. Xu, *et al.*, "Electroabsorption Modulator Frequency Down-Conversion for Uplink Radio-Over-Fiber," *IEEE Photonics Technology Letters*, vol. 20, pp. 1875-1877, 2008.
- [74] E. Awad, *et al.*, "Simultaneous four-wave mixing and cross-absorption modulation inside a single EAM for high-speed optical demultiplexing and clock recovery," *IEEE Photonics Technology Letters*, vol. 17, pp. 1534-1536, 2005.
- [75] T. Mori and H. Kawaguchi, "Characteristics of nondegenerate four-wave mixing in electroabsorption modulator," *Applied Physics Letters*, vol. 85, p. 869, 2004.
- [76] X. Zhang, *et al.*, "A novel millimeter-wave-band radio-over-fiber system with dense wavelength-division multiplexing bus architecture," *IEEE Transactions on Microwave Theory and Techniques*, vol. 54, p. 929, 2006.
- [77] C. Lim, *et al.*, "Investigation of Intermodulation Distortion Reduction Technique for Multi-Channel Fiber-Radio Transmission in Heterogeneous Access Networks," 2006, pp. 264-265.

APPENDIX A

UWB Standardization

IEEE is one of the pioneers in standardizing the UWB. In December 2002, IEEE 802.15.3a was formed to address high data rate UWB. The task groups eventually choose two technologies for UWB: MB-OFDM or Direct sequence (DS) CDMA. MB OFDM approach has more supporters but it failed to achieve super majority (70%). The battle between two sides became more political and the draft standard came to a standstill.

WiMedia

The supporters for MB OFDM approach bypassed IEEE and started their own standardization effort. The group was led by Intel, Texas Instruments, Nokia, HP, Samsung, and Sony and was followed by many others. They formed WiMedia Alliance which is a nonprofit organization that promotes MB OFDM UWB.

ECMA

ECMA International is a standardization body which aims to facilitate the standardization of technologies in information and communication technology. WiMedia submitted its specification to ECMA in 2005. In the same year ECMA approved the publication of the first combined PHY layer and MAC sub layer specification in single document called ECMA-368. ECMA-368 has been widely accepted by most UWB PHY developers. In December 2007 the ECMA-368 underwent another revision. ECMA-368 has also been published by International Organization for Standardization (ISO) and European Telecommunication Standards Institute (ETSI) named ISO/IEC 26907 and ETSI IS 102455 respectively.

Current Worldwide Regulations

US FCC is the pioneer in standardizing the UWB. Other countries quickly followed FCC initiative. After FCC Japan's Ministry of Internal affairs and Communications (MIC) made its rulings in September 2005. MIC introduced some new concepts in their rulings. One of them is the introduction of Detection-And-Avoidance (DAA) scheme. In DAA scheme UWB transceiver first send a beacon signal to detect any other narrowband transmitters in its close proximity and if an interferer is present UWB devices switch to next available frequency sub-

band. On February 21, 2007 European Commission (EC) released a policy document in favor of allocating spectrum for UWB. The policy requires a DAA scheme for Band Group 1. Ministry of Information and Communications (MIC) in Korea adopted a UWB spectrum similar to Japan and EC. Chinese Ministry of information and Industry (MII) has not yet finalized its policy on UWB. MII's draft resolution requires DAA scheme for sub-band 3 of Band group 1.

MB UWB Wireless Transmitter and Receiver

The structure of an MB OFDM transmitter and receiver is shown in Figure A. 1. At the transmitter the input data stream is first scrambled. The purpose of the data scrambler is to convert a data bit sequence into pseudorandom sequence that is free from long strings of simple patterns such as ones and zeroes. Then the data is conventionally encoded which improves the SNR due to addition of patterns of redundancy. The basic coding rate is usually called mother encoding rate. To obtain other coding rates the coded sequence again punctured. Puncturing is a procedure for omitting some encoded bits at the transmitter and inserting dummy zero into the sequence received at the receiver in place of the bits omitted. The third block in the UWB transmitter is the bit interleaver. Bit interleaver provides robustness against burst errors, which consists of a symbol interleaving followed by tone interleaving. Then the bit interleaved sequence is mapped into a sequence of QPSK symbols according to gray coded constellation as shown in Figure A. 2. The complex valued sequence from constellation mapper is then OFDM modulated. The sequence is first converted in to parallel sequence. After adding pilot, guard and null tones the IFFT is performed. The OFDM signal is up-converted to a specific sub band. Each OFDM symbol contains 128 subcarriers with symbol duration of $T_s = 242.42$ ns as presented. After digital to analog conversion, each band or channel will be imposed on a RF carrier.

The operation of the receiver is similar to the transmitter. The high frequency signal is passed through a preselect filter, amplified with an RF amplifier and down converted into baseband. After performing synchronization FFT is done to demodulate QPSK symbols from the received OFDM signal. From the QPSK symbols an estimated bit sequence is reconstructed and de-interleaved. The QPSK sequence is then channel decoded using Viterbi algorithm [5]. Finally the decoder output is descrambled to desired bit sequence.

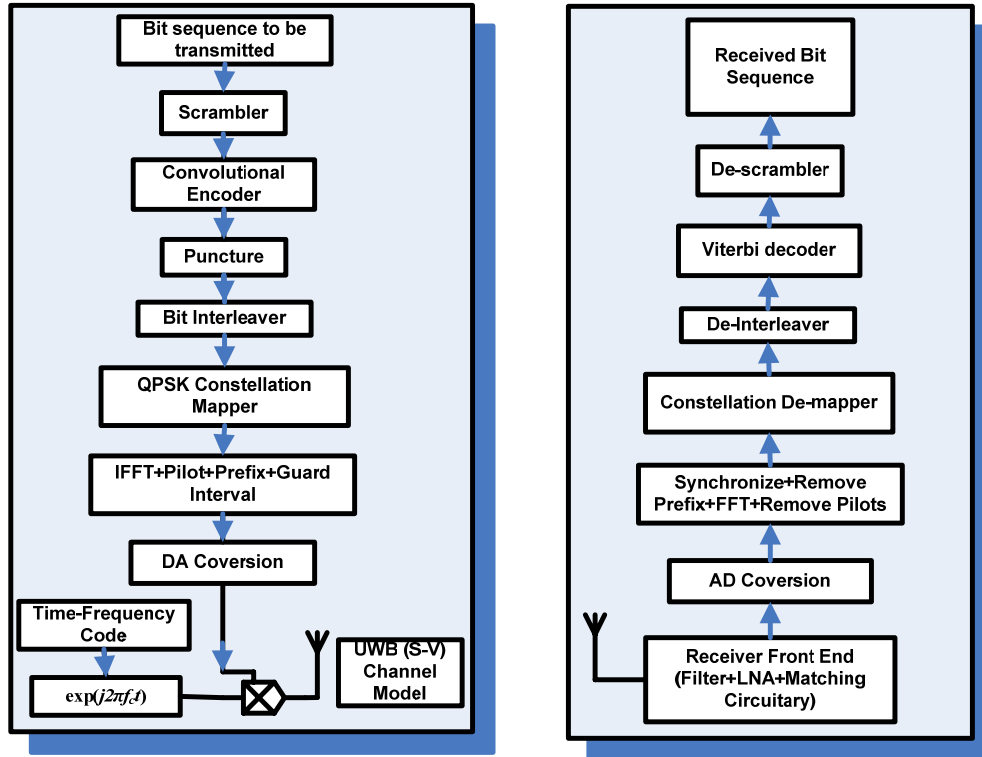


Figure A. 1 UWB transmitter and receiver [5].

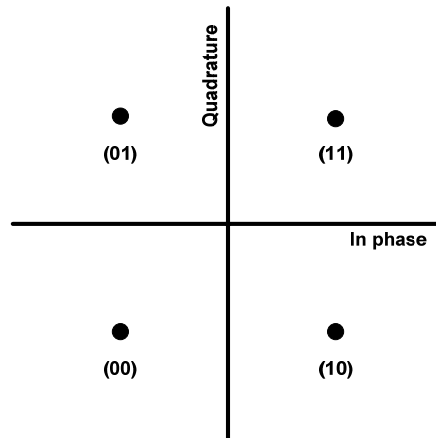


Figure A. 2 QPSK constellation [5].

Timing and Synchronization Parameters

The main timing related parameters for an MB OFDM system are shown in Table A. 1.

Table A. 1 Timing Related Parameters of MB OFDM [5].

Parameter	Description	Value
f_s	Sampling frequency	528 MHz
N_{FFT}	Total number of subcarriers (FFT size)	128
N_D	Number of data subcarriers	100
N_P	Number of pilot subcarriers	12
N_G	Number of guard subcarriers	10
N_T	Total number of subcarriers used	122 ($= N_D + N_P + N_G$)
Δf	Subcarrier frequency spacing	4.125 MHz ($= f_s / N_{\text{FFT}}$)
T_{FFT}	IFFT and FFT period	242.42 ns ($= 1 / \Delta f$)
T_{CP}	Cyclic prefix duration	60.61 ns ($= 32 / 528 \text{ MHz}$)
T_{GI}	Guard interval duration	9.47 ns ($= 5 / 528 \text{ MHz}$)
T_{SYM}	Symbol duration	312.5 ns ($= T_{\text{FFT}} + T_{\text{CP}} + T_{\text{GI}}$)

Modes of Operation

Figure A. 3 and Table A. 2 show different bands MB OFDM UWB. Group 1 is mandatory and other groups are optional. This is mainly due to the unavailability of the CMOS hardware at higher frequencies. As stated earlier the bands are hoped using simple sequences as shown in Table A. 3 to avoid unwanted interference and support multiple users.

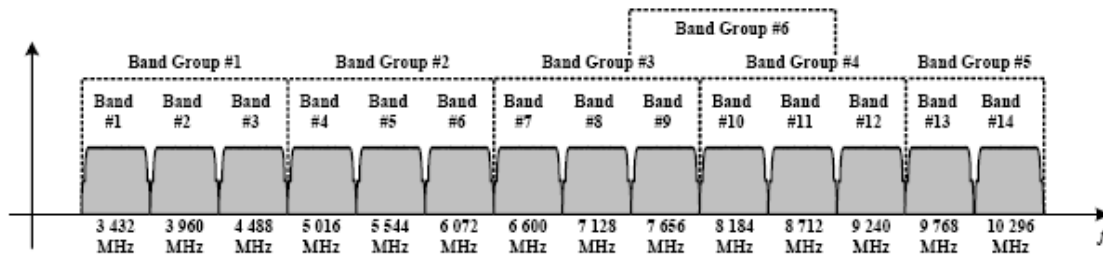


Figure A. 3 Band Group allocation for MB OFDM UWB [7].

Table A. 2 Band Group allocation for MB OFDM UWB [7].

Band Group	BAND ID	Lower Frequency (MHz)	Center Frequency (MHz)	Upper Frequency (MHz)
1	1	3168	3432	3696
	2	3696	3960	4224
	3	4224	4488	4752
2	4	4752	5 016	5280
	5	5280	5544	5808
	6	5808	6072	6336
3	7	6336	6600	6864
	8	6864	7128	7392
	9	7392	7656	7920
4	10	7920	8184	8448
	11	8448	8712	8976
	12	8976	9240	9504
5	13	9504	9768	10032
	14	10032	10296	10560
6	9	7392	7656	7920
	10	7920	8184	8448
	11	8448	8712	8976

Table A. 3 Time frequency codes for Group-1 MB OFDM system [7].

TFC Number	Hoping Sequence					
1	1	2	3	1	2	3
2	1	3	2	1	3	2
3	1	1	2	2	3	3
4	1	1	3	3	2	2
5	1	1	1	1	1	1
6	2	2	2	2	2	2
7	3	3	3	3	3	3
8	1	2	1	2	1	2
9	1	3	1	3	1	3
10	2	3	2	3	2	3

Data Rate Dependent Parameters

Table A. 4 and Table A. 5 lists data rate dependent parameters and receiver sensitivity for an MB OFDM UWB system, respectively. For bit rates lower than 200Mb/s MB-OFDM UWB uses QPSK while for higher bit rate advanced dual carrier modulation technique (DCM) is used. Maximum permissible relative constellation error or root mean square EVM is depicted in Table A. 6.

Table A. 4 Data rate dependent parameters MB OFDM system [7].

Data Rate (Mb/s)	Modulation	Coding Rate (R)	Frequency Spreading	Time Spreading	Coded Bits / 6 OFDM Symbol	Info Bits / 6 OFDM Symbol
53.3	QPSK	1/3	YES	YES	300	100
80	QPSK	1/2	YES	YES	300	150
106.7	QPSK	1/3	NO	YES	600	200
160	QPSK	1/2	NO	YES	600	300
200	QPSK	5/8	NO	YES	600	375
320	DCM	1/2	NO	NO	1200	600
400	DCM	5/8	NO	NO	1200	750
480	DCM	3/4	NO	NO	1200	900

Table A. 5 Sensitivity of UWB receiver [7].

Data Rate (Mb/s)	Minimum Receiver Sensitivity (dBm)
53.3	-80.8
80	-78.9
106.7	-77.8
160	-75.9
200	-74.5
320	-72.8
400	-71.5
480	-70.4

Table A. 6 Permissible Relative Constellation Error (EVM).

Data Rate	Relative Constellation RMS Error		
	No TX Attenuation	TX Attenuation of 2, 4, 6 dB (All TFCs)	TX Attenuation of 8, 10, 12 dB (All TFCs)
53.3 Mb/s, 80 Mb/s, 106.7 Mb/s, 160 Mb/s, 200 Mb/s	−17.0 dB	−15.5 dB	−14.5 dB
320 Mb/s, 400 Mb/s, 480 Mb/s	−19.5 dB	−18.0 dB	−17.0 dB

APPENDIX B ANALYSIS OF OPTICAL RECEIVER NOISE

Let us assume the optical and electrical filter are rectangular with equivalent bandwidth $B_o = \frac{1}{2\pi} \int_{-\infty}^{\infty} |H_F(\omega)|^2 d\omega$ and $B_e = \frac{1}{2\pi} \int_{-\infty}^{\infty} |H_e(\omega)|^2 d\omega$, where $H_F(\omega)$ and $H_e(\omega)$ are the transfer function of the optical and electrical filter respectively. Because the optical bandwidth is considerably larger than the signal bandwidth, the optical filter won't affect the UWB signal but only the ASE noise. Variance of the ASE-ASE beat noise, $\sigma_{I_{ASE-ASE}}^2(t)$, signal-ASE beat noise, $\sigma_{I_{signal-ASE}}^2(t)$, and electrical noise, σ_{elec}^2 , at the receiver can be expressed as [61]

$$\begin{aligned} \sigma_{I_{ASE-ASE}}^2(t) &= 2G_A \Re^2 N_o^2 \frac{1}{2\pi} \int_{-\infty}^{\infty} |H_e(\omega)|^2 \left(|H_F(\omega)|^2 \otimes |H_F(\omega)|^2 \right) d\omega \\ &= 2G_A \Re^2 N_o^2 (2B_o B_e - B_e^2) \end{aligned} \quad (B.1)$$

$$\begin{aligned} \sigma_{I_{signal-ASE}}^2(t) &= 2G_A \Re^2 \frac{1}{2\pi} N_o \int_{-\infty}^{\infty} |H_F(\omega)|^2 \times |S^*(t) e^{j\omega t} \otimes h_e(t)|^2 d\omega \\ &= 2G_A \Re^2 N_o P_{opt} B_e \end{aligned} \quad (B.2)$$

and

$$\begin{aligned} \sigma_{elec}^2(t) &= \left\{ G_A \text{RIN} \left[\Re P_{opt} + \Re N_o B_o + I_d \right]^2 \right. \\ &\quad \left. + 2G_A q \left[\Re P_{opt} + \Re N_o B_o + I_d \right] + N_{th}^2 \right\} \frac{1}{2\pi} \int_{-\infty}^{\infty} |H_e(\omega)|^2 d\omega \\ &= \left\{ G_A \text{RIN} \left[\Re P_{opt} + \Re N_o B_o + I_d \right]^2 + 2G_A q \left[\Re P_{opt} + \Re N_o B_o + I_d \right] + N_{th}^2 \right\} B_e \end{aligned} \quad (B.3)$$

which consists of contribution of RIN, $G_A \text{RIN} \left[\Re P_{opt} + \Re N_o B_o + I_d \right]^2 B_e$, shot noise, $2G_A q \left[\Re P_{opt} + \Re N_o B_o + I_d \right] B_e$, and thermal noise, $N_{th}^2 B_e$, where $S^*(t)$ is the complex conjugate of the received optical signal at the photodetector, $G_A = 26$ dB is the RF amplifier gain at the optical receiver, P_{opt} is the received optical power, and N_o represents the single sided ASE noise density for a single polarization expressed by $N_o = Fhc(G-1)/(2\lambda)$, h - the Plank's constant, λ - the wavelength of the laser source, c - speed of light in vacuum, and noise figure of $F = 4$ dB and gain of $G = 8$ dB of the EDFA. The symbol \otimes denotes the convolution. σ_{elec}^2 is the noise contribution from both optical transmitter and receiver electronic noise, and this is called "back-

to-back” system noise (shot noise, thermal noise, and RIN). q is the electron charge, and $I_d = 100 \text{ nA}$ is the dark current. The variance of thermal noise is given as $N_{th}^2 = 4k_B T F_n B_e / R_L$, where $k_B = 1.38 \times 10^{-23} \text{ J/K}$ is the Boltzman constant, and $F_n = 5 \text{ dB}$ is noise figure of the RF amplifier at the receiver, T is the room temperature in degree Kelvin, and $R_L = 50 \Omega$ is the load resistance. Now, the total noise power will be given as [61]

$$\sigma_n^2(t) = \sigma_{I_{ASE-ASE}}^2(t) + 2\sigma_{I_{Signal-ASE}}^2(t) + \sigma_{elec}^2(t) \quad (B.4)$$

All calculated receiver noise contributions are presented in Figure B. 1 for the back to back. It is shown that ASE-ASE beat noise is negligible because of the low noise figure of the EDFA and narrow bandwidth of the optical filter used. The output from the RF amplifier at the optical receiver in Figure 2.1 is directly connected to the data analyzer. The scope captures the signal in time domain and performs FFT on it. It analyzes the data within 1.6 GHz bandwidth. The thermal noise within this bandwidth is around -71.2 dBm which is small compared to other noise contributions. It is seen that shot noise, RIN and signal-ASE beat noise are the major sources of noise at the receiver for higher optical power.

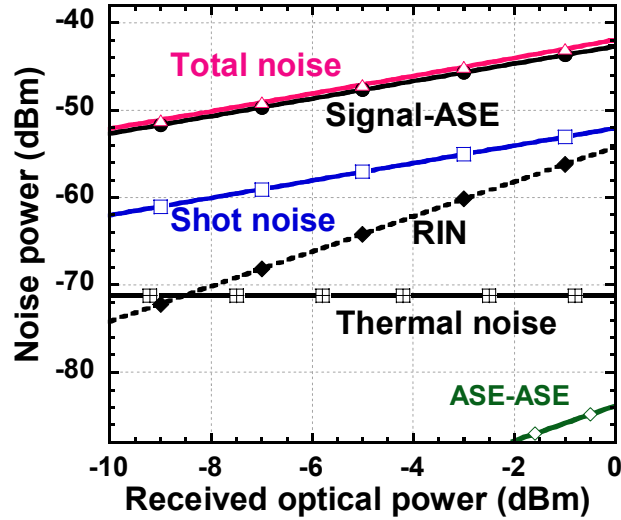


Figure B. 1 Noise power level at the receiver versus received optical power for back-to-back transmission.

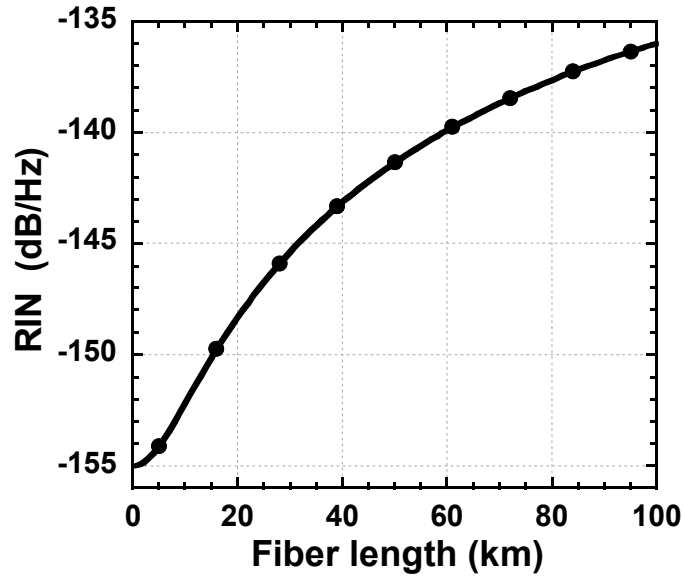


Figure B. 2 Calculated total RIN versus fiber length.

Fiber dispersion changes the laser RIN due phase noise to intensity noise conversion [31-32]. Figure B. 2 shows total RIN due to fiber dispersion for a laser with linewidth of $\Delta\omega/(2\pi)=800$ KHz at 1550 nm by using [31]

$$RIN(L) \approx RIN(0) + \frac{1}{\Omega_u - \Omega_l} \int_{\Omega_l}^{\Omega_u} \frac{8\Delta\omega}{\Omega^2} \sin^2\left(\frac{1}{2}\beta_2 L \Omega^2\right) d\Omega \quad (B.5)$$

where $(\Omega_u - \Omega_l)/2\pi = BW$ is the signal occupied bandwidth, L is the fiber length and $RIN(0) = -155$ dB/Hz is the laser intrinsic RIN.

For the frequency band of 3.176 to 4.744 GHz, the dispersion increases the RIN by 6.7 and 11.8 dB for 20 and 40 km, respectively, compared to the back to back. This is one of the reasons why the EVM degrades with fiber length.

APPENDIX C

We compare the OSSB and ODSB, as commonly used optical external modulation techniques. Figure C. 1(a) and (b) shows measured optical spectrum using OSSB and ODSB, respectively. It is well known that OSSB is used to overcome chromatic dispersion caused power fading by suppression of one of the optical sidebands [1]. However, there is a 3 dB power loss if compared to ODSB. Conversely, ODSB does suffer from power fading specially for back to back because optical sidebands are out of phase and will beat with the optical carrier and add destructively to produce a single RF signal. Figure C. 2 shows comparison of EVM using OSSB and ODSB for back to back and after 20 km of fiber transmission. Figure C. 2 shows that the EVM is -3 dB or 71% at data rate of 200 Mb/s for the back to back with ODSB. At 20 km the EVM is significantly improved compared to the back-to-back because chromatic dispersion of fiber causes each optical sideband to have different phase shift depending on the fiber length, frequency of RF signal and fiber dispersion and thus the power of the detected RF signal changes.

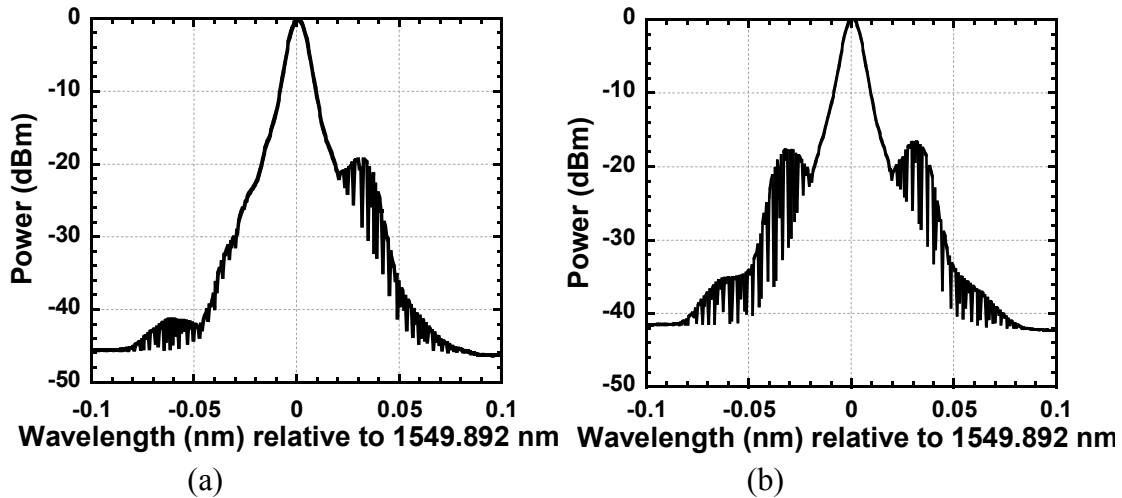


Figure C. 1 Measured optical signal (a) OSSB and (b) ODSB.

In opposition, the OSSB is almost independent of fiber dispersion. As shown in Figure C. 2, the EVM is very close and less than -20 dB for both back-to back and after 20 km of fiber transmission. The power fading in ODSB repeats at periodic fiber lengths and can be compensated using different compensation techniques at the expense of increased complexity

and cost [1]. It is clearly seen from Figure C. 2 that OSSB outperforms ODSB at any power level and fiber length. Therefore only OSSB modulation was considered in Chapter 2.

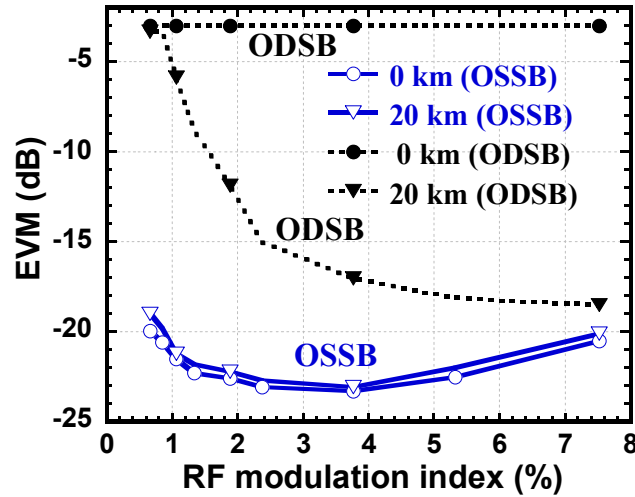


Figure C. 2 Measured EVM using OSSB and ODSB.

With OSSB modulation, the QPSK constellation for data and BPSK constellation for pilots after 20 km at 200 Mb/s is presented in Figure C. 3 (measured with a Lecroy serial data analyzer SDA 11000). The good quality of the constellation is an indication of suitability of the RoF systems for UWB applications.

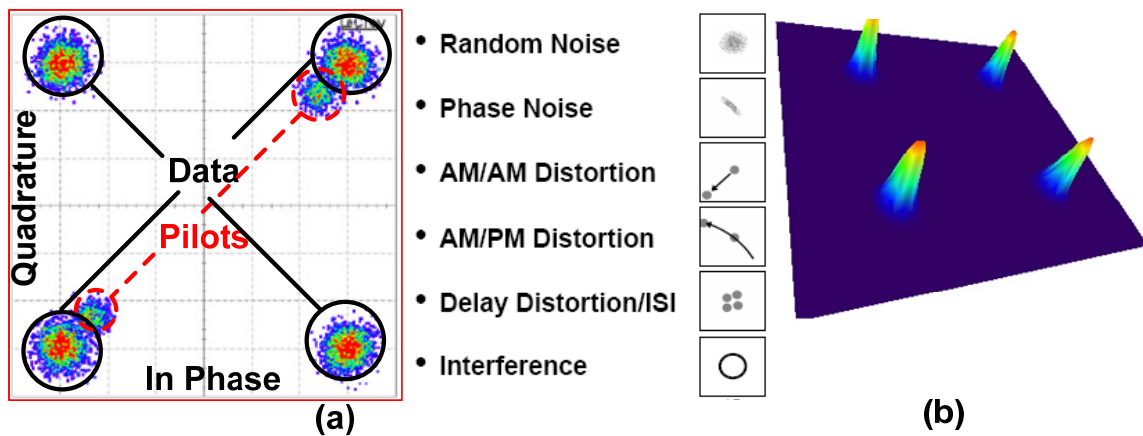


Figure C. 3 QPSK OFDM constellation in a) two dimension b) three dimension received at the real time oscilloscope for band group 1 after 20 Km of fiber transmission with bit rate of 200Mb/s (Colors indicate intensity of power concentration in the received symbol).

APPENDIX D SIMULATED MAGNITUDE AND DELAY RESPONSE OF CHEBYSHEV-II FILTER

Simulated magnitude and delay response of Chebyshev-II filter is presented in Figure D. 1 for third, fifth and seventh order filters with different bandwidths. From Figure D. 1(a) we see Chebyshev-II filter has a flat magnitude response in the passband. Though, out of band ripples increase with filter order, which is not of importance if the side-lobe suppression is higher than the required 20 dB ACPR for WiMedia standard. Figure D. 1(b) shows that the delay increases if the filter order is increased and decreases if the filter bandwidth is increased. Also higher order filters have high delay overshoot at the edges.

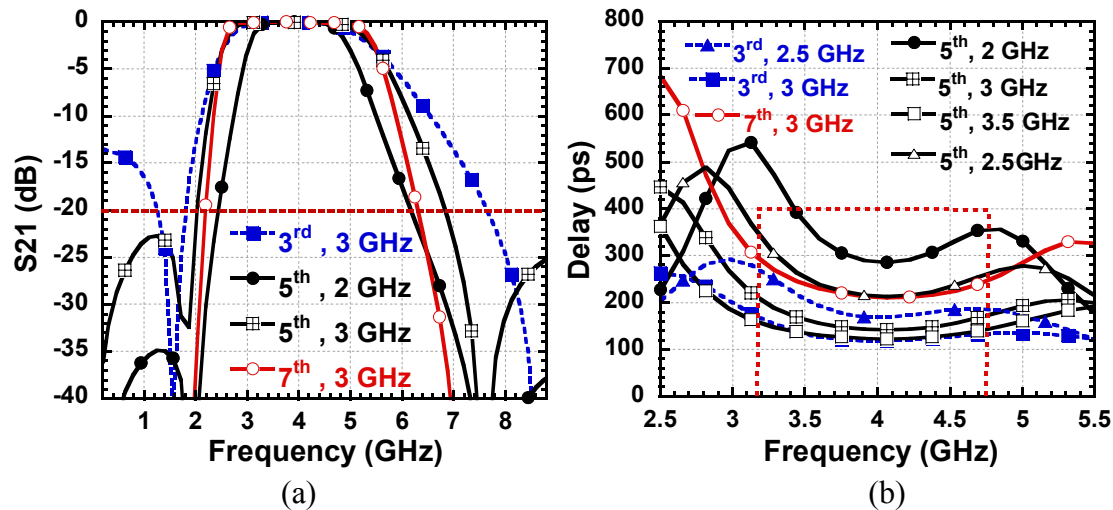


Figure D. 1 Simulated (a) magnitude and (b) delay response of Chebyshev-II filter.

APPENDIX E EXTRACTION OF NONLINEAR TRANSFER FUNCTION OF THE PREDISTORTION CIRCUIT

In this Appendix, we will derive the equations (4.5), (4.6), (4.7) and (4.8). We used the method of nonlinear current source [57] to derive the Volterra series of the voltage at the circuit output, and the coefficient of a_1 and a_3 in the predistortion circuit in (4.2).

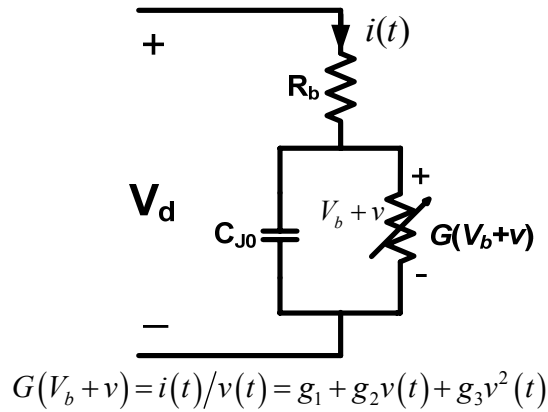


Figure E. 1 Equivalent circuit of the diode, where $G(v)$ indicates the nonlinear conductor of the diode.

The equivalent circuit for one diode is shown in Figure E. 1. R_b is the bulk resistance, C_{j0} is the junction capacitance and $G(V)$ is the nonlinear conductance where $V = V_b + v(t)$, and here we don't consider the inductance and capacitance that come from the diode package. For our used diode, the junction capacitance C_{j0} is 0.1 pF and can be neglected in frequencies of bandgroup 1. We can expand the expression of the V-I characteristic of the diode into Taylor series as,

$$i(t) = I_s e^{\beta(V_b + v(t))} = g_1 v(t) + g_2 v(t)^2 + g_3 v(t)^3 + \dots, \text{ where } g_n = \frac{I_s \beta^n e^{\beta V_b}}{n!}, \text{ } I_s \text{ is the diode reverse}$$

saturation current, and β is the inverse of the thermal voltage V_T , and $\beta = 1/V_T = q/\eta kT$. q is the electron charge, k is the Boltzmann's constant, $1.37 \cdot 10^{-23}$ J/K, and T is the absolute temperature. The factor η (~ 1.08) accounts for the unavoidable imperfections in the junction and other

secondary phenomena. For small signal application, we only consider up to third order, and the nonlinear conductance is then given by $G(V_b + v) = g_1 + g_2 v(t) + g_3 v(t)^2$

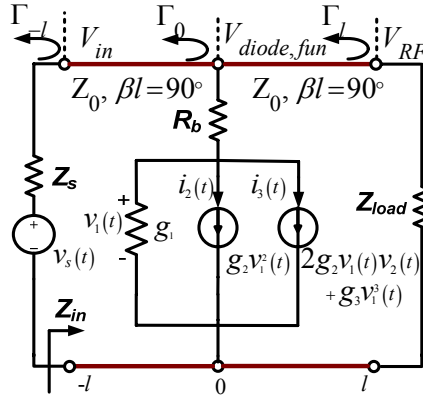


Figure E. 2 Equivalent circuit of the nonlinear diode connected with a voltage source and load.

The Volterra series can be found by using the nonlinear current method [57]. In this method, the nonlinear conductor component is replaced by one linear conductor and several current sources, and the current components are calculated from voltage components of lower order. By substituting the nonlinear conductor G with a conductor g_1 and nonlinear current source $i_2(t)$ and $i_3(t)$ in the predistortion circuit, we can have the equivalent circuit shown in Figure E. 2. In Figure E. 2, a voltage source and load are connected to the nonlinear diode. V_1 is the voltage applied to the conductance g_1 , $Z_{eq} = R_b + 1/g_1$ is the equivalent impedance of the diode, $Z_{load,0}$ is the load impedance at the position of the diode, and $Z_{s,0}$ is the source impedance at the position of the diode. $Z_{eq,total}$ is the total impedance at the position of the diode, and $Z_{eq,total}$ equals Z_{eq} in parallel with $Z_{load,0}$. The reflection coefficient at the diode is Γ_0 , the reflection coefficient at the source is Γ_{-l} , and the reflection coefficient at the load is Γ_l . V_{in} is the total voltage coming out from the RF source.

Now we compute Z_{in} . The $l = \lambda/4$ transmission line is used for impedance matching between the load and the diode, then $Z_{load,0} = Z_0^2 / Z_{load}$.

The total impedance at the position of the diode $Z_{total,0}$ equals the equivalent impedance of the diode $Z_{eq} = R_b + 1/g_1$ in parallel with $Z_{load,0}$, then

$$Z_{total,0} = \frac{Z_{load,0}Z_{eq}}{Z_{load,0} + Z_{eq}} = \frac{(1 + g_1R_b)Z_0^2}{(1 + g_1R_b)Z_{load} + g_1Z_0^2} \quad (E.1)$$

another $l = \lambda / 4$ transmission line is used for impedance matching between the source and the diode, then using (E.1) the input impedance is

$$Z_{in} = \frac{Z_0^2}{Z_{total,0}} = Z_{load} + \frac{g_1Z_0^2}{1 + g_1R_b} \quad (E.2)$$

and the voltage applied at the input of the circuit is

$$V_{in} = \frac{Z_{in}}{(Z_{in} + Z_s)} V_s = \frac{Z_{load}(1 + g_1R_b) + g_1Z_0^2}{(Z_s + Z_{load})(1 + g_1R_b) + g_1Z_0^2} V_s \quad (E.3)$$

To find the voltage of the fundamental carrier and IMD3 at the circuit output, we first need to find the voltage $V_{diode,fun}$ of the fundamental carrier applied to the diode.

Using the transmission line theory [30] with $V_{diode,fun,0}^+$ and $V_{diode,fun,0}^-$ representing the incident and reflected voltage at the position of the diode, the input voltage can be expressed as

$$V_{in} = V_{diode,fun,0}^+ e^{j\frac{\pi}{2}} + V_{diode,fun,0}^- e^{-j\frac{\pi}{2}} = jV_{diode,fun,0}^+ [1 - \Gamma_0] \quad (E.4)$$

$$\text{where } \Gamma_0 = \frac{Z_{total,0} - Z_0}{Z_{total,0} + Z_0}$$

On the other hand, the incident and reflected voltages at the position of the diode can be expressed, respectively, as

$$V_{diode,fun,0}^+ = -j \frac{V_{in}}{1 - \Gamma_0} \quad (E.5)$$

$$V_{diode,fun,0}^- = -j \frac{\Gamma_0 V_{in}}{1 - \Gamma_0} \quad (E.6)$$

then the voltage applied to the diode $V_{diode,fun}$ is expressed by

$$\begin{aligned}
V_{diode,fun} &= V_{diode,fun,0}^+ + V_{diode,fun,0}^- \\
&= -j \frac{1+\Gamma_0}{1-\Gamma_0} V_{in} \\
&= -j \frac{Z_{total,0}}{Z_0} V_{in} \\
&= -j \frac{Z_0}{Z_{in}} V_{in}
\end{aligned} \tag{E.7}$$

Using equations (E.2) and (E.3) in equation (E.7) the applied voltage to the diode becomes

$$V_{diode,fun} = -j \frac{(1+g_1 R_b) Z_0 V_s}{(Z_s + Z_{load})(1+g_1 R_b) + g_1 Z_0^2} \tag{E.8}$$

In similar way using the transmission line theory [30] with $V_{RF,fun}^+$ and $V_{RF,fun}^-$ representing the incident and reflected voltage at the position of the load, $V_{RF,fun}$ can be calculated. The applied voltage to the diode can be rewritten

$$V_{diode,fun} = V_{RF,fun}^+ e^{j\frac{\pi}{2}} + V_{RF,fun}^- e^{-j\frac{\pi}{2}} = j V_{RF,fun}^+ [1 - \Gamma_l] \tag{E.9}$$

$$\text{where } \Gamma_l = \frac{Z_{load} - Z_0}{Z_{load} + Z_0}$$

then the incident and reflected voltage at the position of the load can be expressed, respectively, as

$$V_{RF,fun}^+ = -j \frac{V_{diode,fun}}{1 - \Gamma_l} \tag{E.10}$$

$$\text{and } V_{RF,fun}^- = -j \frac{\Gamma_l V_{diode,fun}}{1 - \Gamma_l} \tag{E.11}$$

then the voltage applied to the load $V_{RF,fun}$ is simply expressed by

$$\begin{aligned}
V_{RF,fun} &= V_{RF,fun}^+ + V_{RF,fun}^- \\
&= -j \frac{1+\Gamma_l}{1-\Gamma_l} V_{diode,fun} \\
&= -j \frac{Z_{load}}{Z_0} V_{diode,fun} \\
&= - \frac{(1+g_1 R_b) Z_{load} V_s}{(Z_s + Z_{load})(1+g_1 R_b) + g_1 Z_0^2}
\end{aligned} \tag{E.12}$$

This is equation (4.5)

For the input RF signal with multi-tones, i.e., $v_s(t) = \frac{1}{2} \sum_{q=-Q}^Q V_{s,q} \exp(j\omega_q t)$, using (E.8) the voltage on the diode $v_{diode,fun}(t)$ can be expressed

$$v_{diode,fun}(t) = -j \frac{1}{2} \frac{(1 + g_1 R_b) Z_o}{(Z_s + Z_{load})(1 + g_1 R_b) + g_1 Z_o^2} \sum_{q=-Q}^Q V_{s,q} \exp(j\omega_q t) \quad (E.13)$$

Then the voltage $v_1(t)$ applied to the conductance g_1 is

$$\begin{aligned} v_1(t) &= \frac{v_{diode,fun}(t)}{1 + R_b g_1} \\ &= -j \frac{1}{2} \frac{Z_o}{(Z_s + Z_{load})(1 + g_1 R_b) + g_1 Z_o^2} \sum_{q=-Q}^Q V_{s,q} \exp(j\omega_q t) \end{aligned} \quad (E.14)$$

and the current source $i_2(t)$ can be expressed

$$\begin{aligned} i_2(t) &= g_2 v_1^2(t) \\ &= -\frac{1}{4} g_2 \frac{Z_o^2}{[(Z_s + Z_{load})(1 + g_1 R_b) + g_1 Z_o^2]^2} \\ &\quad \times \sum_{q_1=-Q}^Q \sum_{q_2=-Q}^Q V_{s,q_1} V_{s,q_2} \exp[j(\omega_{q_1} + \omega_{q_2})t] \end{aligned} \quad (E.15)$$

Correspondingly the equivalent voltage $v_2(t)$, applied on the conductance g_1 due to current source $i_2(t)$, can be computed by finding equivalent impedance loading $i_2(t)$ by using Thevenin's theorem. This impedance is g_1 parallel to Z_t which is the $Z_{s,0}$ (the $\lambda/4$ transformed Z_s) in parallel with $Z_{load,0}$ (the $\lambda/4$ transformed Z_{load}) in series with R_b

$$Z_t = \frac{1}{1/Z_{s,0} + 1/Z_{load,0}} + R_b = \frac{Z_o^2}{Z_{load} + Z_s} + R_b \quad (E.16)$$

Then

$$\begin{aligned}
v_2(t) &= \frac{-Z_t}{Z_t g_1 + 1} i_2(t) \\
&= \frac{1}{4} g_2 \frac{Z_0^2 [Z_0^2 + R_b (Z_s + Z_{load})]}{[(Z_s + Z_{load})(1 + g_1 R_b) + g_1 Z_0^2]^3} \sum_{q_1=-Q}^Q \sum_{q_2=-Q}^Q V_{s,q_1} V_{s,q_2} \exp[j(\omega_{q_1} + \omega_{q_2})t]
\end{aligned} \tag{E.17}$$

Now we have the voltages $v_1(t)$ and $v_2(t)$, we can compute the current $i_3(t)$

$$\begin{aligned}
i_3(t) &= 2g_2 v_1(t) v_2(t) + g_3 v_1^3(t) \\
&= \frac{j}{8} \frac{Z_0^3}{[g_1 Z_0^2 + (1 + g_1 R_b)(Z_s + Z_{load})]^4} \\
&\quad \times \left[(g_1 g_3 - 2g_2^2) Z_0^2 + [g_3(1 + g_1 R_b) - 2g_2^2 R_b] (Z_s + Z_{load}) \right] \\
&\quad \times \sum_{q_1=-Q}^Q \sum_{q_2=-Q}^Q \sum_{q_3=-Q}^Q V_{s,q_1} V_{s,q_2} V_{s,q_3} \exp[j(\omega_{q_1} + \omega_{q_2} + \omega_{q_3})t]
\end{aligned} \tag{E.18}$$

By using circuit theory the third order nonlinear product voltage generated by $i_3(t)$ at the diode can be expressed

$$\begin{aligned}
v_{diode,3}(t) &= \frac{1/Z_t}{1/Z_{s,0} + 1/Z_{load,0}} \frac{Z_t}{1 + Z_t g_1} i_3(t) \\
&= \frac{j}{8} \frac{Z_0^5}{[g_1 Z_0^2 + (1 + g_1 R_b)(Z_s + Z_{load})]^5} \\
&\quad \times \left[(g_1 g_3 - 2g_2^2) Z_0^2 + [g_3(1 + g_1 R_b) - 2g_2^2 R_b] (Z_s + Z_{load}) \right] \\
&\quad \times \sum_{q_1=-Q}^Q \sum_{q_2=-Q}^Q \sum_{q_3=-Q}^Q V_{s,q_1} V_{s,q_2} V_{s,q_3} \exp[j(\omega_{q_1} + \omega_{q_2} + \omega_{q_3})t]
\end{aligned} \tag{E.19}$$

Then after the $l = \lambda / 4$ transmission line, using the same microwave transmission line theory [30] used to get equation (E.7) and (E.12), the third order nonlinear distortion voltage at the circuit output can be expressed in Volterra Series as

$$\begin{aligned}
v_{RF,3}(t) &= j \frac{Z_{load}}{Z_0} v_{diode,3}(t) \\
&= -\frac{1}{8} \frac{Z_{load} Z_0^4}{\left[g_1 Z_0^2 + (1 + g_1 R_b)(Z_s + Z_{load}) \right]^5} \\
&\quad \times \left[(g_1 g_3 - 2g_2^2) Z_0^2 + \left[g_3 (1 + g_1 R_b) - 2g_2^2 R_b \right] (Z_s + Z_{load}) \right] \\
&\quad \times \sum_{q_1=-Q}^Q \sum_{q_2=-Q}^Q \sum_{q_3=-Q}^Q V_{s,q_1} V_{s,q_2} V_{s,q_3} \exp \left[j(\omega_{q_1} + \omega_{q_2} + \omega_{q_3})t \right]
\end{aligned} \tag{E.20}$$

The voltage in (E.20) includes all third-order nonlinear products. But we are only concerned in a special case where the RF signal consists of two tones at ω_1 and ω_2 with equal magnitude. We may not be concerned in all the third order nonlinear products. The most important third-order nonlinear products are IMD3 at frequency of $2\omega_2 - \omega_1$ and $2\omega_1 - \omega_2$. Suppose that these two third order nonlinear products are equal in voltage with $V_{diode,IMD3}$. Using (E.20) we can find the voltage of IMD3 at the load,

$$\begin{aligned}
V_{RF,IMD3} &= -\frac{3}{4} \frac{Z_{load} Z_0^4 V_s^3}{\left[g_1 Z_0^2 + (1 + g_1 R_b)(Z_s + Z_{load}) \right]^5} \\
&\quad \times \left[(g_1 g_3 - 2g_2^2) Z_0^2 + \left[g_3 (1 + g_1 R_b) - 2g_2^2 R_b \right] (Z_s + Z_{load}) \right]
\end{aligned} \tag{E.21}$$

This is equation (4.6).

Using (E.2) we can rewrite (E.12) and (E.21) in terms of V_{in} , respectively, as

$$V_{RF,fun} = -\frac{(1 + g_1 R_b) Z_{load} V_{in}}{Z_{load} (1 + g_1 R_b) + g_1 Z_0^2} \tag{E.22}$$

$$\begin{aligned}
V_{RF,IMD3} &= -\frac{3}{4} \frac{Z_{load} Z_0^4 V_{in}^3}{\left[g_1 Z_0^2 + (1 + g_1 R_b)(Z_s + Z_{load}) \right]^5} \\
&\quad \times \frac{\left[(g_1 g_3 - 2g_2^2) Z_0^2 + \left[g_3 (1 + g_1 R_b) - 2g_2^2 R_b \right] (Z_s + Z_{load}) \right]}{\left[Z_{load} (1 + g_1 R_b) + g_1 Z_0^2 \right]^3}
\end{aligned} \tag{E.23}$$

For an RF input signal to the predistortion circuit with two tones at ω_1 and ω_2 with equal magnitude V_{in} , the coefficient in (4.2) are $a_1 = \frac{V_{RF,fun}}{V_{in}}$ and $a_3 = \frac{4}{3} \frac{V_{RF,IMD3}}{V_{in}^3}$ using (E. 22) and (E.23) we get

$$a_1 = -\frac{(1+g_1 R_b) Z_{load}}{Z_{load} (1+g_1 R_b) + g_1 Z_0^2} \quad (E.24)$$

$$a_3 = -\frac{Z_{load} Z_0^4}{\left[g_1 Z_0^2 + (1+g_1 R_b) (Z_s + Z_{load}) \right]^2} \quad (E.25)$$

$$\times \frac{\left[(g_1 g_3 - 2g_2^2) Z_0^2 + \left[g_3 (1+g_1 R_b) - 2g_2^2 R_b \right] (Z_s + Z_{load}) \right]}{\left[Z_{load} (1+g_1 R_b) + g_1 Z_0^2 \right]^3}$$

These are equations (4.7) and (4.8), respectively.

APPENDIX F DERIVATION OF OPTIMAL PHASE SHIFT AND IMPROVED POWER EFFICIENCY

In this Appendix we show the derivation details of how to obtain equation (5.1). Let $m = \pi m_{RF}/2$, where $m_{RF} = \sqrt{2} V_{RF}/V_{\pi}$ is the modulation index, and V_{π} the halfwave switching voltage of the DE-MZM. The total RF signal applied to upper and lower electrodes of the DE-MZM can be expressed, respectively, as

$$\begin{aligned} & m \sin(\omega_{RF}t + \theta + \pi/2) + m \sin(\omega_{RF}t + \theta + \varphi) \\ &= 2m \sin(\omega_{RF}t + \theta + \varphi/2 + \pi/4) \sin(\varphi/2 + \pi/4) \end{aligned} \quad (F.1)$$

and

$$\begin{aligned} & m \sin(\omega_{RF}t + \theta) + m \sin(\omega_{RF}t + \theta + \varphi + \pi/2) \\ &= 2m \sin(\omega_{RF}t + \theta + \varphi/2 + \pi/4) \cos(\varphi/2 + \pi/4) \end{aligned} \quad (F.2)$$

Then the output optical field from the DE-MZM can be written as

$$E_{out}(t) = \sqrt{\frac{t_{ff} P_{in}}{1 + \delta^2}} e^{j(\omega_c t + \phi_c)} \left[\exp\{j2m \sin(\omega_{RF}t + \theta + \varphi/2 + \pi/4) \sin(\varphi/2 + \pi/4)\} + j\delta \exp\{j2m \sin(\omega_{RF}t + \theta + \varphi/2 + \pi/4) \cos(\varphi/2 + \pi/4)\} \right] \quad (F.3)$$

where $\delta = (\sqrt{ER} - 1)/(\sqrt{ER} + 1)$, ER is the DE-MZM extinction ratio, P_{in} is the input optical power to the DE-MZM, t_{ff} is the optical insertion loss of the DE-MZM. The output signal of the DE-MZM is transmitted through an SMF. By applying the Jacobi-Anger expansion

$$\exp\{jx \sin(\Omega t)\} = \sum_{n=-\infty}^{\infty} J_n(x) \exp(jn\Omega t) \quad (F.4)$$

to (F.3), where $J_n(\cdot)$ is the n^{th} order Bessel function of first kind, the output optical field from the DE-MZM becomes

$$\begin{aligned} E_{out}(t) &= \sum_{n=-\infty}^{\infty} E_n(t) \\ &= \sqrt{\frac{t_{ff} P_{in}}{1 + \delta^2}} e^{j(\omega_c t + \phi_c)} \sum_{n=-\infty}^{\infty} \left\{ J_n(m \sin(\varphi/2 + \pi/4)) + j\delta J_n(m \cos(\varphi/2 + \pi/4)) \right\} \\ &\quad \times \exp\{jn(\omega_{RF}t + \theta + \varphi/2 + \pi/4)\} \end{aligned} \quad (F.5)$$

By only considering the optical carrier and the two first sidebands, the complex amplitude of the photo-detected current at the RF frequency ω_{RF} is expressed as

$$\begin{aligned}
 I_{\omega_{RF}}(t) &= \frac{1}{2} \Re \left[E_0^*(t) E_1(t) \exp \left\{ -j \left(\frac{1}{2} \beta_2 L \omega_{RF}^2 + \beta_1 L \omega_{RF} \right) \right\} \right. \\
 &\quad \left. + E_{-1}^*(t) E_0(t) \exp \left\{ j \left(\frac{1}{2} \beta_2 L \omega_{RF}^2 - \beta_1 L \omega_{RF} \right) \right\} \right] \\
 &= \frac{1}{2} \Re \frac{P_{in} t_{ff} e^{-\alpha L}}{1 + \delta^2} (Z - Z^*) \exp \{ j(\varphi/2 + \pi/4) \} \exp \{ j(\omega_{RF}(t - \beta_1 L) + \theta) \} \quad (F.6) \\
 &= \Re \frac{P_{in} t_{ff} e^{-\alpha L}}{1 + \delta^2} \text{Im}(Z) \exp \{ j(\varphi/2 + 3\pi/4) \} \exp \{ j(\omega_{RF}(t - \beta_1 L) + \theta) \}
 \end{aligned}$$

where \Re is responsivity of the photodetector, α is the fiber loss, L/β_1 is the fiber group delay, $\beta_2 = -\lambda_c^2 D / (2\pi c)$, λ_c is the optical wavelength, c - the speed of light in vacuum, L and D - fiber length and chromatic dispersion, respectively, Z^* stands for complex conjugate of Z and

$$\begin{aligned}
 Z &= \left[J_0(2m \sin(\varphi/2 + \pi/4)) - j\delta J_0(2m \cos(\varphi/2 + \pi/4)) \right] \\
 &\quad \times \left[J_1(2m \sin(\varphi/2 + \pi/4)) + j\delta J_1(2m \cos(\varphi/2 + \pi/4)) \right] \exp(j\theta_2) \quad (F.7) \\
 &= \sqrt{A^2 + B^2} \exp \{ j(\theta_2 + \psi) \}
 \end{aligned}$$

$$\theta_2 = -\frac{1}{2} \beta_2 L \omega_{RF}^2 \quad (F.8)$$

$$A = \left[J_0(2m \sin(\varphi/2 + \pi/4)) J_1(2m \sin(\varphi/2 + \pi/4)) \right. \\
 \left. + \delta^2 J_0(2m \cos(\varphi/2 + \pi/4)) J_1(2m \cos(\varphi/2 + \pi/4)) \right] \quad (F.9)$$

$$B = \delta \left[J_0(2m \sin(\varphi/2 + \pi/4)) J_1(2m \cos(\varphi/2 + \pi/4)) \right. \\
 \left. - J_0(2m \cos(\varphi/2 + \pi/4)) J_1(2m \sin(\varphi/2 + \pi/4)) \right] \quad (F.10)$$

and

$$\psi = \tan^{-1}(B/A) \quad (F.11)$$

Then the photocurrent can be rewritten as

$$\begin{aligned}
 I_{\omega_{RF}}(t) &= \Re \frac{P_{in} t_{ff} e^{-\alpha L}}{1 + \delta^2} \sqrt{A^2 + B^2} \sin(\psi + \theta_2) \\
 &\quad \times \exp \{ j(\omega_{RF}(t - \beta_1 L) + \theta + \varphi/2 + 3\pi/4) \} \quad (F.12)
 \end{aligned}$$

Thus maximum photocurrent amplitude can be reached if and only if $|\sin(\psi + \theta_2)| = 1$, which implies

$$\cos(\psi + \theta_2) = 0 \quad (\text{F.13})$$

This leads to the following expression

$$\tan \psi = B/A = 1/\tan \theta_2 \quad (\text{F.14})$$

By using the small signal condition i.e. $2m \ll 1$, we can write $J_n(z) \sim (z/2)^n/n!$ and applying to (F.9) and (F.10) the equation (F.14) can be simplified to

$$\frac{[(1 + \delta^2) + (1 - \delta^2) \tan(\varphi/2)]}{-2\delta \tan(\varphi/2)} = \tan \theta_2 \quad (\text{F.15})$$

which can be solved for φ as

$$\varphi = -2 \tan^{-1} \left[(1 + \delta^2) / (1 - \delta^2 + 2\delta \tan \theta_2) \right] \quad (\text{F.16})$$

This is expression (5.1) of the required electrical phase shift to maximize the output RF power and compensate for chromatic dispersion induced power fading.

Next, we show the derivation details of how to obtain equation (5.2). First we compute the RF output power when using the proposed ODSB. Using (F.14) and (F.10) we can write

$$\begin{aligned} A^2 + B^2 &= (1 + \tan^2 \theta_2) B^2 \\ &= 2m^2 \delta^2 \sin^2(\varphi/2) (1 + \tan^2 \theta_2) \end{aligned} \quad (\text{F.17})$$

Using (F.15) the above can be rewritten

$$\begin{aligned} A^2 + B^2 &= \frac{1}{2} m^2 \sin^2(\varphi/2) \frac{[(1 + \delta^2)^2 (1 + \tan^2(\varphi/2)) + 2(1 - \delta^4) \tan(\varphi/2)]}{\tan^2(\varphi/2)} \\ &= \frac{1}{2} (1 + \delta^2)^2 m^2 \left[1 + \frac{1 - \delta^2}{1 + \delta^2} \sin \varphi \right] \end{aligned} \quad (\text{F.18})$$

Hence using (F.18) in (F.12), the photocurrent can be expressed as

$$|I_{\omega_{RF}}| = \frac{1}{\sqrt{2}} P_{in} \Re t_{ff} \exp(-\alpha L) m \sqrt{F(\varphi)} \quad (\text{F.19})$$

where

$$F(\varphi) = 1 + \frac{1 - \delta^2}{1 + \delta^2} \sin \varphi \quad (\text{F.20})$$

and the corresponding RF output power is expressed as

$$\begin{aligned} P_{\omega_{RF}} &= 2 |I_{\omega_{RF}}|^2 R_L \\ &= \frac{1}{4} (P_{in} \Re t_{ff} \exp(-\alpha L) \pi m_{RF})^2 F(\varphi) R_L \end{aligned} \quad (\text{F.21})$$

where R_L is the resistance load of the receiver.

Next we compute the RF output power when using OSSB modulation. For OSSB modulation the optical field after the MZM can be expressed, by using Jacobi-Anger expansion (F.4), as

$$\begin{aligned} E_{out}(t) &= \sqrt{\frac{P_{in} t_{ff}}{1 + \delta^2}} e^{j(\omega_c t + \phi_c)} \left[\exp\{j\sqrt{2}m \sin(\omega_{RF} t + \theta)\} \right. \\ &\quad \left. + \delta \exp\{j(\sqrt{2}m \sin(\omega_{RF} t + \theta + \pi/2) + \pi/2)\} \right] \\ &= \sqrt{\frac{P_{in} t_{ff}}{1 + \delta^2}} e^{j(\omega_c t + \phi_c)} \sum_{n=-\infty}^{\infty} (1 + j^{n+1} \delta) J_n(\sqrt{2}m) \exp\{jn(\omega_{RF} t + \theta)\} \end{aligned} \quad (\text{F.22})$$

The optical field at the photodetector can be expressed as

$$E_{link}(t) = \exp(-\alpha L/2) \sum_{n=-\infty}^{\infty} E_n(t) \exp\left\{-j\left(\frac{1}{2} \beta_2 L (n\omega_{RF})^2 + \beta_1 L n\omega_{RF}\right)\right\} \quad (\text{F.23})$$

where

$$E_n(t) = \sqrt{\frac{P_{in} t_{ff}}{1 + \delta^2}} (1 + j^{n+1} \delta) J_n(\sqrt{2}m) \exp\{jn(\omega_{RF} t + \theta)\} e^{j(\omega_c t + \phi_c)} \quad (\text{F.24})$$

By only considering the optical carrier and the two first sidebands, the complex amplitude of the photo-detected current at the RF frequency ω_{RF} is expressed as

$$\begin{aligned}
I_{\omega_{RF}}(t) &= \frac{1}{2} \Re \exp(-\alpha L) \left[\begin{array}{l} E_0(t) E_{-1}^*(t) \exp(-j\theta_2) \\ + E_1(t) E_0^*(t) \exp(j\theta_2) \end{array} \right] \\
&= \frac{\Re P_{in} t_{ff} \exp(-\alpha L)}{2(1+\delta^2)} J_0(\sqrt{2}m) J_1(\sqrt{2}m) \left[\begin{array}{l} (1-\delta)(1-j\delta) \exp(j\theta_2) \\ -(1+\delta)(1+j\delta) \exp(-j\theta_2) \end{array} \right] \\
&\quad \times \exp\{j(\omega_{RF}(t - \beta_1 L) + \theta)\}
\end{aligned} \tag{F.25}$$

Under the small signal assumption the amplitude of the photocurrent can be approximated by

$$|I_{\omega_{RF}}| = \frac{\Re P_{in} t_{ff} \exp(-\alpha L)}{1+\delta^2} \frac{m}{2\sqrt{2}} \sqrt{C} \tag{F.26}$$

where

$$C = 2(1+\delta^2)^2 - 2(1-\delta^2) \left[(1-\delta^2) \cos(2\theta_2) + 2\delta \sin(2\theta_2) \right] \tag{F.27}$$

Applying the following identities to (F.27)

$$\cos(2\theta) = \frac{1 - \tan^2 \theta}{1 + \tan^2 \theta} \tag{F.28}$$

$$\sin(2\theta) = \frac{2 \tan \theta}{1 + \tan^2 \theta} \tag{F.29}$$

And using (F.15), (F.27) can be rewritten, after some calculations and rearrangements, as

$$\begin{aligned}
C &= 2(1+\delta^2)^2 + 2(1-\delta^2) \times \frac{\left[(1-\delta^2)(1 + \tan^2(\varphi/2)) + 2(1+\delta^2) \tan(\varphi/2) \right]}{(1+\delta^2)^2 (1 + \tan^2(\varphi/2)) + 2(1-\delta^4) \tan(\varphi/2)} \\
&= 2(1+\delta^2)^2 + 2(1-\delta^2) \frac{\left[(1-\delta^2) + (1+\delta^2) \sin \varphi \right]}{(1+\delta^2)^2 + (1-\delta^4) \sin \varphi}
\end{aligned} \tag{F.30}$$

Replacing (F.30) into (F.26) the amplitude of the photocurrent can be rewritten as

$$|I_{\omega_{RF}}| = \frac{1}{2} P_{in} \Re t_{ff} \exp(-\alpha L) m \sqrt{\frac{1 + \left(\frac{1-\delta^2}{1+\delta^2} \right)^2 + 2 \left(\frac{1-\delta^2}{1+\delta^2} \right) \sin \varphi}{1 + \left(\frac{1-\delta^2}{1+\delta^2} \right) \sin \varphi}} \tag{F.31}$$

and the RF output power is expressed as

$$P_{\omega_{RF}}^{SSB} = \frac{1}{4} \left(P_{in} \Re t_{ff} \exp(-\alpha L) G \pi m_{RF} \right)^2 G(\varphi) R_L \tag{F.32}$$

where φ is the electrical phase shift given by (E.16) and

$$G(\varphi) = \frac{1}{2} \left(\frac{1 + \left(\frac{1-\delta^2}{1+\delta^2} \right)^2 + 2 \left(\frac{1-\delta^2}{1+\delta^2} \right) \sin \varphi}{1 + \left(\frac{1-\delta^2}{1+\delta^2} \right) \sin \varphi} \right) \quad (\text{F.33})$$

Then the ratio of the RF output power of the proposed ODSB (F.21) to that of the conventional OSSB (F.32) is

$$\eta = \frac{P_{\omega_{RF}}}{P_{\omega_{RF}}^{SSB}} = \frac{F(\varphi)}{G(\varphi)} = \frac{\left(1 + \delta^2 + (1 - \delta^2) \sin \varphi \right)^2}{1 + \delta^4 + (1 - \delta^4) \sin \varphi} \quad (\text{F.34})$$

This is the improvement of the RF power given in equation (5.2).

The variation of function η versus φ is summarized in Table F. 1.

As can be seen from Table F. 1 the function η reaches maximum of 2 and minimum of $8\delta^2/(1+\delta^2)^2 = 2((ER-1)/(ER+1))^2$ at $\sin^{-1}((\delta^2-1)/(1+\delta^2))$ and $\pm\pi/2$, respectively. For high extinction ratios we have $\delta \sim 1$ and $\eta(\varphi) \sim 2$.

Table F. 1 Variation of function η versus φ .

φ	$-\pi$	$-\pi/2$	$\sin^{-1}\left(\frac{\delta^2-1}{1+\delta^2}\right)$	0	$\pi/2$	π
$\frac{d\eta(\varphi)}{d\varphi}$	+	0	- 0 +	+	0	-
$\eta(\varphi)$	$\frac{(1+\delta^2)^2}{(1+\delta^4)}$	2	$\frac{8\delta^2}{(1+\delta^2)^2}$	$\frac{(1+\delta^2)^2}{(1+\delta^4)}$	2	$\frac{(1+\delta^2)^2}{(1+\delta^4)}$